UNIVERSIDADE FEDERAL DE MINAS GERAIS
INSTITUTO DE GEOCIÊNCIAS
PROGRAMA DE PÓS-GRADUAÇÃO EM GEOLOGIA

TESE DE DOUTORADO

Gênese e evolução do depósito arqueano aurífero Lamego: Mapeamento litoestrutural, modelamento 3D, geocronologia, paragênese mineral, mapas químicos e ablação a laser em sulfetos.

Autor: Breno de Souza Martins
Orientação: Lydia Maria Lobato
Coorientação: Carlos Alberto Rosière

BELO HORIZONTE
DATA: 21 de março de 2016

Agradecimentos

Ensinar é mais do que uma profissão, é uma arte à qual se dedica o Professor que não está disposto somente a orientar e ensinar, mas principalmente que está disposto a aprender. Então deixo aqui registrado com muito orgulho o meu humilde e sincero agradecimento à professora e amiga ***Lydia Maria Lobato***. Com toda a calma e paciência do mundo, dedicação e bom humor, conduziu com tanta perfeição e brilhantismo este trabalho ao longo dos últimos anos. Mesmo que às custas de um bom café para despertar e animar quando o cansaço batia após um árduo dia de discussões, não deixou faltar alegria e uma palavra amiga, me acompanhando até o fim desta jornada. Muito obrigado!!!!

Aos coorientadores no Brasil professores ***Carlos Alberto Rosière*** e ***Rosaline Cristina Figueiredo e Silva***, pelas orientações, questionamentos e discussões ao longo desses últimos anos, que contribuíram de forma inequívoca para este trabalho.

Ao coorientador e amigo na Austrália Prof. ***Steffen Hangmann***, que me recebeu de braços abertos com muita simplicidade e afeição no seu jeito risonho e brincalhão brasileiro-germânico de ser. *Many thanks man*!

Aos amigos e companheiros de pesquisa ***João Orestes Santos*** (Curtin University) e ***Malcolm Roberts*** (University of Western Australia) que tanto ajudaram, respectivamente, nos estudos e interpretações de dados geocronológicos e de microssonda eletrônica de varredura.

A minha noiva e amiga ***Bruna Ketlyn Silva Cota*** pela paciência, compreensão e companheirismo. Que não pensou duas vezes em largar tudo no Brasil, família e amigos, e viajar correndo para a Austrália onde tanto me amparou nos momentos difíceis, além de ajudar na confecção e diagramação de figuras que ilustram esse volume.

A amiga geóloga ***Poliany Morais Figueiredo*** que, após cinco anos distantes a encontrei na Austrália, e tanto suporte deu na construção do modelo 3D através do *software* Leapfrog Geo®.

Aos amigos geólogos ***Franco Andre Pacheco Ortiz*** e ***Juliana Pertile*** pelos bons momentos compartilhados regados a vinho, cerveja e churrasco durante nossa estadia no Center for Exploration Targeting (CET). Sem contar as agradáveis noites de sextas feiras no "*balconi"* onde em conjunto com ***Paul Durring***, ***Thomas Angerer***, ***Raphael Baumgartner*** dentre outros nos divertimos tanto.

Aos amigos geólogos do grupo de pesquisa em metalogenia da UFMG nomeadamente ***Yuri Ribeiro***, ***Monica Mendes***, ***Milton Morales***, ***Sergio Martins***, ***Marcos Aurélio***, ***Jorge Roncato***, ***André Vitórino*** e mais recentemente a amiga mineralogista ***Carolin Kresse***, grupo que com bom humor e

lealdade tantos tanto tem contribuído para entender as mineralizações de ferro e ouro do Quadrilátero Ferrífero.

Ao programa de Pós-graduação em Geologia, no nome do professor ***Mário Luiz de Sá Carneiro Chaves***, pela paciência, compreensão e ajuda nos momentos em que os prazos estavam curtos e era necessária alguma declaração e-ou informação de última hora. Muito obrigado professor por sempre estar à disposição para socorrer da melhor forma possível.

Agradecimentos a toda equipe do Centro de Microscopia da UFMG, além do técnico ***Breno Moreira*** que tanto auxiliou na realização dos trabalhos de imageamento de minerais.

Um especial agradecimento ao geólogo ***Orivaldo Baltazar*** da CPRM que sempre esteve a disposição para discutir e ensinar sobre a geologia do Quadrilátero Ferrífero, em especial sobre o *greenstone belt* Rio das Velhas.

Ao CNPq pela bolsa de doutorado recebido e à CAPES, através do Programa Ciência sem Fronteiras, pela bolsa concedida para realização de doutorado sanduíche na Austrália (CSF SDW nº 0451/13-4).

Ao geólogos e amigos da AngloGold Ashanti, por parte da exploração, ***Rodrigo Martins*** e ***Juliano Maciel***, da mina do Lamego ***Lucas Lemos***, ***Fernando Villanova*** e ***Jorge Watanabe***, e da mina Cuiabá ***Raphael***, meu muito obrigado pelo suporte de logística e acesso às dependências da empresa para coleta de amostras, mapeamento e discussões. Agradeço ainda a outros geólogos e técnicos da empresa por todo o suporte recebido.

Por último, mas não menos especial, a meus pais ***Antônio Martins Freitas*** e ***Philomena de Souza Martins***, irmãos e amigos por toda paciência, conversas e por terem sempre dado um grande suporte nos momentos de sufoco.

Lista de figuras:

Lista de tabelas:

Resumo

O depósito de ouro orogênico Lamego (1,3 milhões t de reservas de minério 4,26 g/t Au) localiza-se na porção NE do Quadrilátero Ferrífero, hospedado no *greenstone belt* arqueano Rio das Velhas. A sucessão litológica em Lamego consiste de rochas vulcânicas máficas, *chert* e formação ferrífera bandada (FFB), pelitos carbonosos e micáceos, metamorfizados em fácies xisto-verde. A dobra Lamego controla o depósito e é a estrutura mais visível relacionada com o evento deformacional D_{1-2}, possuindo perímetro aflorante de aproximadamente 4,8 km e largura máxima de 450 m. A dobra é definida pelo contato/acamamento da unidade máfica com (i) porções menores de FFB, e (ii) grandes exposições de pelitos carbonosos e micáceos. É uma dobra sem raiz, reclinada, isoclinal, cilíndrica com traço axial de direção NE-SW, mergulhando para SE com ângulo entre 20º e 30º. A zona de charneira é espessa e os flancos são finos mergulhando para SE. Corpos de minério incluem a (i) FFB (carbonato, ±magnetita, *chert*, matéria carbonosa) Lamego, onde zonas sulfetadas podem estar mineralizadas, e (ii) zonas de silicificação, com ouro livre. Na FFB domina o estilo de mineralização por substituição dos carbonatos, associado com bandas de sulfeto, principalmente pirita, pirita arsenical e arsenopirita. Duas gerações de estruturas, G_1 e G_2, são reconhecidas e abrangem um conjunto de elementos estruturais. A geração G_1 desenvolve em evento de deformação progressiva e resulta em estruturas orientadas NE-SW mergulhando para SE. Estruturas pertencentes a geração G_2 são orientadas N-S mergulhando para W. Os quatro principais corpos de minério são Carruagem, Queimada, Arco da Velha e Cabeça de Pedra. Nesses, os teores de ouro mostram um padrão esferoidal distribuído ao longo da foliação S_{1-2}. Lentes de alto teor representam zonas de charneiras de dobras reclinadas F_2 com o *plunge* dos corpos de minério controlado por eixos de dobras F_2. Já lentes de baixos teores são controladas por estruturas do tipo *pinch-and-swell* e, localmente, *boudins* de quartzo desenvolvidos durante o evento D_{1-2}. Estes *boudins* possuem duas direções ortogonais, uma para NW-SE e outra para NE-SW, definindo, portanto, boudinagem no estilo tablete de chocolate. Com base em observações texturais e mapeamento de elementos químicos por microssonda eletrônica, estudos de paragênese mineral definem sete tipos de piritas, sendo quatro no pelito carbonoso (índice *CP*), Py-1_{CP} até Py-4_{CP}, e três na FFB (índice *BIF*), Py-1_{BIF} até Py-3_{BIF}, bem como Apy-1_{BIF}. Quatro estágios de evolução são estabelecidos: (1) pré-hidrotermal (diagenético) → Py-1_{CP} e, sua recristalização em Py-2_{CP}, (2) cedo hidrotermal → Py-2_{CP} adicional; desenvolvimento de Py-3_{CP} e Py-1_{BIF} mostrando zonamento de S-As-Fe, (3) principal hidrotermal → Py-3_{CP} adicional, desenvolvimento de Py-4_{CP} e Py-2_{BIF}, e (4) tarde hidrotermal → Py-4_{CP}, Py-3_{BIF} evidenciando zonamento de Ni-Co-As, e formação de Apy-1_{BIF}. Análises *in situ* por ablação a laser por espectrômetro de massa nas piritas do pelito carbonoso mostram que Au possui excelente afinidade

com Ag e com elementos crustais como Bi, Pb e Sb, e também está bem correlacionado com Ni, Co, Cu e Te. Além de clara relação do ouro com a geoquímica original do pelito carbonoso (Py-1_{CP}), esse elemento é também fixado nas piritas hidrotermais dessa rocha. Por outro lado, a correlação geoquímica do ouro no caso da FFB está restrita com Ag, As, Pb e Cu, denotando maior influência hidrotermal. A datação por U-Pb SHRIMP em grãos de monazita hidrotermal, presentes em rochas máficas (0,2 g/t Au), indica que formação da mineralização em 2730±42 Ma. Idades mais novas em torno de 2387±46 Ma, também em monazitas hidrotermais, e de 518.5±9 Ma em xenotima, mostram registro de idades sideriana e cambriana no depósito Lamego. Sugere-se que o registro sideriano, ainda pouco entendido para a área, possa ser reflexo da orogenia acrescionária Minas, descrita no Cinturão Mineiro. A idade cambriana reflete os estágios finais do ciclo orogênico Brasiliano, expresso em Lamego pela clivagem de crenulação S_3, orientada NS e mergulhando para E. Essa modificação estrutural cambriana foi responsável pela presente geometria dos corpos de minério no depósito Lamego, mas não causou alteração hidrotermal, não tendo assim remobilizado corpos de minérios ou minerais-minério. O entendimento da reorientação espacial dos corpos de minério, durante o evento Brasiliano, tem importantes implicações em campanhas de exploração regional já que os mesmos foram deslocados da sua posição arqueana original.

Palavras Chave: Depósito de ouro Lamego; *Greenstone belt* Rio das Velhas; Idades arqueanas, sideriana e cambriana em depósito de ouro orogênicos; Modelamento 3D de corpo de minério; ablação à laser em sulfetos.

Abstract

The Lamego orogenic gold deposit (1.3 million t ore resources at 4.26 g/t Au) is located at the north-east portion of the Quadrilátero Ferrífero region, Brazil, hosted in the Archean Rio das Velhas greenstone belt. The lithological succession at Lamego consists of metamorphosed (greenschist facies) mafic volcanic rock, chert and banded iron formation (BIF), carbonaceous and micaceous pelites. The Lamego fold controls the deposit, and is the most visible structure related to the D_1-D_2 event, having a perimeter of about 4.8 km and a maximum width of 450 m. The fold is defined by the layering of the mafic unit with minor BIF and large exposures of carbonaceous and micaceous pelites. It is a rootless, reclined, isoclinal, cylindrical fold with an axial trace striking NW-SE dipping 20º to 30º. The hinge zone is thickened and the limbs are thinned, with the limbs dipping 20º to 30º to the SE. Orebodies include (i) the Lamego BIF (carbonate, ±magnetite, chert, carbonaceous matter), where mineralization is related to sulfide-rich bands, and (ii) silicification zones, containing free gold. The BIF is dominated by replacement-style mineralization where sulfides replace carbonate, and are mainly pyrite, As-rich pyrite, and arsenopyrite. Two structural generations, G_1 and G_2, are recognized and encompass a set of structural elements. The generation G_1 developed in a progressive deformation event and resulted in structures oriented from NE-SW, dipping to the SE. Structures pertaining to the G_2 structural generation are oriented N-S dipping to the W. The four major high-grade gold orebodies are Carruagem, Queimada, Arco da Velha, and Cabeça de Pedra. Their gold grade shows a spheroidal pattern and a distribution that varies along the $S_{1\text{-}2}$ foliation. These lenses represent the hinge zone of F_2 reclined folds with the plunge of the orebodies controlled by the F_2 fold axes. The lower-grade gold lenses are controlled by pinch and swell, and locally quartz boudins developed during $D_{1\text{-}2}$. They have two orthogonal directions, one to the NW-SE and the other to the NE-SW, thereby defining chocolate-tablet style boudinage. Paragenetic studies based on texture and elemental mapping with EPMA define seven pyrite types, four in carbonaceous pelite (CP), Py-1_{CP} (framboidal) to Py-4_{CP}, and three in BIF, Py-1_{BIF} to Py-3_{BIF}, as well as Apy-1_{BIF}. These studies establish four stages of evolution: (1) pre-hydrothermal (diagenetic) → Py-1_{CP} and its recrystallization to Py-2_{CP}, (2) early hydrothermal → additional Py-2_{CP}; development of Py-3_{CP} and Py-1_{BIF} showing S-As-Fe zoning, (3) main hydrothermal → additional Py-3_{CP}, development of Py-4_{CP} and Py-2_{BIF}, and (4) late hydrothermal → Py-4_{CP}, Py-3_{BIF} showing Ni-Co-As zoning, and Apy-1_{BIF}. In situ LA-ICP-MS analyses on pyrite of carbonaceous pelite indicate that Au displays excellent affinity with Ag and with crustal elements such as Bi, Pb and Sb, and also correlates well with Ni, Co, Cu, and Te. Gold is not only related to the original carbonaceous pelite geochemistry (framboidal Py-1_{CP}), but also concentrated in hydrothermal pyrites. On the other hand, in the case of BIF geochemical correlation

is restricted to Ag, As, Pb and Cu, denoting a much more important hydrothermal influence. Age dating by U-Pb SHRIMP on hydrothermal monazite grains, present in a mafic volcanic rocks (0,2 g/t Au), indicate that mineralization formed at 2730±42 Ma. Younger monazite dated at 2387 ± 46 Ma, and xenotime at 518.5±9 Ma suggest Siderian and Cambrian imprint in the Lamego deposit area. The poorly understand Siderian imprint in the area may reflect the Minas acrescionary orogeny, described in the Mineiro belt. The Cambrian age reflects the late stages of the Brasiliano orogenic cycle, which is expressed in the Lamego deposit by the S_3 crenulation cleavage (trending NS and dipping steeply to the E). The Cambrian structural modification was responsible for the present geometry of the Lamego orebodies, did not generate hydrothermal alteration, and also did not caused remobilization of the orebodies or ore minerals. Understanding the spatial reorientation of the orebodies, during the Brasiliano event, has important implications to regional exploration since these have been dislocated from their original Archean position.

Keywords: Lamego gold deposit; Rio das Velhas greenstone belt; Archean, Siderian and Cambrian age in orogenic gold deposit; 3D orebody modeling, laser ablation in sulfides.

PARTE 1 – Introdução e Contexto Geológico

Capitulo 1: Introdução

1.1 Apresentação.

Sequências do tipo *greenstone belts* são formadas por rochas vulcânicas e sedimentares, em geral de idade arqueana, sendo melhor reconhecidas aquelas afetadas por metamorfismo de baixo grau. Estas sequências hospedam expressivos depósitos de ouro em regiões cratônicas de diversos países, onde dentre outros destacam-se Canadá, Austrália e Brasil (DeWitt et al. 1996, 2000).

No Brasil, o *greenstone belt* Rio das Velhas, em grande parte localizado na região do Quadrilátero Ferrífero - QF, Estado de Minas Gerais, é o mais importante distrito aurífero do país, com produção estimada de 30 milhões de onças (Goldfarb et al. 2001).

O depósito aurífero Lamego, alvo deste trabalho, é uma jazida de ouro operada em mina subterrânea pela AngloGold Ashanti do Brasil. Localiza-se na porção norte do QF, município de Sabará, Minas Gerais, distante 40 km da capital, Belo Horizonte.

Os corpos mineralizados em Lamego estão hospedados em rochas arqueanas do Supergrupo, *greenstone belt* Rio das Velhas (Figura 1), associados à alteração hidrotermal, estruturalmente controlados (Martins 2011, Martins et al. 2011). Da base para o topo, o empilhamento litoestrutural no depósito é definido por rochas metavulcânicas, metachert, formação ferrífera bandada – FFB, filito carbonoso e micáceo e rochas metavulcanoclásticas, em condições metamórficas de fácies xisto verde (Sales 1998, Martins 2011). O minério está associado a veios e massas de quartzo, e à FFB alterada hidrotermalmente. O depósito Lamego divide-se em quatro corpos de minério, que são Queimada, Arco da Velha, Cabeça de Pedra e Carruagem (Capítulo 3, Figura 7).

A alteração hidrotermal em Lamego é caracterizada, principalmente, por uma extraordinária silicificação. A mesma se traduz na forma de massas irregulares e veios de quartzo fumê, milimétricos a hectamétricos (Martins 2011, Martins et al. 2011). Essas massas englobam porções reliquiares de rocha, principalmente FFB, resultando em textura brechada, semelhante à brecha de cisalhamento rúptil-dúctil (Taylor 1993). Os veios de quartzo fumê são tanto concordantes como discordantes ao bandamento e foliação, e podem formar brechas do tipo *sheeted veins*. Quartzo leitoso é comum em veios e em zonas de falha, intercrescido ou não com o quartzo fumê.

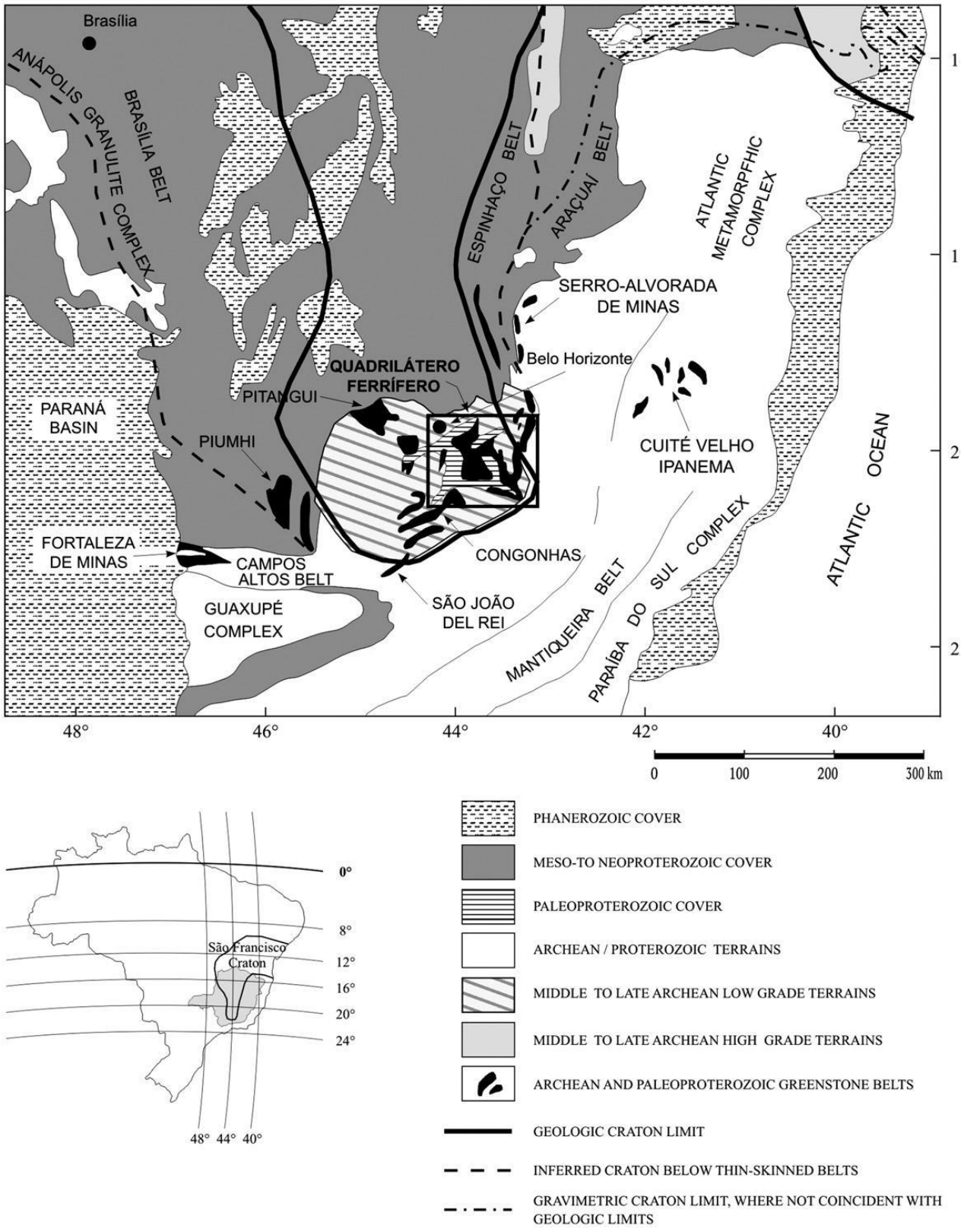

Figura 1: Localização do ***Greenstone Belt*** Rio das Velhas no Distrito do Quadrilátero Ferrífero, sul do Cráton São Francisco. Fonte: (Lobato et al. 2001a).

As feições originais da FFB estão fortemente obliteradas pela alteração. Nas bandas sulfetadas, por exemplo, raros relictos de magnetita são observados, o que sugere que as mesmas podem corresponder em parte a metachert carbonático bandado, por vezes ferruginosas.

Ouro associa-se ao quartzo fumê, tanto no contato entre FFB e xisto carbonoso como no interior dessas mesmas rochas, invariavelmente onde há sulfetos (Martins 2011, Martins et al. 2011, Lobato et al. 2013).

O depósito Lamego é um depósito de ouro orogênico no sentido de Groves et al. (1998), assim como outros no Arqueano do QF, entre os quais citam-se Cuiabá, Morro Velho, Raposos, São Bento e Juca Vieira, diretamente relacionados à evolução do *greenstone belt* arqueano Rio das Velhas (ca. 2,75 Ga, Noce et al. 2005) e suas FFB do tipo Algoma (Ribeiro-Rodrigues 1998; Lobato 1998a, b). Os depósitos auríferos do *greenstone belt* apresentam características similares a outros depósitos de mesmo tipo que ocorrem pelo mundo, em outros crátons arqueanos (Groves et al. 1998).

1.2 Estruturação da Tese

A tese está dividida em 4 partes, cada uma contendo diversos capítulos.

Na Parte 1 são apresentados uma breve introdução sobre as classes dos depósitos de ouro orogênicos, localização e vias de acesso da área, objetivos e métodos de trabalho (Capítulo 1). Segue breve revisão sobre o contexto geológico regional no qual a área está inserida (Capítulo 2).

A Parte 2 apresenta resumo dos estudos petrográficos, tendo como mais importante foco os resultados dos trabalhos de mapeamento geológico na mina subterrânea Lamego, além da estratigrafia, geocronologia U-Pb SHRIMP, modelamento 3D de corpos de minério e proposta de evolução estrutural no contexto regional do QF (Capítulo 3). É exposta na forma de artigo cientifico publicado no periódico Ore Geology Reviews¸ volume 72, parte 1, p. 963-988 de janeiro de 2016. A descrição pormenorizada da geologia do Depósito Lamego é encontrada em Sales (1998) e Martins (2011).

A Parte 3 inclui a caracterização da alteração hidrotermal, para a qual foram feitos estudos petrográficos de detalhe com estabelecimento da paragênese mineral. O estudo dos sulfetos principais envolve análises geoquímicas por microssonda eletrônica, MEV e *LA-ICP-MS*. Este é o Capítulo 4 em formato de artigo submetido para publicação no periódico Mineralium Deposita.

A Parte 4 da tese sumariza importantes considerações para a exploração de novas jazidas de ouro nos QF (Capítulo 5) e as principais conclusões dos trabalhos (Capítulo 6). A lista de referências bibliográficas completa acha-se no Capítulo 7. O estilo das referências bibliográficas ao longo do

texto dos capítulos 3 e 4 segue o padrão dos periódicos dos mesmos, ou seja, Ore Geology Reviews e Mineralium Deposita.

1.3 Localização e vias de acesso

O acesso ao depósito Lamego pode ser realizado a partir de Belo Horizonte indo em direção à cidade de Sabará pela MG-262 (Figura 2), por aproximadamente trinta quilômetros, onde se segue pela mesma rodovia por mais cinco quilômetros. Deste ponto, prossegue-se por estrada vicinal não pavimentada por mais oito quilômetros. A empresa AngloGold Ashanti Córrego do Sítio Mineração Ltda. (AGA) é a detentora da área.

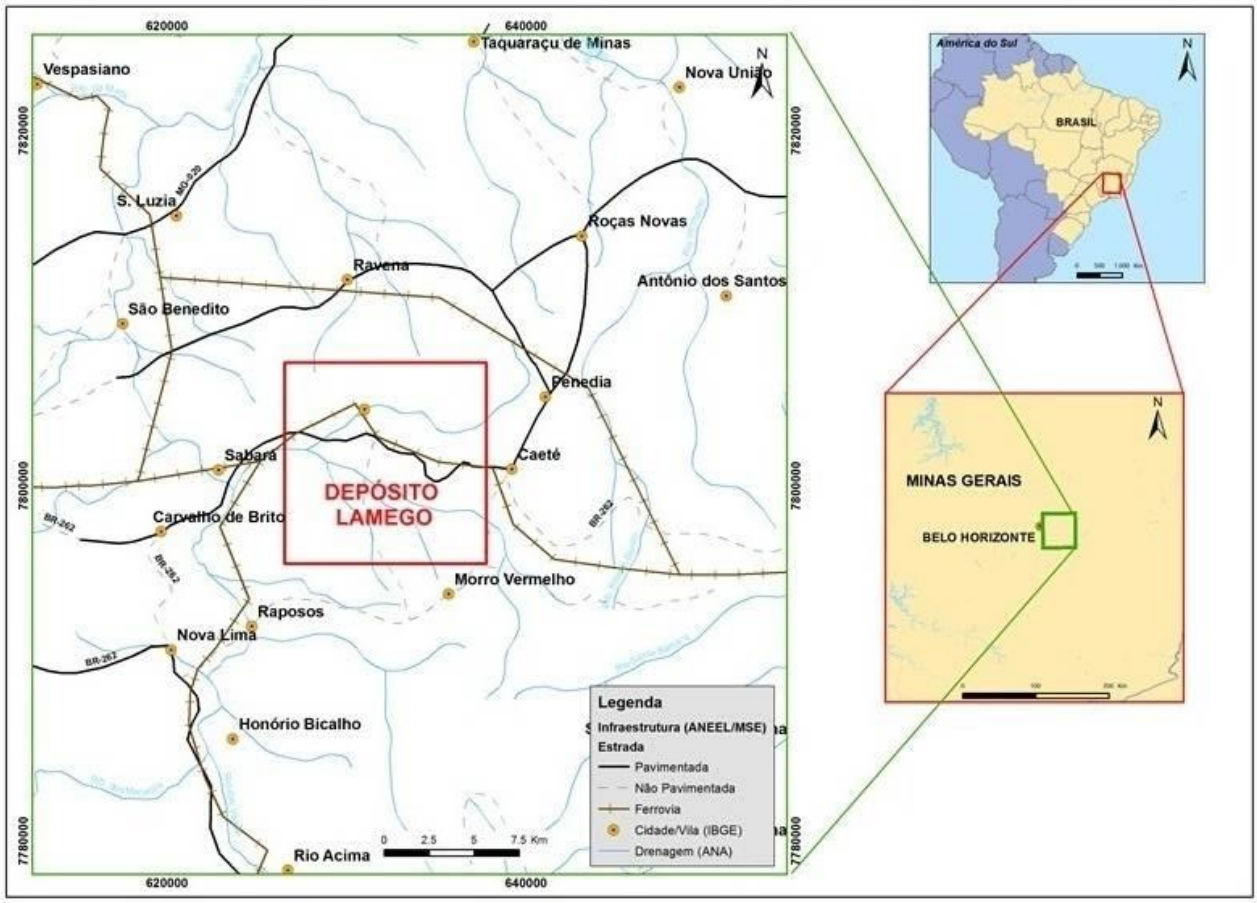

Figura 2: Localização da área e vias de acesso para Sabará.

1.4 Objetivos

Pretende-se, com a tese de doutorado, contribuir para a elaboração do conhecimento científico sobre a região do *greenstone belt* Rio das Velhas e adjacências. Nesse sentido, os principais objetivos a serem destacados são:

(i) Detalhamento geológico e estrutural dos corpos de minério do depósito Lamego, através da elaboração de mapeamento geológico de níveis de minério com foco principal no Corpo

Carruagem em escala 1:100.

(ii) Detalhamento do controle litológico e estrutural da mineralização, na escala de corpo do minério, através de mapeamento de frentes de lavra.

(iii) Modelamento dos corpos de minério, com o uso de modelagem geoquímica *krigagem.*

(iv) Estudos petrográficos detalhados para estabelecimento da mineralogia da zona mineralizada e das rochas encaixantes.

(v) Estudos geocronológicos de monazita e xenotima da zona mineralizada bem como a relação das idades obtidas com a evolução da região do Quadrilátero Ferrífero.

(vi) Estudos de MEV e LA-ICPMS em sulfetos para estabelecer para estabelecimento da paragênese mineral e da possível fonte hidrotermal para os metais presentes na zona mineralizada.

1.5 Metodologias

Visando alcançar os objetivos propostos, foram utilizadas várias técnicas sumarizadas na Tabela 1.

Tabela 1: Resumo das técnicas metodológicas utilizadas.

Metodologia	Objetivos	Processos	Local
Cartografia e amostragem	Levantamento de dados litológicos e estruturais nos corpos de minérios auríferos e perfis estratigráficos	Mapeamento no subterrâneo dos tipos rochosos, estruturas geológicas e reconhecimento e descrição de zonas mineralizadas; Levantamento de dados estruturais; Construção de seções verticais e longitudinais com base na descrição de furos de sondagem; Construção de mapa geológico;	Mina Lamego
Modelamento computacional	Estabelecer a relação entre teor de ouro, tipo litológico e estruturas	Construir modelo tridimensional com a distribuição dos teores de ouro no software Leapfrog Geo®;	Centre for Exploration Targeting, Univ. of Western Australia
Estudos petrográficos macro- e microscópicos	Estudo das características petrográficas /mineralógicas de minérios, protominérios, rochas hospedeiras e encaixantes	Estabelecer: Paragêneses hidrotermais, tanto do minério como de veios e brechas; Grau metamórfico de rochas pouco alteradas, inclusive diques, Minerais e zonamento hidrotermais, Mineralogia e textura de veios de quartzo-carbonato; Definição de zonamento vertical e lateral com respeito ao(s) evento(s) de mineralização.	Laboratório de laminação do CPMTC/IGC/UFMG Microscopia Óptica CPMTC/IGC/UFMG em microscópios ZEISS & Leitz
Estudos de identificação e química mineral	Identificação mineralógica e caracterização química dos diferentes minerais é indispensável, para apoiar estudos petrográficos e geoquímicos	Microscopia eletrônica de varredura (EDS); Quantificação percentual de elementos será realizada por microssonda eletrônica. Ablação a *laser* ICP-MS.	Laboratório do CPMTC/IGC/UFMG Laboratório do Centro de Microscopia da UFMG Laboratório da Universidade da Tasmânia-UTAS, Hobart – em colaboração

Estudos de isótopos radiogênicos	Determinação de idades por análises pelo método U-Pb SHRIMP	Datação da mineralização aurífera nas jazidas estudadas, através da utilização de minerais hidrotermais (de veios e brechas) como monazita e xenotima.	Laboratório da Univ. of Western Australia-Curtin Univ. (Dr. João Orestes dos Santos) Centre for Exploration Targeting, Univ. of Western Australia (Prof. Steffen Hagemann)

Capitulo 2: Contexto geológico regional

2.1 Aspectos Fisiográficos

De acordo com os estudos efetuados pelo Instituto Brasileiro de Mineração (IBRAM 2003), a conformação do relevo do QF expressa forte condicionamento geológico – tanto litológico quanto estrutural. O controle litoestrutural propicia a ocorrência de dois domínios geomorfológicos bem definidos na região: (i) o domínio dos relevos serranos ou linhas de cristas e (ii) domínio de relevos dissecados (Figura 3).

O relevo em (i) é sustentado, principalmente, pelas rochas dos Grupos Itabira e Caraça, apresentando altitudes acima de 1.000 metros e possuindo uma morfologia de vertentes íngremes, com declives acentuados. Por outro lado, o relevo (ii) é sustentado por rochas granito-gnáissicas, com porções mais baixas do relevo em que predominam colinas no padrão côncavo-convexo e vales encaixados, cujas altitudes variam entre 620 a 900 metros.

Figura 3: Principais feições fisiográficas (cristas de serra) e rede hidrográfica nas proximidades de Belo Horizonte e Sabará.

2.2 Estratigrafia e Metamorfismo

O Arcabouço estratigráfico/geotectônico do QF é representado por três grandes unidades (Dorr 1957, 1969): (i) Terrenos granito-gnáissicos; (ii) Supergrupo Rio das Velhas, o qual constitui

a sequência *greenstone belt* arqueana, e (iii) Supergrupo Minas. As duas primeiras são de idade arqueana enquanto a última é proterozóica.

Os trabalhos da presente proposta de pesquisa estão focados no Supergrupo Rio das Velhas, ou seja, na sequência *greenstone*.

2.2.1 Supergrupo Rio das Velhas

O primeiro trabalho de divisão estratigráfica do Supergrupo Rio das Velhas foi proposto por Dorr et al. (1957) que inclui as rochas metavulcanossedimentares do QF na chamada Série Rio das Velhas. Dorr (1969) subdivide a Série Rio das Velhas em Grupos Nova Lima e Maquiné. O Grupo Maquiné é dividido nas Formações Casa Forte (Gair 1962) e Palmital (O'Rourke 1957). Trabalhos clássicos sobre a metalogênese de ouro no *greenstone bel* Rio das Velhas foram desenvolvidos por Ladeira (1980a, b, c; 1981a, b; 1985; 1991). Já trabalhos sobre a alteração hidrotermal descrita nos depósitos de ouro destacam-se Vieira (1988), Lobato et al. (1998a, b; 2001a, b).

Com base em associações litofaciológicas, descritas por Pedreira e Silva (1996), Baltazar e Silva (1996), Baltazar e Pedreira (1998), Zucchetti e Baltazar (1998), e Baltazar e Zucchetti (2007) subdividem os Grupos Nova Lima e Maquiné em unidades litoestratigráficas informais (Figura 4). Esta abordagem resultou no reconhecimento de sete associações de litofácies e quatro ciclos sedimentares resumidas no Tabela 2.

Tabela 2: Associações, ciclos sedimentares e respectivas unidades litoestratigráficas.

Associação	Ciclos	Unidades litoestratigráficas
Associação vulcânico-plutônica máfica-ultramáfica	01	Grupo Quebra Osso e unidade Ouro Fino do Grupo Nova Lima
Associação metavulcanossedimentar química	01	Unidade Morro Vermelho
Associação metassedimentar química-pelítica	02	Unidade Santa Quitéria
Associação metavulcanoclástica	03	Unidades Ribeirão Vermelho e Mestre Caetano
Associação ressedimentada	03	Unidades Mindá e Córrego do Sítio, nos setores norte e leste; unidades Catarina Mendes, Fazenda Velha e Córrego da Paina, no setor sul; Unidade Rio de Pedras da Formação Palmital do Grupo Maquiné
Associação costeira (ou litorânea):	02	Unidades Pau D´Óleo e Andaimes
Associação não-marinha	04	Unidades Chica Dona, Jaguará, Córrego do Engenho e Capanema, da Formação Casa Forte do Grupo Maquiné.

2.2.2 Evolução do *greenstone belt* Rio das Velhas (Baltazar e Zucchetti, 2007)

Baseados em relações de campo entre as associações de litofácies descritas acima (Tabela 2), Baltazar e Zucchetti (2007) propõem o desenvolvimento de bacias sedimentares em quatro ciclos, relacionados com a configuração tectônica. Primeiro ciclo (I) foi responsável pela deposição das associações máfica-ultramáfica e vulcânica sedimentar-química. O segundo ciclo (II) corresponde à

deposição da associação sedimentar clástica-química + turbidídos e associação costeira. O terceiro ciclo (III) corresponde à fase orogênica com formação de arcos de ilha, sendo responsável pelas associações vulcanoclástica e ressedimentada. O quarto ciclo (IV) ocorre com a deposição em bacia do tipo *back–arc foreland*, correspondendo à deposição da associação não marinha

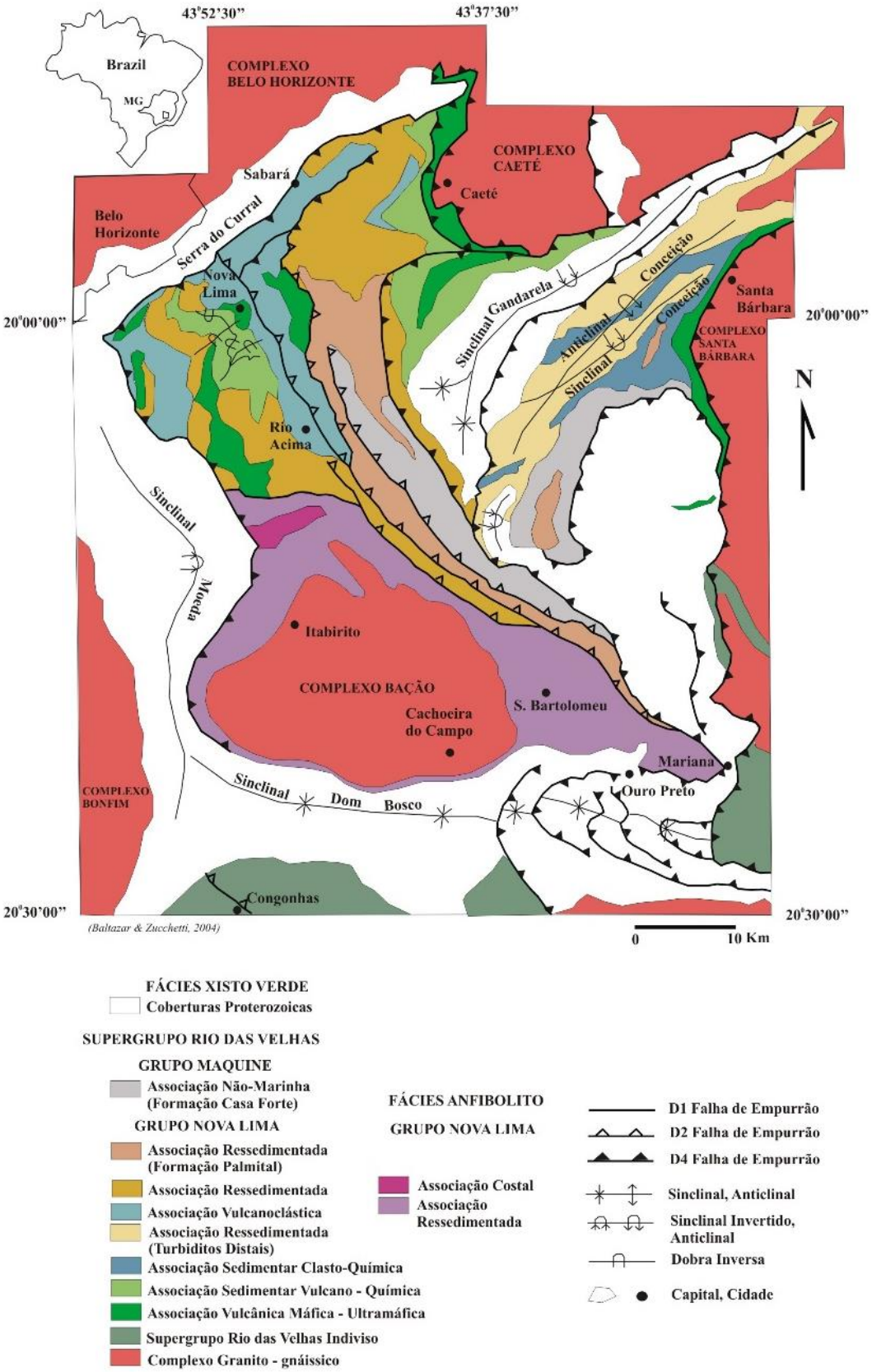

Figura 4: Mapa geológico simplificado do *greenstone belt* Rio das Velhas incluindo o QF. Fonte: Baltazar e Zucchetti (2007).

PARTE 2 – Depósito Lamego: Estratigrafia, Geocronologia e Evolução Estrutural no Contexto do Quadrilátero Ferrífero.

Capítulo 3: Artigo: The Archean BIF-hosted Lamego gold deposit, Rio das Velhas greenstone belt, Quadrilátero Ferrífero: Evidence for Cambrian structural modification of an Archean orogenic gold deposit.

Artigo publicado na *Ore Geology Reviews*, vol. 72(1), p. 963-988, janeiro de 2016.

Breno de Souza Martins[1], Lydia Maria Lobato[1], Carlos Alberto Rosière[1], Steffen G. Hagemann[2], João Orestes Schneider Santos[2], Fernando Lucas dos Santos Peixoto Villanova[3], Rosaline Cristina Figueiredo e Silva[1], Lucas Henrique de Ávila Lemos[3].

[1]Universidade Federal de Minas Gerais, Avenida Antônio Carlos, n.º 6627, Bairro Pampulha, Belo Horizonte, Minas Gerais, CEP 31270-901.
[2]School of Earth and Environment, The University of Western Australia, 35, Stirling Highway, Crawley, WA, 6009, Australia.
[3]AngloGold Ashanti Córrego do Sítio Mineração S/A, Mina do Lamego, Sabará, Minas Gerais.

3.1 Abstract

The Lamego orogenic gold deposit (1.3 million resource contained Au at 7.26 g/t Au) is located at the south-western end of the 5 km-long Cuiabá-Lamego trend, Quadrilátero Ferrífero region, Brazil. Both Archean orogenic gold deposits are situated in the Rio das Velhas greenstone belt with the lithological succession at Lamego consisting of metamorphosed (greenschist facies) mafic volcanic rock, chert and banded iron formation (BIF), carbonaceous and micaceous pelites. The Lamego fold, which controls the Lamego deposit, is the most visible structure related to the D_1-D_2 event, with a perimeter of about 4.8 km and a maximum width of 450 m. The fold is defined by the layering of the mafic unit with minor BIF and large exposures of carbonaceous and micaceous pelites. It is a rootless, reclined, isoclinal, cylindrical fold with an axial trace striking northwest-southeast dipping 20º to 30º. The hinge zone is thickened and the limbs are thinned, with the limbs dipping 20º to 30º to the SE. Orebodies consist of the Lamego BIF, where gold-mineralized zones are related to iron-rich bands, and associated silicification zones. Replacement-style mineralization is associated with sulfide bands; mainly pyrite, As-rich pyrite, and arsenopyrite. Two structural generations, G_1 and G_2, are recognized

and encompass a set of structural elements. The G_1 structural generation developed in a progressive deformation event and resulted in structures oriented from NE-SW and dipping to the SE. Structures pertaining to the G_2 structural generation are oriented N-S dipping to the W. The four major high-grade gold orebodies are Carruagem, Queimada, Arco da Velha, and Cabeça de Pedra. Their gold grade shows a spheroidal pattern and a distribution that varies along the S_{1-2} foliation. These lenses represent the hinge zone of F_2 reclined folds with the plunge of the orebodies controlled by the F_2 fold axes. The lower-grade gold lenses are controlled by pinch and swell, and locally quartz boudins developed during D_1-D_2. They have two orthogonal directions, one to the NW-SE and the other to the NE-SW, thereby defining chocolate-tablet style boudinage. Hydrothermal monazite grains in a mineralized mafic volcanic rock indicate mineralization formed at 2730±42 Ma (U-Pb SHRIMP). Younger monazite dated at 2387 ± 46 Ma, and xenotime dated at 518.5±9 Ma suggest Siderian and Cambrian imprint in the Lamego deposit area. The Cambrian age reflects the late stages of the Brasiliano orogenic cycle, which is expressed in the Lamego deposit by the S_3 crenulation cleavage (trend NS and dip steeply to the E). Importantly, the Cambrian structural modification is responsible for the present geometry of the Lamego orebodies, but is not associated with hydrothermal alteration; it has not introduced any new gold and also has not caused remobilization of the orebodies or ore minerals.

3.2 Keywords

Lamego deposit, Lamego BIF, Rio das Velhas greenstone belt, Quadrilátero Ferrífero, orogenic gold deposit.

3.3 Introduction

Orogenic gold deposits are structurally controlled. In most Archean cases the orebody shape is controlled by the structures formed late in the tectonic evolution of the terrain in which the deposit is emplaced (Bierlein, 2006; Goldfarb et al., 2005; Groves et al., 1998; Hagemann and Cassidy, 2000; Kerrich et al., 2000; 2005). These authors further emphasize that orebodies and ore textures are largely undeformed, and thus interpreted as being related to the last structural-hydrothermal event that caused the precipitation of gold and associated hydrothermal alteration minerals. For this reason, individual orebodies display the original geometry at the time of formation and, therefore, lack any post ore deformation or remobilization. On the other hand, hypozonal gold deposits in Archean terrains that display structural and hydrothermal alteration similarities to orogenic gold systems provide evidence for major remobilization of sulfides and gold. These include examples such as

Hemlo in the Superior province (Tomkins et al., 2004); Challenger in the South Australian craton (Tomkins and Mavrogenis, 2002), and Griffins Find in the Yilgarn craton (Tomkins and Grundy, 2009; Hagemann and Gilg, 2011). In these deposits the timing of gold precipitation is interpreted to be pre-peak (Archean) metamorphism.

Nowadays, Brazil is classified as the 12º largest gold producer with 2.600 t in reserves and production, with 56.7 t of gold exploited by gold companies, and 10.1 t of gold mined by artisanal miners (gold diggers) (Lima et al., 2014). Furthermore, Minas Gerais state is the largest gold producer in Brazil with 52.4% of the production and 28.0% of the reserves (Lima et al., 2014).

The Quadrilátero Ferrífero (QF) region is one of Brazil's most important gold provinces with historical production and present gold reserves exceeding 1.000 t (Vial et al., 2007a). Vial et al., 2007a reported that during the 18th and 19th centuries, the QF was the largest gold producer in the world, including the world-class Morro Velho and Cuiabá deposits (Figura 5), presently owned by AngloGold Ashanti Córrego do Sítio S/A (AGA). The Morro Velho gold mine started production in 1834, and has a cumulative production of about 470 t (15 Moz) of gold (Vial et al., 2007b). The Cuiabá gold mine contains 150 t, 5 Moz produced until 2015 and more 7 Moz in mineral resources (AGA, personal communication).

The Cuiabá-Lamego gold trend is significantly endowed in gold (11 Moz produced,) and shares most of the structural complexities that generally characterize orogenic gold style mineralization in the QF, where Archean ore systems underwent Proterozoic structural modifications (e.g., Baltazar and Zucchetti, 2007). The QF structural evolution is defined by three main periods with a complex structural arrangement. The first between 2.8 and 2.67 Ga verging to NNE, the second between 2.1 and 1.9 with fold and thrust belts verging to the NW, and the third from 650 to 500 Ma verging to the W.

The present investigation on the orogenic Lamego deposit, which is part of the Cuiabá-Lamego gold trend within the Rio das Velhas greenstone belt, in the QF of Brazil (Figuras 5 and 6), provides a detailed documentation of an Archean orogenic gold system that was affected by the Transamazonian orogenic event (Brito Neves, 2011; "Minas accretionary orogeny" most recently proposed by Teixeira et al., 2015), and the 630-480 Ma Brasiliano orogenic events (Alkmim and Marshak, 1998; Baltazar and Zucchetti, 2007; Lobato et al., 2007; Pedrosa Soares et al., 2011). Significantly, the gold orebodies hosted along the Lamego fold (Figura 7a, b, c) lack characteristics of remobilization textures, but the Archean orebody geometry was significantly modified by Cambrian age folds and thrusts.

The aims of this paper are to: (1) characterize the geological setting of the Lamego deposit

including the lithostratigraphy and mineralization styles; (2) provide a detailed structural documentation of the four separate Lamego gold orebodies via detailed underground mapping of several levels; (3) constrain the chronology of structural events and orebody geometries based on the careful documentation of structures in 3-D and cross-cutting relationships; (4) provide geochronological evidence for Archean and Proterozoic timing of mineralization and structures, respectively; (5) introduce a descriptive geological model that is compatible with all the documented geological and geochronological observations; and (6) compare and contrast the structural setting and control of the Lamego gold orebodies with classic orogenic gold deposits in Brazil and worldwide.

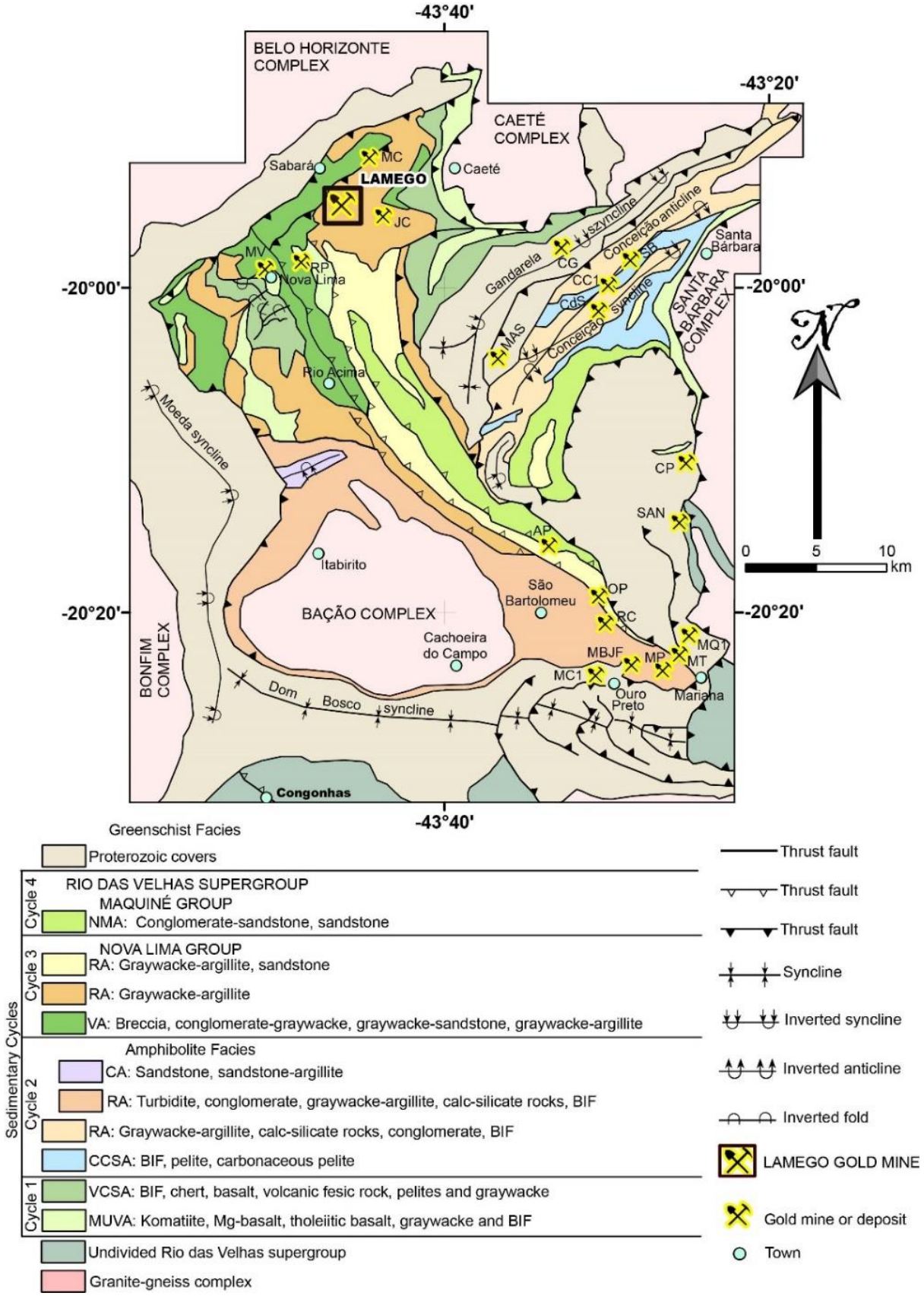

Figura 5: Simplified geological-structural map of the Quadrilátero Ferrífero region showing the location of the Lamego deposit. The Rio das Velhas greenstone belt is separated in lithofacies associations (modified after Baltazar and Zucchetti 2007): MUVA-Mafic-ultramafic volcanic,

VCSA-Volcano-chemical sedimentary, CCSA Clastic-chemical sedimentary, RA-Resedimented, CA-Coastal, VA-Volcaniclastic, NMA-Non-Marine associations. Other gold deposits associated with the Rio das Velhas greenstone belt and the Minas Supergroup are also shown. The gold deposits hosted by the greenstone belt are: CdS-Mina Córrego do Sítio, MC-Mina Cuiabá, MV-Morro Velho, RP-Raposos, SAN-Santo Antônio, SB-São Bento, JC-Juca Vieira. On the other hand, deposits associated with Minas Supergroup are: AP-Antônio Pereira, CC1-Conceição, MQ1-Maquiné, MT-Mata Cavalo, MBJF-Mina Bom Jesus das Flores, MAS-Mina Santo Antônio, AP-Antônio Pereira, OP-Ouro Preto, CP-Cata Preta, MP-Mina da Passagem, RC-Rocinha, and CG-Congo Soco.

3.4 Regional geological setting

The QF is located in the southern portion of the São Francisco Craton (Almeida, 1977) and the stratigraphic subdivision was established by Dorr et al. (1969, 1957) who subdivided the region into: (i) Archean granite-gneissic complexes, older than 2.9 Ga (Machado and Carneiro, 1992; Machado et al., 1989); (ii) Rio das Velhas Supergroup (Figuras 5 and 6), an Archean greenstone belt sequence dated between 3.0-2.7 Ga, (Machado and Carneiro, 1992; Machado et al., 1989); and (iii) Proterozoic Minas Supergroup, Itacolomi Group and Espinhaço Supergroup (Dorr et al., 1969, 1957).

The granite-gneiss terrain is composed of tonalite-trondjhemite-granodiorite (TTG). These consist of 3.2 Ga dome-like granite-gneiss domains associated with intercalations of amphibolites and metasedimentary rocks (Ladeira, 1980a; Lana et al., 2013; Schorscher, 1988), which are intruded by metatonalites, metandesites, metagranites, pegmatites and Proterozoic mafic dikes (Carneiro et al., 1994; Noce, 1995, Noce et al., 2005). Noce et al. (2007) suggest that these TTG derive from igneous protoliths older than 2.9 Ga.

The Archean Rio das Velhas greenstone belt (Figura 6) covers approximately 4.000 km^2 in the QF, and is divided into the basal Nova Lima and top Maquiné Groups (Dorr, 1969, 1957; Oliveira, 1984). The Nova Lima comprises ultramafic rocks, basic lavas, graywackes and sandstones, with intercalations of BIF, quartz-dolomite and quartz-ankerite rocks, conglomerates and carbonaceous pelites (Baltazar and Zucchetti, 2007; Dorr, 1969). The Nova Lima Group hosts a large number of gold deposits (Ladeira, 1991, 1980b; Lobato et al., 2001a, b; 1998 a, b), including Lamego (Martins, 2011; Martins et al., 2011). The Maquiné Group is divided into the basal Palmital (O'Rourke, 1957) and top Casa Forte Formations (Gair, 1962), the former with sandstone and quartz pelite, and the latter with sandstone and conglomerate (Dorr, 1969). The greenstone belt sequence was mainly metamorphosed to the greenschist facies. A thorough review of the literature from the last century focused in this greenstone belt is found in Baltazar and Zucchetti (2007).

Baltazar and Pedreira (1998), Baltazar and Silva (1996), Baltazar and Zucchetti (2007), Pedreira and Silva (1996), subdivide the Rio das Velhas Supergroup from bottom to top into seven

lithofacies associations. For the Nova Lima Group these are the: (i) mafic-ultramafic volcanic, (ii) volcanic-chemical, (iii) clastic-chemical, (iv) volcaniclastic, and (v) resedimented associations. For the Maquiné Group, the (vi) coastal, and (vi) non-marine associations are indicated. These are developed into four sedimentary cycles that were formed between 2.8 to 2.6 Ga (Noce et al., 2007). The platformal Minas Supergroup sequence unconformably lies over the Rio das Velhas Supergroup, and is subdivided into the Caraça, Itabira, Piracicaba and Sabará Groups (Dorr, 1969).

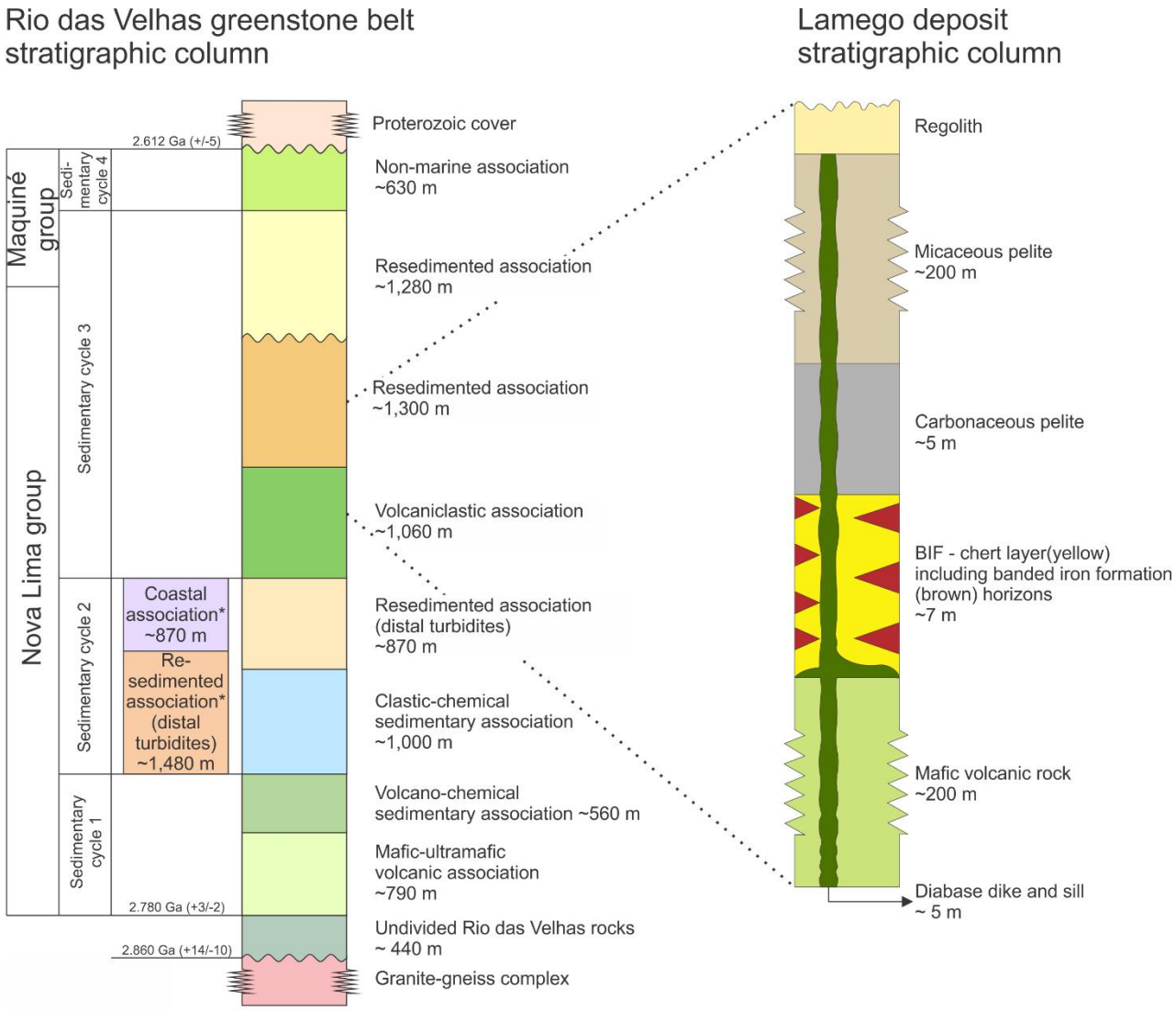

Figura 6: Schematic stratigraphy of the Lamego deposit area based on the geological mapping (Figura 7), combined with the regional stratigraphic column proposed for the Rio das Velhas greenstone belt by Baltazar and Zucchetti (2007). Note that the lithological column at Lamego is related to the resedimented association of the sedimentary cycle 3, and the rock thicknesses do not correspond to those of the regional stratigraphy.

The QF region is characterized by a complex structural arrangement, with Archean basement domes surrounded by large synclines where the Minas Supergroup rocks dominate (Dorr, 1969; Chemale et al., 1994; Alkmim and Marshak, 1998).

Baltazar and Zucchetti (2007) have proposed that the structural evolution of the QF region took place in three main periods, corresponding to the Rio das Velhas Orogeny. The earliest period occurred between 2.8 and 2.67 Ga, corresponding to the evolution of the Rio das Velhas greenstone belt; the second period between 2.1 and 1.9 Ga, related to the Transamazonian event in the Proterozoic; the third period between 650 and 500 Ma, in the Neoproterozoic, related to the Brasiliano orogeny. No consensus exists on how many deformational events the Rio das Velhas Supergroup experienced (see summary in Table 3).

Alkmim and Marshak (1998) proposed three main deformational phases to the Proterozoic tectonic evolution (Minas accretionary orogeny by Teixeira et al. 2015). The first episode generated fold and thrust belts with an NE-SW trend, verging to NW, during the Rhyacian (2.1 - 2.0 Ga). The second phase is related to the Paleoproterozoic orogenic collapse, caused by a regional extensional tectonic event, resulting in the uplift of the Archean granite-gneiss domes and formation of the regional synclines (the dome-and-keel structure of Marshak and Alkmim, 1989). The third event is related to the Neoproterozoic Brasiliano orogeny (0.7 – 0.45 Ga), and was responsible for the formation of fold and thrust belts verging to the west (Alkmim and Marshak, 1998).

Tabela 3: Proposal of QF structural evolution by Marshak and Alkmim (1989), Alkmim and Marshak (1998), and Baltazar and Zucchetti (2007).

Eon (Ga)	Archean	2,5	2,0	Proterozoic	1,5	1,0	0,5	Fanerozoic
Orogeny	Jequié		Transamazonian				Brasiliano	
Alkmim and Marshak (1989, 1998)	Continental crustal fragments older than 3.2 Ga served as basement of Rio das Velhas greenstone belt Formation of Minas basin into a ensialic or passive-margin basin		D_1 compressional event NW-vergent Thin-skinned tectonics D_2 extensional event Oceanic basin Rift-type ensialic basin D_3 colapse/ extensional even Dome-and-keel tectonics				D_4 compressional event W-vergent Thrust-fold belt	
Baltazar and Zucchetti (2007)	D_{1Rio} compressional simple shear event N to S tectonic transport E-striking, S-verging thrust faults S-verging tight to isoclinal folds, with ENE-plunging axes and open, flexural folds Axial–planar S_1 foliation, subparallel to folded S_0 (355/65) Down-dip stretching and mineral lineation, intersection lineation (S_0 and S_1) parallel to fold axes D_{2Rio} compressional simple shear event NE to SW tectonic transport NW-striking thrust faults (03-050/40-60) NW trending, SW-verging tight to isoclinal folds Axial-planar S_2 foliation (060/35; mylonitic foliation) Stretching lineation, mineral lineation (060–070/20–30)		D_{3Rio} extensional event WNW to ESE tectonic transport Nucleation of regional synclines and onset of Minas Supergroup deposition Uplift of granite-gneissic basement as metamorphic core complexes Normal faults around the complexes				D_{3Rio} extensional event WNW to ESE tectonic transport Nucleation of regional synclines and onset of Minas Supergroup deposition Uplift of granit-gneissic basement as metamorphic core complexes Normal faults around the complexes	

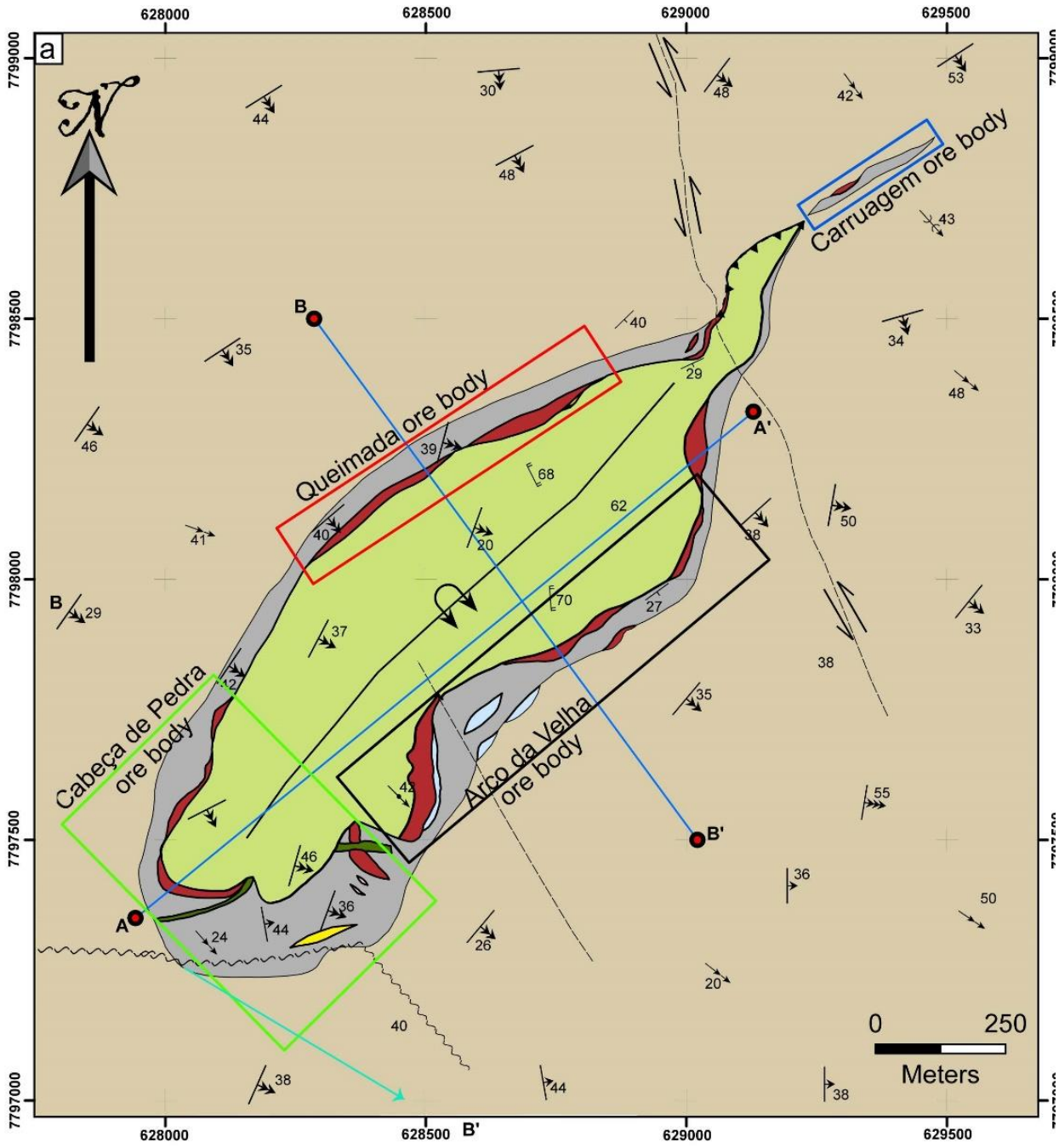

Diabase dike
Micaceous pelite
Carbonaceous pelite
Banded iron formation
Chert
Mafic volcanic rock
A A' Cross section line
Plunge of Lamego fold

D_1-D_2 Structures
Contact
Compositional and gradational bands
S_1 foliation
S_2 foliation
Ductile±brittle shear zone
Strike-slip fault (sinistral)
Thrust fault
Reclining anticline

Inferred fault
L_{1-2} mineral lineation
L_{1-2} crenulation lineation
L_{1-2} intersection lineation
F_2 fold axis
F_2 rotation axis
D_3 Structures
S_3 foliation
Fracture cleavage

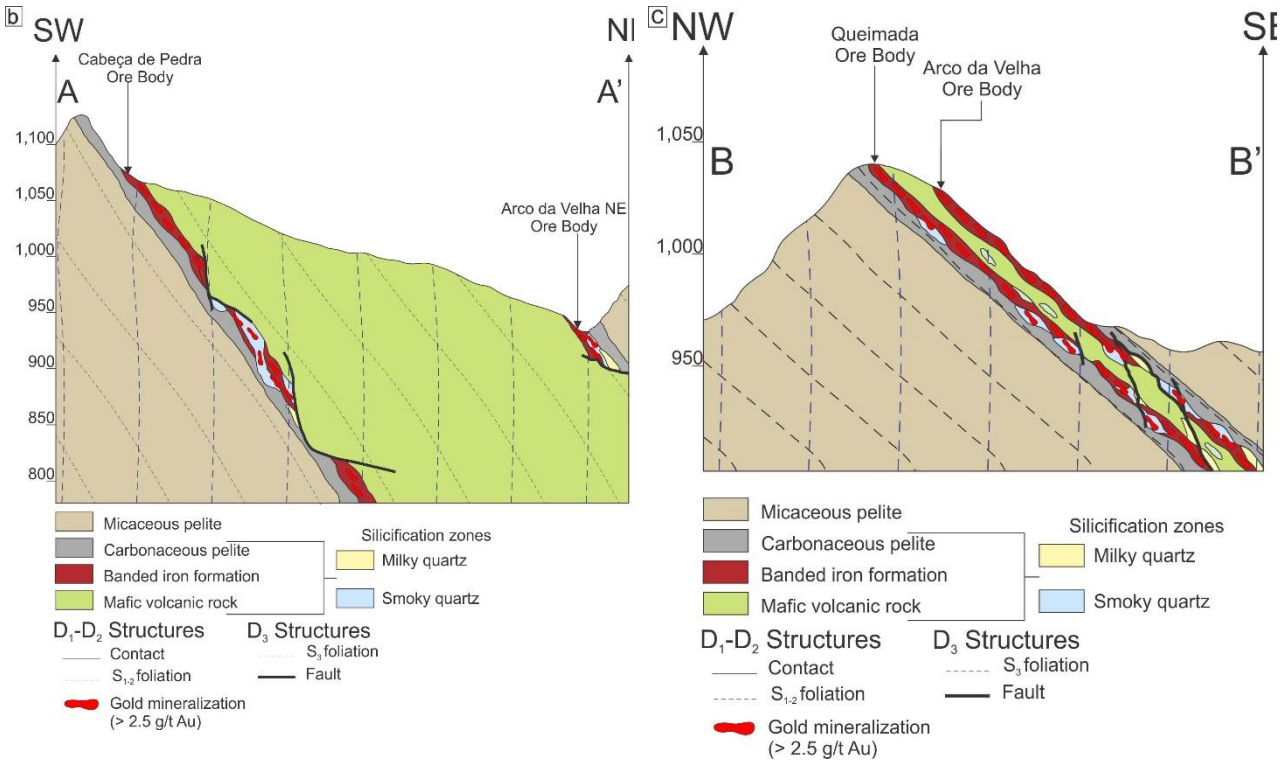

Figura 7: (a) Geological map of the Lamego open pit mine showing the four orebodies, where the macrostructure is represented by a reclined anticline. It has 4.8 km of outcropping perimeter, with NW-SE axis orientation. The overturned limb is the Queimada orebody (red), the normal limb is the Arco da Velha orebody (black), the hinge zone is the Cabeça de Pedra orebody (green), and the limb junction is the Carruagem orebody (blue). Modified after Villanova (2011). (b) NE-SW cross section cutting the Cabeça de Pedra and Arco da Velha orebodies showing the folded Lamego structure. (c) NW-SE cross section cutting the Queimada and Arco da Velha orebodies.

3.5 Lamego deposit: History and production

Exploration at Lamego started between 1985 and 1990, with the identification of several mineralized zones hosted in metachert and BIF. Three promising areas were selected, and named Arco da Velha, Queimada and Cabeça de Pedra orebodies (Figura 7). In 2001, a new drilling campaign targeted the Carruagem orebody and produced positive results, which supported further exploration efforts. Only in 2009 the Lamego Project resulted in the establishment of the Lamego mine and the mine life is estimated to extend to 2026.

More recently, in October 2014, AGA reported Lamego to have 250.000 t gold measured reserves and 1.3 million t measured resources, with an average grade of 7.26 Au g/t and the cut-off grade of 2.68 g/t Au (Table 4). The Lamego ore is processed together with the Cuiabá ore, at the gold plant that has a total annual capacity of 1.7 Mt with a 93% recovery (AGA, 2013).

Tabela 4: Total resource of the Lamego deposit, as of October 2013, COG >2.68 g/t Au. Source: AngloGold Ashanti Córrego do Sítio Mineração S/A.

Orebodies	Total resource of LAMEGO deposit – Oct. 2014 (with 2014 depletion) COG > 2.15 g/t											
	Measured			Indicated			Inferred			Total		
	Tons	Au g/t	Au (Oz)	Tons	Au g/t	Au (Oz)	Tons	Au g/t	Au (Oz)	Tons	Au g/t	Au (Oz)
Carruagem	2,010,374	5.96	384,913	631,907	6.63	134,603	1,038,950	5.36	178,915	3,681,231	5.90	698,431
Cabeça de Pedra	299,702	4.23	40,718	1,121,749	3.56	128,455	615,823	4.56	90,251	2,037,274	3.96	259,424
Arco da Velha	88,309	5.03	14,287	282,276	4.24	38,506	376,741	3.34	40,404	747,326	3.88	93,197
Queimada	4201	6.10	824	496,072	5.53	88,275	558,959	5.39	96,943	1,059,232	5.46	186,041
Arco NE	0,00	0,00	0,00	631,907	6.63	134,603	737,392	3.26	77,244	737,392	3.26	77,244
Total	2,402,586	5.71	440,742	2,532,004	4.79	389,839	3,327,865	4.52	483,756	8,262,455	4.95	1,314,338

3.6 Methodology

3.6.1 Underground geological mapping, petrography and structural analyses

Detailed underground geological mapping at 1:100 scales were undertaken at eight mine levels intersecting the Queimada orebody level 1, the Arco da Velha and Cabeça de Pedra orebodies, both levels 1 and 2, and Carruagem orebody levels 1, 2 and 5.1, although the paper focus on this latter orebody.

Recorded structural data include compositional banding, lithological contacts, foliations, veins, boudins, lineations, folds and thrust/shear zones. These data were used to build the structural evolution of the Lamego deposit in a regional context. In addition, seventy thin sections were made from seven diamond drill holes in order to establish the relationship between lithology, structure and gold mineralization.

3.6.2 Indirect and implicit 3D model

To understand the orebody geometry, gold distribution and the relationship between lithology, and structures, a 3D model of the orebodies was built using the Lamego AGA drillhole database. This model was combined with underground geological maps to highlight the structural behavior of the ore zones. Gold was analyzed via fire assay, each sample with 30 g; samples with results of fusion obtained by ICP-AAS greater than 30 g/t Au were redone using gravimetric analysis.

The colar, survey, geology and assay data were imported into the software package Leapfrog Geo® (version 2.1), and indirect and implicit lithological and grade shells models were built. The indirect method was chosen because of the high geological complexity of the host rocks in the ore zone.

It is considered good practice to do isotropic interpolation (= no preferred orientation) and isosurfacing as a first step into an implicit 3D lithological model to keep the modeling result as objective as possible (Hill et al., 2014, 2013; Vollgger et al., 2013). We interpolated the Au assay values assigned to the drill-hole intervals, and used spheroidal interpolation, since the linear

interpolation tended to create unrealistically voluminous isosurfaces in areas of sparse data (Hill et al., 2014, 2013; Vollgger et al., 2013). In order to avoid nugget effects, we have rejected the highest 30% of gold values for the Leapfrog model (Hill et al., 2014, 2013; Vollgger et al., 2013).

For the computational construction of the ore grade shells (implicit 3D assay model), approximately 54,000 assay samples were used. For the purpose of the present study, the grade shells values have been separated in the following ppm Au intervals: (i) low grades between 0.2-0.5 ppm; (ii) intermediate grades between 0.5-1.5 ppm; and (iii) high grades >1.5 ppm. These are not, however, considered economic grades at the Lamego mine. The interpolation parameters are summarized in Table 5. The histogram of ore grade shells from the four orebodies at Lamego reveal a positively skewed distribution (Figura 8), which is common for gold assay distribution (Hill et al., 2013; Vollgger et al., 2013).

Tabela 5: Summary of the LEAPFROG interpolation parameter used to build the 3D model.

Parameters	Values
Data transform	Log
Variogram model	Spheroidal isotropic
Sill	8.41
Range	50 m
Nugget	3.00
Drift	Constant (Ordinary kriging)
Isosurface resolution	1 m
Isosurfaces values	< 0.5 ppm
	0.5 – 1.5 ppm
	> 1.5 ppm

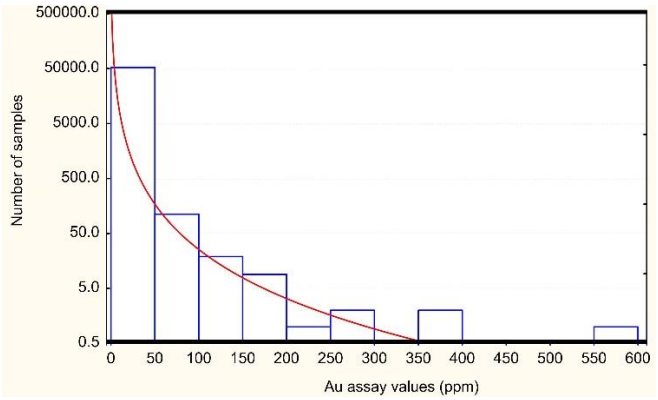

Figura 8: Histogram of gold distribution revealing a positive skewed distribution (data from AngloGold Ashanti Córrego do Sítio Mineração S/A).

3.6.3 U-Pb SHRIMP analyses

The sample selected (Figura 9a) for U-Pb SHRIMP analyses represents the sulfide zone of the lower mafic volcanic rock, at level 3 of the Cabeça de Pedra orebody. It was collected to investigate

the presence of hydrothermal monazite and xenotime, asboth minerals develop along the S_{1-2} foliation.

Eight polished thin sections (Figura 9b) were initially examined by optical microscope and scanning electron microscope (SEM) located in the Centre for Microscopy, Characterisation and Analysis (CMCA), at the University of Western Australia (UWA). The SEM is a TESCAN-VEGA3 equipped with an Oxford Instruments X-Max 50 silicon drift energy dispersive spectrometer (EDS) system with AZtec® and INCA® software. The EDS system was used to identify hydrothermal monazite and xenotime.

The monazite (Figura 9c) revealed to be much more common than xenotime, but only about 5% of the grains are suitable for U-Pb geochronology, and are thus at least 10 µm in size and lack mineral inclusions. Sections L1, L5, L6, and L7 contain the best grains, which were removed by micro-drilling. This generated 22 plugs of 1 mm and 3 mm in diameter that were organized in two epoxy mounts (N14-06 and N14-07). The U-Th-Pb analyses were carried out at the Sensitive High Resolution Ion MicroProbe - SHRIMP II (B) - at Curtin University of Technology, Western Australia, following the analytical procedures described by Foster et al. (2000). The primary ion current was ~0.4 nA, and each analysis consisted of six scans of the isotopic spectrum formed by 13 masses: $^{202}LaPO_2$, $^{203}CePO_2$, ^{204}Pb, $^{204}Background$, $^{205.8}NdPO_2$, ^{206}Pb, ^{207}Pb, ^{208}Pb, ^{232}Th, $^{245}YCeO$, ^{254}UO, $^{264}ThO_2$, and $^{270}UO_2$. Because the composition and amount of Th and U of monazite was unknown prior to the analyses, three standards were analyzed: French (Paquette et al., 1994), Z2234 (Fletcher et al., 2010; Stern and Sanborn, 1998), and Z2908 (Stern and Sanborn, 1998). During the analytical session, the Z2234 standard (1026 Ma; 200 ppm U; 6000 ppm Th) revealed to be closest to the composition of the Lamego monazite, and was established as the main standard for the Pb/U and Pb/Th calibrations.

Xenotime is present only in section L5 (mount N14-06) as three grains of about 12 µm in diameter (Figura 9d). Xenotime analyses were performed in another analytical session, where the primary O_2-beam was about ≤0.3 nA, using eight scans for each analysis of nine masses: $^{194}Y_2O$, ^{204}Pb, $^{204}background$, ^{206}Pb, ^{207}Pb, ^{208}Pb, ^{238}U, ^{248}ThO, and ^{254}UO. Xenotime standards MG-1 and Xeno1 were analyzed in another mount (B99), which was gold coated together with mount N14-06. The Pb/U and U content calibration standard was MG1 (490 Ma; U = ± 1000 ppm), whereas Xeno1 (997 Ma; Stern and Rainbird, 2001) was used to monitor the $^{207}Pb/^{206}Pb$ ratio. The SHRIMP operating procedures followed those of Fletcher et al. (2004) for xenotime, and Fletcher et al. (2010) for monazite. Data reduction was carried out using Squid 2.5 (Ludwig, 2009) and plots prepared using Isoplot 3 (Ludwig, 2003). Analytical details are given in Table 6.

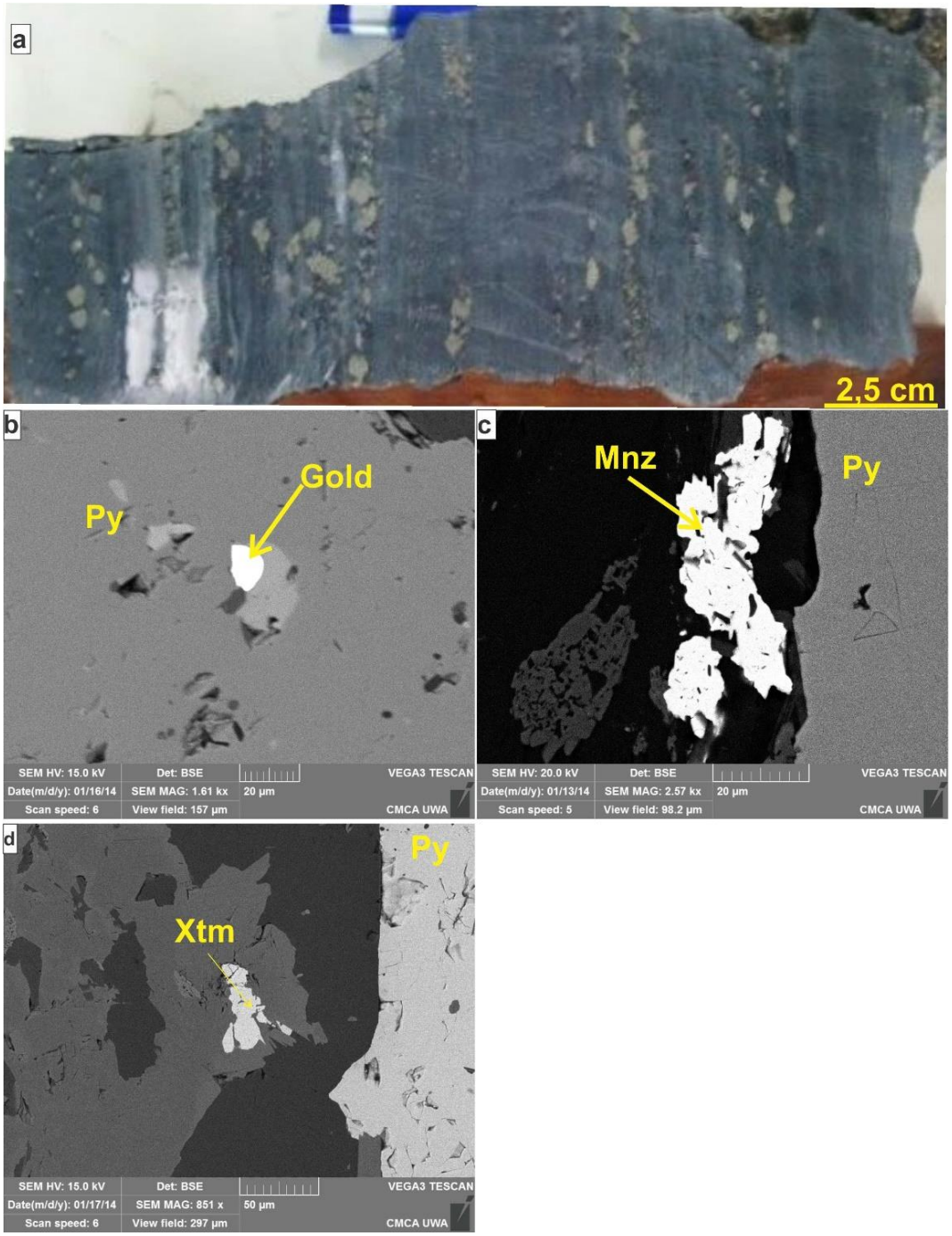

Figura 9: (a) Geological map of the Lamego open pit mine showing the four orebodies, where the macrostructure is represented by a reclined anticline. It has 4.8 km of outcropping perimeter, with NW-SE axis orientation. The overturned limb is the Queimada orebody (red), the normal limb is the Arco da Velha orebody (black), the hinge zone is the Cabeça de Pedra orebody (green), and the limb junction is the Carruagem orebody (blue). Modified after Villanova (2011). (b) NE-SW cross section cutting the Cabeça de Pedra and Arco da Velha orebodies showing the folded Lamego structure. (c) NW-SE cross section cutting the Queimada and Arco da Velha orebodies.

Tabela 6: U-Pb zircon SHRIMP isotopic data from hydrothermal monazite and xenotime crystals, Lamego gold deposit.

							Isotopic ratios					Ages			
spot	U ppm	Th ppm	Th/U	^{206}Pb ppm	^{208}Pb ppm	4f^{206} %	^{207}Pb/^{206}Pb	^{207}Pb/^{235}U	^{206}Pb/^{238}U	error correl.	^{208}Pb/^{232}Th	^{208}Pb/^{232}Th	^{206}Pb/^{238}U	^{206}Pb/^{207}Pb	disc. %
monazite															
a.1-1	37	21157	587	7	579	8.55	0.13138 ± 5.26	5.8774 ± 35.3	0.2053 ± 9.76	0.276	0.0305 ± 2.93	608 ± 18	1204 ± 107	2887 ± 551	63.6
c.1-1	36	29410	839	3	698	11.94	0.24249 ± 5.95	2.0384 ± 26.1	0.0864 ± 8.45	0.324	0.0265 ± 3.28	528 ± 17	534 ± 43	2568 ± 412	82.3
d.1-1	57	13646	246	13	558	17.75	0.32699 ± 8.49	7.2345 ± 26.9	0.2612 ± 8.34	0.310	0.0461 ± 3.34	901 ± 30	1496 ± 111	2833 ± 417	52.7
e.1-1	44	22345	520	11	804	5.18	0.16739 ± 4.81	7.7494 ± 19.1	0.2755 ± 7.66	0.401	0.0401 ± 3.56	796 ± 28	1568 ± 107	2859 ± 285	50.6
h.1-1	63	8344	136	17	292	5.19	0.23060 ± 2.61	8.2212 ± 8.48	0.3085 ± 4.88	0.576	0.0393 ± 3.32	774 ± 25	1733 ± 74	2770 ± 114	42.5
h.1-2	133	7450	58	49	450	3.03	0.20851 ± 1.53	10.9391 ± 4.96	0.4252 ± 3.77	0.760	0.0678 ± 4.85	1317 ± 62	2284 ± 72	2712 ± 53	18.7
h.1-3	77	5469	73	17	210	6.47	0.20954 ± 8.15	6.8930 ± 13.3	0.2682 ± 8.23	0.620	0.0434 ± 6.30	854 ± 53	1532 ± 112	2711 ± 172	48.7
j.1-1	59	12102	212	17	546	2.00	0.16806 ± 4.60	8.6872 ± 11.5	0.3389 ± 5.08	0.443	0.0502 ± 3.14	992 ± 30	1881 ± 83	2706 ± 169	35.0
m.1-1	67	7977	123	24	734	0.93	0.19680 ± 15.4	11.9128 ± 15.7	0.4213 ± 4.26	0.270	0.1026 ± 3.11	1975 ± 59	2266 ± 81	2867 ± 247	24.8
m.1-2	74	7815	109	24	764	1.47	0.13879 ± 2.37	8.0543 ± 6.77	0.3848 ± 4.18	0.617	0.1089 ± 3.05	2092 ± 61	2099 ± 75	2367 ± 91	13.3
m.1-3	62	5486	92	21	497	0.57	0.15950 ± 2.34	8.3306 ± 5.32	0.3913 ± 4.21	0.792	0.1012 ± 3.16	1947 ± 59	2129 ± 76	2395 ± 55	13.0
m.1-4	34	14168	437	5	526	9.36	0.27879 ± 4.10	4.8590 ± 16.1	0.1774 ± 6.54	0.406	0.0415 ± 7.46	821 ± 60	1053 ± 64	2815 ± 240	67.6
xenotime															
f.1-2	500	1948	4	35	46	0.58	0.05924 ± 6.61	0.6716 ± 7.36	0.0822 ± 3.24	0.440	0.0265 ± 3.21	525 ± 21	509 ± 16	576 ± 144	12
f.1-1	801	3614	5	59	87	2.22	0.05734 ± 11.5	0.6731 ± 11.9	0.0851 ± 3.01	0.253	0.0278 ± 3.99	537 ± 20	527 ± 15	505 ± 253	-4.5
f.2-1	650	2782	5	47	67	1.40	0.05829 ± 9.06	0.6724 ± 9.63	0.0837 ± 3.13	0.347	0.0273 ± 3.60	531 ± 20	518 ± 16	540 ± 199	3.7

3.7 Geological setting of the Lamego gold deposit

3.7.1 Lithostratigraphy

The Lamego deposit is hosted by metamorphosed volcano-sedimentary rocks of the Nova Lima Group, which is represented by a concordant lithostratigraphic package (Figura 6). The orebodies are disposed along the Lamego fold (Figura 7a, b, c; Lobato et al., 2013; Martins, 2011; Martins et al., 2011).

From bottom to top the deposit's stratigraphy comprises metabasalt (chlorite-carbonate-sericite-quartz schists), banded chert layers with BIF that are both carbonaceous and/or ferruginous, and carbonaceous and micaceous phyllites, with mineral paragenesis compatible with the greenschist facies mineralogy. The rocks are metamorphosed (Figura 6); hence, the prefix "meta" applies to rock names but is hereafter omitted for brevity.

3.7.2 Mafic volcanic rock

Green, fine-grained and massive mafic volcanic rock is the oldest unit exposed in the core of the Lamego deposit (Figura 6). The best exposures are located at level 1 of the Queimada, Arco da Velha and Cabeça de Pedra orebodies. They are up to 200 m thick (Sales, 1998), with a lateral extent of approximately 1.7 km; this rock may exhibit chert layers up to 1 m thick (Figura 7a).

In foliated portions, the mafic rock is defined by sericite and carbonate schists that encircle sigmoidal aggregates mainly formed by pyrite, where an anastomosed fabric and crenulated trails developed (Figura 10a).

If present, the pre-hydrothermal paragenesis includes plagioclase, amphibole, epidote, and titanite. Plagioclase is partly replaced by hydrothermal carbonate, quartz, and sericite, whereas the mafic minerals are mainly replaced by chlorite (Figura 10b).

3.7.3 The Lamego chert and banded iron formation (Lamego BIF)

Chert bands vary from light creamy to dark colored, the latter impregnated by carbonaceous matter, and may contain centimeter-thick carbon films. Ferruginous chert usually contains very fine siderite (rarely magnetite), where this rock may locally grade into true BIF (defined by >15% Fe-content: Brandt et al., 1972; James, 1954; Percival, 1954). In this paper, both chert and BIF bands are referred to as the Lamego BIF.

Locally in the BIF bands, a 15- to 20-cm thick, foliated and sulfidized mafic horizon is intersected in the Cabeça de Pedra orebody level 2. The relationship between the amount of chert bands and true BIF varies for each orebody. In the Arco da Velha, Cabeça de Pedra and Carruagem orebodies chert dominates BIF over 50%. For the Queimada orebody the relationship is inverted, with BIF dominating over 50%. The chert beds can be up to 2 m thick, with the best exposure in level 2 of the Arco da Velha orebody, and level 1 of the Cabeça de Pedra orebody.

The Lamego BIF is associated with volcanic rocks thus compatible with Algoma-type BIF (Gross, 1980, 1965). The thickness of the BIF ranges between 1 to 8 meters (Sales, 1998), whereas the lateral extent of the BIF horizon is discontinuous and extends up to 500 m in length (Figura 7a).

The bands of the Lamego-BIF are characterized by alternating, dark carbonate-quartz (±magnetite) and light quartz-carbonate bands (Figura 10c, d). The BIF is comprised of quartz, carbonate, chlorite, sericite, pyrite, arsenopyrite, pyrrhotite (and minor chalcopyrite, galena and sphalerite), and accessory minerals such as sericite, rutile and carbonaceous matter (Figura 10e, f).

3.7.4 Pelitic rocks

Carbonaceous and micaceous pelites (Figura 10g, h) are at the top of the stratigraphic succession in the Lamego deposit. They envelop the entire Lamego deposit, with the carbonaceous pelite being 1 to 5 m thick, and the micaceous pelites up to 200 m thick (Sales, 1998). Both have a lateral extent of up to 1.7 km (Figura 7a).

The carbonaceous pelites (Figura 10g) are dark, finely laminated, thinly bedded, and made up

of carbonaceous matter, quartz, chlorite, carbonate and minor sericite. Locally, these rocks form 0.50- to 1-m thick lenses in the mafic rock and BIF.

The greenish to light grayish, micaceous pelites (Figuras 6 and 10h) overlie the carbonaceous pelites; they are laminated and display gradational and compositional stratification. The micaceous pelites contain sericite, muscovite, quartz, carbonate and subordinate amounts of carbonaceous matter.

3.7.5 Diabase intrusions

These are exposed mainly in the Carruagem orebody level 1, and in the Cabeça de Pedra open pit (Figura 7a). They may be parallel to or crosscut both carbonaceous and micaceous pelites, and BIF. They extend for about 200 meters with an average width of up to 5 meters. These are fine-grained textured, green rocks, and although foliated near the contacts with wall rocks, they grade to medium grained over short distances towards the core of the intrusion, where the foliation is not prominent. The dikes and sills are composed of green hornblende, actinolite-tremolite, epidote, chlorite, carbonate, plagioclase, sericite and quartz. The main accessory minerals are titanite and ilmenite (Villanova, 2011).

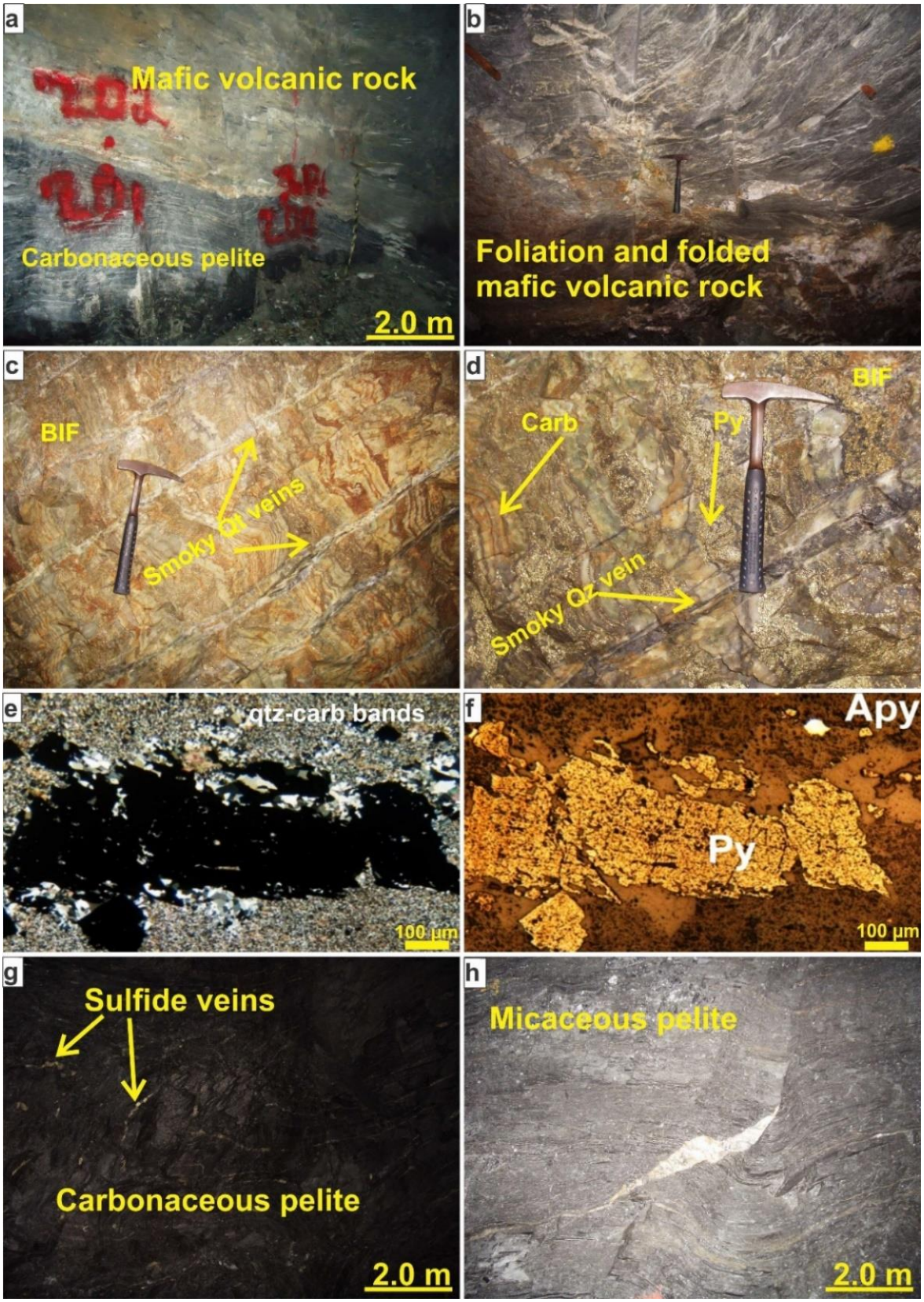

Figura 10: Mafic volcanic rock in a (a) Foliated portion in contact with the carbonaceous pelite; Carruagem orebody, level 5.1, Az. 30º, and (b) In a massive and folded portion; Carruagem orebody, level 1, Az. 25º. (c) BIF showing smoky quartz (Qz) veins cutting the bands, systematically characterizing a spaced cleavage. (d) BIF showing smoky quartz (Qz) veins and associated bands with carbonate (Carb) and sulfides, mainly pyrite (Py) (both **c** and **d**: Cabeça de

Pedra orebody, level 2, respectively Az. 90º and 270º). (e) Photomicrograph of pyrite (Py) and arsenopyrite (Apy) as the main sulfides of BIF; uncrossed nicols, reflected light (200X); (f) Photomicrograph of carbonate (Carb) and smoky quartz (Qz) of BIF; crossed nicols, transmitted light, (200X). (g) Outcrop of carbonaceous pelite, composed mainly by carbonaceous matter, with sulfide veins; Cabeça de Pedra orebody, level 2, Az. 180º. (h) Outcrop of greenish to light grayish, foliated micaceous pelite, with milky quartz sigmoids; Carruagem orebody, level 2, Az. 300º.

3.8 The Carruagem, Queimada, Arco da Velha and Cabeça de Pedra orebodies at the Lamego deposit

Gold at Lamego is recovered from four orebodies (Figura 7a, b, c), Carruagem being the most significant, followed by Queimada, Arco da Velha, and Cabeça de Pedra.

The Carruagem orebody (Figura 11a, b, c) is located in the NE portion of the Lamego fold. It carries the highest gold grades at Lamego, and contains 62% of the reserves. From levels 1 to 5.1, mineralization is predominantly associated with smoky quartz veins. From levels 5.1 to 8, the BIF thickens, and the amount of gold increases proportionately. The underground lithological and structural maps of the Carruagem orebody, at levels 1, 2 and 5.1, show significant geological variations at depth, such as: mafic rocks that dominate in the central portions of the mapped areas; decrease in the volume of BIF; increases in silicification zones from level 1 to 5; and encircling of carbonaceous pelites around silicification zones (see Table 7).

The Queimada orebody is at the overturned limb and is located in the NW of the Lamego fold. It carries the lowest gold grades at Lamego, and is not mined yet. At level 1, mineralization is predominantly associated with BIF.

The Arco da Velha orebody is at the normal limb and located in the SE of the Lamego fold. In level 2, this orebody shows a continuous, mappable chert layer measuring 194.08 m^2 and massive sulfide zones associated with a silicification zone totalizing 6.73 m^2.

The Cabeça de Pedra orebody is at the hinge zone and is located in the SW of the Lamego fold. This orebody displays the best expression of continuous mappable chert layer with a thickness ranging between 1 to 2 meters, totalizing 4,976,27 m^2, and massive sulfide zones associated with zones of silicification and chert layers, totalizing 9.42 m^2.

In general, between levels 1 and 2 the silicification zones increase in thickness and volume with depth, while BIF decreases. Faults develop mainly between the mafic volcanic rock and carbonaceous pelites and less with BIF, silicification zones and micaceous pelites. In Table 7, the geological features observed in the geological maps (Figura 11) are summarized.

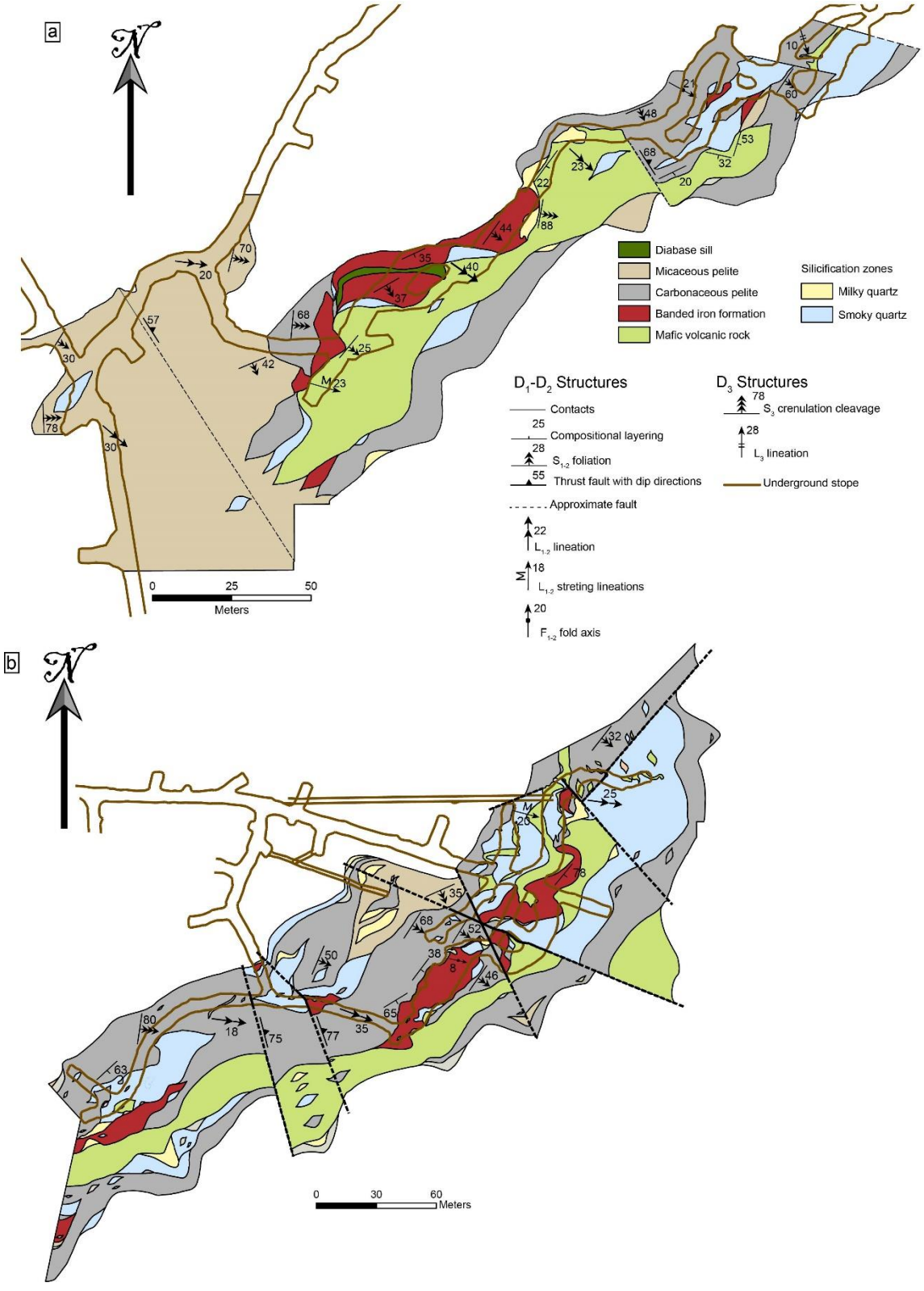
a
N
Diabase sill
Micaceous pelite
Carbonaceous pelite
Banded iron formation
Mafic volcanic rock
Silicification zones
Milky quartz
Smoky quartz
D1-D2 Structures
Contacts
Compositional layering
S1-2 foliation
Thrust fault with dip directions
Approximate fault
L1-2 lineation
L1-2 streting lineations
F1-2 fold axis
D3 Structures
S3 crenulation cleavage
L3 lineation
Underground stope
0 25 50
Meters
b
N
0 30 60
Meters

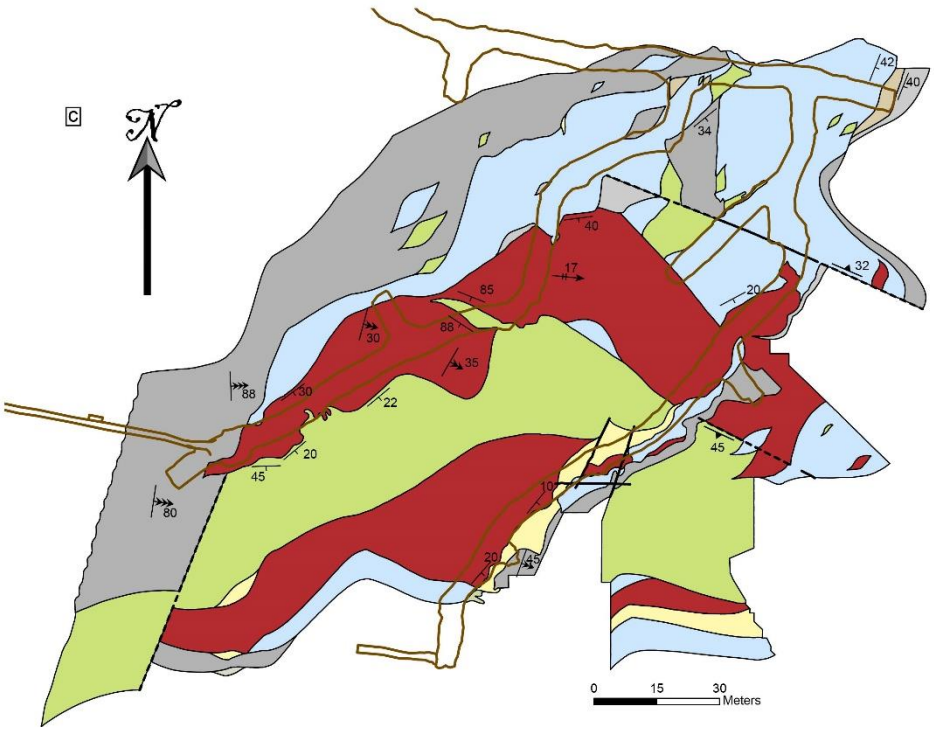

Figura 11: Geological maps of the Lamego underground mine showing 3 levels of the Carruagem orebody. (a) Level 1 elevation 800 m, where BIF dominates the SW and smoky quartz the SE portions of the map, respectively. (b) Level 2 elevation 750 m, where BIF dominates on the central portion, while smoky quartz dominates both the SE and SW portions. (c) Level 5.1 elevation 650 m, which corresponds to the SE portion of levels 1 and 2, in this case with an increase in BIF volume and smoky quart.

Tabela 7: Summary of the orebodies characteristics resulted by underground geological mapping.

Orebody	Structural position in Lamego fold	Levels	Mafic rock	Lamego BIF	Carbonaceous pelite	Micaceous pelite	Silicification zones
Carruagem	Limb junction (in NE)	1	Center of map	NW portion	Dominates and thickens in NE Thinning out in SW	SW portion	NE portion
		2	SW and SE portions	Center of map and less in NE portion	Thick in center and SW of map	Local, in center of map	NE portion
		5.1	SW portion and center of map	SE and SW portions	NE and NW portions	–	NE portion and between BIF and carbonaceous pelites
Queimada	Overturned limb (in NW)	1	Center of map	Dominates the entire map Thick in SE and SW portions Thin in NE and SW portions	Encloses all other lithologies	Local, in NW portion	Only small areas between BIF and carbonaceous pelites
Arco da Velha	Normal limb (in SE)	1	In footwall of orebody	Dominates the entire map	On top of BIF Also as lenses in BIF	On top of carbonaceous pelites	Restricted to BIF
		2	In footwall of orebody	SW portion	Thick in SW and NE	Local in NE portion	Predominance in the NE and center parts of the map Thinning out in SW
Cabeça de Pedra	Hinge zone (in SW)	1	Center of map	NE, NW and center of map	Thickens from SE to SW	–	SE and SW portions
		2	Center of map	SE to SW	Thickens from SE to SW	–	SE to SW portions Local in the NE portion

3.9 Hydrothermal alteration, mineralization styles and location of gold grains

3.9.1 Hydrothermal alteration

Hydrothermal alteration in the BIF-hosted gold deposits of the Nova Lima Group are discussed by Junqueira et al. (2007), Lobato et al. (1998 a, b; 2001a); Martins Pereira et al. (2007),

Ribeiro Rodrigues (1998), Ribeiro Rodrigues et al. (2007), Vial et al., a, b, c (2007) and Vieira (1991). For the specific case of Lamego, Sales (1998) detailed the hydrothermal alteration of the mafic rock unit. Lobato et al. (2013), Martins (2011), and Martins et al. (2011) described significant silicification in the proximal alteration zones of ore-hosting rocks.

There are three main types of hydrothermal alteration that dominate and affect all rock types. They are represented by quartz, carbonate and sulfide, and developed parallel to the S_{1-2} foliation. These alteration minerals are best exposed in BIF and carbonaceous pelites (Figura 12a), but less well developed in the mafic volcanic footwall rock and micaceous pelites (Figura 12b, c).

Silicification is the dominant hydrothermal alteration type in the Lamego deposit, containing smoky and milky quartz veins (Figura 10c, d), and minor carbonates, sericite, pyrite and carbonaceous matter. These zones are characterized by high-modal percentage quartz (>85%). They locally form hydraulic breccias that may or may not be boudinaged. The width ranges between 1 to 35 m, where quartz grains can be >0.5-cm long (Figura 12a, b, c, d).

Three quartz generations are present (Figura 12e): (i) deformed, coarse- to medium-grained smoky quartz as irregular masses, both concordant and discordant, within the mineralized zones; (ii) fine-grained, granoblastic, white and milky quartz, which formed from the recrystallization of smoky quartz, and (iii) milky quartz, particularly in fault zones cutting across generations (i) and (ii).

Sulfidation is defined by sulfide veins (5 mm to 7 cm wide; Figura 12f). They locally replace entire Fe-carbonate-rich bands in the BIF (Figuras 10d and 12g). The sulfides are mostly represented by pyrite, As-rich pyrite, arsenopyrite, less chalcopyrite and sphalerite, and also minor pyrrhotite and galena (Figura 13a, b, c, d). This alteration zone also contains small amounts of sulfosalt minerals as tennantite-tetrahedrite and nickeline, as well as the phosphate monazite.

Carbonatization is defined mainly by ankerite, and is best developed as coarse-grained crystals (up to 2 cm) in BIF (Figuras 10e, f and 12g).

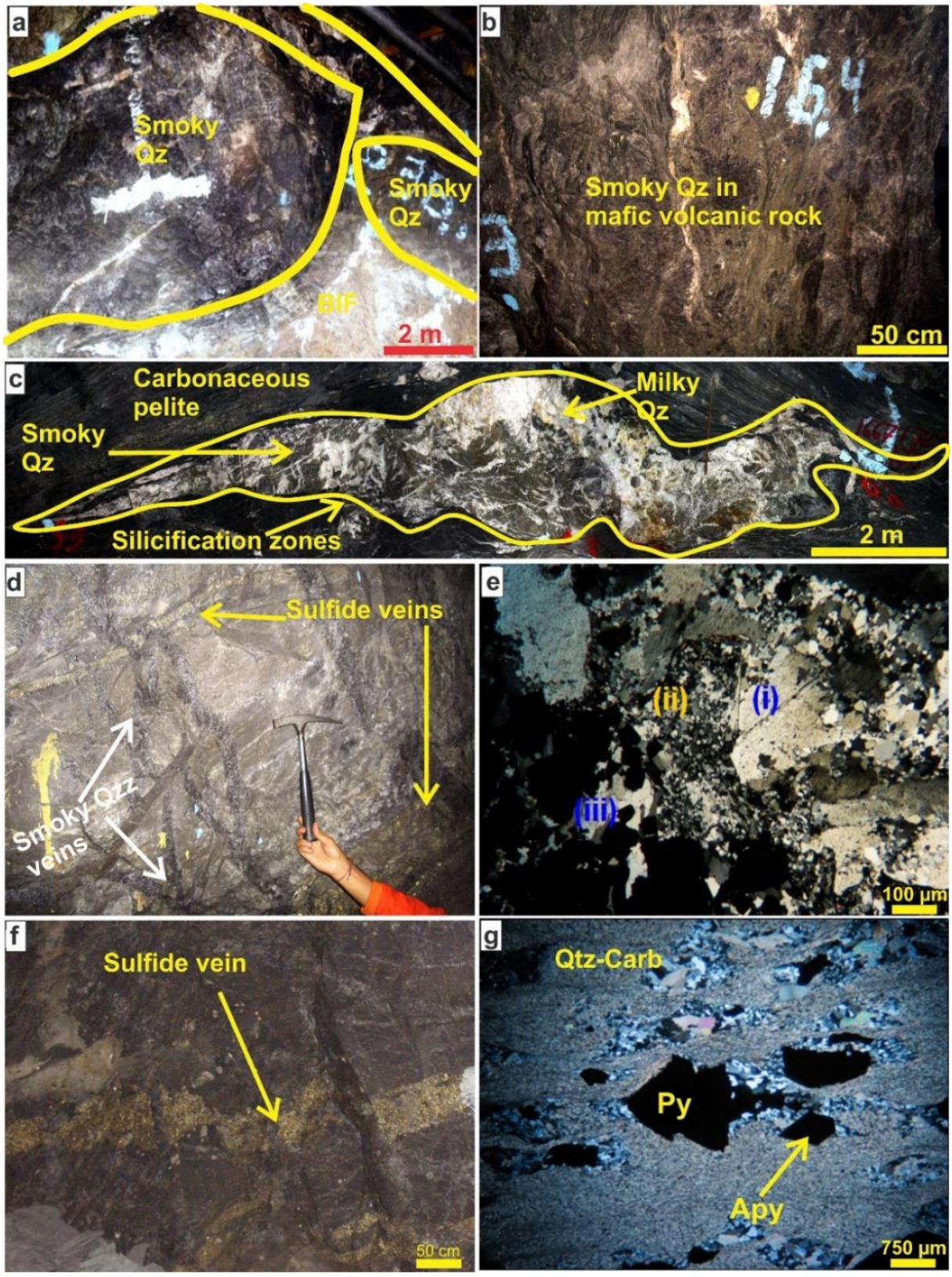

Figura 12: (a) Boudinaged, smoky quartz (Qz) restrained to a fragment of BIF; Carruagem orebody, level 1, Az. 200º. (b) Smoky quartz (Qz) in mafic volcanic rock; Carruagem orebody, level 2, Az. 290º. (c) Sigmoidal, smoky quartz (Qz) in carbonaceous pelite that is structurally controlled by the S_{1-2} foliation; note that the smoky quartz (Qz) turns into milky quartz along the edges; Carruagem orebody, level 1, Az. 190º. (d) Pyrite-dominated silicification zone formed where chert/BIF

previously dominated. In detail coarse-grained, smoky quartz (Qz) forms veins that cut the silicification zone and are associated with pyrite (Py); Arco da Velha orebody, level 1, Az. 320º. (e) Photomicrograph of a silicification zone showing three types of quartz: (i) anhedral to locally subhedral, irregular, fractured, medium- to coarse-grained smoky quartz, (ii) fine-grained, polygonal granoblastic quartz, white and milky quartz, developed from the recrystallization of smoky quartz, and (iii) milky quartz, polygonal and subhedral, coarser than (ii); crossed nicols, transmitted light (250X); (f) Pyrite-dominated sulfide veins, in BIF fragment; Arco da Velha orebody, level 1, Az. 350º. (g) Photomicrograph of carbonate (Carb) alteration zone with siderite and associated sulfides, mainly pyrite (Py) and arsenopyrite (Apy); crossed nicols, transmitted light (250X).

3.9.2 Mineralization styles

At least three main gold mineralization styles are identified in the Lamego deposit. In the mineralized BIF, V_2 veins dominate (Figura 10c, d) in association with sulfide replacement of the Fe-carbonate and rare magnetite (Figura 10d). In the mafic rock and carbonaceous pelites the disseminated style dominates (Figura 12a).

The *vein style* includes quartz-carbonate±sulfides veins and quartz boudins, which range in thickness from 2 mm to 5 cm (Figs. 6d and 8a, b, c). These veins crosscut all lithologies, but are best developed in BIF that locally shows stockwork texture. The irregular smoky/milky quartz zones can reach widths of >35 m (Figura 12d, f, g). Gold grades from ore shells in both veins and quartz zones range from 1.6 to 15.8 ppm, locally attaining 300 ppm.

The *replacement style* is typical of BIF, and characterized by the confinement of sulfides to this lithology, where favorable Fe-rich carbonate bands (Figura 10d, e, f) are replaced by sulfides (Figura 13a, b, c, d). Gold grades vary from 0.03 to 6.63 ppm, with values as high as 89.0 ppm.

The *disseminated style* is characteristic of the mafic rock unit and carbonaceous pelites (Figura 12c), with the best exposures located at the Cabeça de Pedra orebody. Disseminated sulfides commonly develop in 5-10-cm-wide shear zones parallel to the S_{1-2} foliation (Figura 12c). The gold grade ranges from 0.03 to 3.8 ppm.

3.9.3 Location of gold grains

Gold grains in sulfide-rich BIF vary from 0.04 to 0.05 mm, and are hosted in pyrite and As-rich pyrite, filling As-rich pyrite and porous pyrite (Figura 13a, b), along the contacts between carbonate, smoky quartz and arsenopyrite (Figura 13c, d). In silicification zones gold may be "free", included in pyrite, arsenopyrite, and sphalerite (Figura 13d), along arsenopyrite edges, and as trails in pyrite.

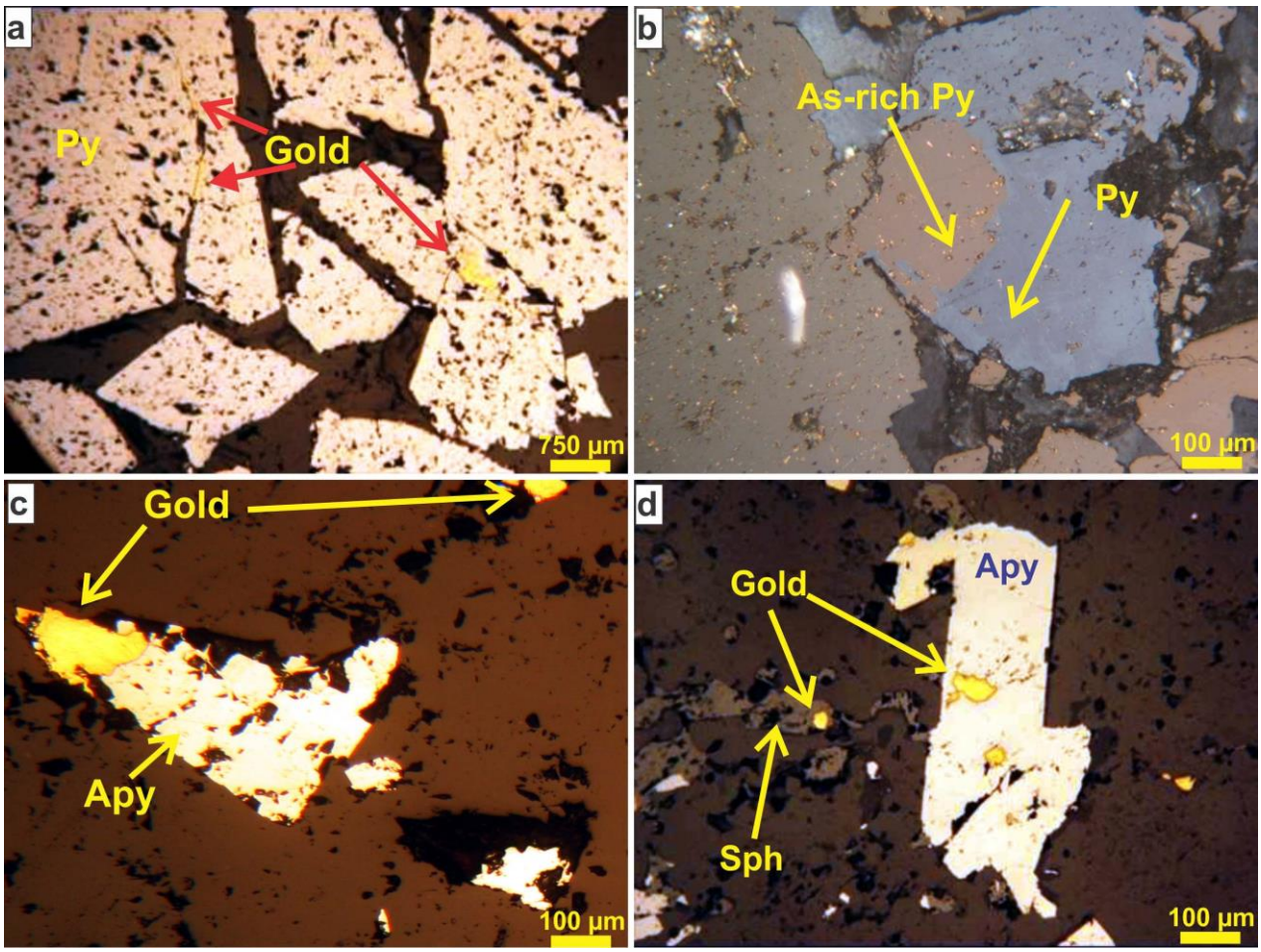

Figura 13: (a) Gold strips associated with porous pyrite (Py), filling fractures and pores; crossed nicols, reflected light (100X). (b) As-rich pyrite and pyrite (Py) in contact; uncrossed nicols, reflected light, (200X). (c) Gold associated with arsenopyrite (Apy); crossed nicols, reflected light (200X). (d) Gold particles included in arsenopyrite (Apy), sphalerite (Sph) and smoky quartz (Qz); reflected light, crossed nicols (200X).

3.10 Chronology of deformational events at the Lamego deposit

Lobato et al. (2013), Martins (2011), Martins et al. (2011) and Sales (1998) describe the deformational history at the Lamego deposit. It includes two structural generations, referred to herein as G_1 and G_2, each one encompassing a set of structural elements.

The G_1 structural generation developed in a progressive deformation event and resulted in structures oriented from NE-SW and dipping to the SE. Structures pertaining to the G_2 structural generation are oriented N-S dipping to the W.

3.10.1 G_1 - First structural generation

The G_1 structures include sheared, relict gradational and compositional bands (S_0); a penetrative axial-planar foliation (S_{1-2}); a lineation (L_{1-2}) (mineral, stretching and fold axis); veins (V_1

and V_2); boudins; pinch-and-swell structures; folds (F_2); and shear zones (Table 8).

Tabela 8: Structural elements and evolution of the Lamego gold deposit.

Chronological Deformational Events	Structures	Geometry
G_1 Structures	Lamego fold	Isoclinal recumbent anticline
		NW-SE axial trace
		Dipping 20º to 30º to the SE
	S_0 gradational and compositional bands	Plunges 29º-41º towards 108º-148º
	S_{1-2} foliation	Plunges 28º-42° towards 124º-134º
	L_{1-2} Lineations	Plunges 28º-40º towards 128º-155º
	V_1 veins	Plunges 20º-60º towards 20º-80º
	V_2 veins	Plunges 20-60 towards 98-160
	F_2	Recumbent folds
	F_2 fold axes	Plunge 10º-28º towards 90º-160º
	Shear zone	Plunge 22º-70º towards 102º-168º
G_2 Structures	S_3 crenulation cleavage	Plunge 80º-90º toward N-S
	L_3 crenulation lineation	Plunge 30º toward 180º
	F_3	Open folds
	F_3 fold axes	Plunge 15-30 towards 180º-200º
	Conjugate pair faults	15º-75º towards 20-80
		20º-90º towards 185-240

The Lamego fold is the most visible structure related to the G_1 structures, with a perimeter of about 4.8 km and a maximum width of 450 m (Figura 7a). The fold is defined by the layering of the mafic unit with minor BIF and large exposures of carbonaceous and micaceous pelites. It is a rootless, reclined, isoclinal, cylindrical fold with an axial trace striking northwest-southeast dipping 20º to 30º. The hinge zone is thickened (Figura 7b) and the limbs are thinned (Figura 7c), with the limbs dipping 20º to 30º to the SE.

The oldest planar structures at Lamego are the gradational and compositional bands (S_0) (Figura 14a) that represent the sedimentary layering, and the deformation associated with G_1 tends to partly or entirely transpose S_0. Even with consecutive and intense G_1 and G_2 deformational events, there are portions of the bands that preserve the primary structures. The lithological contacts between the rocks are normal, folded and sheared, but maintain the normal lithostratigrapy. The pole figures of the compositional bands show that S_0 is concentrated in the SE, and dip 29º-41º towards 108º-148º (Figura 14b).

The S_{1-2} foliation is the most conspicuous planar structure of the Lamego deposit (Figura 14c). It is defined by the arrangement of chlorite, sericite, quartz and carbonates. It is best developed in the carbonaceous and micaceous pelites, and in the hydrothermally altered mafic volcanic unit. The S_{1-2} foliation is parallel to sub parallel in the S_0, and dips 28º-42° towards 124º-134º (Figura 14d).

The L_{1-2} stretching mineral lineation (Figura 14c) is defined by elongated quartz, carbonate, sericite and sulfides; it is best developed in the mafic unit and in the carbonaceous and micaceous pelites. The L_{1-2} lineation is oriented to E-SE, and plunges 28º-40º towards 128º-155º (Figura 14d).

The vein system consists mostly of quartz-carbonate-sulfide veins, namely V_1 and V_2. The V_1

veins follow the trend of the spaced cleavage and crosscut all structures (Figura 14e), whereas V_2 veins are folded, and may display pinch-and-swell structures and boudinage (Figura 14f). Where V_1 veins crosscut BIF along hinge zones, the associated minerals migrate along the lateral bands forming the V_2 veins and imposing a pseudo-stratification (Figura 14f). In stereographic projection, V_1 veins are oriented in the NE quadrant, and dip 20º-60º towards 20º-80º (Figura 15a). The V_2 veins are oriented in the SE quadrant, and dip 20-60 towards 98-160 (Figura 15b).

The F_2 reclined folds only have a local exposure (Figura 15c), and have a close to open geometry. In stereographic projection, F_2 fold axes plunge 10º-28º towards 90º-160º (Figura 15d), and are parallel to sub-parallel to mineral lineation L_{1-2}. However, the best expression of the F_2 fold is displayed in BIF at the Carruagem orebody level 5.1, where folds are also reclined with a close to open geometry, but their axes plunge 5º-20º towards 90º-118º.

A northeast-trending, 1-2-m thick shear zone is oriented parallel to the axial plane of the F_2 folds and preferentially developed in all schistose layers with the best exposure in the Carruagem orebody (Figura 15e; left upper corner of photo). Shear zones are perpendicular to the F_2 fold axes, and dip 22º-70º towards 102º-168º (Figura 15f).

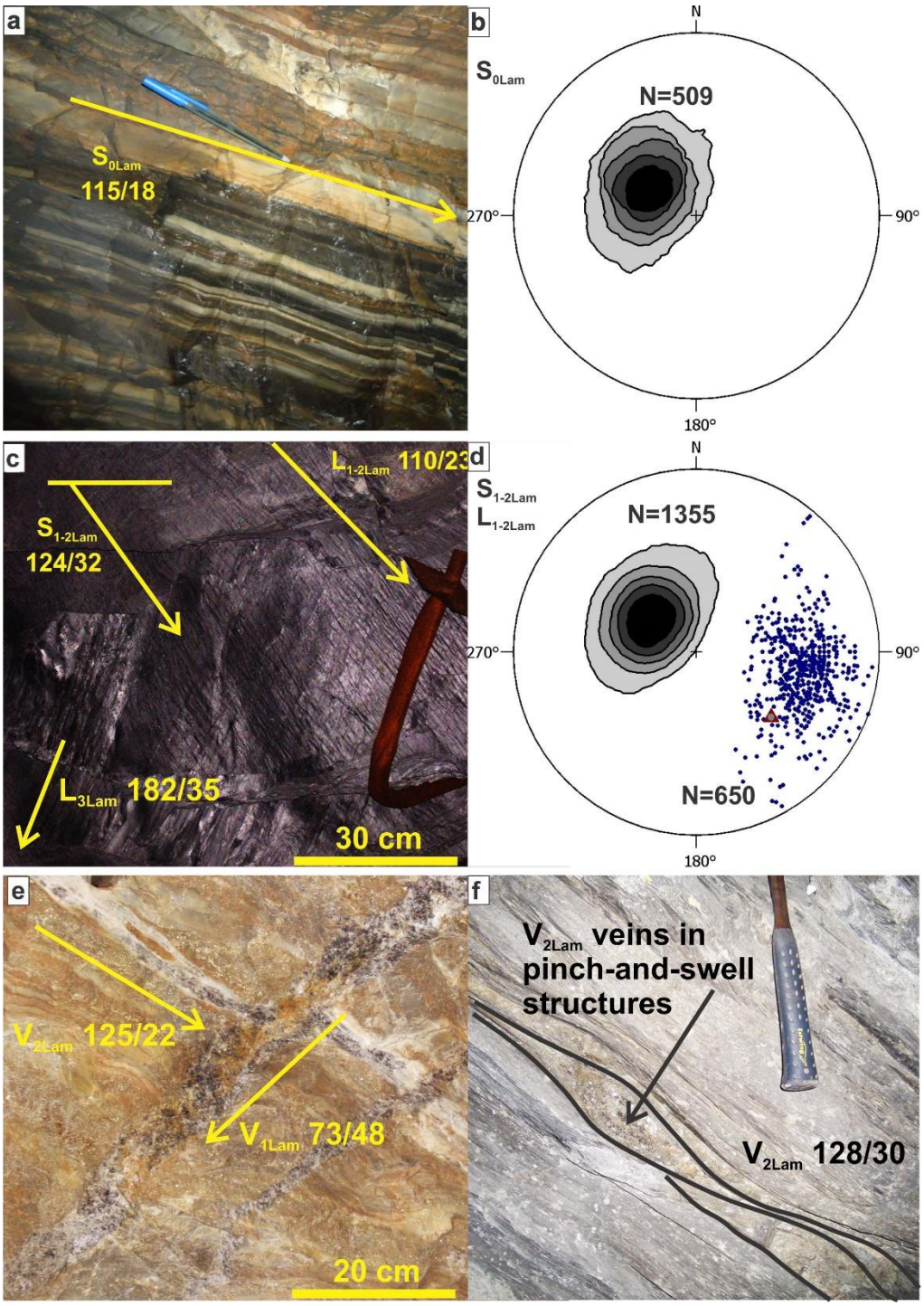

Figura 14: Photo plates showing the relative timing of structural elements and stereographic projection that are displayed by density, equal-angle projection and lower hemisphere. (a) Transposed gradational and compositional S_0 bands; Arco da Velha orebody, level 2, Az. 340º. (b) S_0 plunge concentrated to the SE. (c) S_{1-2} foliation and L_{1-2} on this plane, with L_3 lineation also observed; Arco da Velha orebody, level 1, Az. 15º. (d) S_{1-2} foliation with a geometry similar to the S_0 band, and both concentrated in the SE, with the L_{1-2} lineation also plunging to the SE; the brown triangle on the figure represents the foliation intersection. (e) Photo displays a V_1 vein following the trend of the spaced-cleavage and crosscuting all structures in BIF; Cabeça de Pedra orebody, level 2, Az. 285º. (f) V_2 vein that migrates along the lateral band of a carbonaceous pelite, and imposing a pseudo-stratification; it develops as boundinage that evolves into pinch-and-swell structures; Cabeça de Pedra orebody, level 1, Az. 220º.

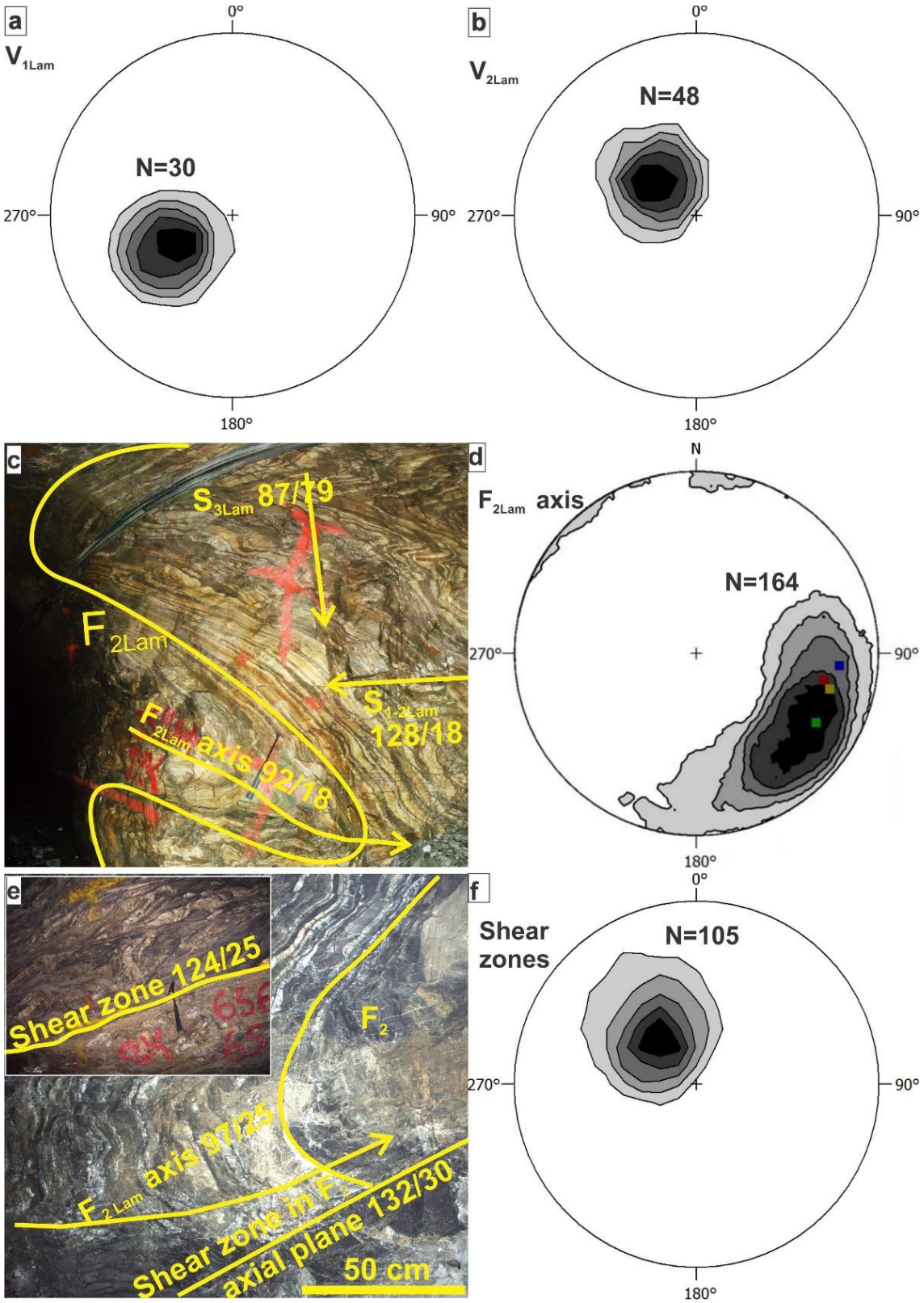

Figura 15: Photo plates showing the relative timing of structural elements and stereographic projection that are displayed by density, equal-angle projection and lower hemisphere. (a) V_1 veins oriented in the NE, and (b) V_2 veins oriented in the SE. (c) F_2 folded BIF with an axis attitude of 92/18. The fold was affected by S_{1-2} foliation in the planar-axial position and by the S_3 spaced cleavage; Carruagem orebody, level 5.1, Az. 210º. (d) F_2 fold axis concentrated in the SE. The

squares indicate the plunge of the orebodies: blue for Carruagem - plunging 22 towards 95; red for Queimada - plunging 29 towards 102; yellow for Arco da Velha - plunging 25 towards 102; and green for Cabeça de Pedra - plunging 25 towards 120. The plunges are concentrated on the main fold axis dispersion. (e) Shear zone oriented parallel to the axial plane of the F_2 folds. In detail (left upper corner of photo) note shear zone approximately one-meter thick; Carruagem orebody, level 2, Az. 340º. (f) Shear zones also showing dip to the SE.

3.10.2 G_2 - Second structural generation

The G_2 structural generation (Table 8) is composed of the crenulation cleavage (S_3), the crenulation lineation (L_3), the open fold (F_3) and faults.

The S_3 crenulation cleavage is defined by sericite, and its expression depends on rock types. The S_3 crenulation cleavage is well developed in the micaceous and carbonaceous pelites (Figuras 14a and 16a), and the hydrothermally altered mafic unit. It is poorly developed in BIF, where it appears as S_3 spaced cleavage (Figura 15c). These foliations are oriented N-S/80º-90º (sub vertical), but can dip less than 60º (Figura 16b).

The L_3 crenulation lineation is defined by the intersection between S_{1-2} foliation and S_3 crenulation cleavage (Figura 16a). In stereographic projection the L_3 crenulation lineations appear on an N-S great circle with an average plunge of 30º towards 180º (Figura 16b).

The F_3 open folds (Figura 16c) are developed in micaceous and carbonaceous pelites showing low amplitudes, with a width of up to 3 meters. The F_3 fold axes plunge with angles of less than 30º, oriented to S with azimuth between 180 to 200º (Figura 16d).

A significant conjugate pair of faults is observed at the Lamego deposit (Figura 16e). They have northwest-southeast and northeast-southwest orientation, and developed as normal and reverse faults cutting all rocks; locally the faults in the carbonaceous pelite vary their dip angles from 30° to 90°. In stereographic projections (Figura 16f), these faults show two distinct populations: (i) concentrated to the NE dipping 15º-75º towards 20-80; and (ii) concentrated to the SW, dipping 20º-90º towards 185-240.

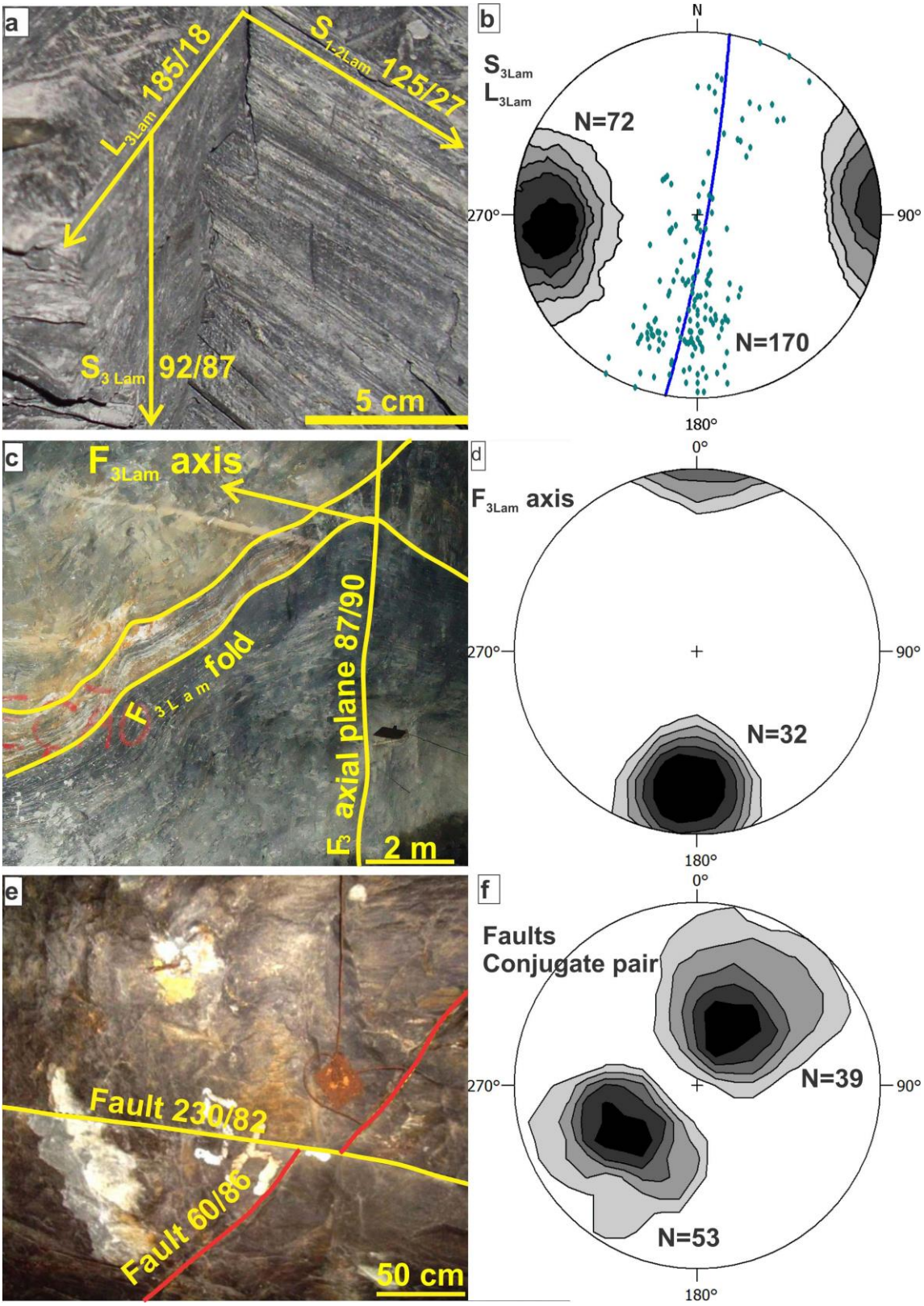

Figura 16: Photo plates showing the relative timing of structural elements and stereographic projection that are displayed by density, equal-angle projection and lower hemisphere. (a) Geometrical relationship between S_{1-2} and the vertical S_3 foliation that gave place to the formation of L_3; Arco da Velha orebody, level 1, Az. 15º. (b) The S_3 is oriented N-S/80º-90º and the L_3 in the N-S great circle has an average plunge of 70º. (c) F_3 folds develop in the carbonaceous pelites up to 3 meters; Carruagem orebody, level 5.1, Az. 30º. (d) F_3 fold axes plunge 30º towards 180 to

200º. (e) Conjugate pair of faults developed as normal and reverse faults; Queimada orebody, level 1, Az. 315º. (f) Stereographic projection of fault pairs showing two distinct populations: one concentrated in the NE, and another in the SW.

3.11 Structural control of orebody geometry

Gold resources for the Lamego deposit are calculated based on the geological characteristics of the orebodies. The general gold grade distribution for the Lamego deposit, including the Carruagem orebody levels 1 and 2, are described below.

The resulting indirect and implicit lithological model reveals an outline marked by the footwall mafic and pelitic rocks that has a general NE direction dipping to the SE; the continuity of these rock types is confirmed to depths below level 5.1. Areas where drill-hole data are lacking, the lithological model is uneven as observed in Figura 17a.

The trends of the Lamego orebodies vary from NE to SW, and dip to the SE. Their plunge ranges from 22º towards 95º in the Carruagem orebody to 25º towards 120º in the Cabeça de Pedra orebody; the Queimada orebody plunges 29º towards 102º, and the Arco da Velha 25º towards 102º (Figura 17b).

For the Carruagem orebody level 1, gold grades between 0.2 and 0.5 ppm are measured in all rock types. Intermediate gold grades of 0.5 ppm are restricted mainly to BIF, silicification zones, and less to carbonaceous pelites. These grades in the NE portion are related to fault zones. On the other hand, grades >1.5 ppm are associated with BIF, silicification zones, and also contact zones between carbonaceous pelites with BIF. Areas of equal gold grades (isosurfaces) are interrupted by three NW-SE faults that crosscut these surfaces, resulting in gold grades distributed in two main directions: NE-SW and to N-S both dipping to the SE (Figura 17c).

As for the Carruagem orebody level 2, gold grades between 0.2 and 0.5 ppm are measured in all rock types. Intermediate gold grades of 0.5 ppm are restricted mainly to BIF, silicification zones, and less to carbonaceous pelites. Gold grades >1.5 ppm are associated mainly with fold hinge zones of BIF, coeval to the development of the Lamego fold. However, in the NE portion where the silicification zones are dominated by breccia and fault zones with gold grades > 1.5 ppm (Figura 17d).

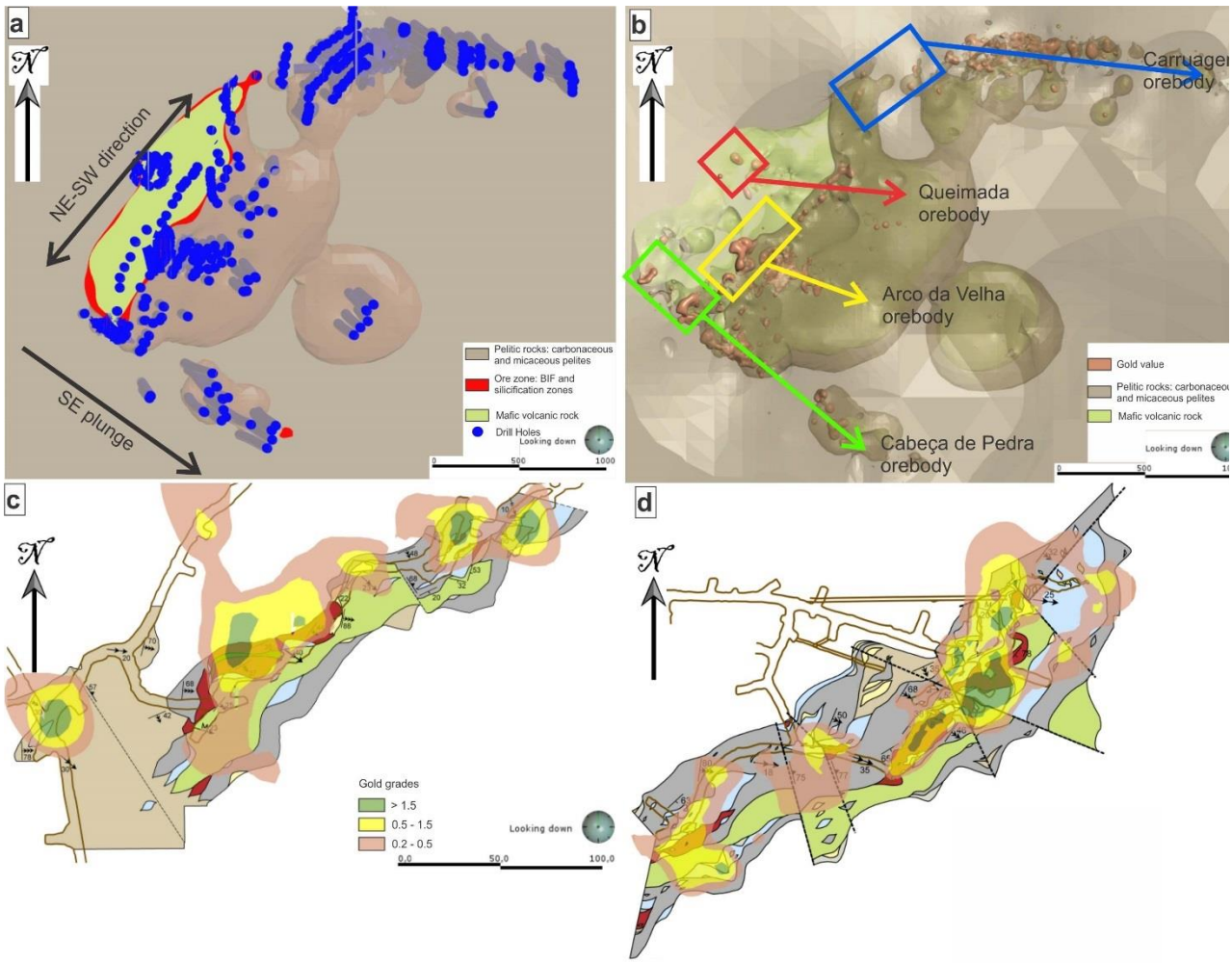

Figura 17: (a) Outline marked by the footwall mafic and the hanging wall pelitic rocks that have both a general NE direction dipping to the SE. (b) Orebodies plunge according to legend of Figura 8. Arrows follow the same color scheme as Figura 8 for the Carruagem (blue), Queimada (red), Arco da Velha (yellow), and Cabeça de Pedra (green) orebodies. (c) Gold grades are represented as isosurfaces for the Carruagem orebody, level 1. (d) Idem, for Carruagem level 2.

A section through the Carruagem orebody (Figura 18a) shows that mineralization is concentrated in several parallel to sub-parallel, 2-5-m thick, irregular tabular ore zones that crosscut the S_{1-2} foliation, and these plunge generally 25-35º towards E to SE. When viewed in sections cut perpendicular to the S_{1-2} foliation (Figura 18b), high-grade gold lenses show an ellipsoidal pattern and a distribution that varies along the S_{1-2} foliation plane. On the other hand, when observed in sections cut parallel to the L_{1-2} mineral lineation (Figura 18c), high-grade gold lenses show a discontinuous distribution, and display a boudinage and pinch-and-swell geometry forming necks.

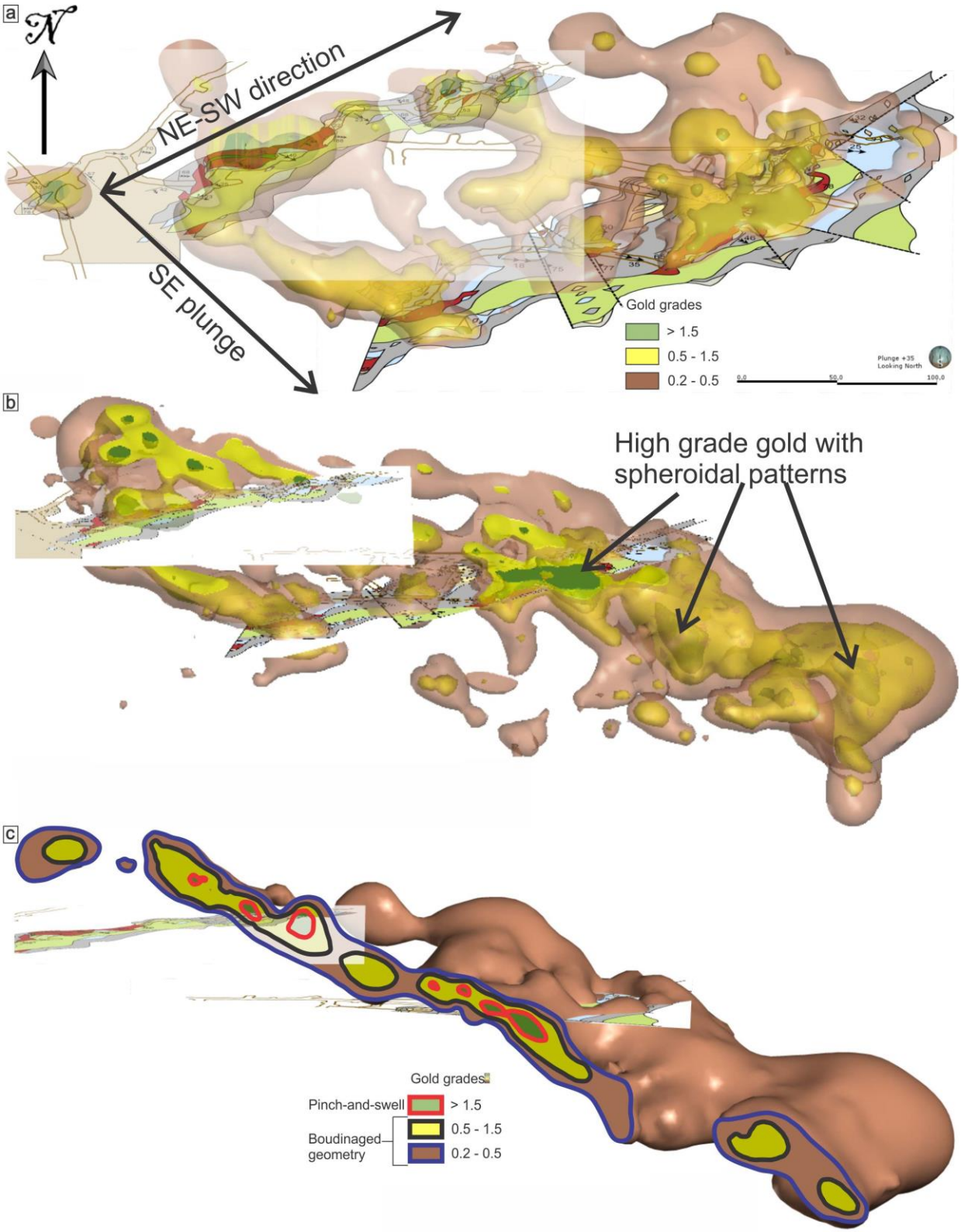

Figura 18: (a) Section through the Carruagem orebody showing the mineralization parallel to sub-parallel to the S_{1-2} foliation. (b) Sections cutting parallel to the S_{1-2} foliation, with the high-grade gold lenses exhibiting a spheroidal pattern. (c) Sections cutting perpendicular to the S_{1-2} foliation show a boudinaged geometry that evolves into pinch-and-swell.

3.12 SHRIMP U-Pb geochronology

Sample LM-CP is a mineralized sericite-quartz-carbonate±chlorite±pyrite schist, and represents the sulfide zone of the lower mafic volcanic rock, level 3 of the Cabeça de Pedra orebody (Figura 9a). It is intercalated with albite-bearing, sub-parallel, V_2 quartz veins. Pyrite with multiple inclusions replaces carbonates, and is mostly associated with quartz veinlets. Gold particles are included in pyrite (Figura 19a), and the gold grade is close to 0.2 g/t Au.

*Monazit*e: About 30 grains were tested and only 12 analyzed. The majority of the grains are very poor in radiogenic ^{206}Pb (3 ppm or less), and also relatively rich in common lead. The analyses of 18 grains were aborted during the first scan. Using a spot size of 10 μm, the resulting 12 analyses were U (average = 62 ppm), and ^{206}Pb poor (average = 17 ppm), and also extremely poor in ^{207}Pb (average = 3.2 ppm). The small spot size combined with the weak primary beam and the low content of radiogenic ^{206}Pb and ^{207}Pb produced large uncertainties in the $^{207}Pb/^{206}Pb$ ages (average = 234 Ma).

All data are discordant to highly discordant (discordance from 13% to 82%), where 10 results align in the same regression line intercepting the concordia curve at 2730 ± 42 Ma (2 sigma; MSWD=0.51) (Figura 19b).

Two of the monazite grains crystals are younger and align in another regression line, intercepting the concordia curve at 2387 ± 46 Ma. The Lamego monazite grains have much more Th (average = 1.3%) than U, and consequently their main radiogenic lead is ^{208}Pb (average = 555 ppm). The Th/Pb ages (uncertainties average = 42 Ma) are more precise than the $^{207}Pb/^{206}Pb$ ages (uncertainties average = 234 Ma), and could provide a better age establishment for the monazite population. However, there was a ^{208}Pb loss even stronger than the ^{206}Pb and ^{207}Pb losses; the twelve $^{208}Pb/^{232}Th$ ages are all scattered between 528 and 2092 Ma. These ages are considered meaningless.

Xenotime: Only three analyses were performed and the results show reasonable U (average = 650 ppm) and high Th contents (Th/U ratios from 4.03 to 4.66). The Pb/U and U calibration used the MG-1 standard (490 Ma; 1000 ppm U). Xeno1 was used to monitor the $^{207}Pb/^{206}Pb$ ratio, but normalization of this ratio was not required because the obtained $^{207}Pb/^{206}Pb$ age (997 Ma) coincides with the age of the standard. The average ^{206}Pb is 47 ppm, whereas the average of ^{207}Pb is only 2.7 ppm. The low amount of ^{207}Pb reflects large uncertainties for the $^{207}Pb/^{206}Pb$ ages (from 144 to 253 Ma), when compared to the uncertainties of the $^{206}Pb/^{238}U$ ages (15 to 16 Ma). The data are concordant and the inverse concordia age is 518.5 ± 9 Ma (MSWD=0.41; 2 sigma) (Figura 19c).

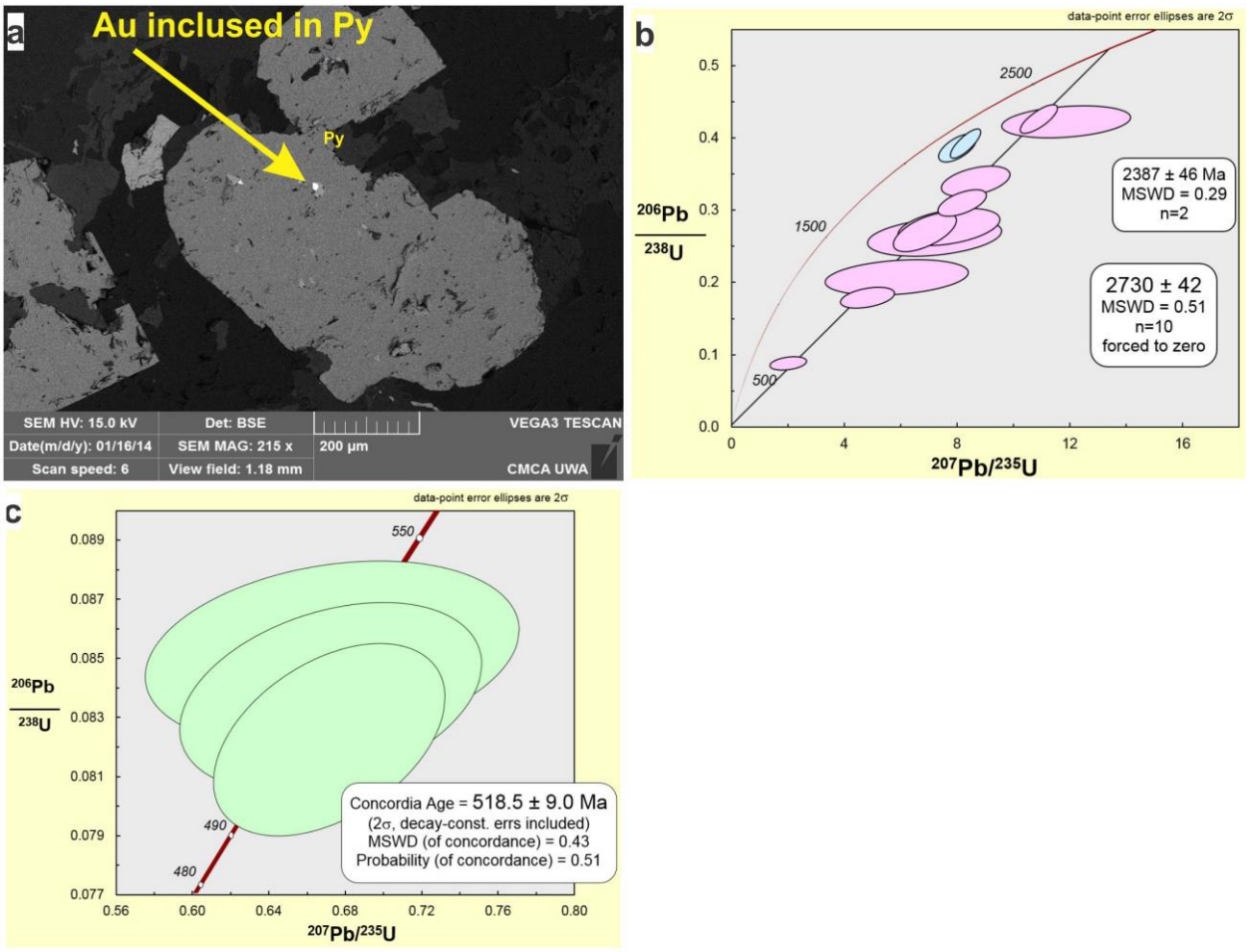

Figura 19: Back-scattered electrons image and concordia diagrams of mafic volcanic rock (mineralized sericite-quartz-carbonate±chlorite±pyrite schist; LM-CP), selected for geochronological studies at the Lamego deposit (data in Table 6); Cabeça de Pedra orebody, level 3. (a) Representative back-scattered electron images of sulfide crystals showing gold grain included in pyrite. (b) Concordia plot of SHRIMP U-Pb data for hydrothermal monazite. The weighted mean $^{207}Pb/^{206}Pb$ age of the main concordant cluster is 2730 ± 42 Ma (2 sigma; MSWD=0.51). Two monazites are discordant, younger at 2387 ± 46 Ma. (c) Concordia plot of SHRIMP U-Pb data for hydrothermal xenotime. The weighted mean $^{207}Pb/^{206}Pb$ age of the main concordant cluster is 518.5 ± 9 Ma (MSWD=0.41; 2 sigma).

3.13 Geological evolution of the Lamego deposit in the QF regional context

The geological evolution of the Lamego deposit is considered in the context of the tectonic framework of the QF, mainly in view of the new geochronological data presented in this contribution. In particular, we must take into account the 2749-2670 Ma Archean, the Paleoproterozoic (2.22 - 2.05 Ga; Brito Neves, 2011), and the 630-480 Ma Brasiliano orogenic events (Alkmim and Marshak, 1998; Baltazar and Zucchetti, 2007; Lobato et al., 2007; Pedrosa Soares et al., 2011).

3.13.1 Archean progressive deformation event and the first structural generation - G_1

At a regional scale, Baltazar and Zucchetti (2007) described a progressive D_1-D_2 event that is characterized by a NNE to SSW tectonic transport, with folds and faults verging to NNE. The D_1 event took place between 2749 to 2670 Ma, whereas the progressive D_2 event took place at approximately 2700 Ma (table 3 of Baltazar and Zucchetti, 2007; Lobato et al., 2001a, b; Table 3).

This regional D_1-D_2 deformation event was responsible for the first generation structures - G_1 at the Lamego deposit (Figura 20a). It is interpreted to have formed the Lamego fold and associated gold mineralization (Figura 20a).

The G_1 structures are understood as progressive because the folds associated with both the S_0 compositional bands and S_{1-2} foliation show parallelism and geometrical similarities; these are reclined folds with the axial folds concentrated and plunging to the SE quadrant (Figs. 10b, d and 11d; Martins, 2011; Martins et al., 2011).

The main G_1 structures are the V_1 and V_2 veins, the S_{1-2} foliation, the L_{1-2} mineral lineation, F_2 folds, and shear zones that formed along the axial plane of F_2 folds. The Lamego V_1 veins appear to be the only structural feature related to the commencement of the regional progressive D_1 event (e.g., Baltazar and Zucchetti; 2007; Figura 20a). The veins strike NNS, dip to the NE, and their geometry coincides with regional faults and shear zones (Table 8). Accepting these relations, we interpret the formation of the V_1 veins to have started at 2749 Ma (table 3 of Baltazar and Zucchetti, 2007). As V_1 veins evolved to form the V_2 veins, during the G_1 folding and shearing event, these latter veins develop the same geometry as the S_{1-2} foliation (Figura 20b), striking to the NE and dipping to the SE.

The continuous development of the S_{1-2} foliation resulted in the formation of metric- to decametric-scale reclined folds, striking to the NE and dipping to the SE (Figura 15c, d). These folds formed during the NW-SE regional tectonic transport (Figura 20b; Martins, 2011; Martins et al., 2011).

While the S_{1-2} foliation plane shows a consistent orientation dipping to the SE (Figura 15c), the trend of the L_{1-2} mineral lineation and fold axes L_{b1-2} is variable (Figura 15c), indicating a coeval relation between F_2 folds and shearing that caused axis rotation, coaxial refolding and disruption of the limbs.

As folds are subsequently flattened, pinch-and-swell structures and boudins are developed (Figura 20b, c). The final stage of flattening imposes a prolate deformation model, since two stretching directions are established: (i) the longest deformation axis trends NW-SE, which represents

the tectonic transport direction during thrusting, and (ii) the intermediate axis trends NE-SW, which represents the lateral escape direction in a triaxial, non-planar deformation. This resulted in a chocolate-tablet, boudin-type structure with two orthogonal stretching directions (cf. Davis, 1996; Ramsay, 1987), developed during the Lamego mineralization (Figura 18a, b, c; Martins, 2011; Martins et al., 2011).

The deformation related to the first structural generation G_1 also gave place to faults and shear zones, disposed along the F_2 fold axial plane oriented in the NE-SW direction and dipping to the SE (Figura 20b, c). These faults and shear zones, associated with V_1 and V_2 veins, served as hydrothermal fluid pathways in the Archean (Lobato et al., 2007; 2001a, b). Interaction between hydrothermal fluids and host rocks resulted in the precipitation of hydrothermal minerals such as quartz, pyrite, carbonate, sericite, and gold. The richest orebodies represent the loci where the mineralizing fluids were concentrated during folding, resulting in mineralization hosted preferentially in F_2 hinge zones and boudins. The F_2 fold axes control the plunge of the orebodies (Figura 17b and 18b, c).

The original G_1 structures, responsible for gold mineralization, probably corresponded to the Archean NW-SE Rio das Velhas trend, demonstrated by the new SHRIMP U-Pb monazite age at 2730±42 Ma (MSWD=0.51) (Tabela 6, Figura 19b).

3.13.2 Paleoproterozoic deformation event and its relationship to the first structural generation - G_1

At a regional scale, and following the D_1-D_2 regional Archean progressive deformation, two other deformation events affected rocks of the QF, namely D_3 and D_4 (Baltazar and Zucchetti, 2007). The D_3 corresponds to the Minas accretionary orogeny (Teixeira et al., 2015), which affected the Minas Supergroup in the Paleoproterozoic (Alkmim and Marshak, 1998; Table 3; Marshak and Alkmim, 1989).

It is noteworthy that Alkmim and Marshak (1998) comment that the Paleoproterozoic NW-verging, thin-skinned thrusting event, compatible with D_3 of Baltazar and Zucchetti (2007; Table 3), did not generate a strong regional foliation. The maximum attitude of this foliation has a plunge of 67 towards 111 (D_1 of Alkmim and Marshak, 1998; Table 1), with bedding having a maximum plunge of 64 towards 140 (structural data in Alkmim and Marshak, 1998, Figura 12b), some 5 km NW from Lamego.

These Paleoproterozoic attitudes, both foliation and bedding, are similar for the same structures, S_{1-2} and S_0, in our study. They have been ascribed to the first structural generation G_1 evolved during the D_1-D_2 regional deformation events, which are interpreted to be of Archean age. In

light of this geometrical similarity, it is likely that the regional D_3 foliation is overprinted and parallelized with S_{1-2} foliation (G_1 structures) at the Lamego deposit area. Baltazar and Zucchetti (2007) also recognized this regional overprinting in the Cuiabá and Farias gold deposits areas.

3.13.3 Cambrian deformation event and the second (post-mineralization) structural generation - G_2: relationship to the G_1 structures

The regional Cambrian deformation characterized as D_4 corresponds to the Brasiliano orogenic event (630-480 Ma; e.g., Pedrosa Soares et al., 2011) that affected rocks of the Rio das Velhas and Minas Supergroups, with an E to W tectonic transport. This gave rise to N-S structures dipping to the E and W (Alkmim and Marshak, 1998; Baltazar and Zucchetti, 2007; Marshak and Alkmim, 1989).

At the deposit scale, the regional D_4 event is evidenced by the second structural generation - G_2, defined by the S_3 crenulation cleavage, which developed during the transposition of the S_{1-2} foliation, and therefore formed the intersection L_3 crenulation lineation and F_3 folds (Figura 20d). The F_3 fold axes as well as the L_3 crenulation cleavage lineation are distributed along a great circle with an approximate N-S direction. The crenulation cleavage strikes NS and dips to the E (Lobato et al., 2013; Martins, 2011; Martins et al., 2011).

Two aspects that corroborate the Brasiliano orogenic event imprint on the Lamego gold deposit must be taken into consideration: (i) the direction and dip of the G_2 structures at Lamego are similar to the regional D_4 regional structures, defined as the Brasiliano orogenic event (Alkmim and Marshak, 1998; Baltazar and Zucchetti, 2007; Marshak and Alkmim, 1989), (ii) the age of the hydrothermal xenotime at 518.5 ± 9 Ma (MSWD=0.41; Table 6, Figura 19c).

We interpret that the present position of the Lamego orebodies is due to their structural modification during the regional D_4 Brasiliano event.

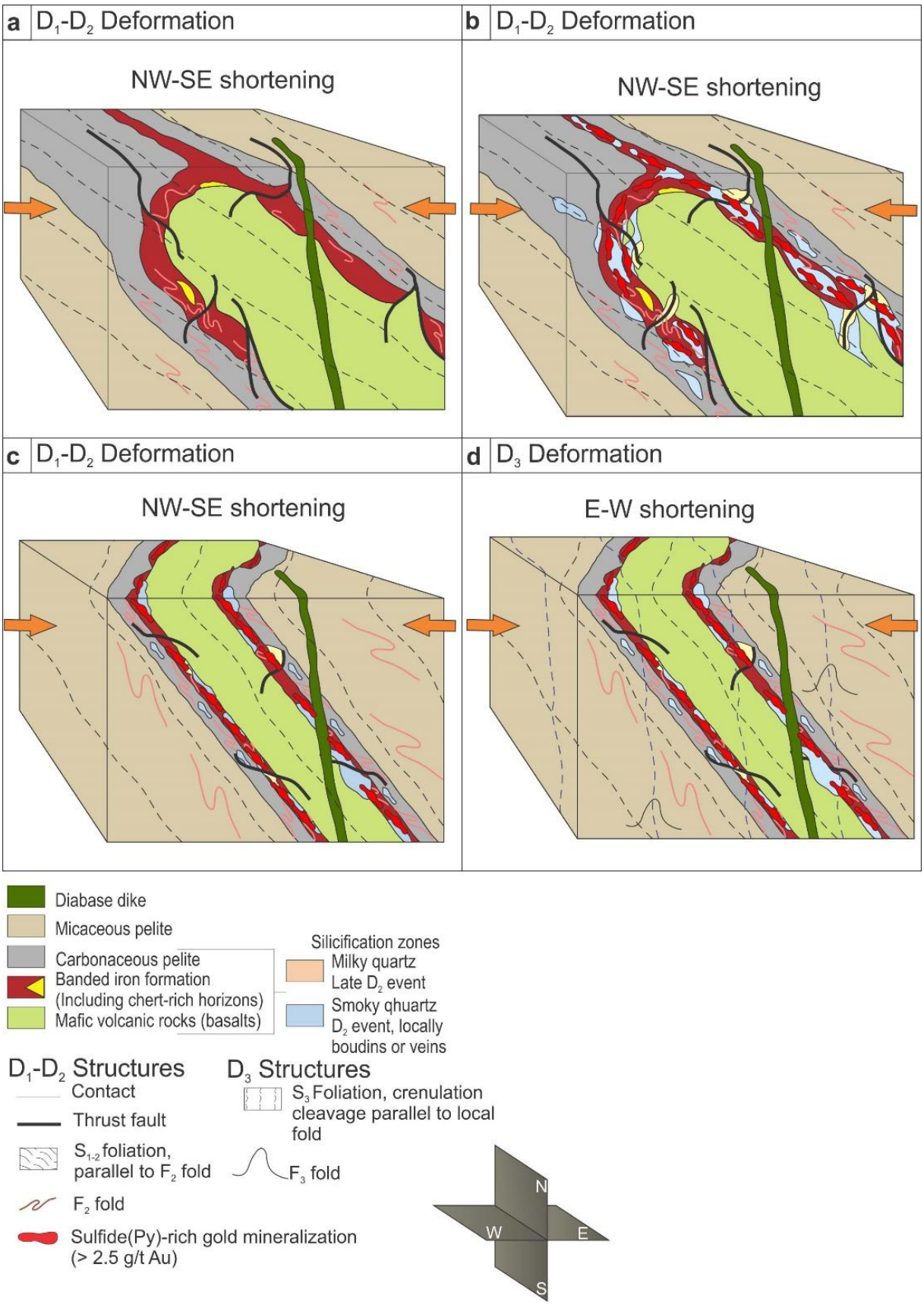

Figura 20: Schematic cartoon structural model without scale for the formation of the Lamego gold deposit. (a) The lithologies are folded and shear zones started to develop; (b) As shear zones progressed, veins evolved and both functioned as pathways for hydrothermal fluids, which

precipitated coarse-grained, irregular zones of smoky quartz in massive veins. These veins were progressively deformed, assumed the structural aspect of boudins, and as their recrystallization advanced, fine-grained milky quartz formed. Gold mineralization generally coincides with the development of pyrite and As-rich pyrite, sulfide zones. (c) Refolding of the Lamego structure as part of the D_1-D_2 progressive event. (d) Final stage of the Lamego gold deposit evolution with the modification of the orebodies in the Cambrian probably as a result of the late stages of the Brasiliano orogeny (see text for explanation).

3.14 Discussion

3.14.1 Evolution, age of mineralization and deformation events, and implications for the development of the Lamego orebodies

The evolution at the Lamego deposit indicates that gold mineralization formed close to 2730 ± 42 Ma (MSWD=0.51; Figura 19b), based on new age data obtained from hydrothermal monazite grains associated with gold-bearing sulfides (Table 8, Figura 19b). This is corroborated by the age of the Cuiabá and Morro Velho gold deposits at 2672±14Ma (MSWD=2.3; Lobato et al., 2007), although the latter study did not detect younger Proterozoic ages. This is also in tune with the long-standing notion of NE-SW compression resulting in NW-SE-trending structures as being of Archean age.

The discordant 2387 ± 46 Ma age on hydrothermal monazite, developed along S_{1-2} (Figura 19b), is interpreted with much caution, since it was obtained with two discordant (13% disagreement) monazite grains. The importance or significance of this age for gold mineralization at the Lamego deposit with respect to the regional context is not yet fully understood.

The Minas Supergroup is an 8 km-thick passive-margin to syn-orogenic sedimentary package (Alkmin and Noce, 2006), deposited between ~2.5 and 2.12 Ga (Alkmim and Marshak, 1998; Dorr, 1969; Hartmann et al., 2006; Machado et al., 1992), and deformed during the Rhyacian. The Paleoproterozoic TTG suites of the QF region and surroundings are usually dated between 2.2-2.1 Ga (e.g., Almeida et al., 2000).

In a recent contribution, Teixeira et al. (2015) obtained a LA-ICPMS U-Pb zircon age of 2351 ± 48 Ma for the tholeiite-sourced Resende Costa orthogneiss suite in the Mineiro belt, some 190 km SW of the Lamego deposit. Seixas et al. (2012) dated the high-aluminium Lagoa Dourada TTG suite, in the same belt, at 2350 Ma (zircon, U-Pb ID-TIMS). These data led Teixeira et al. (2015) to suggest that both the Resende Costa-Lagoa Dourada rocks characterize the precocious arc magmatism of the Minas accretionary orogeny, which would have lasted some 350 Ma.

The 2387 ± 46 Ma age (Figura 19b) may be related to the early stages of the Minas accretionary orogeny of Teixeira et al. (2015), and represent the imprint on the Rio das Velhas greenstone belt, which affected the Lamego deposit area. Despite this possible mineral growth at 2387

± 46 Ma, the Paleoproterozoic regional D_3 gave place to a weakly developed foliation (Alkmim and Marshak, 1998), which was not defined at the mine site, or conceivably, parallelized to S_{1-2}.

Goldfarb et al. (2001) indicate two major episodes of orogenic gold deposit formation in the Precambrian, during the intervals from 2800 to 2550 Ma and from 2100 to 1800 Ma. Despite the monazite age at 2387 ± 46 Ma, it is difficult to envisage the Archean gold mineralization remobilized at this time. As pointed out by Fyfe (1987), remobilization of ore deposits is improbable, unless large fluid volumes are involved, or the crust undergoes major tectonic re-arrangement. For the most part, remobilization of existing ores must take place via interaction of new fluids; the chemical environment associated with the influx of new fluids must differ from that associated with deposition, otherwise new transfer processes would not operate (Hobbs, 1987). Wilkinson et al. (1999, and references therein) discuss H_2O-CO_2-NaCl-dominated fluids in orogenic gold systems, and indicate that low-temperature, high-salinity brines may be interpreted as a product of late-stage phase separation, or as overprinting fluids that reset isotopic systematics and introduce new mineral phases. However, the genetic relationship, if any, between such brines and gold mineralization has proven difficult to establish (Wilkinson et al., 1999).

It is also interesting to note that DeWitt et al. (2000) and Thorpe et al. (1984) documented a Paleoproterozoic isotopic disturbance on some Rio das Velhas greenstone-belt-hosted gold deposits using Pb-Pb model ages.

Xenotime crystals yielded an 518.5±9 Ma age (Table 6, Figura 19c), which reveals the strong imprint of the Brasiliano orogenic event recognized in the QF region by many authors (e.g., Alkmim and Marshak, 1998; Baltazar and Zucchetti, 2007; Table 3).

The Brasiliano event in the Araçuaí orogen, in the eastern portion of the São Francisco Craton, is established at the range of 0.630 and 0.480 Ga, based on a succession of five granitic events G1 to G5 (Pedrosa Soares et al., 2011). In this orogen, there is one region that is known as the N-S-trending Eastern Brazilian Pegmatite Province, where these granitic events are associated with G4 and G5 granites (Pedrosa Soares et al., 2011). The 518.5 ± 9 Ma xenotime age falls in the G4 super suite time of formation (535 to 500 Ma), somewhat in transition to the G5 (520 to 480 Ma). Pegmatites associated with the Brasiliano event are also intruded in rocks of the Minas Supergroup, as is the case of the Piracicaba Group, about 140 km east of Lamego, where a Rb-Sr date of 545 Ma was obtained on amazonite (Herz, 1970). The author considers this to be the result of a thermal, magmatic event about 500 Ma ago. We suggest that the 518.5 ± 9 Ma xenotime age records the (i) N-S-trending G_2 post-mineralization structures and the regional D_4, linked to the regional E-W shortening, and the (ii) Brasiliano thermal magmatic event that is locally expressed by the presence of pegmatites, which

intrude the Minas Supergroup that in turn overlies and variably deforms the Rio das Velhas Supergroup.

3.14.2 Comparison with other Archean orogenic gold deposits in Brazil and worldwide

Orogenic gold deposits in Archean greenstone belt terrains are recognized as major gold producers. Examples include deposits located in the Yilgarn craton of Western Australia and the Superior province of Canada (Goldfarb et al., 2005, 2001; Groves et al., 2003; 1998; Hagemann et al., 2000, Robert et al., 2005). In both examples, the gold deposits are: (i) related to collision tectonic environments, (ii) controlled by structures such as fault systems, shear zones and folds, (iii) hosted by a variety of rocks including volcanic-sedimentary, such as BIF, and granites, (iv) associated with hydrothermal alteration, with pyrite, arsenopyrite and pyrrhotite being the main sulfide minerals.

Orogenic gold deposits in the Rio das Velhas greenstone belt (e.g., Lobato et al., 2001a, Vial et al., 2007a) show similarities with other Archean BIF-hosted deposits around the world. They are confined by Fe-rich portions of the BIF These portions are structurally controlled by shear zones and folds, and plunge consistently to the SE, as is the case at Lamego, Cuiabá and Morro Velho. They contain gold associated with pyrrhotite, pyrite and arsenopyrite (e.g., Raposos - Junqueira et al., 2007; São Bento - Martins Pereira et al., 2007; Cuiabá - Ribeiro-Rodrigues et al., 2007; Morro Velho - Vial et al., 2007b; Figura 5). Geological characteristics at Lamego that are compatible with BIF-hosted orogenic gold deposits around the world are: (i) mineralization structurally controlled and associated with crustal compression, defined by the G_1 structures as F_2 folds, boudins and shear zones; (ii) structural controls of orebodies associated with F_2 fold axis and L_{1-2} lineations plunging to the SE; (iii) high-gold grades confined to Fe-rich host lithologies and silicification zones; (iv) silicification, sulfidation and carbonatization as the major hydrothermal alteration processes in the mineralized zones, and (v) three styles of gold mineralization including vein, replacement and disseminated.

The Lamego deposit also displays differences when compare to other BIF-hosted deposits in the Rio das Velhas greenstone belt. These include individual orebodies in the Lamego deposit that show different plunge directions. For example, the Cabeça de Pedra orebody plunges 25 towards to 130, and the Carruagem orebody plunges 22 towards 95, here interpreted as a structural modification imposed by the Brasiliano tectonic cycle, which had a particularly strong effect on the Lamego orebodies.

That opens the possibility that other BIF-hosted gold deposits in the QF display more than one plunge direction. Further detailed structural analysis combined with gold grade distribution need

to be applied to test this possibility. Such analysis associated with high-precision geochronology can provide a good insight on the tectonic evolution of the deposit.

3.14.3 Implications for exploration in the QF

The combined structural and geochronological analysis of the Lamego deposit provides significant constrains to the targeting of the orogenic gold systems in the Archean terrain of the QF. At least three important observations can be summarized from the structural lithological mapping of the Lamego deposit.

Firstly, in the volcano-sedimentary rock package hosting the Lamego gold deposit the carbonaceous pelites are the primary lithological exploration target. That is because the carbonaceous pelites acted as a seal whereby the gold-bearing hydrothermal fluids stopped at the contact with BIF-carbonaceous pelites. These contact zones display the highest grade in the entire Lamego gold deposit. Furthermore, they also contain the high-gold grade silicification zones that represent one significant mineralization style at Lamego.

Secondly, the main structural exploration targets in the Lamego area, NW portion of QF, are the NW-SE plunging, F_2 reclined folds. That is the case because the hinge zones of these folds represent the highest-grade gold ore zones in the Lamego deposit.

Thirdly, the regional D_4 Brasiliano event - related with normal fault zones and crenulation cleavage - affected the entire QF (Figura 5). In the Lamego deposit, these structures can also be observed and have resulted in significant modification of the established orebodies (Figura 7a, b, c). The modification includes lateral offset of the ore shoots, thinning of ore zones and decrease in gold contents. Importantly, the orebodies are not cut off, and they continue below the areas affected by regional D_4 Brasiliano-related structures (Figuras 15 and 16). That poses the question of whether the deposits interrupted by these younger structures, as for the São Bento deposit (Figura 5), indeed continue below them. The targeting of the extension of orebodies below these structures has to be considered during drilling campaigns.

3.15 Conclusions

The detailed lithological and structural geological mapping of several orebodies at different mine levels, structural analysis and indirect and implicit 3D orebody modeling at the Lamego gold deposit, with special emphasis on the Carruagem orebody, combined with high-precision U-Pb geochronology, reveal the following conclusions:

(1) From bottom to top the lithostratigraphy at the Lamego deposit is defined by mafic volcanic

rock, a metabasalt (chlorite-carbonate-sericite-quartz schist); banded chert with BIF that is both carbonaceous and/or ferruginous; and carbonaceous and micaceous pelites (Figura 6). These all contain metamorphic index minerals (sericite-chlorite-quartz-carbonate), which are indicative of greenschist facies metamorphism.

(1) Both chert and BIF bands are referred to as the Lamego BIF. The bands of the Lamego BIF are characterized by alternating dark carbonate-quartz (±magnetite) and light quartz-carbonate bands (Figura 10c, d).

(2) Pelitic rocks are represented by carbonaceous and micaceous pelites (Figura 10g, h), and they envelop the entire Lamego deposit.

(3) The macrostructure Lamego fold is defined as a rootless, reclined, isoclinal, cylindrical fold with an NE-SW striking axial plane, dipping 30º to the SE (map in Figura 7a). The fold hinge zone in the SW quadrant is represented by the Cabeça de Pedra orebody (Figura 7b); the normal limb (SE quadrant) is the Arco da Velha orebody (Figura 7c); the overturned limb (SE quadrant) is the Queimada orebody (Figura 7c); and the limb intersection (NE quadrant) is the Carruagem orebody.

(4) Two structural generations, G_1 and G_2, are recognized at the Lamego deposit (Table 8). The G_1 structures are represented by: (i) the planar structures S_{1-2} foliation, V_1 and V_2 veins, and shear zones; these are generally oriented NE-SW, dip to the SE, with the exception of V_1 veins that dip to the NE and probably represent the oldest structures at the Lamego deposit; and (ii) the linear structures L_{1-2} lineation and F_2 fold axis that plunge to the SE. The G_2 structures are represented by: (i) the N-S oriented S_3 crenulation cleavage, dipping to the E; and (ii) the F_3 fold axis and L_3 crenulation lineation that are N-S oriented and plunge to the S.

(5) Since the regional Paleoproterozoic D_3 foliation is not clearly recognized at the Lamego deposit, and its regional trend is similar to both S_0 and S_{1-2}, it is likely that this regional foliation overprinted the S_{1-2} and, therefore, both are indistinguishable.

(6) The S_3 spaced/crenulation cleavage is related to the regional D_4 Brasiliano N-S-trending regional folds and thrusts, with vergence to the E. These regional D_4 folds moved the G_1 structures to their current position; the G_1 structures had an original NW-SE direction, which was probably the trend of the Rio das Velhas Archean belt.

(7) The main hydrothermal alteration minerals are quartz, pyrite, arsenopyrite and pyrrhotite, and they are developed parallel to the S_{1-2} foliation in all rock types.

(8) The quartz-rich (silicification) zone is characterized by three quartz types: (i) deformed, coarse-grained smoky quartz that occurs as irregular masses, both concordant and discordant, within the mineralized zones; (ii) fine-grained, granoblastic, white and milky quartz formed from the

recrystallization of smoky quartz; and (iii) milky quartz, particularly in fault zones cutting across (i) and (ii) types.

(9) Three styles of gold mineralization are identified at the Lamego deposit, namely vein, replacement and disseminated styles. The Lamego mineralization is mainly hosted by sulfide-associated, replacement style.

(10) High-grade gold lenses (Figuras 17c, d and 18a) show a spheroidal pattern and a distribution that varies along the S_{1-2} foliation. These lenses represent the hinge zone of F_2 reclined folds with the plunge of the orebodies controlled by the F_2 fold axes.

(11) The lower-grade gold lenses are controlled by pinch and swell, and locally quartz boudins. The latter have two orthogonal directions, one to the NW-SE and the other to the NE-SW, thereby defining chocolate-tablet style boudinage.

(12) The hydrothermal monazite age of 2730 ± 42 Ma (2 sigma; MSWD=0.51; Figura 19b) is interpreted to represent the age of gold mineralization synchronous to the G_1 structures.

(13) Though discordant, the 2387 ± 46 Ma age obtained on hydrothermal monazite (Figura 19b) may be interpreted as relating to the early stages of the Minas accretionary orogeny, and represents the structural imprint on the Rio das Velhas greenstone belt, which affected the Lamego deposit area. Despite this monazite age, it is difficult to envisage the Archean gold mineralization remobilized at this time, since remobilization of gold deposits would require very large fluid volumes, which cannot be clearly established for Lamego.

(14) The xenotime age of 518.5 ± 9 Ma (MSWD=0.41; 2 sigma) is interpreted as the strong imprint of the Brasiliano orogenic event in the QF region, which is reflected by: (i) the N-S-trending G_2 structural generation post-mineralization deformation and the regional D_4 structures, linked to the regional E-W shortening, and (ii) an important Brasiliano thermal, magmatic event described in the Araçuaí orogen, expressed locally by the presence of pegmatites intruding the Minas Supergroup that overlies the Rio das Velhas Supergroup.

(15) Although the Brasiliano-age deformation, which was responsible for the development of the G_2 structures, dislocated the orebodies in the Lamego mine, there is no evidence for the formation of new hydrothermal alteration minerals, sulfides and gold. There is also no evidence for any recrystallization of the Archean hydrothermal alteration zones or mineralized areas including sulfides and gold.

(16) Development of exploration targeting criteria for the preferred location of gold in BIF-hosted orogenic gold deposit in the QF and partially worldwide include: (i) carbonaceous pelites along the contact with BIF, and (ii) F_2 reclined folds.

(17) The regional D_4-type structures that affect the Lamego's orebodies need to be considered for the exploration criteria since this caused the modification of a Lamego Archean orogenic gold deposit.

3.16 Acknowledgments

This research is the result of the on-going Ph. D. thesis by the first author at the Federal University of Minas Gerais-UFMG, which is fully financed by Brazil's National Council of Technological and Scientific Development-CNPq, Vale and AngloGold Ashanti Córrego do Sítio Mineração S/A-AGA. The student's scholarship is granted by CNPq. LML and CAR also acknowledge grants from the CNPq.

The authors thank AGA for their logistic and technical support, and for allowing the publication of this manuscript. Special thanks are due to Rodrigo Martins who has maintained his commitment to our research group throughout. We are indebted to present and past colleagues at the Lamego mine, especially Jorge Watanabe, for the many technical debates and mine visits. Discussions with Orivaldo Baltazar from the CPRM-Brazil's Geological Survey over the regional overviews were fundamental. We also acknowledge the support of UFMG, UWA, CAPES, FAPEMIG and FUNDEP. Special thanks to Bruna Ketlyn Silva Cota who helped draw the pictures, images and tables; Geoffrey Batt that granted the Leapfrog Geo license used to do the 3D model and geologist Polyane Figueiredo for the collaboration in the discussion about the 3D geological model. Marcelo Freitas of Aranz Geo, for granting us with an academic Leapfrog license.

PARTE 3 – Estudos Mineralógicos de Sulfetos: Paragêneses Mineral e estudos de Microprobe e LA-ICP-MS.

Capítulo 4: Artigo: Archean orogenic Lamego gold deposit, Quadrilátero Ferrífero, Brazil: paragenetic sequence and implications for the source of hydrothermal ore fluids and metals based on EPMA and LA-ICP-MS sulfide analyses in BIF and carbonaceous pelite

Artigo submetido à Mineralium Deposita em março de 2016

Breno de Souza Martins[1], Lydia Maria Lobato[1], Steffen G. Hagemann[2], Rosaline Cristina Figueiredo e Silva[1], Leonid Danyushevsky,[3] Malcolm Roberts[4]

[1]Universidade Federal de Minas Gerais, Avenida Antônio Carlos, n.º 6627, Bairro Pampulha, Belo Horizonte, Minas Gerais, CEP 31270-901

[2]School of Earth and Environment, The University of Western Australia, 35, Stirling Highway, Crawley, WA, 6009, Australia

[3]CODES ARC Centre of Excellence in Ore Deposits, University of Tasmania, Private Bag 126, Hobart, TAS 7001, Australia

[4]Centre for Microscopy, characterization and Analysis, The University of Western Australia, 35, Stirling Highway, Crawley, WA, 6009, Australia

4.1 Abstract

The Archean, BIF-hosted Lamego gold deposit (1.3 Mt resources, 7.26 g/t Au average grade), Rio das Velhas greenstone belt, Brazil, is associated with a rootless, reclined, isoclinal, cylindrical fold where mafic rocks, chert, banded iron formation (BIF), carbonaceous and micaceous pelites are pervasively hydrothermallyzed. Mineralization is controlled by NE-SW-trending structures dipping to the SE.

Paragenetic studies based on texture and elemental mapping with EPMA define seven pyrite types, four in carbonaceous pelite (CP), Py-1_{CP} (framboidal) to Py-4_{CP}, and three in BIF, Py-1_{BIF} to Py-3_{BIF}, as well as Apy-1_{BIF}. These studies establish four stages of evolution: (1) pre-hydrothermal (diagenetic) → Py-1_{CP} and its recrystallization to Py-2_{CP}, (2) early hydrothermal → additional Py-2_{CP}; development of Py-3_{CP} and Py-1_{BIF} showing S-As-Fe zoning, (3) main hydrothermal → additional Py-3_{CP}, development of Py-4_{CP} and Py-2_{BIF}, and (4) late hydrothermal → Py-4_{CP}, Py-3_{BIF} showing Ni-Co-As zoning, and Apy-1_{BIF}.

In situ LA-ICP-MS analyses on pyrite of carbonaceous pelite indicate that Au displays excellent affinity with Ag and with crustal elements such as Bi, Pb and Sb, and also correlates well with Ni, Co, Cu, Ag and Te. Gold is thus not only related to the hydrothermal fluid composition, but also to the original carbonaceous pelite geochemistry. On the other hand, in the case of BIF geochemical correlation is restricted to Ag, As, Pb and Cu, denoting a much more important hydrothermal influence.

4.2 Introduction

The Quadrilátero Ferrífero (QF - Figura 21) region is one of the most important gold-producing provinces in Brazil, with reserves exceeding 1000 t (Vial et al. 2007a). It is located in the south portion of the São Francisco craton in Minas Gerais, Brazil (Almeida, 1977).

The Cuiabá-Lamego deposit area, with an estimated production of 11 Moz of ore, is located at the northwestern portion of the QF. The Lamego deposit, located in the southeastern portion of this same trend, contains resources in the order of 1.3 tons, with an average grade at 7.26 g/Au (Martins et al. 2016).

The Archean orogenic BIF-hosted Lamego deposit (Figura 22a), owned by AngloGold Ashanti Córrego do Sítio S/A (AGA) is hosted in rocks of the Nova Lima Group, base of the Rio das Velhas Supergroup, a greenstone belt of Archean age (e.g., Baltazar and Zucchetti 2007). It has a concordant stratigraphic package (Figura 22b) composed of mafic rocks, BIF/chert layers, carbonaceous and micaceous pelites where quartz veins crosscut all lithologies. The deposit is structurally defined by the rootless, reclined, isoclinal, cylindrical Lamego fold (Figura 22a), with an axial trace striking northwest-southeast, dipping 20º to 30º. The hinge zone is thickened and the limbs are thinned, with the limbs dipping 20º to 30º to the SE (Martins et al. 2016; Figura 22c).

The four major high-grade gold orebodies are Carruagem, Queimada, Arco da Velha, and Cabeça de Pedra (Figura 22a). The mineralization is structurally controlled, and consists of quartz-carbonate sulfide veins and quartz boudins with 2 mm to 5 cm width. Irregular zones of smoky and milky quartz of up to 35 meters wide are also present. Replacement style in BIF is also observed, where sulfides, minerals replace iron carbonate bands, and these encompass especially pyrite, arsenian pyrite (As-pyrite) and arsenopyrite (Martins et al. 2016).

This paper presents a detailed study on ore mineralogy, mineral paragenesis, textural aspects of sulfide minerals, and geochemistry of trace elements of the various pyrite stages present in BIF and carbonaceous pelite. Its main objectives are to: (1) document the complexity of the ore mineralogy, mineral chemistry and metal zonation, (2) discuss the formation of different (two) pyrite

generations: a) pyrites in the carbonaceous pelite, considered to be of sedimentary origin, and b) pyrites in carbonaceous pelite and BIF, considered to be hydrothermal, and (3) discuss the origin and genesis of gold in the Lamego deposit.

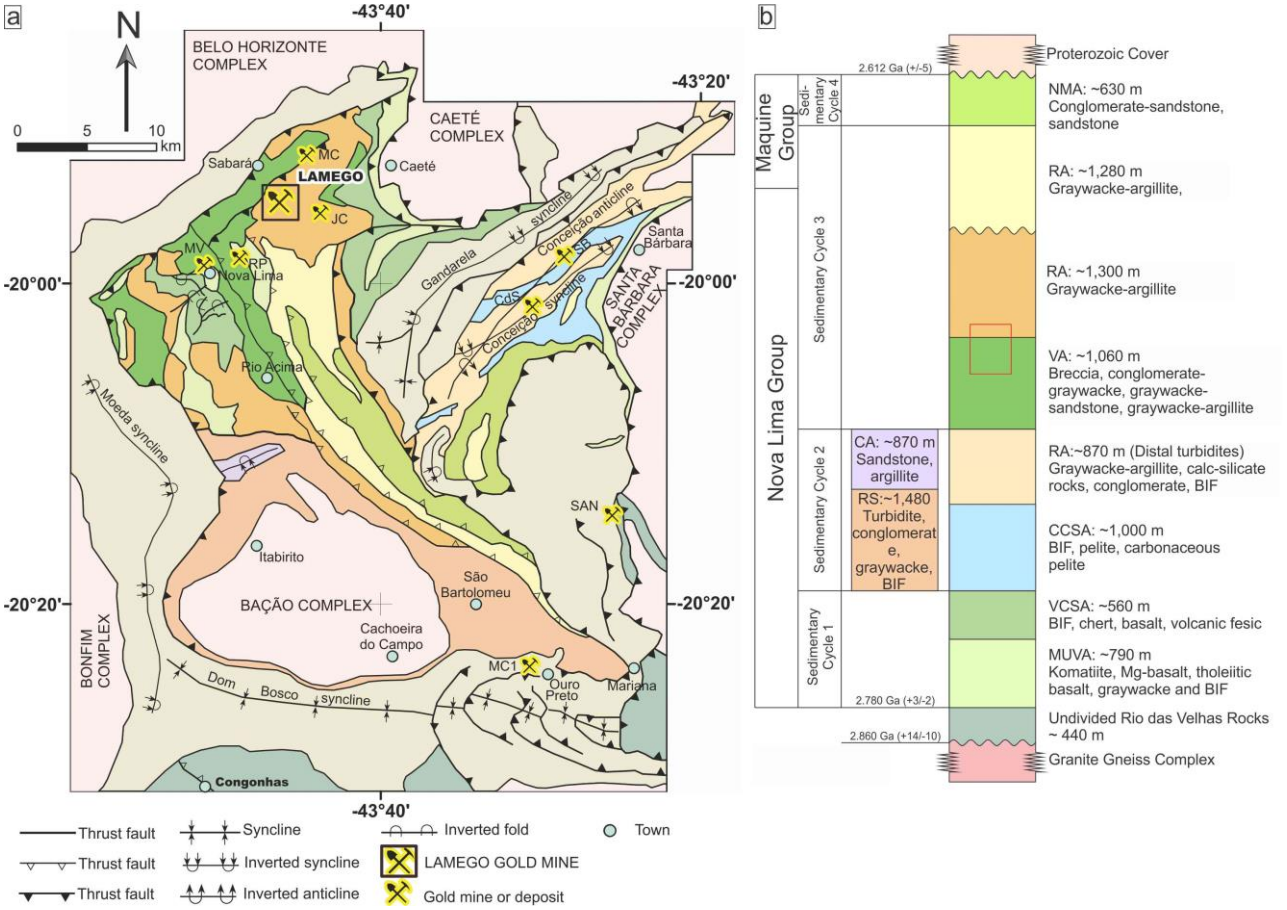

Figura 21: (a) Regional geological setting of the Rio das Velhas greenstone belt showing the location of the Lamego gold deposit. (b) A regional stratigraphic column is also displayed, with their respective sedimentary facies associations after Baltazar and Zucchetti (2007): MUVA-Mafic-ultramafic volcanic, VCSA-Volcano-chemical sedimentary, CCSA-Clastic-chemical sedimentary, RA-Resedimented, CA-Coastal, VA-Volcaniclastic, NMA-Non-Marine associations. Other gold deposits associated with the Rio das Velhas greenstone belt and the Minas Supergroup are also shown. The gold deposits hosted of the greenstone belt are: CdS-Mina Córrego do Sítio, MC-Mina Cuiabá, MV-Morro Velho, RP-Raposos, SAN-Santo Antônio, SB-São Bento, JC-Juca Vieira. The red rectangle represents the position where the structural Lamego window exposes rocks that are underneath the volcaniclastic and resedimented associations. Geology after Baltazar and Zucchetti (2007), with modifications from Martins et al. (2016).

4.3 Regional geology setting

Dorr et al. (1957, 1969) were the first to establish the stratigraphy of the QF region, and subdivided it into the: (1) Archean granite-gneissic complexes, (2) Rio das Velhas Supergroup (Figura 21), an Archean greenstone belt, and (3) Proterozoic Minas Supergroup, Itacolomi Group and Espinhaço Supergroup (corresponding to the Proterozoic covers of Fig. 1)

The granite-gneiss terrain is composed of tonalite-trondjhemite-granodiorite (TTG) complexes. These consist of 3.2 Ga dome-like granite-gneiss domains associated with intercalations of amphibolites and metasedimentary rocks (Ladeira 1980, 1991; Lana et al. 2013; Schorscher 1988), which are intruded by metatonalites, metandesites, metagranites, pegmatites and Proterozoic mafic dikes (Carneiro et al. 1994; Noce 1995; Noce et al. 2005). Noce et al. (2007) suggest that these TTG derive from igneous protoliths older than 2.9 Ga.

The Archean Rio das Velhas greenstone belt (Figura 21) covers approximately 4.000 km^2 in the QF, and exhibits ages between 3.0-2.7 Ga, (Machado and Carneiro 1992; Machado et al. 1989). The greenstone belt sequence is subdivided into the basal Nova Lima and top Maquiné Groups (Dorr 1969, 1957; Oliveira 1984). The Nova Lima Group comprises ultramafic rocks, basic lavas, graywackes and sandstones, with intercalations of BIF, quartz-dolomite and quartz-ankerite rocks, conglomerates and carbonaceous pelite (Baltazar and Zucchetti 2007; Dorr 1969). The Nova Lima Group hosts a large number of gold deposits (Ladeira 1980, 1991; Lobato et al. 1998 a, b; 2001a, b), including Lamego (Martins 2011; Martins et al. 2011, 2016). The Maquiné Group is divided into the basal Palmital (O'Rourke 1957) and the top Casa Forte Formations (Gair 1962), the former with sandstone and quartz pelite, and the latter with sandstone and conglomerate (Dorr 1969). The Rio das Velhas greenstone belt rocks were mainly metamorphosed to the greenschist facies. A thorough review of the literature from the last century focused in this greenstone belt is found in Baltazar and Zucchetti (2007).

The QF region displays a complex structural arrangement, with Archean basement domes surrounded by large synclines where the Minas Supergroup rocks dominate (Alkmim and Marshak 1998; Chemale et al.1994; Dorr 1969). No consensus exists on how many deformational events the Rio das Velhas Supergroup experienced. Baltazar and Zucchetti (2007) have proposed that the structural evolution of the QF region took place in three main periods. The earliest period occurred between 2.8 and 2.67 Ga, corresponding to the Rio das Velhas orogeny, with the evolution of the Rio das Velhas greenstone belt; the second period between 2.1 and 1.9 Ga is related to the Transamazonian event in the Proterozoic event (Brito Neves 2011; “Minas accretionary orogeny” most recently proposed by Teixeira et al. 2015); the third period between 650 and 500 Ma, in the Neoproterozoic, related to the Brasiliano orogeny (see table 3 of Baltazar and Zucchetti 2007).

4.4 Local geological setting of the Lamego gold deposit

The deformational history at the Lamego deposit area has been addressed mainly by Lobato et al. (2013), Martins (2011), Martins et al. (2011) and Sales (1998). More recently, Martins et al. (2016)

described and discussed the geological features and structural evolution at the deposit, and most of the information below is based on their work.

4.4.1 Lithostratigraphy

The intermediate part of the Nova Lima Group, of the volcaniclastic and resedimented association (Baltazar and Zucchetti, 2007, red rectangle in Figura 22b). It represents a structural window in the area, exposing rocks that are underneath these associations.

A concordant lithostratigraphic package of metamorphosed volcano-sedimentary rocks host the Lamego deposit (Figura 22a), it is related to the Nova Lima Group. From bottom to top the lithostratigraphy is defined by mafic volcanic rocks represented by metabasalt and chlorite-carbonate-sericite-quartz schist; banded metachert with metamorphosed BIF that are both carbonaceous and/or ferruginous, and carbonaceous and micaceous pelites (phyllites), which envelop the entire Lamego deposit (Figura 22b). These all contain metamorphic index minerals (sericite-chlorite-quartz-carbonate), which are indicative of greenschist facies metamorphism.

Green, fine-grained and massive *mafic volcanic rock* is the oldest unit exposed in the core of the Lamego deposit. It is up to 200 m thick, with a lateral extent of approximately 1.7 km (Figura 22a, b).

The *Lamego chert and banded iron formation* (Figura 22a, b), here referred to as the Lamego BIF, consist of chert bands that vary from light creamy to dark colored, with the latter being impregnated by carbonaceous matter, and locally containing centimeter-thick films of carbonaceous pelite. Ferruginous chert usually contains very fine siderite (rarely magnetite), where this rock may grade into true BIF. Alternating, dark carbonate-quartz (±magnetite) and light quartz-carbonate bands characterize bands of the Lamego-BIF.

Pelitic rocks are both carbonaceous and micaceous (Figura 22a, b), at the top of the stratigraphic succession that envelop the entire Lamego deposit. One- to 5-m-thick carbonaceous pelite (carbonaceous matter, quartz, chlorite, carbonate and minor sericite) are dark, finely laminated and thinly bedded. The micaceous pelite (sericite, muscovite, quartz, carbonate and minor carbonaceous matter) display gradational and compositional stratification, laminated and up to 200 m thick. Both have a lateral extent of up to 1.7 km (Figura 22a, b).

Diabase intrusions (hornblende, actinolite-tremolite, epidote, chlorite, carbonate, plagioclase, sericite and quartz) develop as dikes and sills that may be parallel to or crosscut both carbonaceous and micaceous pelites, and BIF. They extend for about 200 meters with an average width of up to 5 meters (Figura 22a, b).

4.4.2 Structural deformation events

The deformational history at the Lamego deposit has been addressed by Martins et al. (2016), who describe two structural generations, generations 1 and 2 (G_1 and G_2), each encompassing a set of structural elements.

The *G_1 structural generation* developed in a regional, Archean progressive deformation event, resulting in structures oriented from NE-SW and dipping to the SE (Figura 22c). The most visible structure related to the G_1 structures is the rootless, reclined, isoclinal, cylindrical Lamego fold (Figura 22a), along which four orebodies are disposed. The Lamego fold has a perimeter of about 4.8 km and a maximum width of 450 m with an axial trace striking NW-SE dipping 20º to 30º. The Cabeça de Pedra (Figura 22a) orebody is located in the thickened hinge zone. The limbs are characterized by the Arco da Velha and Queimada orebodies (Figura 22a), respectively representing the normal and overturned limbs, dipping 20º to 30º to the SE. The Carruagem orebody (Figura 22a) is located in the NE portion of the Lamego fold and corresponds to the intersection between the normal and overturned limbs.

Other G_1 structures (Figura 22c) include sheared, relict gradational and compositional bands (S_0: 29º-41º towards 108º-148º); a penetrative axial-planar foliation (S_{1-2}: 28º-42° towards 124º-134º); a lineation that involves mineral, stretching and fold axis (L_{1-2}: 28º-40º towards 128º-155º); V_1 and V_2 veins (V_1: 20º-60º towards 20º-80º; V_2: 20-60 towards 98-160; Fig. 3A, B)). The F_2 reclined folds with a close to open geometry and F_2 fold axes plunge 10º-28º towards 90º-160º, and are parallel to sub-parallel to mineral lineation L_{1-2}. A northeast-trending, 1-2-m thick shear zone is oriented parallel to the axial plane of the F_2 folds and preferentially developed in all schistose layers, dipping 22º-70º towards 102º-168º (Figura 22c).

Structures pertaining to the *G_2 structural generation* (Figura 22c) are oriented N-S dipping to the W, and are composed of the crenulation cleavage S_3 (N-S/80º-90º), crenulation lineation L_3 (30º towards 180), open fold F_3 (30º towards 180-200), and conjugate pair of faults (15º-75º towards 20-80 and 20º-90º towards 185-240).

Martins et al. (2016) propose that the G_2 structural generation is post-mineralization linked to a regional E-W shortening. The S_3 spaced/crenulation cleavage must have rearranged the G_1 structures to their current position, dislocated the orebodies in the Lamego mine, with no evidence of new hydrothermal alteration minerals having been formed, including gold.

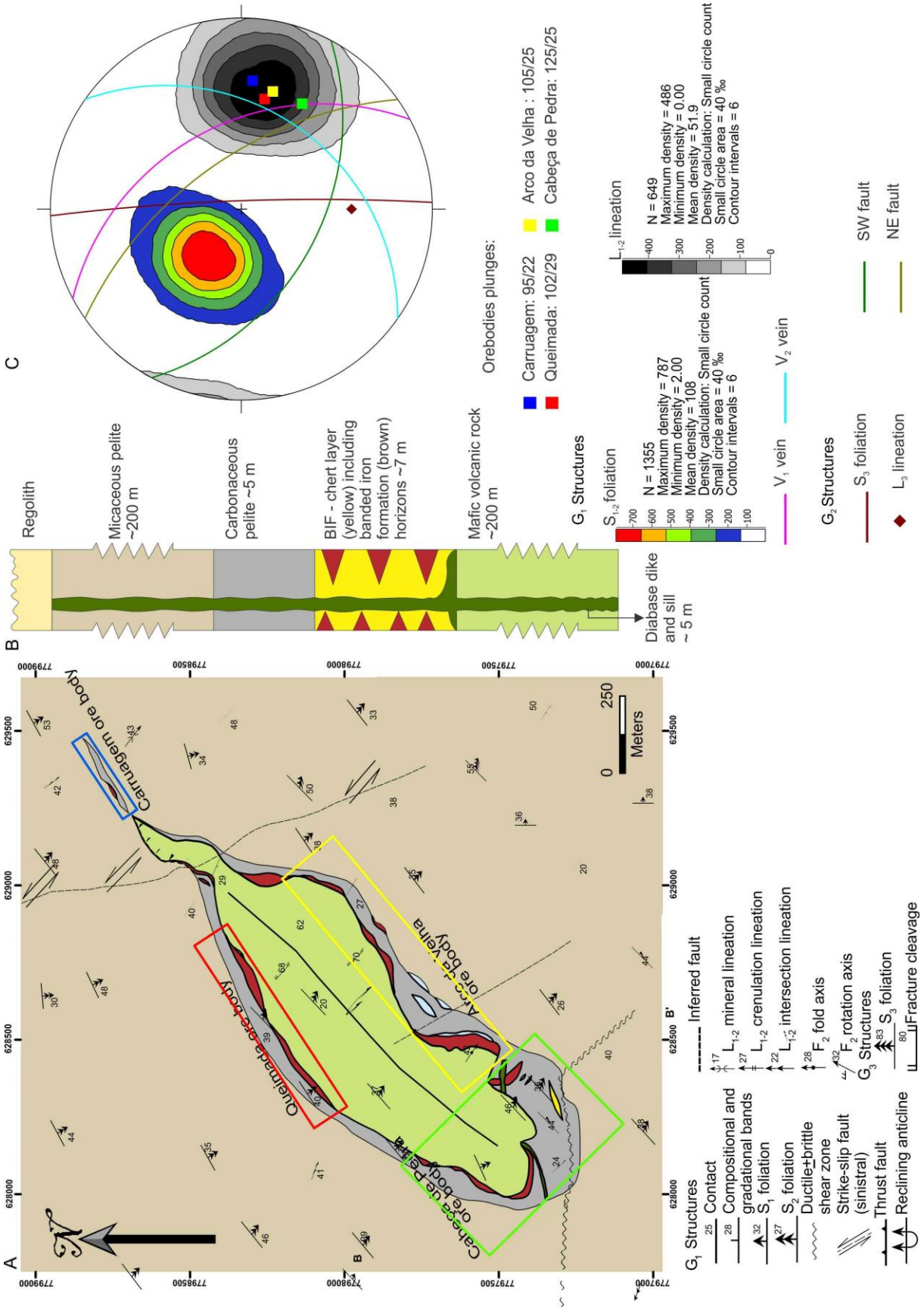

Figura 22: Summary of the geological setting at the Lamego deposit: (a) Surface geological map; (b) Stratigraphic column; at the mine, representing a structural window into the resedimented and volcaniclastic association; and (c) Schematic stereographic projection showing the main structures.

Note that in (a) the green and blue boxes correspond respectively to the Cabeça de Pedra and Carruagem orebodies, which are the focus of the in situ LA-ICP-MS analyses on sulfide minerals. The same colours represent the orebodies plunges in the stereographic projection figure (c).

4.5 Gold mineralization styles at Lamego

Orebodies are associated with the Lamego BIF, where gold-rich zones are related to iron-rich bands of BIF and silicification zones. Replacement-style mineralization is linked to sulfide bands, mainly pyrite, As-pyrite, and arsenopyrite. Carruagem, Queimada, Arco da Velha, and Cabeça de Pedra represent the four major high-grade gold orebodies (Fig. 2A).

Martins et al. (2016) describe that the high-grade gold lenses show a spheroidal pattern and a distribution that varies along the S_{1-2} foliation. These lenses represent the hinge zone of F_2 reclined folds with the plunge of the orebodies controlled by the F_2 fold axes (Figura 22c). The lower-grade gold lenses are controlled by pinch and swell, and locally quartz boudins. The latter have two orthogonal directions, one to the NW-SE and the other to the NE-SW, thereby defining chocolate-tablet style boudinage. Based on the age of hydrothermal monazite associated with gold-bearing pyrite, gold mineralization is interpreted to have developed synchronous to the G_1 structures at 2730 ± 42 Ma (Martins et al. 2016).

Using the observations from underground, drilling holes, polished sections and thin sections, four mineralization styles are defined. Of the four, the first two are the most important for gold mineralization, and for this study we have focused on the first three styles.

4.5.1 Vein style

The *vein style* encompasses quartz-carbonate, quartz boudins and quartz-carbonate-sulfide veins ranging in thickness from 2 mm-5 cm to >35 m (Fig. 5) in irregular smoky/milky quartz masses (Figura 23a). The veins crosscut all lithologies, but they are best developed in BIF, with local stockwork texture, and are detailed by Morales et al. (2016). Sulfides comprise pyrite, As-rich pyrite, arsenopyrite, sphalerite, galena and less chalcopyrite. The gold contents in this style vary from 1.6 to 15.8, locally attaining 300 ppm (AGA, personal communication).

4.5.2 Replacement style

Replacement-style mineralization dominates the BIF (Figura 23a), and is characterized by confinement of sulfides to this lithology, mostly associated with chemically favorable Fe-rich carbonate layers where siderite and ankerite are replaced by pyrite, As-pyrite, arsenopyrite,

pyrrhotite, sphalerite and galena. The gold contents in this style range from 0.03 to 6.63 ppm; values as high as 89.0 ppm may occur (AGA, personal communication).

4.5.3 Disseminated style

The *disseminated style* consists of sulfides disseminated mainly in mafic and carbonaceous pelitic rocks with the best exposures at the Cabeça de Pedra orebody; and less in micaceous pelite.

In carbonaceous pelite, this style is typically developed parallel to the S_{1-2} foliation, to sheared bedding S_0 (Figura 23b) and folded. It is characterized by the presence of: (1) rounded aggregates, under 1 cm in size, constituted by euhedral microcrystalline pyrites (Figura 23c), and (2) nodular pyrite aggregates, usually < 2 cm, which are oval shaped, and show edges transitioning to euhedral pyrite; these may also be surrounded by pyrite-quartz bands (Figura 23d).

Where developed in mafic rocks, disseminated sulfides are located in small-scale shear zones (< 2 cm) also parallel to the S_{1-2} foliation. Pyrite is the main sulfide ranging in size from 1 to 5 mm. Other sulfides are As-pyrite, arsenopyrite, sphalerite, and chalcopyrite. Nickeline is locally present (Figura 23e).

The gold content ranges from 0.03 to 1.9 ppm in the mafic rocks, 0.03 to 2.18 ppm in the carbonaceous pelite, and 0.03 to 1.9 ppm in the micaceous pelite. Locally, high-gold content of 18.3, 2.9 and 3.8 ppm respectively develop in mafic, carbonaceous and micaceous pelitic rocks.

4.5.4 Pyrite-quartz veinlets

Pyrite-quartz veinlets are restricted to carbonaceous pelite, crosscut the sheared bedding S_0 and S_{1-2} foliation, and may be folded. The veinlets are up to 1 cm thick, and host over 90% of the pyrite volume where gold concentration may reach 1.05 ppm (Figura 23f).

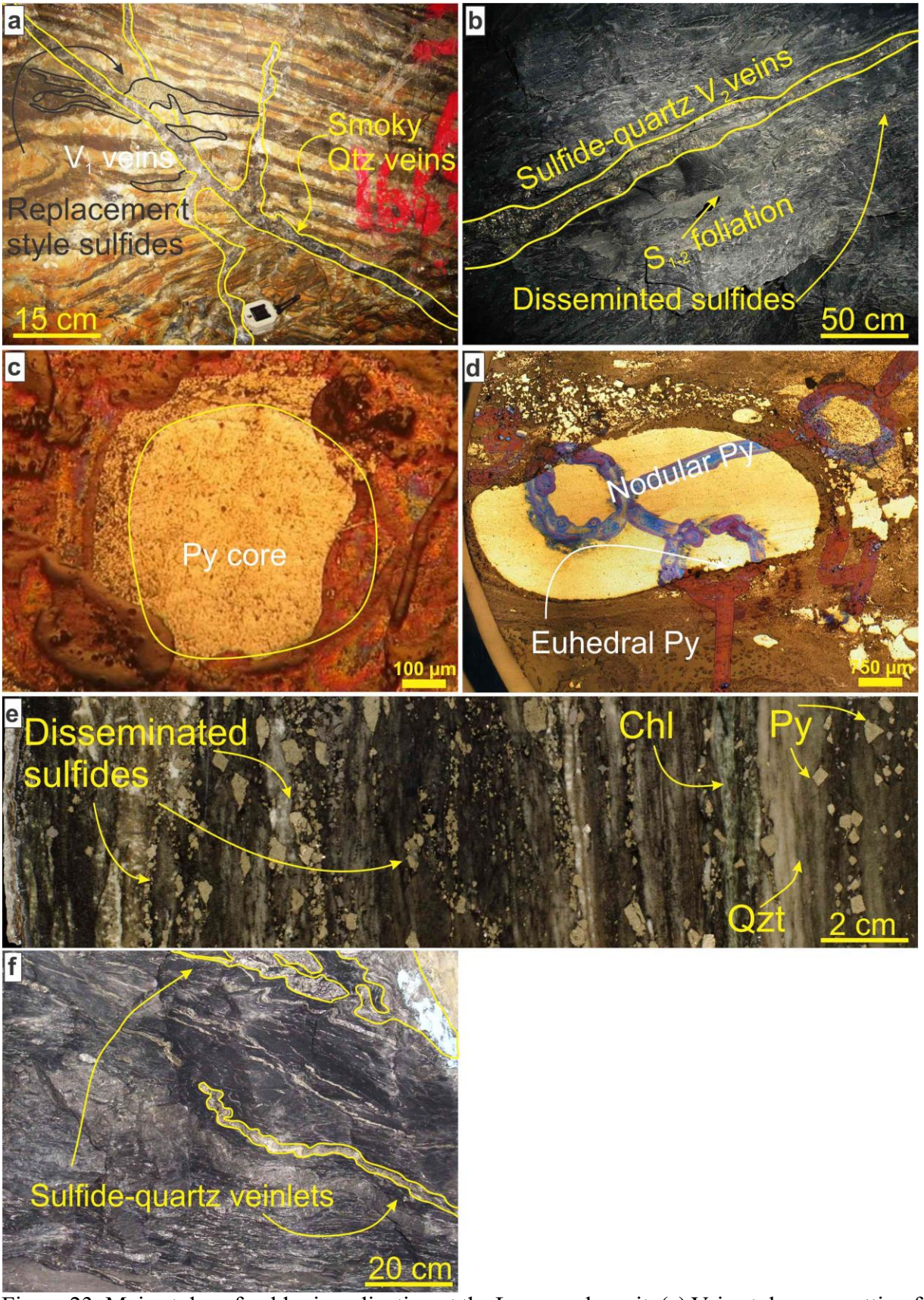

Figura 23: Main styles of gold mineralization at the Lamego deposit. (a) Vein style crosscutting folded BIF. In detail, irregular smoky-gray/milky quartz masses and veins. Replacement style in BIF; main replacement minerals are pyrite and arsenopyrite. (b) Disseminated style in foliated portion of

carbonaceous pelite. The main sulfide is pyrite that may exhibit preserved cores of euhedral microcrystalline pyrite (c), and (d) nodular pyrite, both in carbonaceous pelite (c and d: photomicrographs, reflected light, crossed polars). (e) Disseminated sulfides in shear zones of mafic rock. (f) Sulfide-quartz veinlets in carbonaceous pelite. Py: pyrite.

4.6 Hydrothermal alteration in BIF and carbonaceous pelite

The hydrothermal alteration that dominates and affects all rock types is represented mainly by the development of quartz, as well as carbonate and sulfide minerals parallel to the S_{1-2} foliation (Figura 23b); chlorite, sericite and albite also form. Quartz, carbonate and sulfides are principally well exposed in the BIF and in carbonaceous pelite along their contacts with BIF, and therefore a detailed account of their characteristics is provided. Chlorite is mostly abundant in the mafic volcanic footwall rock. Hydrothermal alteration of the micaceous pelite is not so clear.

The presence of hydrothermal minerals pertaining to the three main alteration types is attested by: (1) their coarser grain size in comparison to the pre-existing, metamorphic crystals, (2) the irregular nature of their contacts, and (3) the characteristics that overprint the original rock texture and typically truncate the rock bedding.

4.6.1 The Lamego BIF-metachert

The Lamego BIF-metachert present different hydrothermal alteration stages and is in general comprised of quartz (chert- 35%), carbonate (20%), chlorite (15%), sericite (10%), and sulfides (10%), which include pyrite, arsenopyrite, chalcopyrite, sphalerite and pyrrhotite. Other phases (10%) are muscovite, magnetite, gold, rutile and carbonaceous matter (Figura 24).

Pervasive silicification is defined in BIF by deformed zones of smoky *quartz*, sulfide minerals in sericite veinlets, carbonates and chlorite (Figura 25a, b). In these zones, quartz forms two types: (1) fine- to medium-grained, anhedral and deformed crystals with serrated edges (smoky type) that may be stretched - Qtz (1), and (2) anhedral to subhedral, inequigranular, fine- to medium-grained, with irregular to polygonal contacts - Qtz (2), (Figura 25a, b), after the recrystallization of Qtz (1). *Chlorite* is green, euhedral to subhedral, with a variable size, and may define an incipient foliation (Figura 25c). *Sericite* and *muscovite* are present in fine- to medium-grained, anhedral to subhedral flakes, with a poikiloblastic texture (Figura 25d).

Carbonate minerals develop in veinlets, strips and/or bands, where there is intense carbonate alteration and portions of smoky quartz. There are two carbonate types: (1) anhedral, fine- and fine- to medium-grained crystals, with polygonal to irregular contacts - Cb (1), and (2) stained and stretched crystals exhibiting a radial habit - Cb (2), interpreted to be hydrothermal (Figura 25d, e).

Two types of *magnetite* encompass: (1) very fine-grained crystals, (possibly siderite - Mgt (1)) in the carbonate bands, and (2) coarser-grained crystals, in fine aggregates (possibly ankerite-siderite - Mgt (2)), associated with the carbonate bands, interpreted to be hydrothermal (f).

Sulfide alteration is mainly associated with carbonates (Figura 25g, h). *Pyrite* dominates in subhedral to euhedral, fine- to medium-grained, locally coarse-grained (1 cm), porous crystals, in bedding-parallel veins (Figura 25h, i). *Arsenopyrite* is euhedral, poikiloblastic, fine to medium grained, with coarse-grained crystals (1 cm) displaying rhomboidal habit, and developing after pyrite (Figura 25i). *Chalcopyrite* in rare, anhedral, fine-grained aggregates with sphalerite and *galena* that is subhedral to euehdral (Figura 25j). *Sphalerite* forms irregular agglomerates, in anhedral, fine- to medium-grained crystals associated with carbonate and quartz (Figura 25j). *Pyrrhotite* is an early-stage sulfide, in subhedral and anhedral crystals after magnetite (Figura 25f).

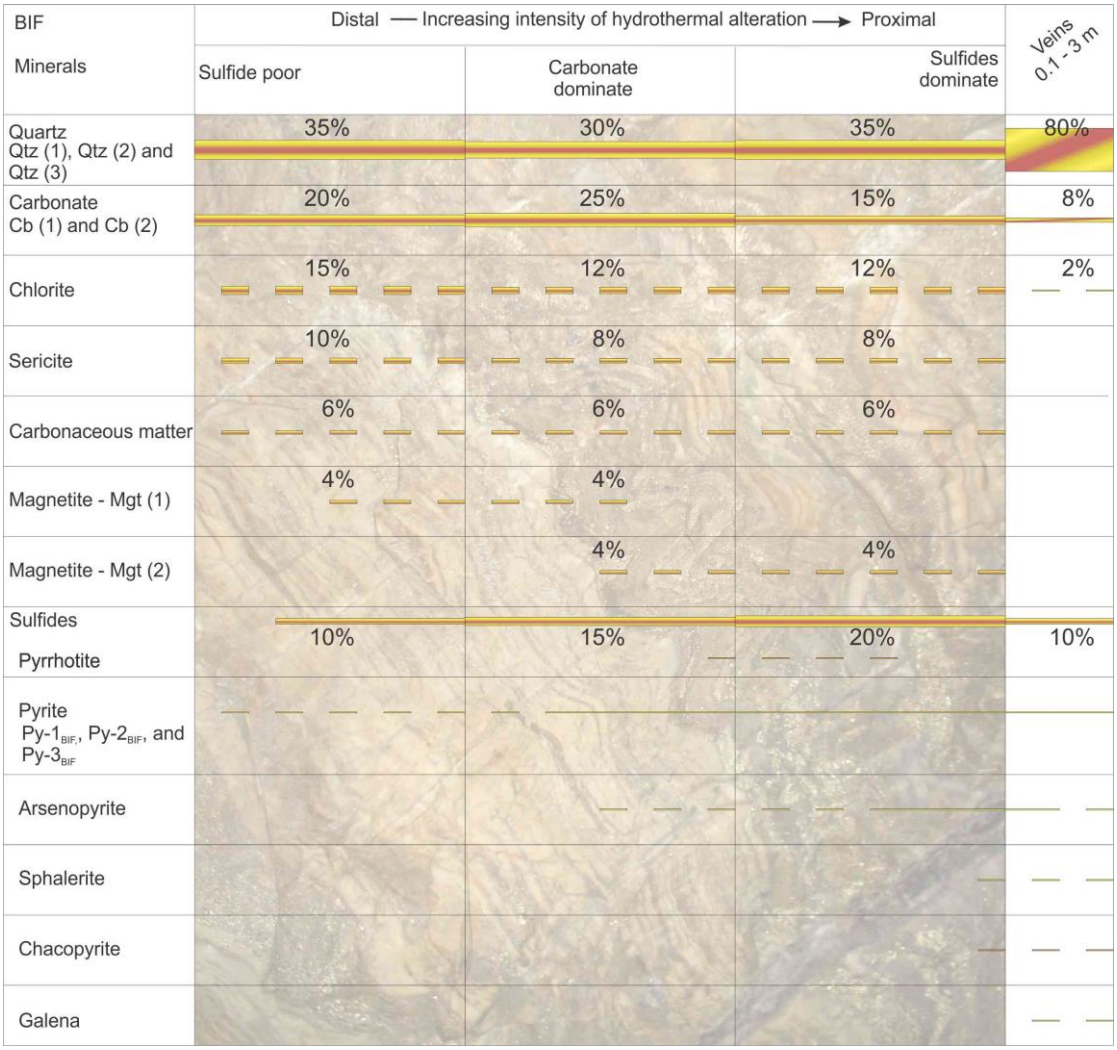

Figura 24: Modal constituents of the Lamego BIF distributed according to the intensity of hydrothermal alteration into distal, intermediate and proximal zones. Data interpreted from underground mapping, diamond core logging, petrography (cross-cutting relationship) and textural aspects. Carbonate minerals comprise siderite and ankerite, the latter dominating as the hydrothermal phase.

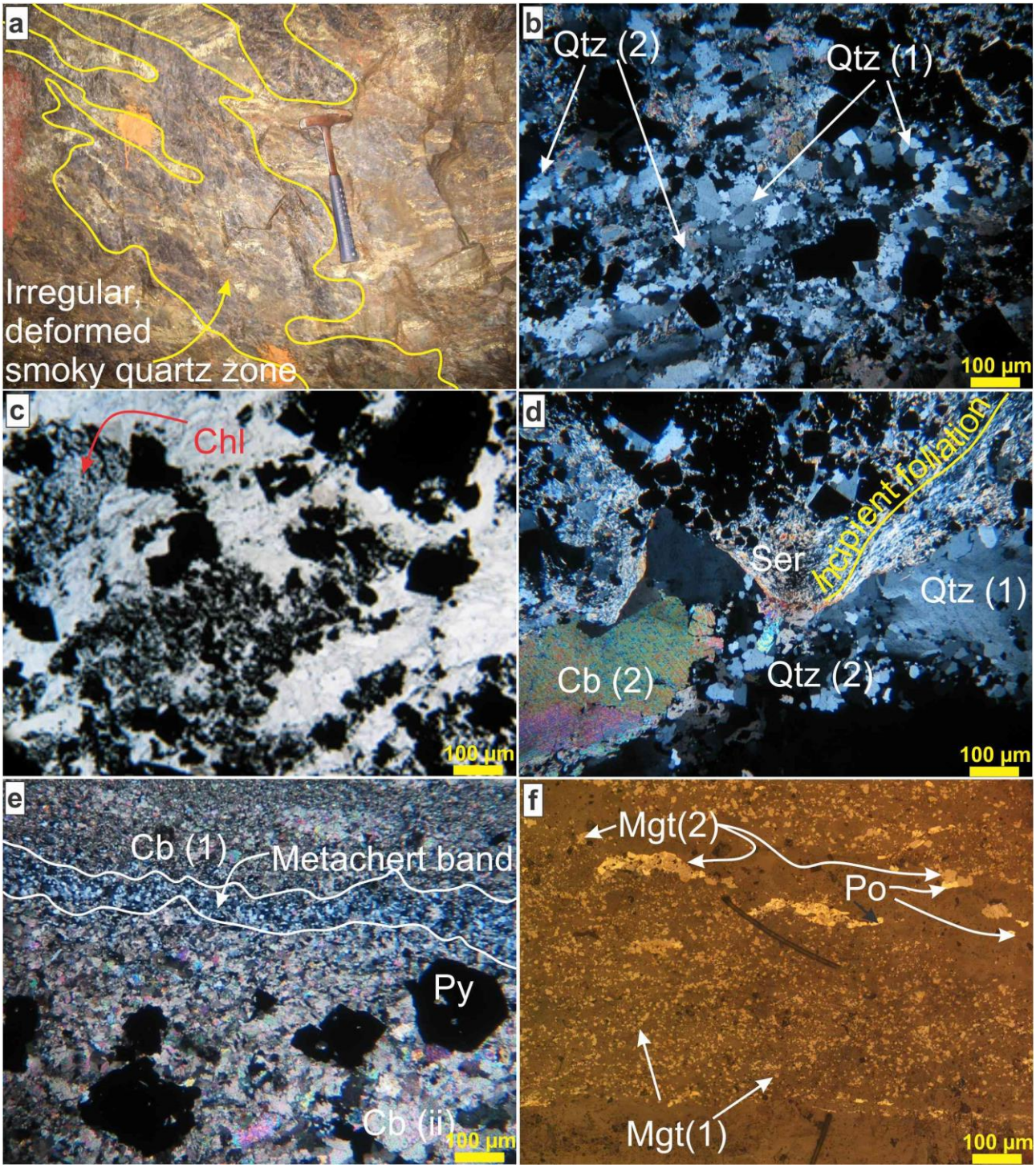
a
Irregular,
deformed
smoky quartz zone
b
Qtz (2)
Qtz (1)
100 µm
c
Chl
100 µm
d
Ser
incipient foliation
Qtz (1)
Cb (2)
Qtz (2)
100 µm
e
Cb (1)
Metachert band
Py
Cb (ii)
100 µm
f
Mgt(2)
Po
Mgt(1)
100 µm

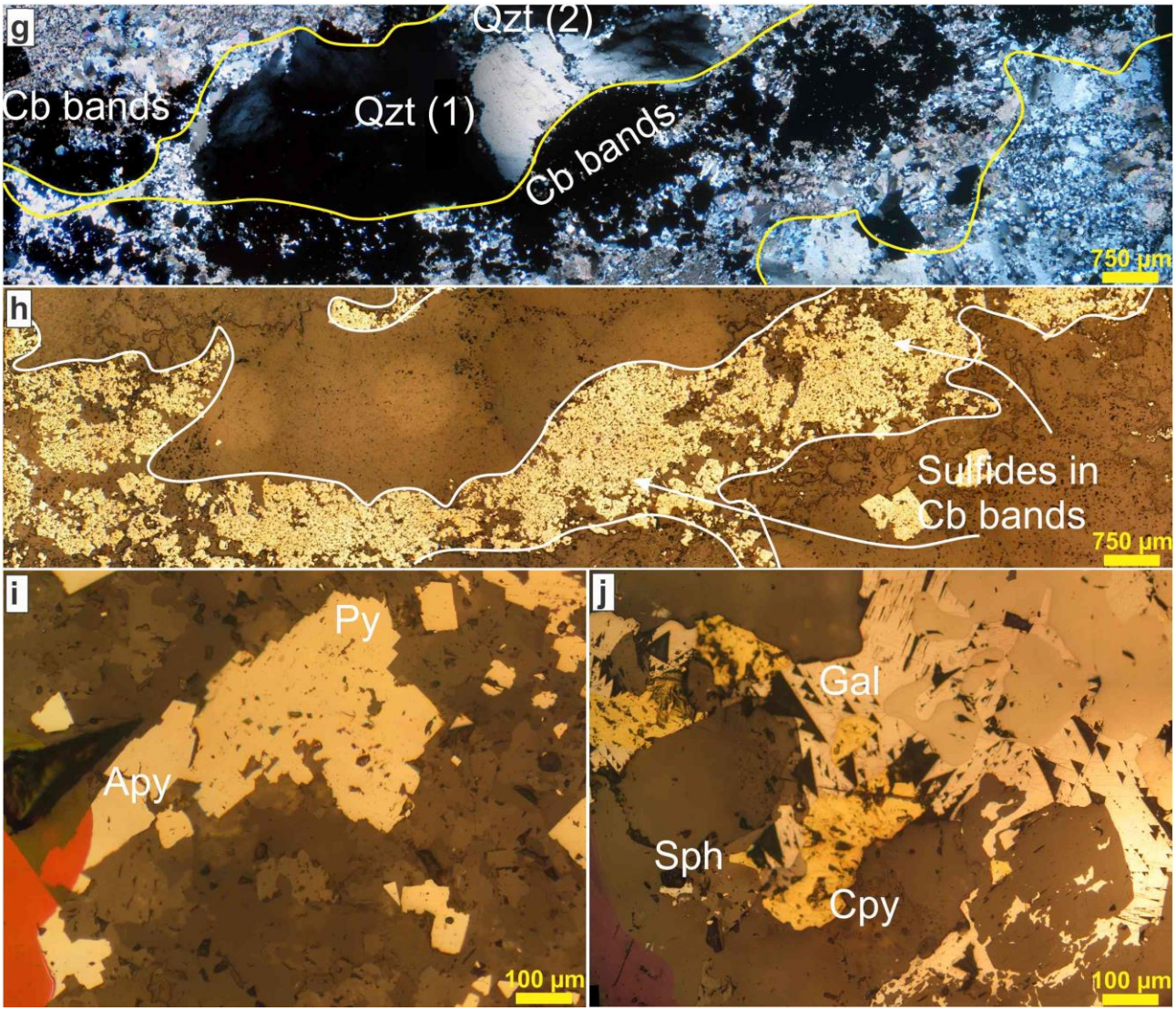

Figura 25: (a) Irregular and deformed zones of smoky quartz, defining pervasive silicification in BIF. (b) to (j) photomicrographs, crossed nicols; (b) to (e) and (g) transmitted light; (f), (h) to (j) reflected light. (b) Two quartz types: Qtz (1) xenoblastic and deformed crystals with serrated edges, and Qtz (2) anhedral, fine-grained with polygonal contacts. Incipient foliation defined by (c) chlorite and (d) sericite. Two types of carbonates (e): Cb (1) fine, anhedral, and Cb (2) coarser grained; note a band of metachert. (f) Two magnetite types: Mgt (1) euhedral and fine grained, oriented parallel to banding, and Mgt (2) at the edges of the vein. Note that the pyrrhotite grows on the magnetite edges. In the sulfide bands (g, h), pyrite and arsenopyrite are observed (1). Other sulfide minerals are (j) chalcopyrite and sphalerite that grow in veins. Apy: arsenopyrite; Cb: carbonate; Chl: chlorite; Cpy: chalcopyrite; Mgt: magnetite Py: pyrite; Qtz: quartz; Gal: galena; Ser: sericite; Sph: sphalerite.

4.6.2 Carbonaceous pelite

Carbonaceous pelite is composed mainly of carbonaceous matter (60%), quartz (clastic- 10%), carbonate (10%), chlorite (10%) and muscovite (5%), as well as accessory minerals (5%) including pyrite, As-pyrite, arsenopyrite, chalcopyrite and sphalerite (Figura 26). These rocks are finely

laminated, strongly foliated (sericite, chlorite and quartz) and folded (Figura 27a), fine-grained rocks that exhibit lepidoblastic to granolepidoblastic texture.

Silicification is represented by elongated and oriented, fine- and medium- (rock matrix) to coarse- (this one in veins) grained, deformed smoky quartz, with irregular edges (Figura 27b, c).

Carbonate alteration gives place to subhedral to euhedral carbonate minerals that are elongated, fine- and medium- (rock matrix) to coarse- (veins) grained, oriented with irregular edges (Figura 27b, c). Chlorite is associated with carbonate minerals, in fine flaky crystals, anhedral to subhedral, locally crenulated, alternating with quartz levels (Figura 27b).

Sulfidation is predominantly represented by pyrite in fine- and medium- to coarse-grained, subhedral to euhedral crystals, oriented parallel to banding, associated with vein portions or bands with quartz and rare sphalerite (Figura 27a, d, e, f). Other sulfides are arsenopyrite, medium- to coarse-grained, subhedral and euhedral, along pyrite edges (Figura 27e); chalcopyrite, anhedral to subhedral, in fine grains associated with carbonates and quartz; sphalerite, anhedral and associated with carbonate (Figura 27f).

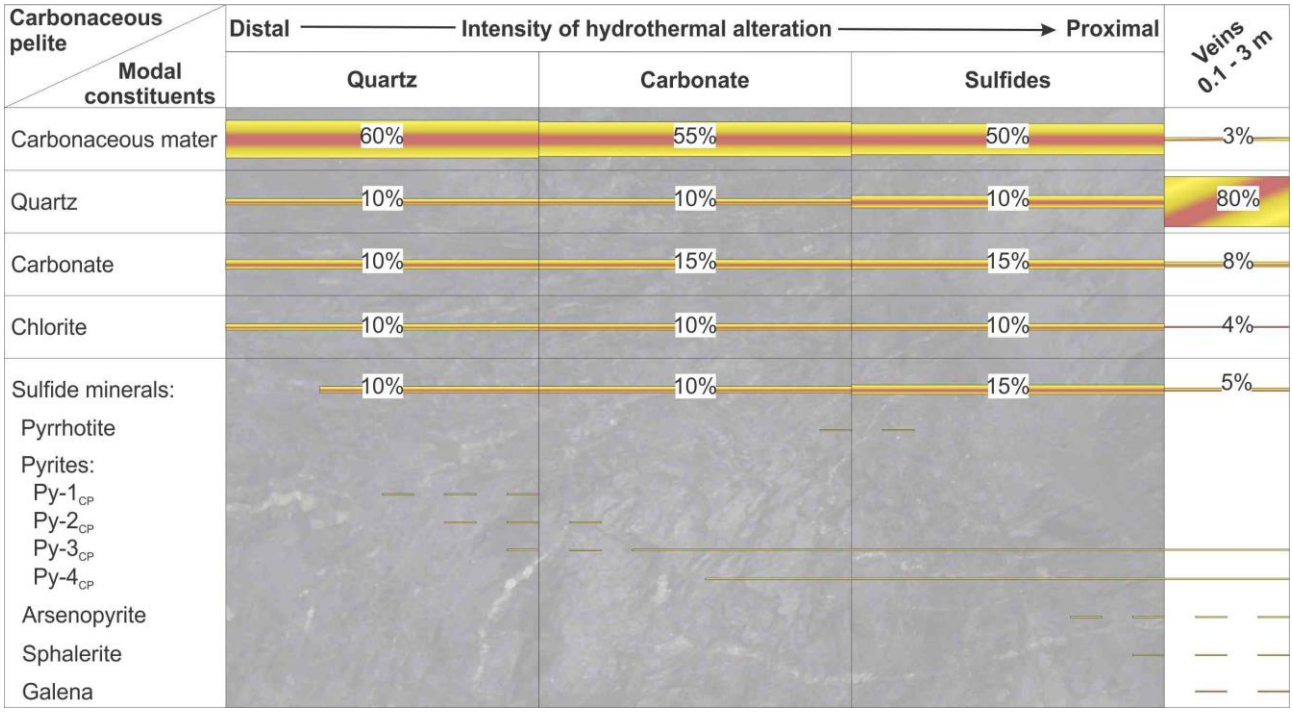

Figura 26: Modal constituents of the Lamego carbonaceous pelite distributed according to the intensity of hydrothermal alteration into distal, intermediate and proximal zones. Data interpreted from underground mapping, diamond core logging, petrography (cross-cutting relationship) and textural aspect. Carbonate minerals comprise siderite and ankerite, the latter dominating as the hydrothermal phase.

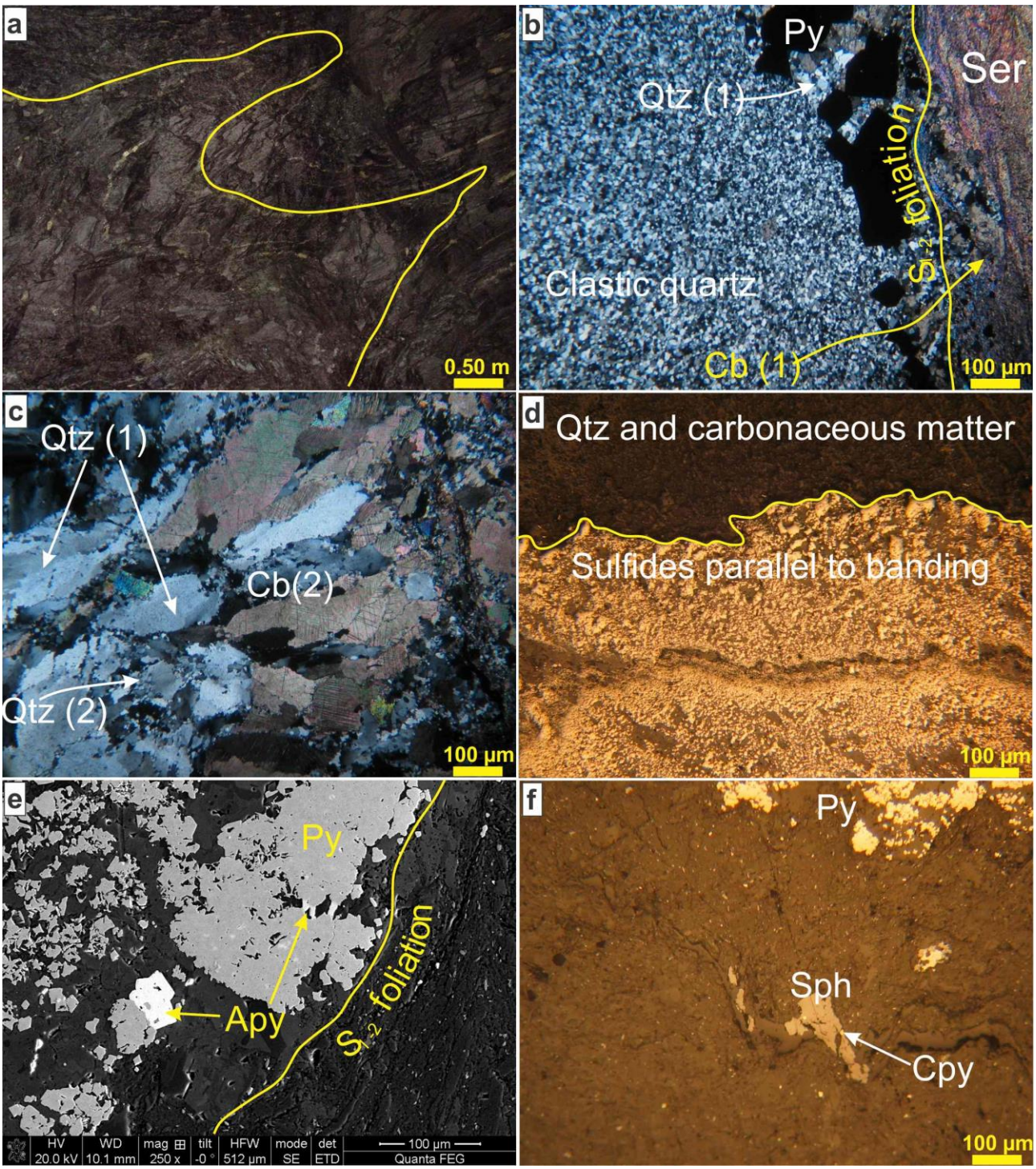

Figura 27: Carbonaceous pelite displaying folded sulfide-quartz veins (a). (b) to (d), and (f) are photomicrographs, crossed nicols; (b) and (c) transmitted light; (d) and (f) reflected light. (e) is a back-scattered image. (b) and (c) show quartz and carbonate as fine-grained and oriented crystals displayed according to the $S_{1\text{-}2}$ foliation (b), medium- to fine-grained quartz and carbonate discordant to $S_{1\text{-}2}$. (c). Quartz and carbonaceous matter are oriented according to $S_{1\text{-}2}$, with sulfidation predominantly represented by folded and/or oriented pyrite (d). In smaller proportions, other sulfides are (e) arsenopyrite at the edges of pyrite, sphalerite and chalcopyrite. Apy: arsenopyrite; Cb: carbonate; Cpy: chalcopyrite; Py: pyrite; Qtz: quartz; Ser: sericite; Sph: sphalerite.

4.6.3 Veins (silicification zones)

Pervasive zones of silicification, similar to zones of silica flooding (i.e., Colvine et al. 1988), are one of the most important characteristics in the Lamego deposit; these are distributed throughout the whole deposit. They contain randomly dispersed, irregularly shaped quartz aggregates and veins, controlled by the contact of carbonaceous pelite and the S_{1-2} foliation. They include large volumes of smoky quartz; portions of milky quartz are intermingled in the smoky quartz, and develop as a result of the smoky quartz recrystallization. Gold is strongly associated with these zones.

The most relevant characteristics of the smoky quartz vein/zones are: (1) coarse grain size, locally > 0.5 cm (a), scaled in centimeters to decameters (b,c,d), (2) association with sulfide and carbonate minerals (a,c), (3) related mainly to BIF, carbonaceous pelite and, in smaller proportion, mafic rock (b, c, d), and (4) occurrence as veins that are concordant and/or discordant to the BIF banding, going from discordant to concordant, and cutting through portions that are already silicified and sulfidized (e). Silicification zones may have: (5) boudinaged smoky quartz in a pinch-and-swell structure (b), (6) tension gashes (d), (7) veinlets, close by to shear and fault zones (f, g) (8) brecciated BIF (g,h), (9) subordinate portions of milky quartz, which seem to originate from smoky quartz, (10) *en-échelon* vein arrays (i), and (11) stockwork texture (j). Smoky and milky quartz make up for 85-90% of the silicification zones. In smaller proportions, carbonate, mica, pyrite, chalcopyrite, sphalerite, arsenopyrite, galena, tennantite-tetrahedrite, gold and carbonaceous matter are also present. Quartz () (a), carbonate minerals (b) and micas, mainly sericite (b), are present in a similar fashion as in the other alteration zones that develop in BIF and carbonaceous pelite. The only exception is quartz that exhibits a third type, milky quartz - Qtz (3), particularly in fault zones cutting across generations Qtz (1) and Qtz (2).

Pyrite is porous, subhedral to euhedral, of medium- to coarse-grain size (c), whereas As-pyrite is euhedral, medium to coarse grained. Arsenopyrite forms fine-grained, subhedral and euhedral grains, and preserves the same habit of pyrite (d, e) after which it is formed (i). Other sulfides are: (1) fine- to medium-grained, subhedral pyrrhotite (e), as inclusions in arsenopyrite, (2) coarse-grained, subhedral galena, located between strips of carbonate and quartz, in apparent textural equilibrium with chalcopyrite (f), (3) fine- to medium-grained, anhedral sphalerite, replaced by pyrite and chalcopyrite along the edges (d), and (4) rare, fine-grained, euhedral chalcopyrite.

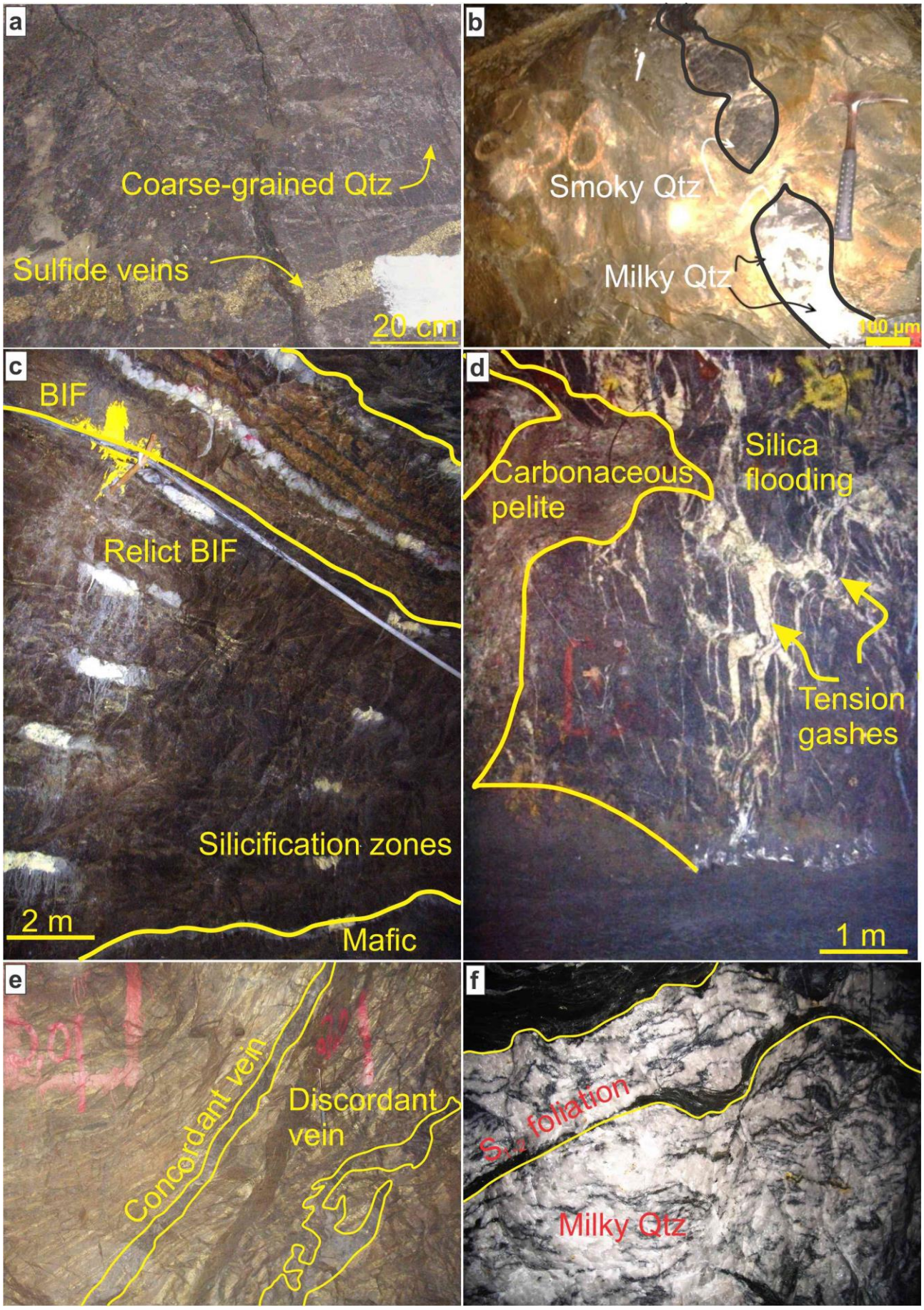
a
Coarse-grained Qtz
Sulfide veins
20 cm
b
Smoky Qtz
Milky Qtz
100 µm
c
BIF
Relict BIF
Silicification zones
2 m
Mafic
d
Carbonaceous pelite
Silica flooding
Tension gashes
1 m
e
Concordant vein
Discordant vein
f
S1 foliation
Milky Qtz

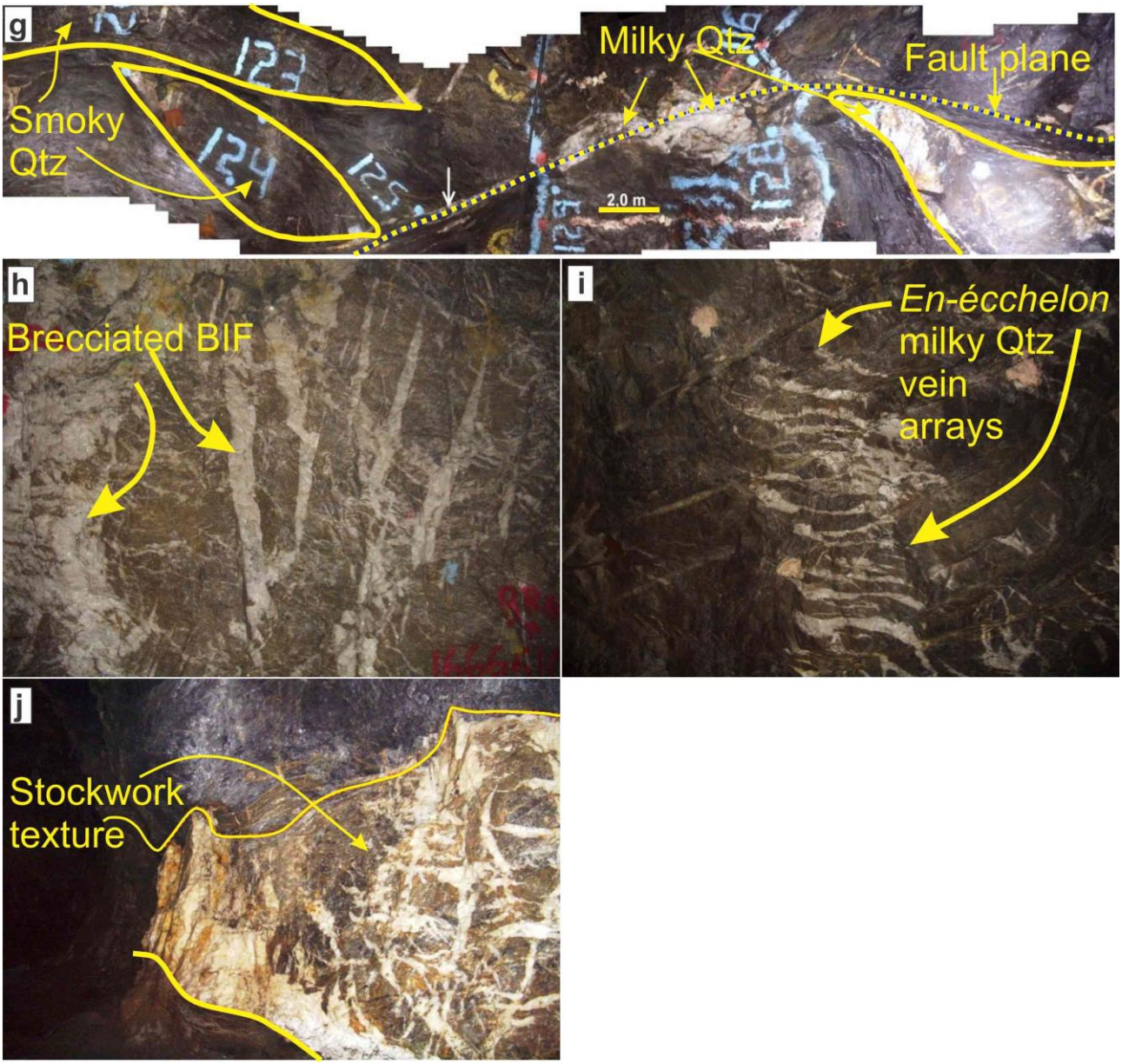

Figura 28: Widespread, pervasive silicification zones with coarse-grained quartz crystals (a). Zones are characterized by silica flooding and vary from centimeters (b) to meters (c, d), constrained below the carbonaceous pelite (c, d), and developing veins that may be concordant or not (e). Silicification zones occur as pinch and swell (b), tension gashes (d), and veinlets (f); also in boudinaged smoky quartz veins recrystallized to milky quartz in fault zone edges (g), in brecciated BIF, (h), in *en-échelon* vein arrays (i), and in stockwork texture (j). Qtz: quartz.

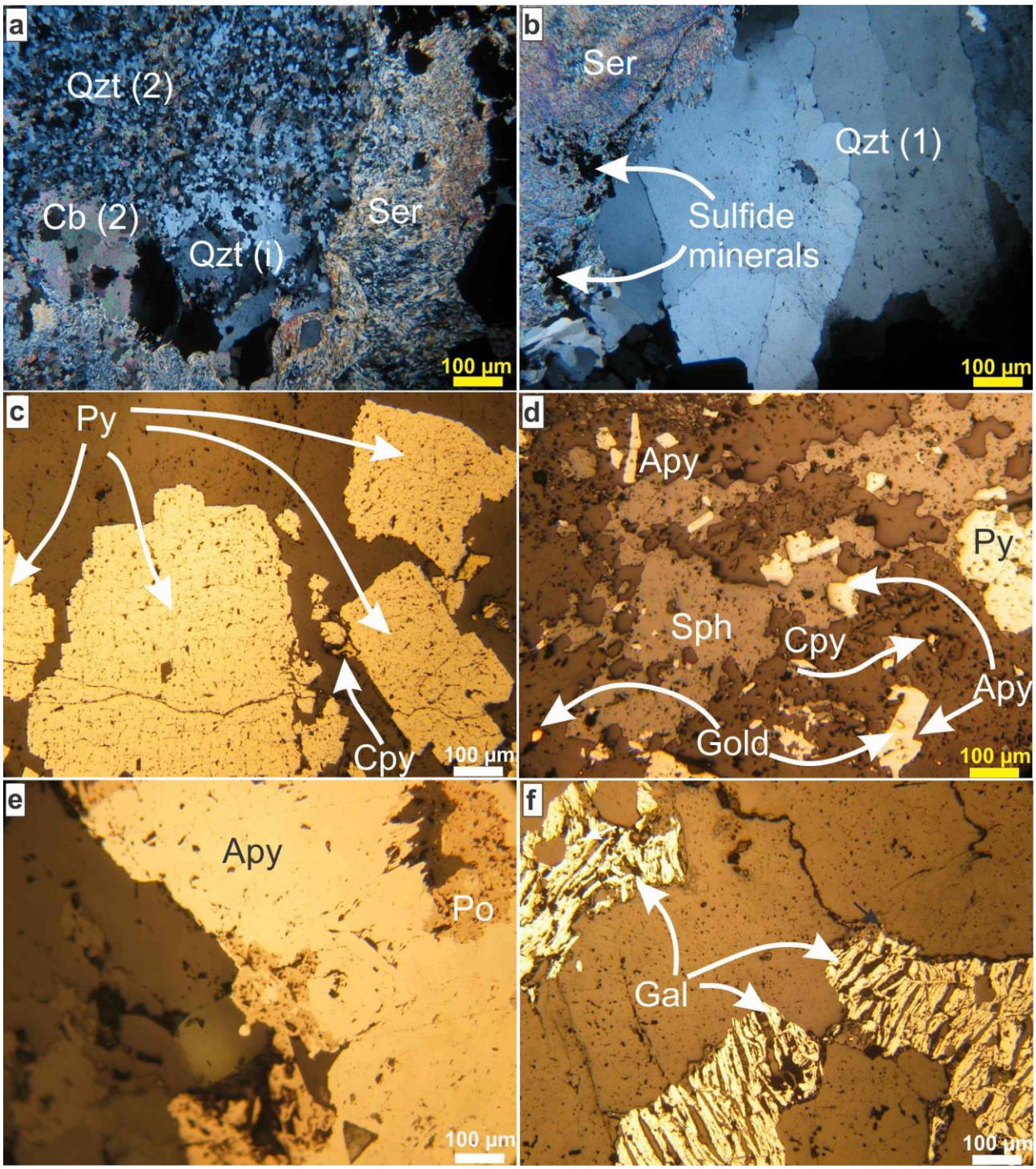

Figura 29: Photomicrographs (crossed nicols) of minerals in major silicification zones. Euhedral quartz and carbonates occur in the same manner as that of other rocks; (a), (b), transmitted light; (c) to (f) reflected light. The present sulfides are euhedral pyrite (c), arsenopyrite (d, e), galena (f), chalcopyrite (d) and sphalerite (d). Apy: arsenopyrite; Cb: carbonate; Cpy: chalcopyrite; Gal: galena; Po: pyrrhotite; Py: pyrite; Qtz: quartz; Ser: sericite; Sph: sphalerite.

4.7 Sampling, methods and analytical techniques

4.7.1 Sampling

Four drill holes were selected for this study, two intersecting the Cabeça de Pedra and two the Carruagem orebodies. In both cases, two drill holes start at surface and intercept the orebodies underground. The other two are horizontal drill holes within the mineralized zones. Interpretative cross-cutting geological sections (a, b) use a wide range of drill hole information, provided by AngloGold Ashanti Córrego do Sítio S/A (AGA), which were combined with detailed underground geological maps (Lobato et al. 2013; Martins 2011; Martins et al. 2016).

A total of 26 thin-polished sections were used to produce detailed textural studies of carbonaceous pelite (Figura 31) and BIF (Figura 32), and establish the mineral parageneses (Figura 33). Out of these 26, 4 representative polished sections were selected in order to investigate mineral composition, zoning and LA-ICP-MS analyses in sulfides.

For the Cabeça de Pedra orebody, drill hole LCPD0013 starts at elevation 1020.70 m with a maximum depth of 378.80 m. The sample 13-22 (Figura 31a) comes from 213.44 m deep (807.26 m elevation), with 0.18 ppm Au, where ten areas were selected for analyses on the thin-polished section; each area was labeled 13-22-A1 to 13-22-A10 (Figura 31b). The horizontal, underground drill hole LCPD1003 is at elevation 842.30 m, and has 88.21 m of maximum extension. Sample 14-23 (Figura 31c) is from interval 60.50 m (842.30 m elevation), with 0.18 ppm Au, where five selected areas are labeled 14-23-A1 to 14-23-A5 (Figura 31d).

Drill hole LCRD0159 from the Carruagem orebody starts at elevation 918.45 m with a maximum depth of 389.85 m. Its sample 1-01 is from the interval 343.35 (515.10 m elevation), and contains 12.36 ppm Au; four areas selected for analyses are labeled 1-01-A1 to 1-01-A5 (Figura 32c). The horizontal hole LCRD1104 at elevation 744.60 m has a maximum extension of 64.15 m. One sample of this drill hole 5-06 is from interval 26.00 m (744.10 m elevation), with 2.63 ppm Au, where eight areas were selected for the analyses and labeled 5-06-A1 to 5-01-A8 (Figura 32d).

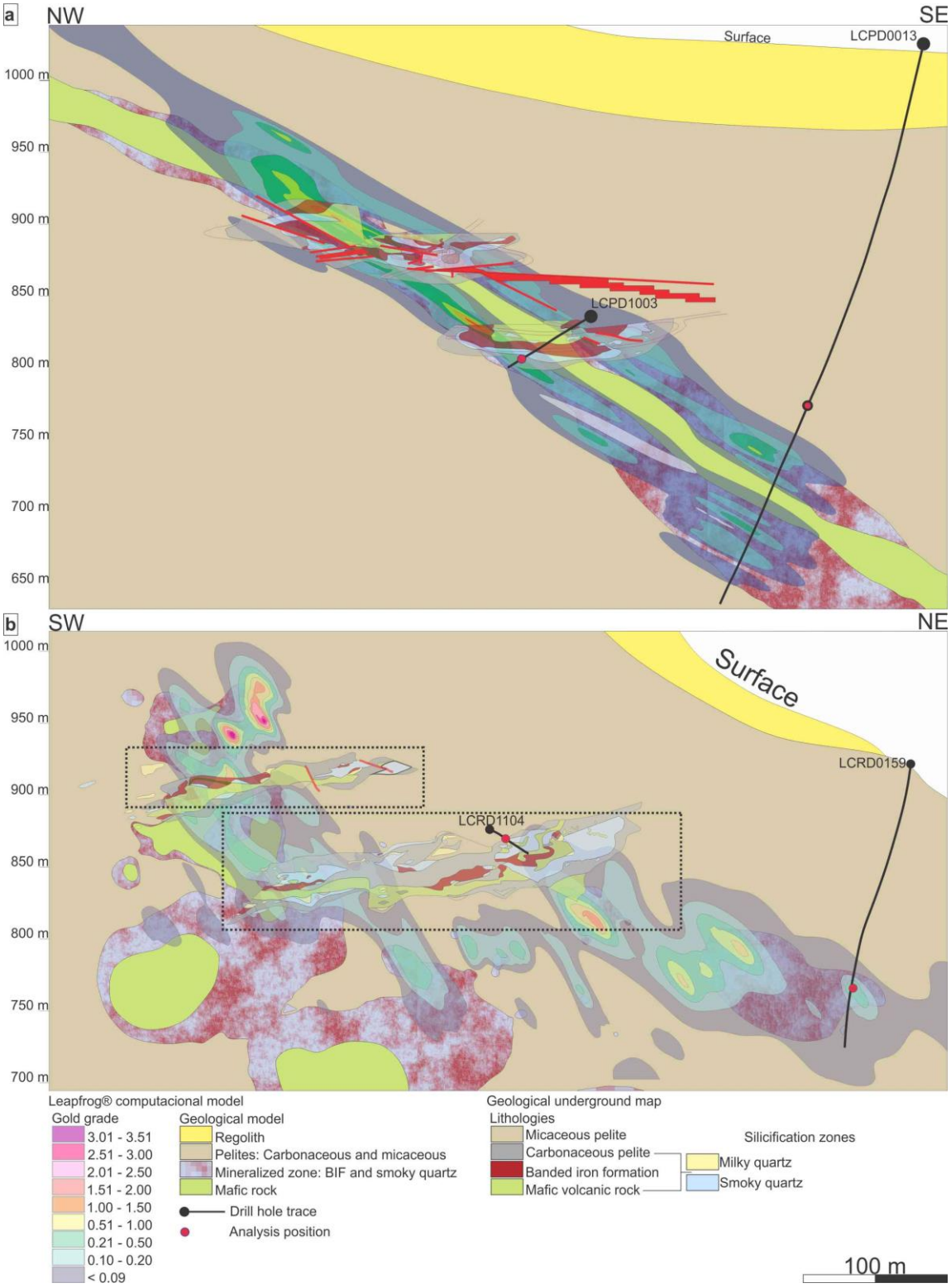

Figura 30: Integration of the Lamego gold deposit data combining: (1) geological information obtained by 1:100 underground mapping (detailed in dotted rectangles, in plan view), (2) 3-D geological computational model, and (3) 3-D gold grade distribution. Note that: (1) data integration is possible via superposition of information listed in (1) to (3), (2) in the rectangular areas, two mineralized portions (BIF and smoky-quartz zones) are distinguished in all four mapped areas, and (3) the 3-D geological computational model combines both BIF and quartz zones as one mineralized portion, but it does not distinguish carbonaceous and micaceous pelites. (a) The NW-SE cross section

of the Cabeça de Pedra orebody corresponds to the hinge zone of the Lamego fold. The mineralized zone, mafic rock, and pelites are concordant and continuous, dipping to the SE. Gold grades vary from 0.9 to 2.0 g/t. Sampled areas from drill holes LCPD0013 and LCP31003 are located out of the mineralized portions in the carbonaceous pelite. (b) The SW-NE cross section of the Carruagem orebody dips to the SE. Gold grades vary from 0.9 to 3.51 g/t. The mineralized zone and mafic rock are discordant and discontinuous. Sampled areas from drill holes LCRD0159 and LCRD1104 correspond to mineralized portions of BIF. The 3-D model was generated using Leapfrog Geo® software, and based on data from 2,623 drill cores conceded by AGA.

4.7.2 EPMA

Compositional analyses were acquired on a JEOL 8530F hyperprobe equipped with 5 tunable wavelength dispersive spectrometers. The operating conditions were 40 degrees take-off angle, and beam energy of 20 keV. The beam current was 50 nA, and fully focussed.

Elements were acquired using analyzing crystals LiF crystals LiF for V kα, Fe kα, Ti kα, Au lα, Te lα, Cu kα, Ni kα, Co kα, Zn kα, Hg lα, PETJ for S kα, Ag lα, Cd lα, PETH for Sb lα, Pb mα, Bi mα and TAP for As lα, Se lα. The standards employed were an assortment of commercially available metals, oxides, sulphides and tellurides.

Counting time was 20 seconds for S kα, Fe kα, 60 seconds for Ni kα, Zn kα, As lα and Se lα, and 120 seconds for Pb mα, Sb lα, Ag lα, Cd lα, Te lα, Bi mα, and Au lα. Mean atomic number background corrections were employed throughout (Donovan & Tingle, 1996). Unknown and standard intensities were corrected for deadtime and the ZAF algorithm utilized for matrix absorption (Armstrong, 1988). On peak interference corrections were applied as appropriate (Donovan et al., 1993) Detection limits ranged from 0.005 wt % for Sb to 0.035 wt % for Au lα.

Quantitative chemical maps were acquired using the calibration set up described above for S, As, Sb, Co, Fe, Ag, Se, Pb, Zn and Ni. Detection limit maps were acquired for these elements and applied as the minimum cut-off values for all maps. Map acquisition utilised an 80 nA beam current with a 2 x 2 μm pixel dimension and 200 msec dwell time per pixel. Data were processed using the Calcimage software package and output to Surfer® for further processing and enhancement.

4.7.3 Laser ablation

Seventy samples were collected from the ore zone and wall rocks at different levels (Figuras 22 and 23), and polished into thin sections for petrographic studies. From these, some samples were selected for sulfide trace element analyses using the in situ LA-ICP-MS technique.

The analyses were carried out in the CODES LA-ICP-MS facility at the University of Tasmania, Australia. The analytical instrumentation engaged in this study consists of a 213 nm New

Wave UP-213 nm laser ablation system coupled with an Agilent 7500a Quadrupole ICP-MS for arsenopyrite analyses; and a 193 nm Resolution ArF excimer laser ablation system coupled with an Agilent 7700s Quadrupole ICP-MS for pyrite analyses.

Depending on the sulfide size, analyses were performed with laser beam diameters of 15-43 μm and at a repetition rate of 5 Hz. The laser beam energy used was 90 mJ and the fluence used for ablating sulfides was maintained between at 2.7 J cm^{-2} with the 193 nm laser and at 3.5 J cm^{-2} with the 213 nm laser and 5.0 J cm^{-2}. The analysis time for each sample was 90 s, which includes 30 s of background measurement with laser off and 60 s of analysis with laser on. Acquisition time for all masses was set to 0.02 s, with a total sweep time of ~0.6 s.

Data reduction was performed according to standard methods (Longerich et al. 1997), with Fe as the internal standard. Calibration was performed using the in-house standard STDGL2b-2, comprising of powdered sulfides doped with certified element solutions and fused to a lithium borate glass disk (Danyushevsky et al. 2011). The standard was analyzed twice every 1.5 h with a 100-μm beam size at 10 Hz to correct for instrument drift. Accuracy is expected to be better than 20% for most elements (Danyushevsky et al. 2011). A set of 35 elements was chosen for spot analysis (Na^{23}, Mg^{24}, Al^{27}, Si^{29}, Ca^{43}, Ti^{49}, V^{51}, Cr^{53}, Mn^{55}, Fe^{57}, Co^{59}, Ni^{60}, Cu^{65}, Zn^{66}, As^{75}, Se^{77}, Zr^{90}, Mo^{95}, Ag^{107}, Cd^{111}, Sn^{118}, Sb^{121}, Te^{125}, Gd^{157}, Hf^{178}, Ta^{181}, W^{182}, Pt^{195}, Au197, Hg^{202}, Tl^{205}, $Pb^{206, 207, 208}$, Bi^{209}, Th^{232} and U^{238}).

4.8 Texture of pyrites, other sulfides and gold: Lamego paragenetic sequence

The opaque minerals at the Lamego deposit are represented by sulfides, oxides, sulfosalts and gold. The phosphate monazite is also identified. Pyrite (FeS_2), arsenopyrite (FeAsS), sphalerite (ZnS), chalcopyrite ($CuFeS_2$), galena (PbS) and pyrrhotite ($Fe_{(1-X)}S$) dominate. Magnetite (Fe_3O_4) is the only oxide; nikeline (NiAs) and tennantite-tetrahedrite ($Cu_9Fe_3Sb_4S_{13}$) represent minerals of the sulfosalt group. These were all examined using an optical microscope in a total of 70 polished thin sections and 26 polished sections, and a scanning electron microscope. Some results were published by Lobato et al. (2013), Martins (2011), Martins et al. (2011, 2016). However, this is the first paper to report aspects of mineral textures and geochemistry and associated precious metals with specific emphasis on carbonaceous pelite and BIF.

4.8.1 Mineral types and textures

Figures 24 and 26 show the abundance of minerals in the mineralized zones that include the Lamego BIF, carbonaceous pelite and silicification zones (veins). For the purpose of this study, attention is

focused mainly on the most important sulfides, pyrite and arsenopyrite.

Pyrite is the dominant sulfide in all rocks, but clearly more abundant as one approaches the mineralized zone (Figuras 23a, b, c, 25g, h, 27d and 28c). This phase is present: (1) in textural equilibrium with pyrrhotite and arsenopyrite (Figura 28e), (2) intergrown with sphalerite and chacopyrite (Figura 28d), and (3) with galena, chalcopyrite and sphalerite inclusions (Figuras 28d, 27e, f, and 25j).

In the carbonaceous pelite, pyrites occur in four different textural types where sulfide bands are related to carbonate and sericite (Figura 31a, b). A microcrystalline pyrite Py-1_{CP} is framboidal, with <0,008 mm in diameter, subhedral and euhedral, in concentric shapes where sphalerite develops along the edges (Figura 31a, c, e, f, g); the nodular pyrite Py-2_{CP} is subhedral, with diameters of up to 0,3 mm, formed as of Py-1_{CP} aggregates (Figura 31b, h, I, j, k). The Py-3_{CP} is a fine-grained, clear, euhedral and recrystallized pyrite, with diameter of up to 0,06 mm and developed along the borders of Py-2_{CP} (Figura 31c, d, h, j, k), whereas Py-4_{CP} is a porous to clear, fine- to coarse-, but predominantly medium-grained up to 0,05 mm, euhedral and recrystallized pyrite, in randomly distributed grains (Figura 31d, l, m).

The BIF has three textural pyrite types, Py-1_{BIF}, Py-2_{BIF}, and Py-3_{BIF} (Figura 32c, d). The Py-1_{BIF} represents the massive aggregate of very fine-grained, anhedral to subhedral pyrites, that agglutinate to form fine- to coarse-grained, characteristically porous crystals up to 0,3 mm, containing galena, chalcopyrite, sphalerite, carbonate and quartz inclusions. They are anhedral to subhedral, forming centimetric bands (Figura 32c, d, e, f). The medium- to coarse-grained, porous to smooth Py-2_{BIF} forms subhedral to euhedral, randomly distributed crystals, with diameters of up to 0,4 mm, showing galena and arsenopyrite inclusions (Figura 32c, d, e, h, i). Finally, the Py-3_{BIF} is a clear (smooth), fine- to medium-grained, subhedral to euhedral As-pyrite along the borders of Py-2_{BIF}, up to 0,8 mm (Figura 32c, d, j, k).

Other sulfides are: pyrrhotitte, sphalerite, chalcopyrite and galena. Pyrrhotitte has a diameter up to 0,02 mm, and is intergrown with magnetite and pyrite (Figura 25f). Sphalerite and galena develop as vein minerals, while chalcopyrite is present not only in veins, but also in the mafic rock. Sphalerite has diameters to 0,3 mm, intergrown with pyrite, arsenopyrite, galena, chalcopyrite and tennantite-tetrahedrite (Figura 25j). Chalcopyrite with diameters between 0,01 to 0,03 mm exhibits galena inclusions. Galena with diameters of until 0,04 mm is the most common inclusion mineral (Figura 25j).

Other minerals found mainly in veins that cut the BIF and pelitic rocks include nickeline, the most common, the phosphate monazite and the sulfosalt tennantite-tetrahedrite. The former is in textural

equilibrium with pyrite and chalcopyrite; with anhedral crystals sized to 0,01mm. Anhedral to subhedral monazite is sized to 0,003 mm, and is essentially in veins that crosscut BIF (also mafic rocks). Tennantite-tetrahedrite commonly forms large anhedral to subhedral aggregates, sized to 0,002 mm, with myrmekitic intergrowth textures with galena + chalcopyrite ± sphalerite (Figura 25j).

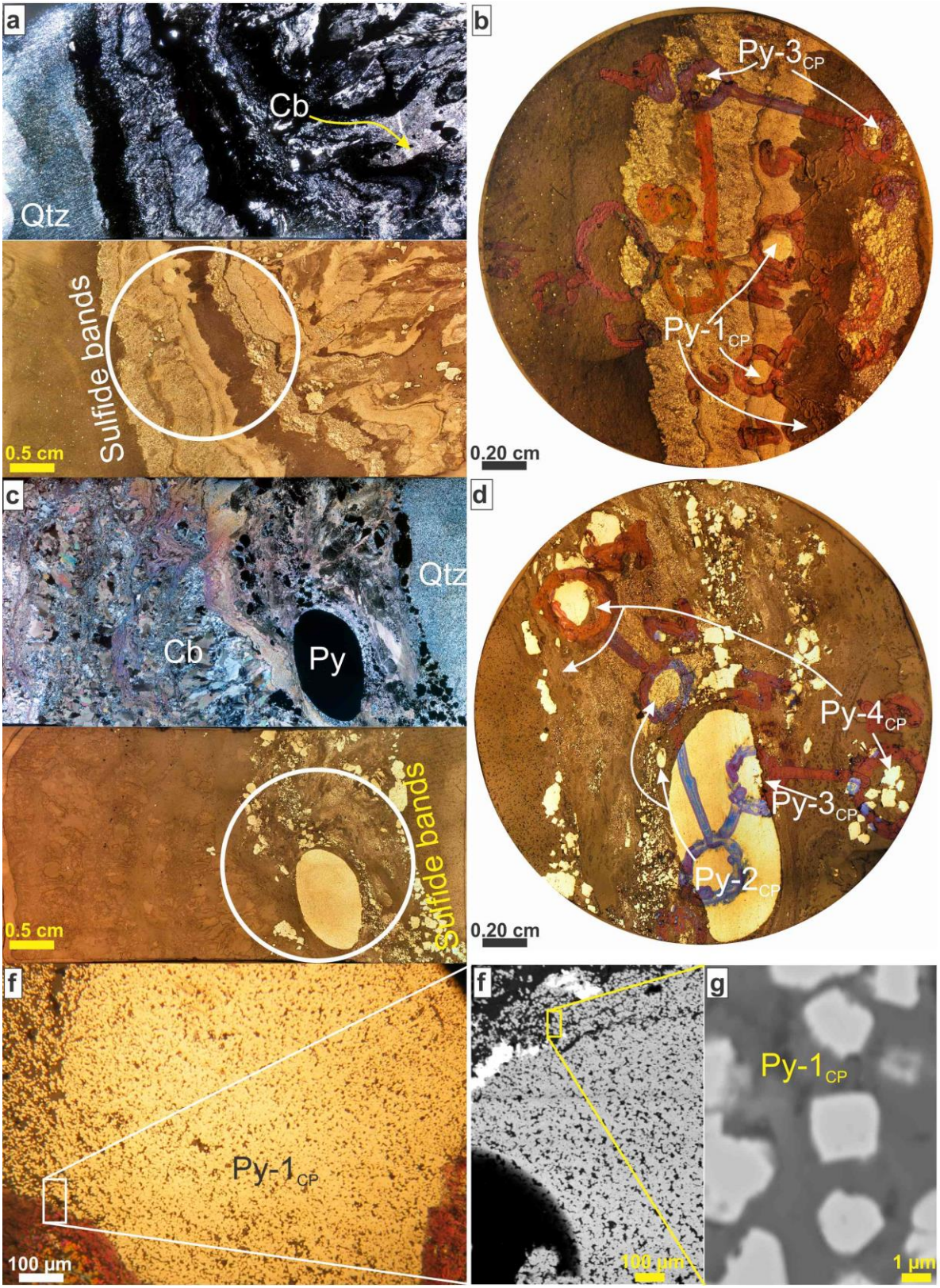

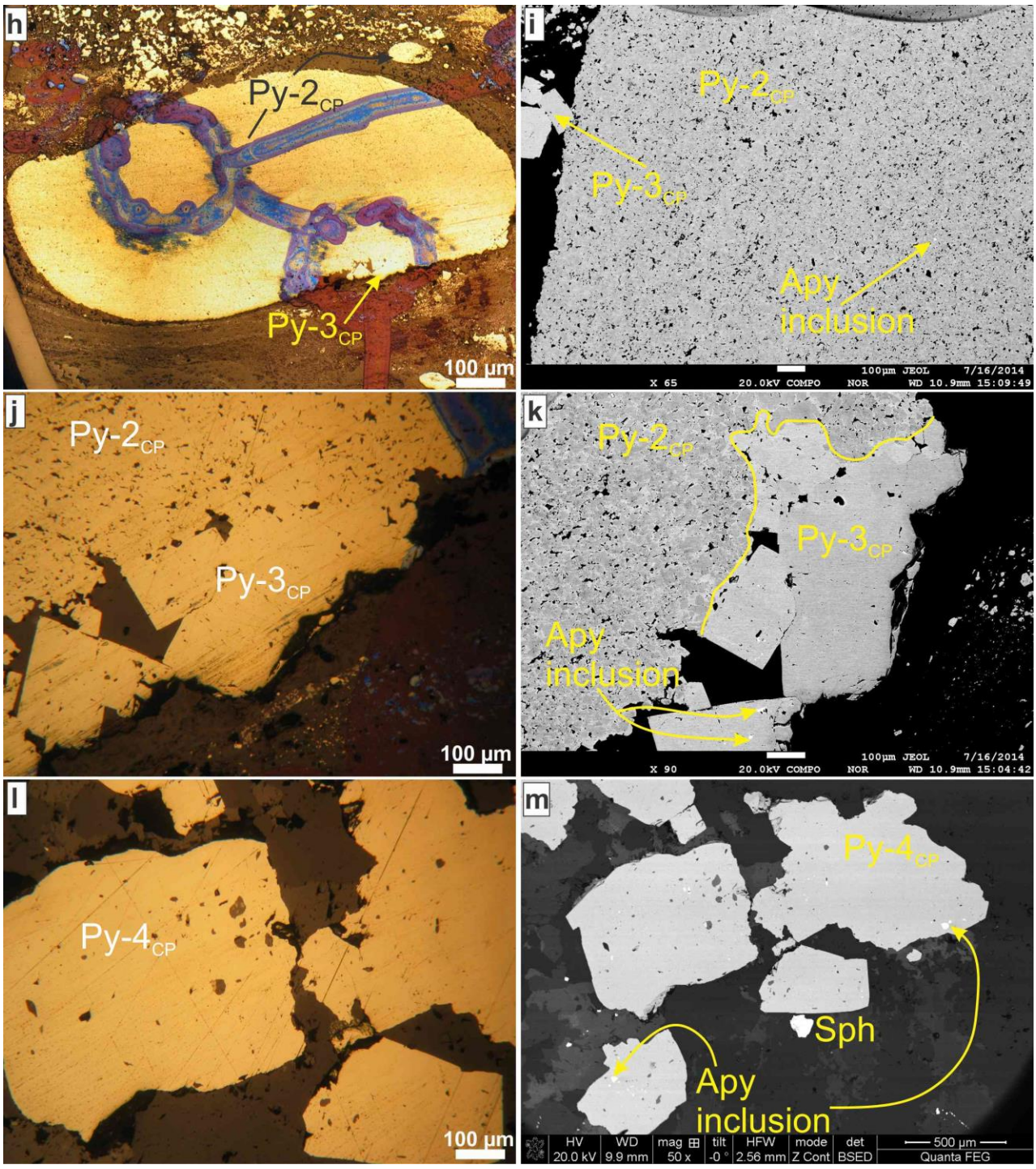

Figura 31: Four pyrite types in carbonaceous pelite, Cabeça de Pedra orebody, which were analyzed by in situ LA-ICP-MS. (a), (b) foliation-controlled, sulfide banding (sample 13-22), showing Py-1_{CP}, Py-2_{CP}, and Py-3_{CP}. (c), (d), (e), (f) sample 13-22; (c) scattered pyrites showing Py-2_{CP}, Py-3_{CP} and Py-4_{CP}. (e) detail of Py-1_{CP}; (f) and (g) back-scattered images showing that Py-1_{CP} constitutes pyrite microcrystals (~1.5 µm). (h) to (m) sample 14-23; (h) nodular Py-2_{CP} with border partly recrystallized to Py-$3_{CP;}$ note the presence of arsenopyrite inclusions in Py-2_{CP}. (j), (k) magnification of Py-3_{CP} highlighting the different textural aspects between Py-2_{CP} and Py-3_{CP}. (l), (m) coarse-grained Py-4_{CP} with inclusions of arsenopyrite; sphalerite is also present. Apy: arsenopyrite; Cb: carbonate; Py: pyrite; Qtz: quartz; Sph: sphalerite. Photomicrographs, crossed nicols: (a) to (e), (h), (j) and (i). Transmitted and reflected light: (a) and (b). All others: reflected light. Back-scattered images: (f), (g), (i), (k) and (m).

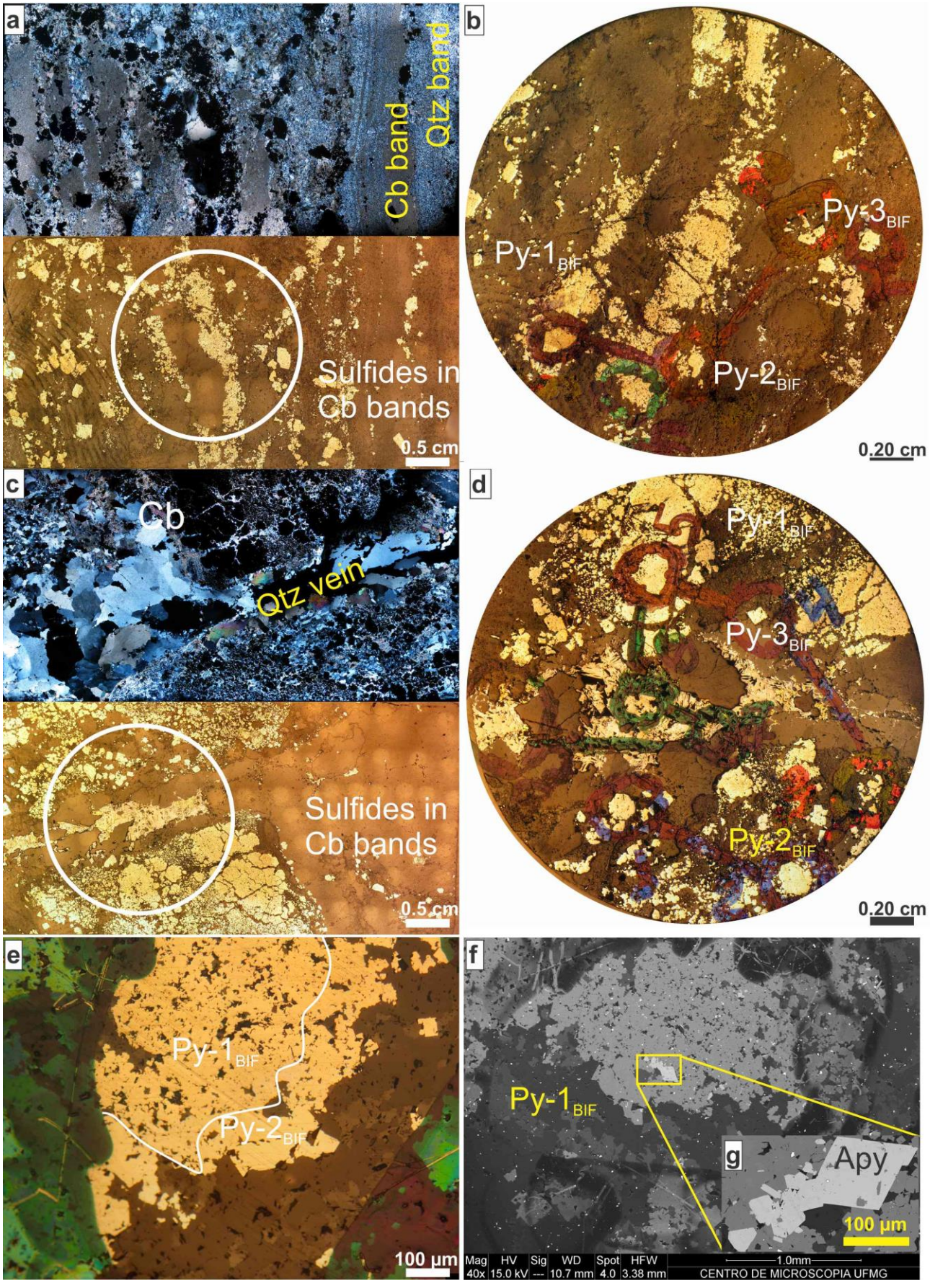
a
Cb band
Qtz band
Sulfides in
Cb bands
0.5 cm
b
Py-3BIF
Py-1BIF
Py-2BIF
0.20 cm
c
Cb
Qtz vein
Sulfides in
Cb bands
0.5 cm
d
Py-1BIF
Py-3BIF
Py-2BIF
0.20 cm
e
Py-1BIF
Py-2BIF
100 µm
f
Py-1BIF
g
Apy
100 µm
Mag HV Sig WD Spot HFW
40x 15.0 kV --- 10.7 mm 4.0 3.38 mm
1.0mm
CENTRO DE MICROSCOPIA UFMG

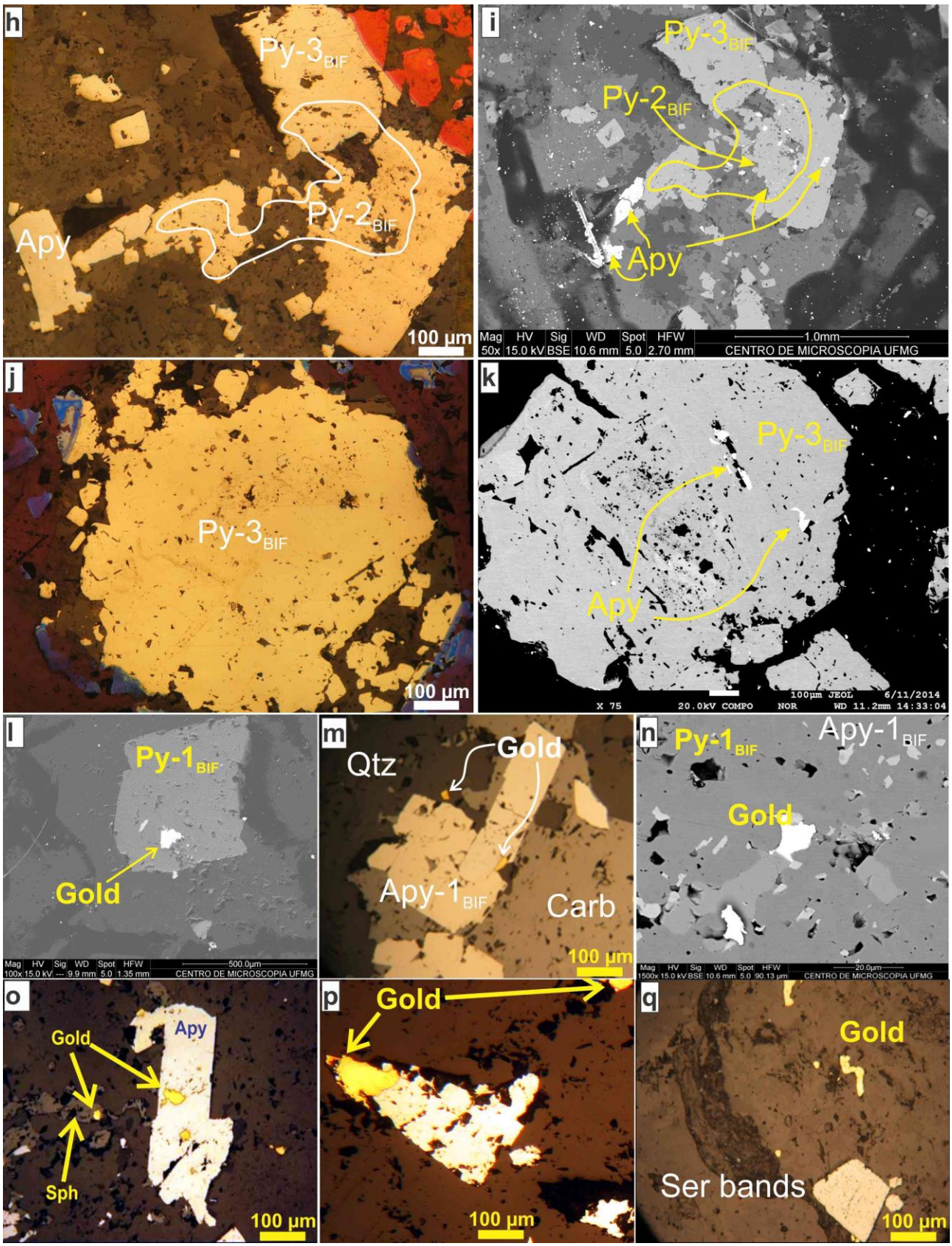

Figura 32: Three pyrite types in BIF, Carruagem orebody, which were analyzed by in situ LA-ICP-MS. (a), (b) sulfides along BIF banding (sample 101), showing Py-1_{BIF}, Py-2_{BIF} and Py-3_{BIF}. (c) and (d) quartz vein with Qtz (1) and (2) types, crosscutting BIF banding, with Py-1_{BIF}, Py-2_{BIF} and Py-3_{BIF} (sample 5-06). (e), (f) grain of Py-1_{BIF} surrounded by Py-2_{BIF} with (g) inclusion of arsenopyrite

grain (sample 1-01). (h), (i) grain of Py-2_{BIF} surrounded by Py-3_{BIF} with inclusion of isolated arsenopyrite grains. Py-3_{BIF} forms randomly distributed grains (sample 1-01). (j), (k) coarse-grained Py-3_{BIF} with (k) arsenopyrite inclusions in pores (sample 5-06). Gold are located as: inclusions in Py (l), (n) Apy (o) Sph (o); in contact between Qtz, Apy and Carb (m) and along sericite band (q). Photomicrographs, crossed nicols: (a) to (e), (h), (j), (m), (o) to (q). Transmitted and reflected light: (a) and (b). All others: reflected light. Back-scattered images: (f), (g), (i), (k), (l) and (n).

4.8.2 Location of gold

Gold grains in sulfide-rich BIF vary from 0.04 to 0.05 mm. They are hosted in As-rich Py-1_{BIF} and Py-2_{BIF}, filling their pores (Figura 32l), and also along the contacts between carbonate, smoky quartz and arsenopyrite (Figura 32m).

Free gold is present in silicification zones, which also contain particles: (1) included in pyrite, arsenopyrite, chalcopyrite and sphalerite (Figura 32n), (2) as abundant inclusions associated with smoky quartz (Figura 28d), (3) along arsenopyrite edges (Figura 32o); (4) fillets in arsenopyrite fractures, and (5) forming trails in pyrite along the contact between smoky quartz-sericite bands (Figura 32q; Martins et al. 2016; Morales et al. 2016).

These minerals have been used to construct the paragenetic sequence represented in Figura 13, which takes into consideration the advancement of the hydrothermal alteration and the structural generations described by Martins et al. 2016.

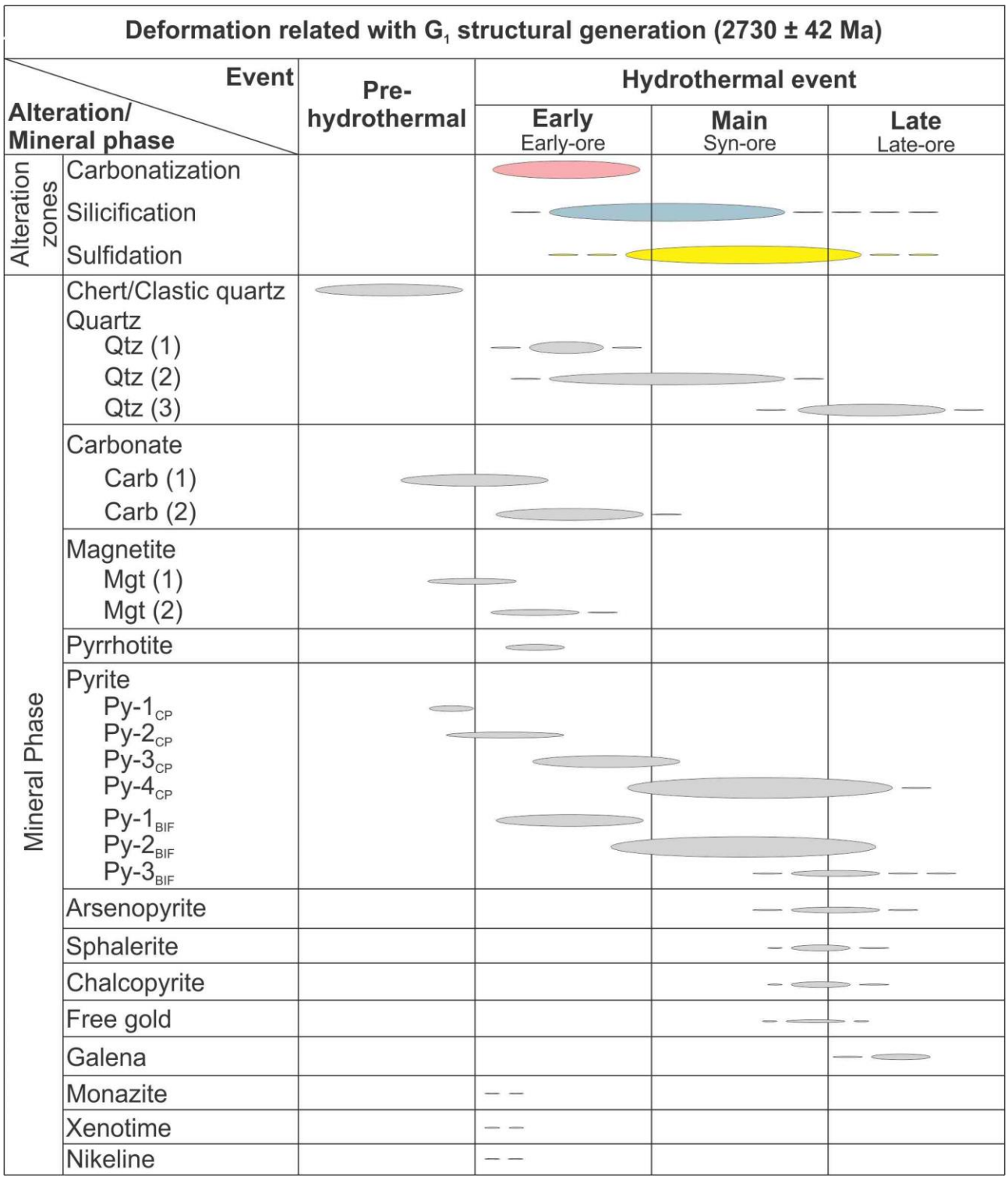

Figura 33: Paragenetic sequence for major minerals of the Lamego gold deposit interpreted from texture and in situ LA-ICP-MS analyses on sulfide minerals.

4.9 Sulfides composition and zoning

Five samples from the drill holes that intersect the Cabeça de Pedra (Figura 30a) and Carruagem (Figura 30b) orebodies were used for elemental mapping with EPMA of different pyrites. From the Cabeça de Pedra orebody, samples 13-22-A4 (Figura 31a), 13-22-A8 (Figura 31a) and 14-

23-A4 (Figura 31b) were selected, hosted in carbonaceous pelite, where Py-1_{CP}, Py-2_{CP}, Py-3_{CP} and Py-4_{CP} were mapped. From the Carruagem orebody, BIF samples 1-01-A1 and 5-06 were selected, and Py-1_{BIF}, Py-2_{BIF}, Py-3_{BIF} were mapped. The results of all analyses are indicated in parentheses along the text, and are quantified in wt%.

The Py-1_{CP} (Figura 34a) was mapped in sample 13-22-A4 (Figura 31a, b) and covers about 2/3 of a concentric area, where all the analyzed elements display a general homogeneous distribution, except for gold with a few nuggets in the left corner of the image, located at the edge of the grain, coinciding with the presence of minute pores (Figura 34i). The analyzed elements are: S (23.04-57.85), As (0.04-2.26), Mn (9.21 x 10^{-9}-0.41), Fe (21.08-50.90), Sb (1.02 x 10^{-8}-1.82), Tl (9.34 x 10^{-9}-1.67), Hf (9.86 x 10^{-9}-1.07 x 10^{-8}). Au (1.44 x 10^{-8}-1.45 x 10^{-8}), Ni (0.001-3.29), and Co (8.45 x 10^{-9}-0.61), and correspond to Figura 14 b to k.

The mapped area in sample 14-23-A4 (Figuras 31c, d and 35a) corresponds to a strip of the Py-2_{CP} transitioning to Py-3_{CP}, with three patterns of geochemical behavior (Figura 35b-k): (1) homogeneous distribution in Py-2_{CP} and Py-3_{CP} for Mn (8.95 x 10^{-9}- 1.20 x 10^{-8}), Sb (1.02 x 10^{-8}-3.48), Tl (9.00 x 10^{-9}-1.82), Hf (9.34 x 10^{-9}-1.77) and Au (1.28 x 10^{-8}-1.51 x 10^{-8}), with gold in Py-3_{CP} locally showing minute nuggets, (2) homogeneous distribution, but with a larger concentration, in Py-2_{CP} than in Py-3_{CP}, of S (1.09 x 10-8 - 59.72 wt%) and Fe (0.39 - 51.45 wt%), and (3) homogeneous distribution in Py-2_{CP} of As (1.16 x 10^{-8} - 3.45 wt%), Ni (8.02 x 10^{-9} - 3.44 wt%) and Co (7.84 x 10^{-9} - 0.64 wt%), with contents that rise towards the edges where Py-3_{CP} develops. The Py-3_{CP} is zoned, with Ni enriched towards the edges and in the core; Co has a predominantly homogeneous distribution, but a small strip exhibits larger concentration, where Ni is depleted.

The Py-4_{CP} (a) is mapped in sample 13-22-A8 (Figura 31c, d), where the analyzed elements (Figura 36b-j) exhibit two patterns: (1) homogeneous distribution of S, F, Mn, Sb, Tl, Hf and Au, and (2) chemical zoning of As, Ni and Co. Both As and Ni are enriched along the edges and depleted in the core, while Co exhibits minor enrichment on the edges and homogeneous distribution in the center.

The Py-1_{BIF} and Py-2_{BIF} (Figura 37a) are investigated in sample 1-01-A1 (Figura 32a), where three distribution patterns (Fig. 17b-k) are described: (1) Ag (9.58 x 10^{-9}-61.50) and Au (1.12 x 10^{-8}-39.77) nuggets are dispersed in a few areas and filling pores, (2) Fe (1.92-64.4), Sb (9.67 x 10^{-9}-2.26), Ni (7.92 x 10^{-9}-1.89) and Co (8.68 x 10^{-9}-0.63) homogenously distributed in the entire mapped surface, (3) S (3.83 x 10-4-64.75117) and As (1.16 x 10^{-8}-50.01) that, define a chemical zoning. Sulfur has low concentrations in the core (Py-1_{BIF}) and is enriched in the edges where Py-2_{BIF} predominates,

while As is the opposite. Manganese (6.68 x 10^{-9}-2.83) is concentrated outside the pyrite crystal, and is present in the BIF matrix.

Sample 5-06-01 (Figura 31b) is marked by the presence of Py-3_{BIF} (Figura 37a). The study (Figura 37b-j) reveals a chemical zoning controlled by Co-Ni. Nickel (7.92-2.55) defines three well delimited zones: the first one is shapeless and has corroded edges in the core of the area; the second one is well defined, surrounding the first one; and the third is concentric, surrounding the second zone. Cobalt (8.68 x 10^{-9}-1.12) has a homogeneous distribution coinciding with the nickel zoning areas one and three; and displays a more significant concentration, giving way to a zoning that coincides with the first and second Ni enrichment zones. Gold (1.12 x 10^{-8}-21.44) and silver (9.58 x 10-9-73.67) nuggets fill pores, with Au distributed between the second and third Ni zoning; it also appears in minor concentrations of Ag dispersed in concentric shapes, coinciding with the third Ni zoning.

Other elements are: S (48.99-58.67) that is regularly distributed, but with a smaller concentration in the core of the analyzed area; small amounts of As (1.16x10^{-8}-39.39), but with regions of higher concentration coinciding with places where the level of sulfur is lower; Fe (41.69-50.14) and Sb that are homogeneously distributed (lower values of Fe coincide with enriched As regions); and Mn (6.68x10^{-9}-8.37), in very low concentration, but exhibiting minor concentric distribution.

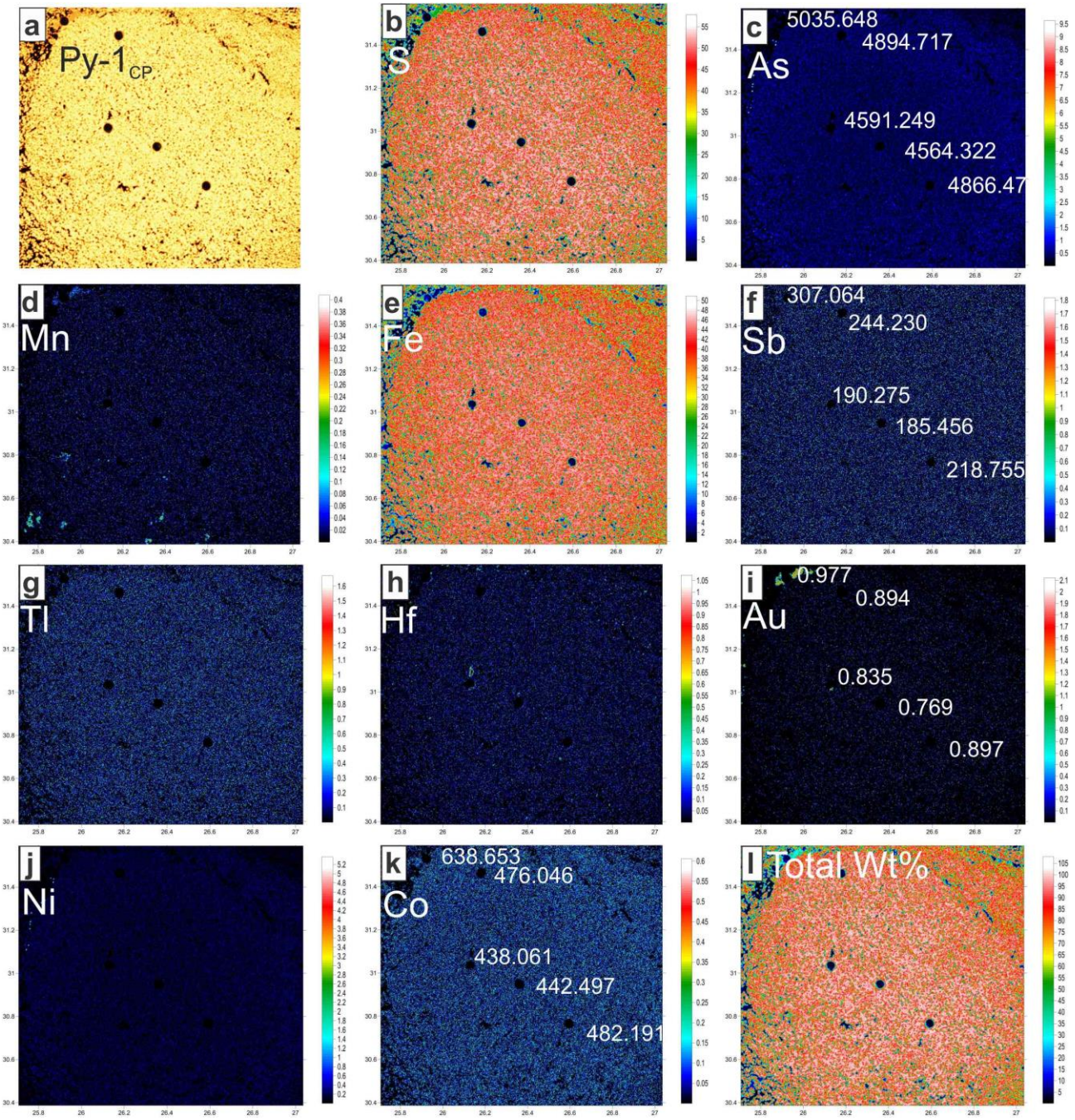

Figura 34: Photomicrograph of Py-1_{CP} and elemental mapping with EPMA of selected elements of sample 13-22-A4, with scales in wt%. All elements are homogeneously distributed. In the case of As, Sb, Au, Ni, Co, the laser data are given in ppm shown on images; values increase from center to border.

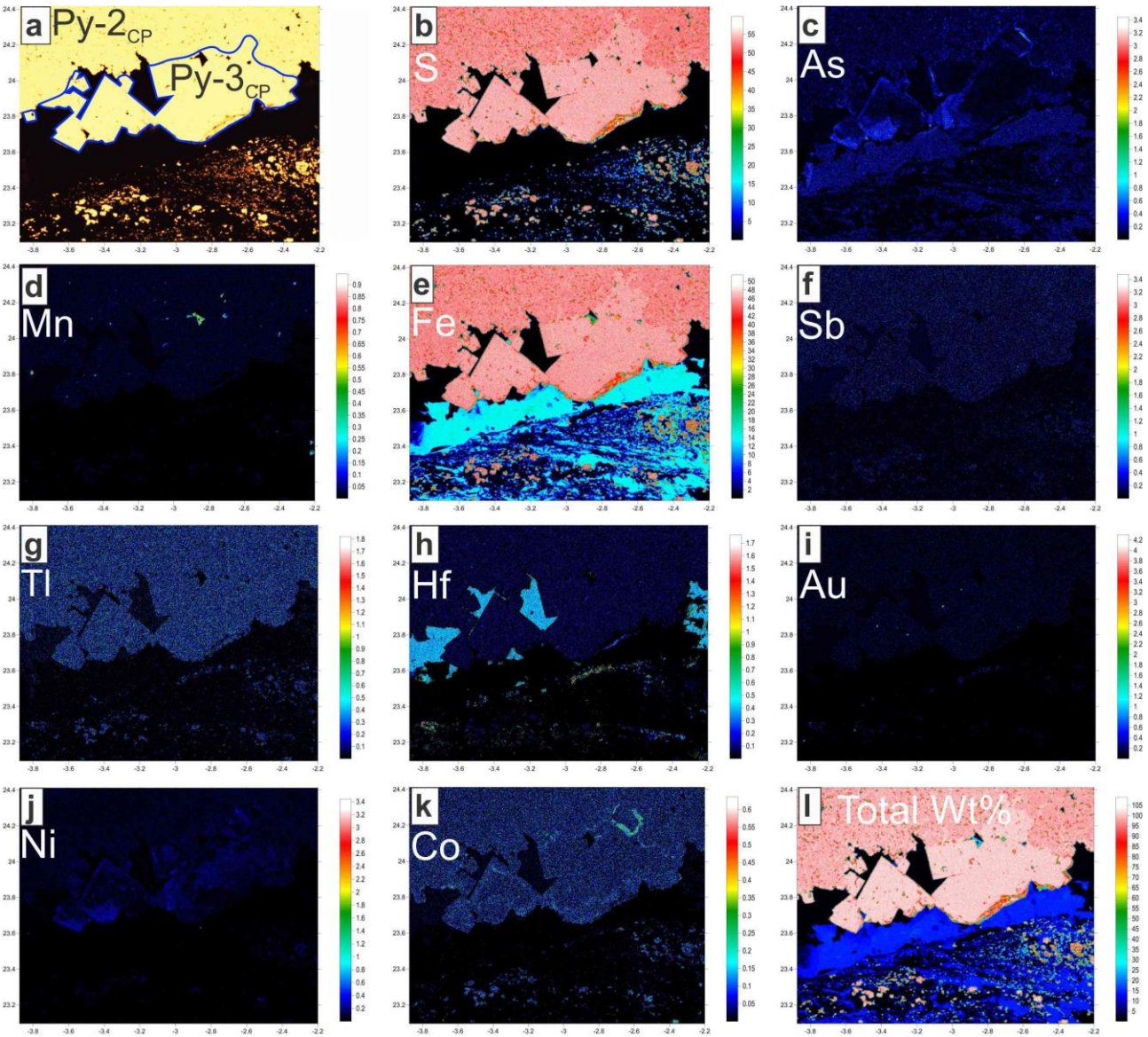

Figura 35: Photomicrograph of Py-2_{CP} in contact with Py-3_{CP}, and elemental mapping with EPMA of selected elements of sample 13-23-A4, with scales in wt%. Elements are homogeneously distributed in Py-2_{CP}. However, Py-3_{CP} displays As-Ni zoning, with remaining elements homogeneously distributed.

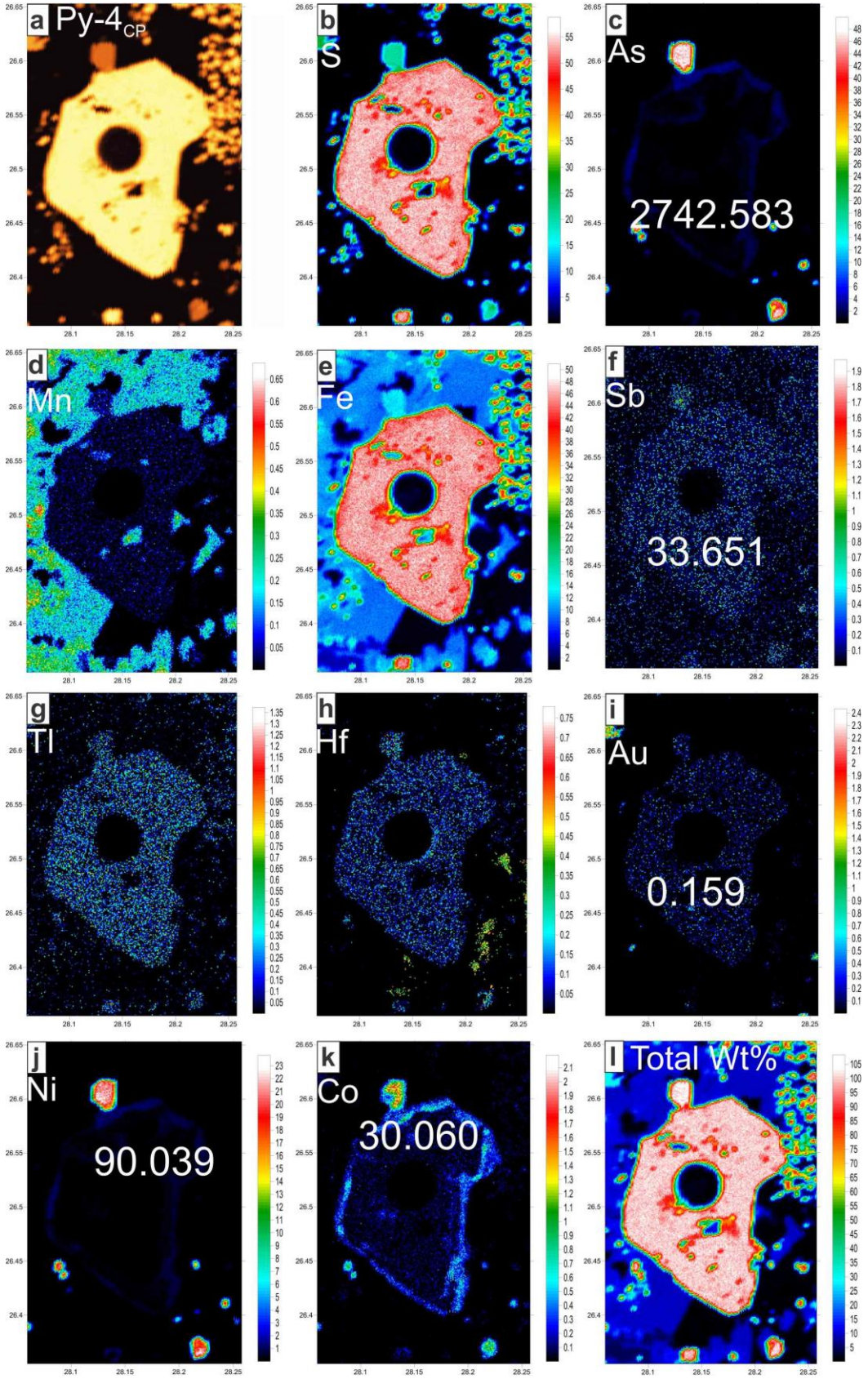

Figura 36: Photomicrograph of Py-4_{CP} and elemental mapping with EPMA of selected elements of sample 14-23-A8, with scales in wt%. There is As-Ni-Co zoning, with remaining elements homogeneously distributed.

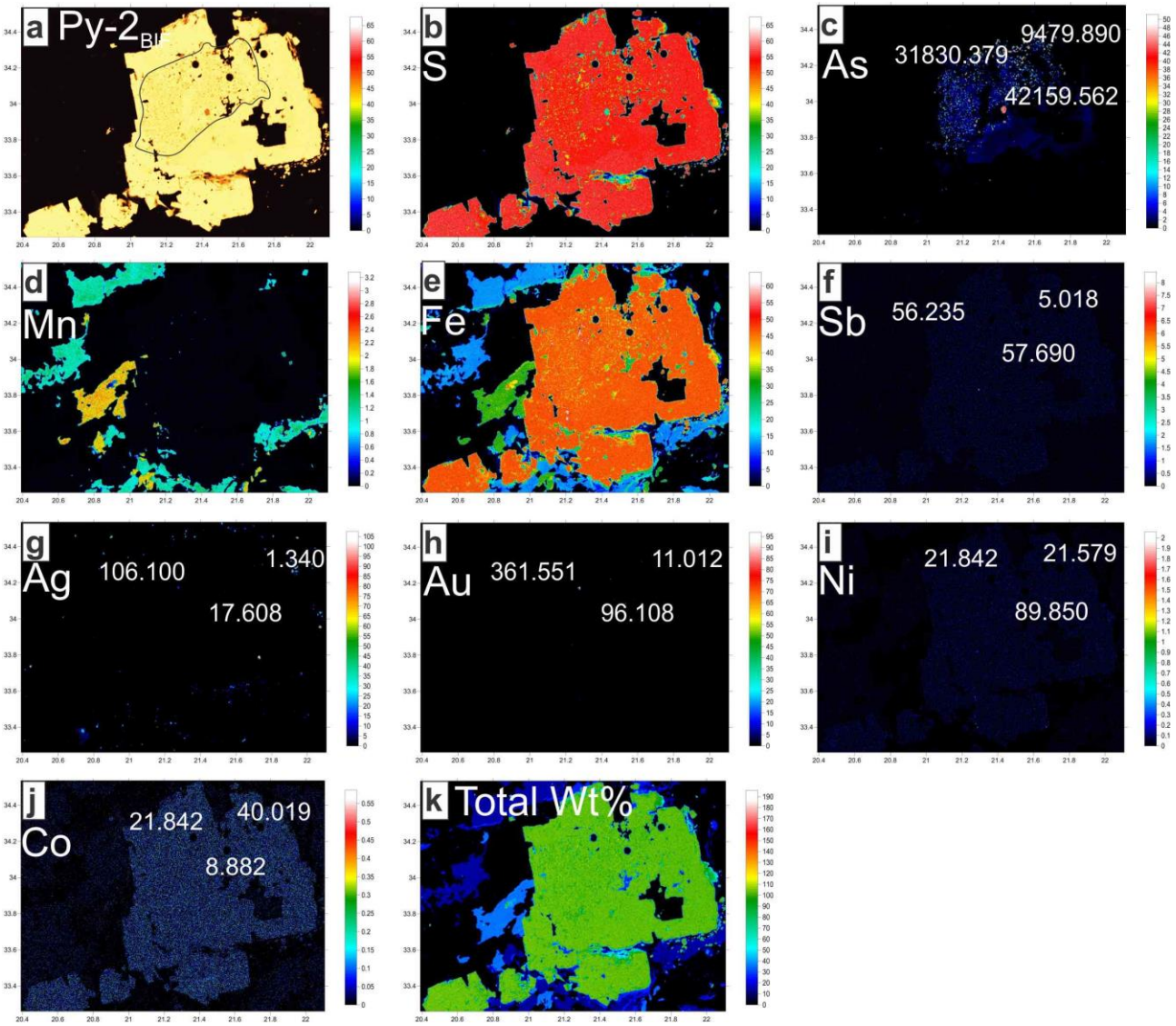

Figura 37: Photomicrograph of Py-2_{BIF} and elemental mapping with EPMA of selected elements of sample 1-01-A, with scales in wt%. There is S-As-Fe zoning in the center of the analyzed grain, which probably corresponds to Py-1_{BIF}. Remaining elements homogeneously distributed. Some spot analyses are indicated in ppm, with values increasing from Py-1_{BIF} to Py-2_{BIF}.

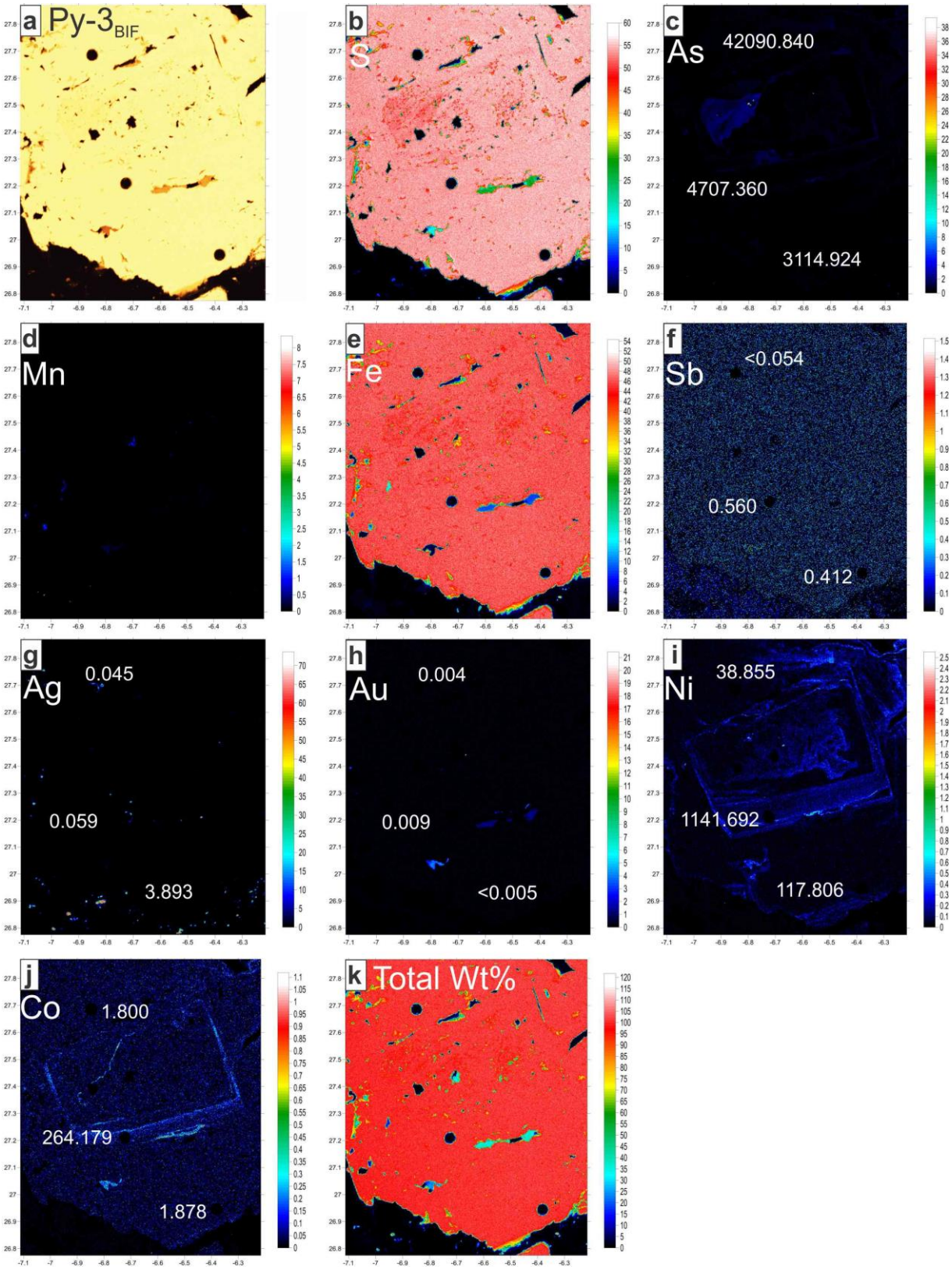

Figura 38: Photomicrograph of Py-3_{BIF} and elemental mapping with EPMA of selected elements of sample 5-06-A1, with scales in wt%. Center of grain is typified by S-As-Fe zoning, surrounded by a Ni-Co ring zone.

4.10 LA-ICP-MS trace element geochemistry of pyrites and arsenopyrite

The trace element composition in the different types of pyrites was determined via 105 spot analyses using the LA-ICP-MS technique, where the typical ICP-MS output counts are presented in Figura 39 presents the results in ppm, whereas has the descriptive statistics relative to each pyrite type. Figura 40 shows the box plot of selected elements separated by groups of ferroalloys, minor metals, base metals, precious metals, semimetals and fissionable metals.

The data of the selected and analyzed trace elements are presented based on the average concentration from the highest to the lowest values, for each sulfide type.

In each sulfide type, there are always two distinctive LA-ICP-MS traces (Figura 39). One appears as a fairly flat pattern, similar to the behavior of Fe, which suggests that the element is contained in the structure of the sulfide in question. These are referred to as lattice-bond elements. Another type of LA-ICP-MS trace appears as spikes for particular elements, indicating the presence of nanoinclusions of a mineral containing that element.

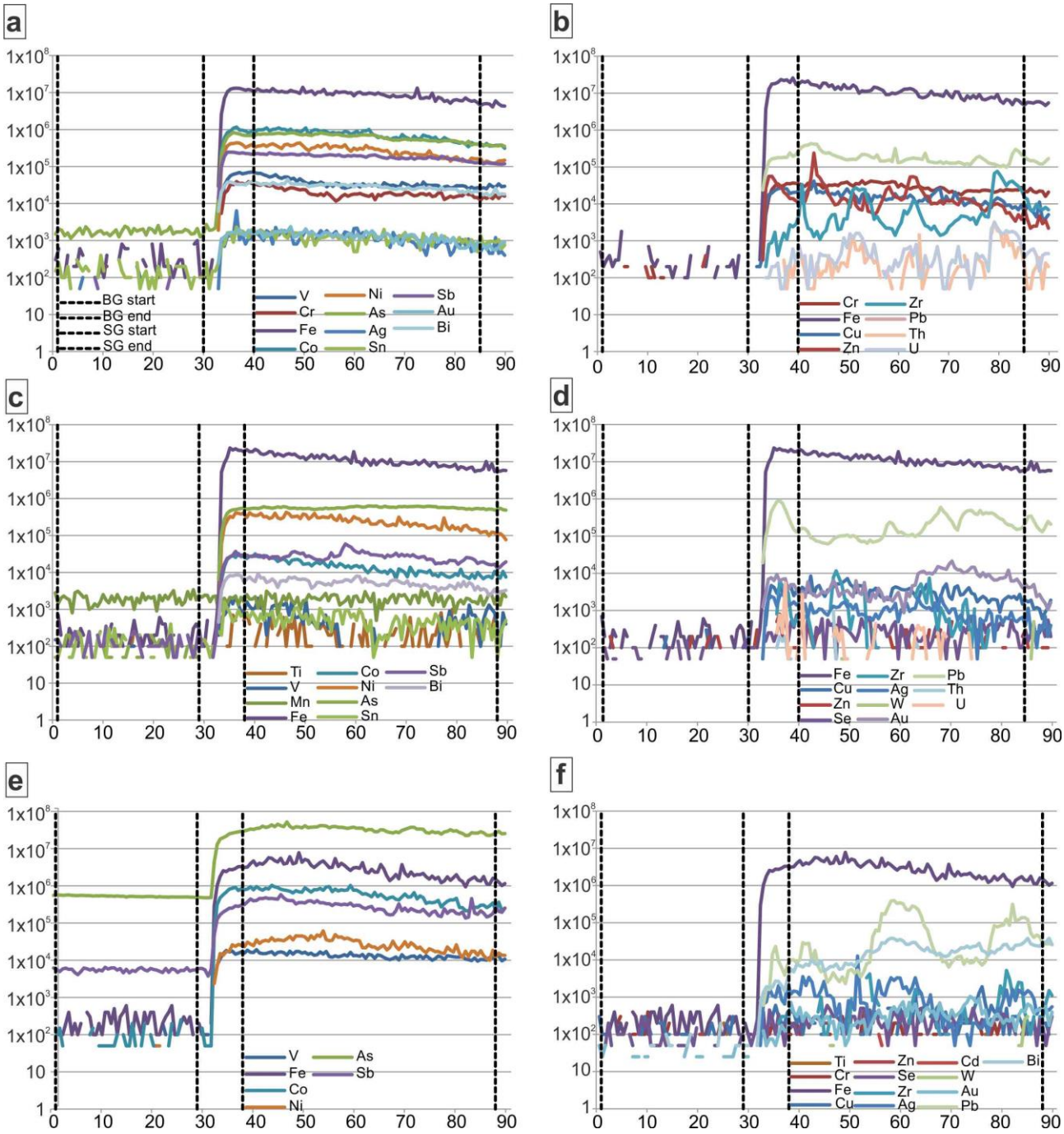

Figura 39: Typical ICP-MS counts output for pyrite analyses by laser ablation in carbonaceous pelite (a), (b) and BIF (c), (d). Titanium, V, Cr, Fe, Co, Ni, Cu and Sb are lattice-bond elements (a), (c) whereas Zn, Zr, Pb and Bi probably represent mineral nano-inclusions (b), with Cu mineral nano-inclusions only in the case of BIF (d).

Tabela 9: Selected LA-ICPMS analyses of different types of pyrites from carbonaceous pelite and BIF.

Pyrites	Ti^{49}	V^{51}	Cr^{53}	Mn^{55}	Co^{59}	Ni^{60}	Cu^{65}	Zn^{66}	As^{75}	Se^{77}	Zr^{90}	Mo^{95}	Ag^{107}	Cd^{111}	Sn^{118}	Sb^{121}	Te^{125}	W^{182}	Au^{197}	Pb^{206}	Bi^{209}	Th^{232}	U^{238}
$Py\text{-}1_{CP}$	757.88	96.57	634.79	37.52	561.47	1029.02	61.88	1061.89	2744.45	2.93	19.31	0.98	1.20	3.61	3.74	343.10	4.93	9.99	1.19	235.25	11.93	1.01	0.28
	640.74	126.84	868.12	21.88	480.19	860.77	50.71	153.67	2317.35	3.23	10.93	15.44	1.10	0.49	4.33	237.04	3.95	9.21	0.87	143.95	9.80	0.12	0.14
	3224.24	122.03	862.42	33.75	492.95	844.32	75.88	172.43	2420.45	3.09	56.33	1.80	0.96	0.70	5.45	269.11	3.83	36.83	0.67	163.42	9.40	0.66	0.72
	1830.24	63.81	620.80	22.70	638.65	1361.11	117.95	9408.57	5035.65	8.34	18.01	1.23	1.41	36.51	3.32	307.06	3.76	24.05	0.98	211.54	11.27	0.27	0.33
	418.20	31.87	250.75	30.81	482.19	1298.48	60.02	105.58	4866.48	10.66	13.75	0.54	1.50	0.30	1.45	218.75	2.89	5.96	0.90	285.45	8.36	0.16	0.26
	448.69	43.62	381.78	17.44	476.05	1359.93	84.55	104.61	4894.72	8.45	3.48	0.43	1.43	0.41	1.67	244.23	3.12	4.55	0.89	207.89	9.60	0.06	0.10
	240.12	31.03	239.75	12.89	438.06	1223.07	57.71	85.29	4561.25	9.25	6.39	0.30	1.45	0.36	1.28	190.28	2.44	3.47	0.83	184.86	8.20	0.15	0.19
	159.86	30.68	255.48	12.15	442.50	1205.52	52.43	90.25	4564.32	9.45	6.52	0.21	1.39	0.33	1.17	185.46	2.44	1.63	0.77	230.39	7.84	0.07	0.13
	135.33	66.05	429.04	323.68	529.85	958.48	66.47	182.07	2320.11	5.84	2.31	0.62	1.43	0.61	2.64	271.78	5.07	1.38	1.31	237.15	11.84	0.03	0.10
	95.26	37.10	192.20	49.03	849.94	1543.92	50.15	1859.66	4197.48	4.56	0.87	0.44	2.05	5.73	1.71	331.73	6.06	0.90	2.01	504.38	16.00	0.01	0.03
$Py\text{-}2_{CP}$	196.47	27.26	169.44	7.92	1044.88	1464.85	72.32	27.82	5124.71	18.95	65.68	0.32	1.59	0.12	0.98	199.35	2.65	2.45	0.96	255.41	8.55	0.85	0.79
	30.96	23.07	5.84	1.89	246.14	546.24	62.50	5.63	1265.82	7.08	3.13	0.48	1.28	0.13	0.34	218.08	1.16	0.24	1.55	249.31	3.40	0.21	0.03
	59.00	34.96	12.43	12.13	195.18	479.31	76.58	23.37	1098.02	7.89	1.59	1.20	1.45	0.11	0.46	177.11	1.27	0.42	1.45	415.83	3.57	0.12	0.03
	163.90	50.65	19.88	29.86	199.14	450.11	74.92	63.30	1253.03	7.16	1.61	0.27	1.09	0.07	0.50	131.38	0.96	0.68	0.90	280.02	2.48	0.09	0.14
	21.15	3.05	8.10	12.85	76.00	496.41	151.79	6.58	853.36	4.54	1.38	0.40	1.96	0.20	0.27	337.05	1.05	0.10	1.55	253.13	3.44	0.04	0.01
	10.81	1.58	6.22	17.16	18.59	479.21	110.04	21.17	946.25	5.36	0.80	0.38	1.77	0.17	0.20	328.50	1.03	0.09	1.44	265.89	3.24	0.04	0.02
	9.20	2.36	7.12	19.85	11.18	386.31	98.82	16.20	809.75	4.70	0.44	0.23	1.53	0.19	0.23	267.51	0.72	0.09	1.17	185.71	2.61	0.02	0.01
	10.74	1.32	8.72	25.73	25.33	463.22	116.37	11.92	936.41	4.95	0.39	0.33	1.92	0.15	0.25	320.07	0.92	0.07	1.61	237.67	3.27	0.04	0.01
	9.51	2.29	10.72	15.65	44.07	387.68	160.61	15.35	905.38	4.94	0.95	0.20	1.70	0.21	0.18	232.04	0.84	0.10	1.21	163.62	2.41	0.03	0.01
	9.80	2.29	17.04	14.78	26.35	385.70	95.18	17.15	921.11	5.01	0.98	0.54	1.60	0.17	0.25	241.53	0.83	0.14	1.16	203.22	2.46	0.04	0.02
	7.82	1.87	10.16	16.90	29.27	385.05	89.27	9.78	854.69	5.05	0.19	0.19	1.61	0.14	0.23	230.17	0.63	0.06	1.08	130.81	2.15	0.05	0.01
	8.75	1.85	8.06	21.88	39.54	356.19	93.28	12.43	789.82	4.17	0.10	0.22	1.76	0.15	0.23	241.42	0.71	0.08	1.00	158.30	2.46	0.01	0.00
$Py\text{-}3_{CP}$	29.97	1.29	10.64	36.87	56.32	235.66	17.57	6.08	1246.31	19.79	5.79	0.12	0.62	0.06	0.23	79.48	0.86	0.38	0.32	71.29	2.72	0.16	0.13
	121.80	4.43	36.56	1.51	30.06	90.04	71.51	3.85	2742.58	17.27	12.69	0.08	0.20	0.03	0.37	33.65	0.35	1.94	0.16	32.95	0.92	0.38	0.21
	20.09	2.71	18.67	6.83	1096.28	2774.26	130.27	2269.80	4916.52	5.91	0.78	0.87	4.00	8.01	0.78	1041.98	17.83	0.28	5.34	686.15	43.60	0.01	0.01
	2.87	bdl	bdl	bdl	0.10	140.86	bdl	0.55	662.75	10.60	bdl	bdl	bdl	bdl	0.10	bdl	bdl	0.01	bdl	0.06	bdl	bdl	bdl
	2.25	bdl	bdl	bdl	0.39	386.84	bdl	0.43	243.20	14.19	bdl	bdl	bdl	0.01	0.13	bdl	0.03	0.00	bdl	0.15	0.00	0.00	bdl
	3.11	bdl	bdl	bdl	0.20	422.38	0.14	0.46	608.07	10.94	bdl	0.01	0.04	bdl	0.12	0.23	0.03	bdl	bdl	0.40	0.01	0.01	bdl
	2.46	bdl	bdl	bdl	0.02	114.67	2.22	0.36	590.37	13.90	bdl	bdl	0.03	0.00	0.14	2.16	0.59	0.00	0.04	10.25	0.12	0.00	bdl
$Py\text{-}4_{CP}$	8.60	0.70	4.98	6.19	929.90	3134.98	141.60	2200.82	5195.80	9.27	0.57	0.81	4.47	7.45	0.54	1166.83	23.15	0.16	8.41	767.58	52.90	0.03	0.01
	17.81	5.41	32.52	2.98	1219.82	3172.49	137.96	22662.19	6492.10	7.01	0.69	0.42	4.90	67.15	1.19	919.39	18.63	0.26	7.54	996.26	43.11	0.01	0.02
	122.11	37.74	313.41	18.82	811.41	2111.94	144.20	4054.39	3977.93	21.10	4.50	3.15	3.08	12.61	2.11	769.97	12.60	1.46	4.49	592.22	30.91	0.04	0.05
	20.84	2.07	13.70	6.98	1004.53	3043.45	172.76	13054.15	5414.02	16.48	0.26	0.91	4.82	41.48	1.00	1169.38	22.98	0.18	7.73	1141.68	50.53	0.02	0.01
	18.59	2.12	14.10	54.54	656.38	1742.37	9.06	7.40	7119.54	8.41	7.26	0.13	0.19	bdl	0.26	47.67	0.67	0.33	0.22	61.64	1.91	0.76	0.15
	155.54	6.96	42.83	93.39	617.50	1047.78	6.00	3.82	4935.34	10.92	0.05	0.00	0.04	0.01	0.58	21.93	0.12	2.00	0.09	24.11	0.69	0.00	bdl
	16.76	1.19	2.58	9.54	106.22	557.55	157.66	4.72	1073.62	8.96	0.16	0.90	2.14	0.23	0.20	472.44	1.33	0.15	1.75	388.05	5.18	0.01	0.00
	78.08	37.47	13.62	4.95	122.38	612.89	131.71	3.52	1096.79	4.11	2.82	0.74	1.69	0.21	0.48	503.61	1.46	0.53	1.69	437.90	6.00	0.05	0.04
	24.44	6.37	4.62	5.90	113.71	492.26	110.67	4.54	1078.70	4.22	1.36	0.70	1.55	0.18	0.25	408.19	1.17	0.36	1.30	287.64	4.42	0.06	0.02

*bdl: below detection limit

Tabela 9: Selected LA-ICPMS analyses of different types of pyrites from carbonaceous pelite and BIF.

Pyrite	Ti^{49}	V^{51}	Cr^{53}	Mn^{55}	Co^{59}	Ni^{60}	Cu^{65}	Zn^{66}	As^{75}	Se^{77}	Zr^{90}	Mo^{95}	Ag^{107}	Cd^{111}	Sn^{118}	Sb^{121}	Te^{125}	W^{182}	Au^{197}	Pb^{206}	Bi^{209}	Th^{232}	U^{238}
$Py\text{-}1_{BIF}$	2.37	0.87	1.66	83.15	13.34	32.29	8.75	1.18	4843.92	11.60	0.91	0.03	1.24	bdl	0.41	36.75	0.32	0.02	11.06	88.45	1.94	0.00	0.04
	3.06	0.43	2.26	4.37	14.62	31.42	12.57	0.33	5046.99	12.11	1.09	0.01	1.41	bdl	0.52	38.56	0.22	0.03	9.94	117.48	2.22	0.01	0.03
	2.03	bdl	bdl	bdl	1.05	30.64	396.17	999.50	3893.68	10.58	0.01	0.03	15.71	4.54	233.13	40.89	0.13	0.03	21.09	143.35	1.33	0.00	0.00
	2.62	bdl	bdl	295.53	31.51	103.11	10.04	1.26	14651.70	10.56	2.25	0.25	2.26	0.02	0.14	7.67	bdl	0.01	3.74	24.42	0.19	bdl	0.03
$Py\text{-}2_{BIF}$	11.80	0.43	0.64	86.65	21.84	49.93	132.50	82.98	31830.38	13.54	7.53	0.09	106.10	0.41	29.30	56.23	0.77	0.34	361.55	237.20	1.76	0.05	0.12
	5.43	0.04	bdl	1.44	8.88	89.85	51.92	12.38	42159.56	15.84	5.34	0.01	17.61	0.06	0.81	57.69	0.61	0.13	96.11	344.94	2.14	0.02	0.03
	2.07	0.02	bdl	bdl	40.02	21.58	9.14	0.48	9479.90	10.96	0.28	bdl	1.34	bdl	0.14	5.02	0.02	bdl	11.01	11.18	0.08	0.00	0.00
	2.03	bdl	bdl	bdl	0.13	17.47	bdl	0.32	555.24	13.62	bdl	bdl	0.46	bdl	0.09	bdl	0.01	bdl	bdl	0.02	bdl	0.00	bdl
	6.07	0.24	0.63	32.61	6.05	43.90	21.13	0.71	9405.50	13.99	0.28	0.03	1.88	0.01	0.23	17.21	0.15	0.14	6.09	86.19	0.58	0.00	0.01
	2.20	bdl	bdl	bdl	2.81	39.98	2.23	0.35	4246.58	13.46	bdl	bdl	0.59	0.02	0.11	7.94	bdl	0.01	1.31	30.39	0.26	bdl	bdl
	3.70	bdl	bdl	bdl	10.04	28.78	28.27	0.55	22845.72	8.98	0.10	bdl	0.73	0.00	0.13	5.35	bdl	0.04	86.87	12.76	0.18	0.00	0.00
	2.05	0.03	0.32	1.75	3.66	63.18	324.60	183.83	8396.31	9.96	0.22	0.01	9.05	0.82	55.78	41.84	0.23	0.03	35.36	468.42	2.15	0.00	0.00
	60.27	0.77	3.04	12.30	10.50	27.96	14.79	0.81	9816.43	15.32	8.69	0.03	0.91	0.01	0.35	6.81	0.25	3.00	8.45	21.46	0.21	0.09	0.17
	2.71	bdl	bdl	bdl	0.29	7.69	21.12	0.28	5526.55	35.27	bdl	bdl	0.31	bdl	0.09	3.66	3.57	bdl	1.62	7.06	0.96	bdl	0.00
	1.78	bdl	bdl	bdl	25.63	121.61	0.51	0.35	2880.73	4.87	0.01	0.01	0.33	bdl	0.08	0.65	bdl	0.00	0.03	2.42	2.92	bdl	bdl
	2.10	bdl	bdl	bdl	0.23	3.84	bdl	0.37	1631.61	4.49	0.04	bdl	0.09	bdl	0.09	bdl	0.04	bdl	0.00	0.07	0.02	bdl	0.00
	10.66	0.89	2.27	27.43	53.51	458.30	1250.79	10406.19	132.00	19.32	0.38	0.10	30.90	33.21	0.70	113.98	4.22	0.18	0.56	5044.88	80.76	0.01	0.01
$Py\text{-}3_{BIF}$	1.48	0.06	bdl	1.05	1.80	117.81	bdl	bdl	3114.92	4.09	0.00	bdl	3.89	bdl	0.11	0.42	bdl	bdl	bdl	1.87	0.08	bdl	bdl
	2.25	bdl	0.29	bdl	264.18	1141.69	bdl	bdl	4707.36	12.09	bdl	0.00	0.06	bdl	0.10	0.56	bdl	bdl	0.01	1.32	0.02	bdl	bdl
	1.91	bdl	bdl	bdl	1.88	38.86	0.12	bdl	4290.84	12.94	bdl	bdl	0.04	bdl	0.10	bdl	bdl	bdl	0.00	bdl	0.03	0.00	0.00
	2.30	bdl	bdl	0.98	322.17	767.02	16.57	1.12	8452.68	16.04	0.01	0.01	3.05	0.01	0.15	52.08	0.71	bdl	4.47	281.74	6.23	bdl	bdl
	2.32	bdl	0.29	4.25	69.63	828.39	4.65	28.03	5711.49	11.05	bdl	0.29	2.46	0.10	0.13	30.32	1.27	0.01	0.33	67.64	6.20	0.00	bdl
	1.68	bdl	bdl	bdl	80.82	1473.96	15.74	bdl	630.01	21.41	bdl	bdl	0.58	0.02	0.11	3.43	0.43	0.00	0.22	2.82	0.79	bdl	bdl
	1.71	bdl	bdl	bdl	12.03	257.91	bdl	0.39	4190.48	7.25	bdl	0.00	0.62	bdl	0.10	bdl	bdl	0.00	bdl	0.06	0.00	bdl	bdl
	1.74	bdl	bdl	bdl	0.49	39.54	0.12	0.26	1644.18	5.33	0.02	0.00	bdl	bdl	0.09	bdl	bdl	bdl	bdl	0.10	0.01	0.00	bdl
	2.21	bdl	bdl	bdl	73.24	903.17	0.62	0.48	6048.79	6.45	0.26	bdl	0.75	bdl	0.09	8.06	0.41	bdl	0.07	8.25	1.67	0.01	0.00
	2.10	bdl	bdl	bdl	164.06	1092.09	0.20	0.33	9012.52	8.49	0.15	0.01	0.03	bdl	0.09	bdl	0.03	bdl	0.00	0.04	0.03	0.00	0.00
	15.34	0.46	1.68	8.11	102.15	106.47	80.88	1149.49	4592.88	12.35	1.11	bdl	4.55	5.46	0.43	52.90	1.02	0.17	2.87	484.64	11.62	0.03	0.05
	27.84	0.22	1.65	4.52	39.57	2089.68	2.29	bdl	125.39	19.57	0.80	0.01	1.13	0.01	0.28	17.79	0.98	2.17	0.04	71.68	4.07	0.03	0.02
$Apy\text{-}1_{BIF}$	1.89	3.55	2.78	7.84	1.71	83.91	1.49	18.68	-	70.86	0.02	0.33	0.75	bdl	0.10	483.79	34.09	bdl	0.78	59.86	0.67	0.00	bdl
	bdl	bdl	bdl	4.11	12.52	184.12	0.68	bdl	-	56.23	0.17	0.11	0.27	bdl	bdl	388.95	29.61	bdl	0.56	3.09	0.15	bdl	bdl
	bdl	bdl	bdl	1.07	7.80	209.29	1.47	bdl	-	58.81	3.29	0.27	0.60	bdl	0.15	249.15	53.48	bdl	0.75	13.92	0.53	0.02	0.07
	bdl	bdl	bdl	bdl	7.52	209.70	0.52	bdl	-	28.82	0.03	bdl	0.20	bdl	bdl	252.61	6.12	bdl	0.18	2.35	0.14	0.00	bdl
	bdl	bdl	bdl	2.72	12204.70	6017.22	bdl	738.01	-	25.00	bdl	0.14	5.37	2.45	0.09	391.51	15.18	bdl	bdl	10.62	0.20	bdl	bdl
	bdl	bdl	bdl	bdl	999.26	9635.79	bdl	bdl	-	10.64	0.01	bdl	1.41	bdl	bdl	219.67	4.19	bdl	0.27	245.25	1.94	bdl	bdl
	5.74	3.69	bdl	bdl	2118.10	3409.28	0.93	bdl	-	41.84	0.09	0.10	1.19	bdl	0.38	230.92	42.82	0.05	0.16	276.94	3.04	0.01	0.01

*bdl: below detection limit

Tabela 10: Descriptive statistics for LA-ICPMS analyses of selected elements from the Lamego deposit.

Mineral type	Elements	N.º Analysis	Group size	Sucess %	Lower far outlier	Lower outlier	Min regular (whisker)	Q1 (bottom of box)	Median (line)	Q3 (top of box)	Max regular (whisker)	Upper outlier
Py-1CP	Au	11	10	90.91	-	-	0.67	0.82	0.90	1.22	2.01	-
	Ag	11	10	90.91	-	-	0.96	1.18	1.42	1.46	1.50	2.03
	Cu	11	10	90.91	-	-	50.15	52.00	60.94	77.96	117.95	-
	Pb	11	10	90.91	-	-	143.95	179.25	220.77	248.40	285.45	405.22
	Zn	11	10	90.91	-	-	85.29	100.82	162.78	1221.57	9408.57	-
	Sn	11	10	90.91	-	-	1.17	1.41	2.12	3.88	5.45	-
	Mn	11	10	90.91	-	-	12.15	16.17	26.45	40.11	49.03	156.68
	Ni	11	10	90.91	-	-	844.32	933.06	1214.26	1360.23	1543.92	-
	Cr	11	10	90.91	-	-	192.20	247.96	404.72	685.34	868.12	-
	Mo	11	10	90.91	-	-	0.21	0.40	0.58	1.35	1.80	8.57
	W	11	10	90.91	-	-	0.90	1.57	5.21	12.45	36.83	-
	V	11	10	90.91	-	-	30.68	31.66	52.76	102.38	126.84	-
	Co	11	10	90.91	-	-	438.06	467.43	487.54	579.85	638.65	801.14
	Cd	11	10	90.91	-	-	0.30	0.35	0.54	4.05	36.51	-
	Ti	11	10	90.91	-	-	95.26	153.34	433.18	944.77	3224.24	-
	Zr	11	10	90.91	-	-	0.87	3.14	8.44	18.33	56.33	-
	Bi	11	10	90.91	-	-	7.84	8.32	9.70	11.86	16.00	-
	As	11	10	90.91	-	-	2317.35	2394.97	4375.59	4873.52	5035.65	-
	Sb	11	10	90.91	-	-	185.46	211.26	256.37	313.05	343.10	-
	Te	11	10	90.91	-	-	2.44	2.77	3.79	4.96	6.06	-
	Se	11	10	90.91	-	-	2.93	3.20	6.98	9.30	10.66	-
	Th	11	10	90.91	-	-	0.01	0.05	0.13	0.34	1.01	-
	U	11	10	90.91	-	-	0.03	0.10	0.16	0.29	0.72	-
Py-2CP	Au	12	12	100.00		-	0.90	1.02	1.19	1.52	1.61	-
	Ag	12	12	100.00	-	1.12	1.28	1.47	1.60	1.77	1.96	-
	Cu	12	12	100.00	-	-	62.50	75.33	94.23	114.76	160.61	-
	Pb	12	12	100.00	-	-	130.81	168.88	243.42	263.23	415.83	-
	Zn	12	12	100.00	-	-	5.63	10.28	15.77	22.80	63.30	-
	Sn	12	12	100.00	-	-	0.18	0.23	0.25	0.42	0.98	-
	Mn	12	12	100.00	2.35	-	7.92	12.30	16.26	21.35	29.86	-
	Ni	12	12	100.00	-	-	356.19	385.86	456.62	492.08	546.24	-
	Cr	12	12	100.00	-	-	5.84	7.35	9.42	15.75	19.88	-
	Mo	12	12	100.00	-	-	0.19	0.22	0.33	0.46	1.20	-
	W	12	12	100.00	-	-	0.06	0.08	0.10	0.36	2.45	-
	V	12	12	100.00	-	-	1.32	1.85	2.32	26.14	50.65	-
	Co	12	12	100.00	-	-	11.18	25.58	41.74	198.15	1044.88	-
	Cd	12	12	100.00	-	-	0.07	0.13	0.15	0.19	0.21	-
	Ti	12	12	100.00	-	-	7.82	9.27	10.78	50.22	196.47	-
	Zr	12	12	100.00	-	-	0.10	0.40	0.97	1.60	3.13	12.88
	Bi	12	12	100.00	-	-	2.15	2.46	2.91	3.43	3.57	5.65
	As	12	12	100.00	-	-	789.82	853.69	928.72	1212.34	1265.82	-
	Sb	12	12	100.00	-	-	131.38	203.88	236.68	306.03	337.05	-
	Te	12	12	100.00	-	-	0.63	0.75	0.94	1.14	1.27	2.12
	Se	12	12	100.00	-	-	4.17	4.76	5.03	7.14	7.89	13.12
	Th	12	12	100.00	-	-	0.01	0.03	0.04	0.11	0.21	0.65
	U	12	12	100.00	-	-	0.00	0.01	0.02	0.03	0.14	0.25

Tabela 10: Descriptive statistics for LA-ICPMS analyses of selected elements from the Lamego deposit.

Mineral type	Elements	N.º Analysis	Group size	Sucess %	Lower far outlier	Lower outlier	Min regular (whisker)	Q1 (bottom of box)	Median (line)	Q3 (top of box)	Max regular (whisker)	Upper outlier
Py-3CP	Au	7	4	57.14	-	-	0.04	0.05	0.22	2.64	5.34	-
	Ag	7	5	71.43	-	-	0.03	0.03	0.20	1.57	4.00	-
	Cu	7	5	71.43	-	-	0.14	0.55	17.57	96.52	130.27	-
	Pb	7	7	100.00	-	-	0.06	0.15	10.25	71.29	686.15	-
	Zn	7	7	100.00	-	-	0.36	0.43	0.55	6.08	6.08	322.68
	Sn	7	7	100.00	-	-	0.10	0.12	0.14	0.37	0.78	-
	Mn	7	3	42.86	-	-	1.51	1.51	6.83	36.87	36.87	-
	Ni	7	7	100.00	-	-	90.04	114.67	235.66	422.38	2774.26	-
	Cr	7	3	42.86	-	-	10.64	10.64	18.67	36.56	36.56	-
	Mo	7	4	57.14	-	-	0.01	0.01	0.10	0.53	0.87	-
	W	7	6	85.71	-	-	0.00	0.00	0.05	0.57	1.94	-
	V	7	3	42.86	-	-	1.29	1.29	2.71	4.43	4.43	-
	Co	7	7	100.00	-	-	0.02	0.10	0.39	56.32	1096.28	-
	Cd	7	5	71.43	-	-	0.00	0.01	0.03	0.72	8.01	-
	Ti	7	7	100.00	-	-	2.25	2.46	3.11	29.97	121.80	-
	Zr	7	3	42.86	-	-	0.78	0.78	5.79	12.69	12.69	-
	Bi	7	6	85.71	-	-	0.00	0.01	0.34	5.44	43.60	-
	As	7	7	100.00	-	-	243.20	590.37	662.75	2742.58	4916.52	-
	Sb	7	5	71.43	-	-	0.23	0.70	33.65	287.79	1041.98	-
	Te	7	6	85.71	-	-	0.03	0.03	0.46	1.84	17.83	-
	Se	7	7	100.00	-	-	5.91	10.60	13.90	17.27	19.79	-
	Th	7	6	85.71	-	-	0.00	0.00	0.01	0.19	0.38	-
	U	7	3	42.86	-	-	0.01	0.01	0.13	0.21	0.21	-
Py-4CP	Au	9	9	100.00	-	-	0.09	0.54	1.75	7.64	8.41	-
	Ag	9	9	100.00	-	-	0.04	0.54	2.14	4.64	4.90	-
	Cu	9	9	100.00	-	-	6.00	31.66	137.96	150.78	172.76	-
	Pb	9	9	100.00	-	-	24.11	133.16	437.90	874.48	1141.68	-
	Zn	9	9	100.00	-	-	3.52	4.17	7.40	7275.07	22662.19	-
	Sn	9	9	100.00	-	-	0.20	0.25	0.54	1.09	2.11	-
	Mn	9	9	100.00	-	-	2.98	5.41	6.98	32.04	93.39	-
	Ni	9	9	100.00	-	-	492.26	584.57	1742.37	3088.87	3172.49	-
	Cr	9	9	100.00	-	-	2.58	4.80	13.70	37.32	313.41	-
	Mo	9	9	100.00	0.00	-	0.13	0.23	0.74	0.90	3.15	-
	W	9	9	100.00	-	-	0.15	0.17	0.33	0.88	2.00	-
	V	9	9	100.00	-	-	0.70	1.57	5.41	16.15	37.74	-
	Co	9	9	100.00	-	-	106.22	117.97	656.38	966.50	1219.82	-
	Cd	9	8	88.89	-	-	0.01	0.18	1.30	30.80	67.15	-
	Ti	9	9	100.00	-	-	8.60	17.28	20.84	97.64	155.54	-
	Zr	9	9	100.00	-	-	0.05	0.21	0.69	3.56	7.26	-
	Bi	9	9	100.00	-	-	0.69	2.90	6.00	46.67	52.90	-
	As	9	9	100.00	-	-	1073.62	1087.70	4935.34	5928.60	7119.54	-
	Sb	9	9	100.00	-	-	21.93	139.49	503.61	1035.75	1169.38	-
	Te	9	9	100.00	-	-	0.12	0.89	1.46	20.69	23.15	-
	Se	9	9	100.00	-	-	4.11	5.44	8.96	13.41	21.10	-
	Th	9	9	100.00	-	-	0.00	0.01	0.03	0.06	0.76	-
	U	9	8	88.89	-	-	0.00	0.01	0.02	0.05	0.15	-

Tabela 10: Descriptive statistics for LA-ICPMS analyses of selected elements from the Lamego deposit.

Mineral type	Elements	N.º Analysis	Group size	Sucess %	Lower far outlier	Lower outlier	Min regular (whisker)	Q1 (bottom of box)	Median (line)	Q3 (top of box)	Max regular (whisker)	Upper outlier
Py-1BIF	Au	4	4	100.00	-	-	3.74	4.77	10.49	17.94	21.09	-
	Ag	4	4	100.00	-	-	1.24	1.28	1.79	9.68	15.71	-
	Cu	4	4	100.00	-	-	8.75	9.06	11.23	167.19	396.17	-
	Pb	4	4	100.00	-	-	24.42	33.69	101.94	136.39	143.35	-
	Zn	4	4	100.00	-	-	0.33	0.46	1.22	188.27	999.50	-
	Sn	4	4	100.00	-	-	0.14	0.18	0.46	50.71	233.13	-
	Mn	4	3	75.00	-	-	4.37	4.37	83.15	295.53	295.53	-
	Ni	4	4	100.00	-	-	30.64	30.83	31.85	77.13	103.11	-
	Cr	4	2	50.00	-	-	1.66	1.66	1.93	2.26	2.26	-
	Mo	4	4	100.00	-	-	0.01	0.01	0.03	0.15	0.25	-
	W	4	4	100.00	-	-	0.01	0.01	0.03	0.03	0.03	-
	V	4	2	50.00	-	-	0.43	0.43	0.61	0.87	0.87	-
	Co	4	4	100.00	-	-	1.05	1.98	13.96	26.01	31.51	-
	Cd	4	2	50.00	-	-	0.02	0.02	0.29	4.54	4.54	-
	Ti	4	4	100.00	-	-	2.03	2.11	2.49	2.94	3.06	-
	Zr	4	4	100.00	-	-	0.01	0.02	1.00	1.88	2.25	-
	Bi	4	4	100.00	-	-	0.19	0.31	1.60	2.14	2.22	-
	As	4	4	100.00	-	-	3893.68	4112.15	4944.41	11224.69	14651.70	-
	Sb	4	4	100.00	-	-	7.67	11.35	37.64	40.30	40.89	-
	Te	4	4	100.00	-	-	0.13	0.13	0.22	0.32	0.32	-
	Se	4	4	100.00	-	-	10.56	10.56	11.08	11.98	12.11	-
	Th	4	2	50.00	-	-	0.00	0.00	0.00	0.01	0.01	-
	U	4	4	100.00	-	-	0.00	0.00	0.03	0.03	0.04	-
Py-2BIF	Au	13	12	92.31	-	-	0.00	0.69	7.17	69.39	361.55	-
	Ag	13	13	100.00	-	-	0.09	0.39	0.91	12.63	106.10	-
	Cu	13	11	84.62	-	-	0.51	9.14	21.13	132.50	1250.79	-
	Pb	13	13	100.00	-	-	0.02	4.13	21.46	286.04	5044.88	-
	Zn	13	13	100.00	-	-	0.28	0.35	0.55	32.06	10406.19	-
	Sn	13	13	100.00	-	-	0.08	0.09	0.14	0.75	0.81	17.91
	Mn	13	6	46.15	-	-	1.44	1.67	18.37	41.63	86.65	-
	Ni	13	13	100.00	-	-	3.84	19.41	39.98	75.34	458.30	-
	Cr	13	5	38.46	-	-	0.32	0.45	0.64	2.62	3.04	-
	Mo	13	7	53.85	-	-	0.01	0.01	0.03	0.09	0.10	-
	W	13	9	69.23	-	-	0.00	0.02	0.13	0.25	3.00	-
	V	13	7	53.85	-	-	0.02	0.03	0.24	0.77	0.89	-
	Co	13	13	100.00	-	-	0.13	0.90	8.88	23.66	53.51	-
	Cd	13	8	61.54	-	-	0.00	0.01	0.03	0.69	33.21	-
	Ti	13	13	100.00	-	-	1.78	2.06	2.71	8.04	60.27	-
	Zr	13	10	76.92	-	-	0.01	0.08	0.28	5.82	8.69	-
	Bi	13	12	92.31	-	-	0.02	0.19	0.74	2.15	80.76	-
	As	13	13	100.00	-	-	132.00	2168.00	8396.31	14975.43	42159.56	-
	Sb	13	11	84.62	-	-	0.65	5.02	7.94	56.23	113.98	-
	Te	13	10	76.92	-	-	0.01	0.03	0.24	1.13	4.22	-
	Se	13	13	100.00	-	-	4.49	9.46	13.54	15.58	19.32	32.96
	Th	13	9	69.23	-	-	0.00	0.00	0.00	0.04	0.09	-
	U	13	10	76.92	-	-	0.00	0.00	0.01	0.05	0.17	-

Tabela 10: Descriptive statistics for LA-ICPMS analyses of selected elements from the Lamego deposit.

Mineral type	Elements	N.º Analysis	Group size	Sucess %	Lower far outlier	Lower outlier	Min regular (whisker)	Q1 (bottom of box)	Median (line)	Q3 (top of box)	Max regular (whisker)	Upper outlier
Py-3BIF	Au	12	11	91.67	-	-	0.00	0.01	0.07	0.97	4.47	-
	Ag	12	9	75.00	-	-	0.03	0.06	0.75	3.05	4.55	-
	Cu	12	11	91.67	-	-	0.12	0.16	2.29	16.15	80.88	-
	Pb	12	11	91.67	-	-	0.04	0.10	2.82	71.68	484.64	-
	Zn	12	7	58.33	-	-	0.26	0.33	0.48	28.03	1149.49	-
	Sn	12	12	100.00	-	-	0.09	0.09	0.11	0.15	0.28	0.29
	Mn	12	5	41.67	-	-	0.98	1.01	4.25	6.06	8.11	-
	Ni	12	12	100.00	-	-	38.86	109.20	797.12	1129.08	2089.68	-
	Cr	12	4	33.33	-	-	0.29	0.29	0.69	1.67	1.68	-
	Mo	12	7	58.33	-	-	0.00	0.00	0.01	0.01	0.01	-
	W	12	5	41.67	-	-	0.00	0.00	0.01	0.60	2.17	-
	V	12	3	25.00	-	-	0.06	0.06	0.22	0.46	0.46	-
	Co	12	12	100.00	-	-	0.49	2.99	71.41	145.74	322.17	-
	Cd	12	5	41.67	-	-	0.01	0.01	0.02	0.73	5.46	-
	Ti	12	12	100.00	-	-	1.48	1.72	2.16	2.31	2.32	-
	Zr	12	7	58.33	-	-	0.00	0.01	0.15	0.80	1.11	-
	Bi	12	12	100.00	-	-	0.00	0.02	0.26	5.58	11.62	-
	As	12	12	100.00	-	354.94	630.01	1928.96	4439.29	5962.64	9012.52	-
	Sb	12	8	66.67	-	-	0.42	0.88	11.98	45.49	52.90	-
	Te	12	7	58.33	0.03	-	0.41	0.41	0.71	1.02	1.27	-
	Se	12	12	100.00	-	-	4.09	6.64	11.56	15.20	21.41	-
	Th	12	7	58.33	-	-	0.00	0.00	0.00	0.03	0.03	-
	U	12	5	41.67	-	-	0.00	0.00	0.00	0.03	0.05	-
Apy-1BIF	Au	1	1	100.00	-	-	0.03	0.03	0.03	0.03	0.03	-
	Au	7	6	85.71	-	-	0.16	0.17	0.39	0.76	0.78	-
	Ag	7	7	100.00	-	-	0.20	0.27	0.75	1.41	5.37	-
	Cu	7	8	114.29	-	-	0.52	0.59	0.93	1.48	1.49	-
	Pb	7	7	100.00	-	-	2.35	3.09	13.92	245.25	276.94	-
	Zn	7	2	28.57	-	-	18.68	18.68	117.42	738.01	738.01	-
	Sn	7	4	57.14	-	-	0.09	0.09	0.12	0.30	0.38	-
	Mn	7	4	57.14	-	-	1.07	1.35	3.34	6.67	7.84	-
	Ni	7	7	100.00	-	-	83.91	184.12	209.70	6017.22	9635.79	-
	Cr	7	1	14.29	-	-	2.78	2.78	2.78	2.78	2.78	-
	Mo	7	5	71.43	-	-	0.10	0.10	0.14	0.30	0.33	-
	W	7	1	14.29	-	-	0.05	0.05	0.05	0.05	0.05	-
	V	7	2	28.57	-	-	3.55	3.55	3.62	3.69	3.69	-
	Co	7	7	100.00	-	-	1.71	7.52	12.52	2118.10	12204.70	-
	Cd	7	1	14.29	-	-	2.45	2.45	2.45	2.45	2.45	-
	Ti	7	2	28.57	-	-	1.89	1.89	3.30	5.74	5.74	-
	Zr	7	6	85.71	-	-	0.01	0.02	0.05	0.36	3.29	-
	Bi	7	7	100.00	-	-	0.14	0.15	0.53	1.94	3.04	-
	As (EPMA)	7	6	85.71	-	-	444802.00	444980.50	447535.47	451076.10	453349.00	-
	Sb	7	7	100.00	-	-	219.67	230.92	252.61	391.51		-
	Te	7	7	100.00	-	-	4.19	6.12	29.61	42.82	53.48	-
	Se	7	7	100.00	-	-	10.64	25.00	41.84	58.81	70.86	-
	Th	7	4	57.14	-	-	0.00	0.00	0.00	0.01	0.02	-

4.10.1 Pyrites from carbonaceous pelite

For carbonaceous pelite, the typical ICP-MS signals indicate (Figura 39) that most commonly Mn, Ni, W, Mo, V, Bi, Co, Cd, Sn, Au, Ag, Sb, As, Te and Se are lattice-bound elements. However, spikes for elements such as Zn, Pb, Cu, Cr, Zr Ti, Th and U suggest the presence of inclusions, such as sphalerite, galena (Pb and Bi), chalcopyrite, chromite, zircon and Th- and U-rich inclusions.

Considering the average values (Tabela 10 and Figura 39a) of pyrites in carbonaceous pelite, three possibilities are envisaged: (1) manganese, Ni, Mo, W, V, Co, Cd, Ti, Bi, Zn, Sn, Sb, As, Te and Th, decrease from Py-1_{CP} to Py3_{CP}, and increase to Py-4_{CP}, (2) chromium, Zr, Se and U, decrease from Py-1_{CP} to Py-2_{CP}, increase to Py-3_{PC}, and decrease again to Py-4_{CP}, and (3) copper, Pb, Au and Ag increase from Py-1_{CP} to Py-2_{CP}, decrease to Py-3_{CP}, and increase to Py-4_{CP}.

On the other hand, if the statistical compositional range is taken as the main variation parameter (Tabela 9 and Figura 40a), six patterns are detected, and differ from those described above for the average values: (1) manganese, Mo, Co, Bi, Cu, Pb, Zn, Au, Ag, Sb and Th for Py-1_{CP}, Py-2_{CP} and Py-4_{CP}, statistically display the same range, whereas in Py-3_{CP} they are significantly lower, (2) nickel, Cd, As and Te in Py-1_{CP} and Py-4_{CP} display a similar range with the highest values, while Py-2_{CP} and Py-3_{CP} have the lowest values, (3) chromium, W, V and U for Py-2_{CP}, Py-3_{CP} and Py-4_{CP} are statistically the same, whereas in Py-1_{CP} they reach significantly higher values, (4) selenium is similar in Py-1_{CP} and Py-2_{CP}, and again in Py-3_{CP} and Py-4_{CP} which contain the highest values, (5) zirconium is similar in Py-1_{CP} and Py-3_{CP}, with the highest values, and again in Py-2_{CP} and Py-4_{CP}, and (6) Tin and Sn characterize three distinct situations: Py-1_{CP} with the highest range, Py-2_{CP} and Py-4_{CP} statistically have the same range, and Py-3_{CP} has the lowest range.

Binary plots for pyrites from carbonaceous pelite (Figura 40a-e) were constructed using a group of selected elements. Gold values in ppm for pyrites are the following: Py-1_{CP} 0.68 to 2.01 (average 0.99); Py-2_{CP} 0.90 to 1.61 (average 1.23); Py-3_{CP} 0.04 to 5.34 (average 0.32); and Py-4_{CP} 0.090 to 8.41 (average 1.76). These plots show that gold has a positive correlation with Ag, Bi, Pb, Sb and Te. The Py-1_{CP} and Py-2_{CP} are together in the same interval for Ag, Pb and Sb, while for Bi and Te typifies a distinct group. In all cases for Py-3_{CP} and Py-4_{CP}, Ag, Bi, Pb, Sb and Te increase with gold where the highest values refer dominantly to Py-4_{CP}.

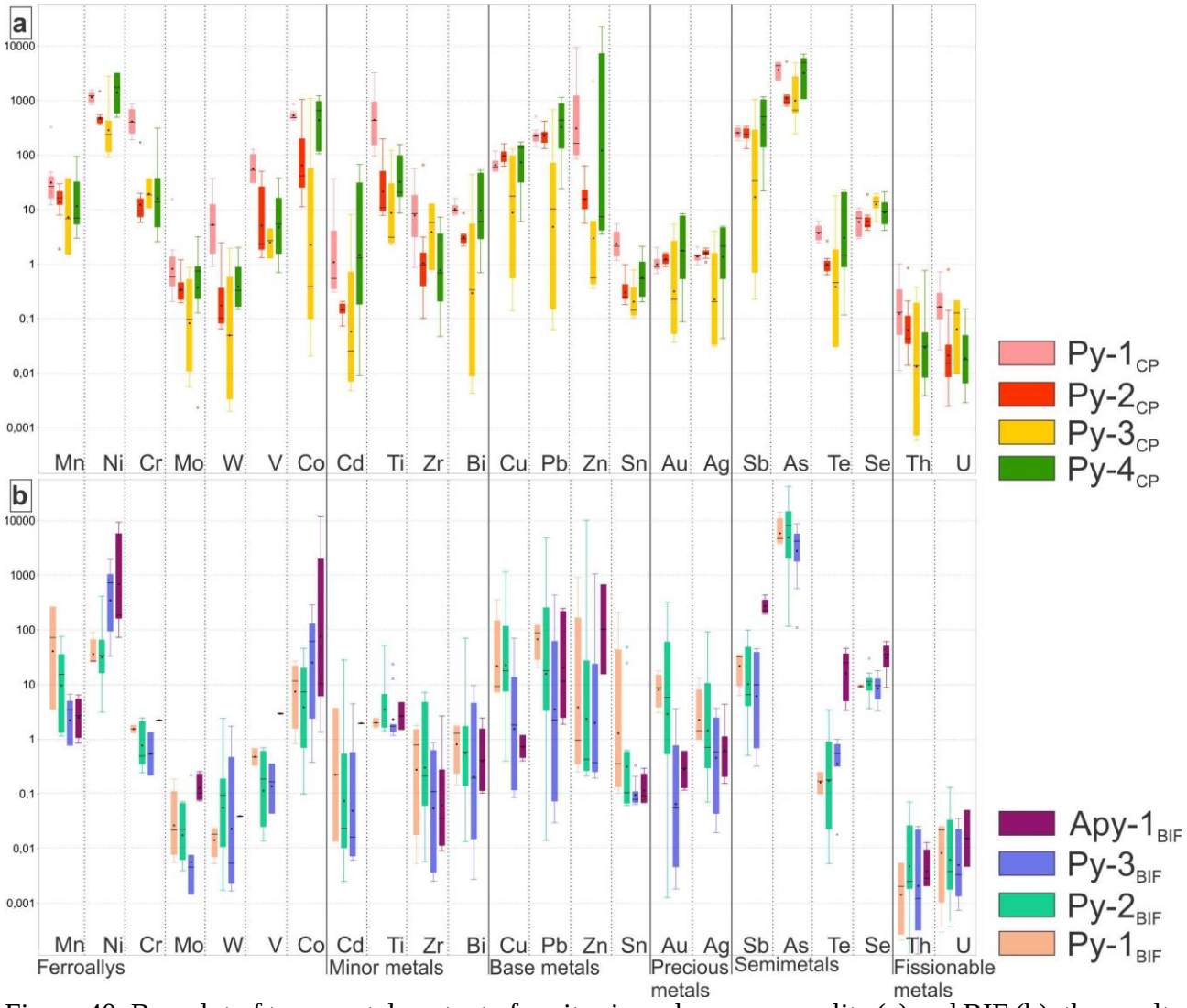

Figura 40: Box plot of trace metal content of pyrites in carbonaceous pelite (a) and BIF (b); the results are given in ppm for all analysis. The mean values of precious metals and semi-metals are higher in pyrites from BIF.

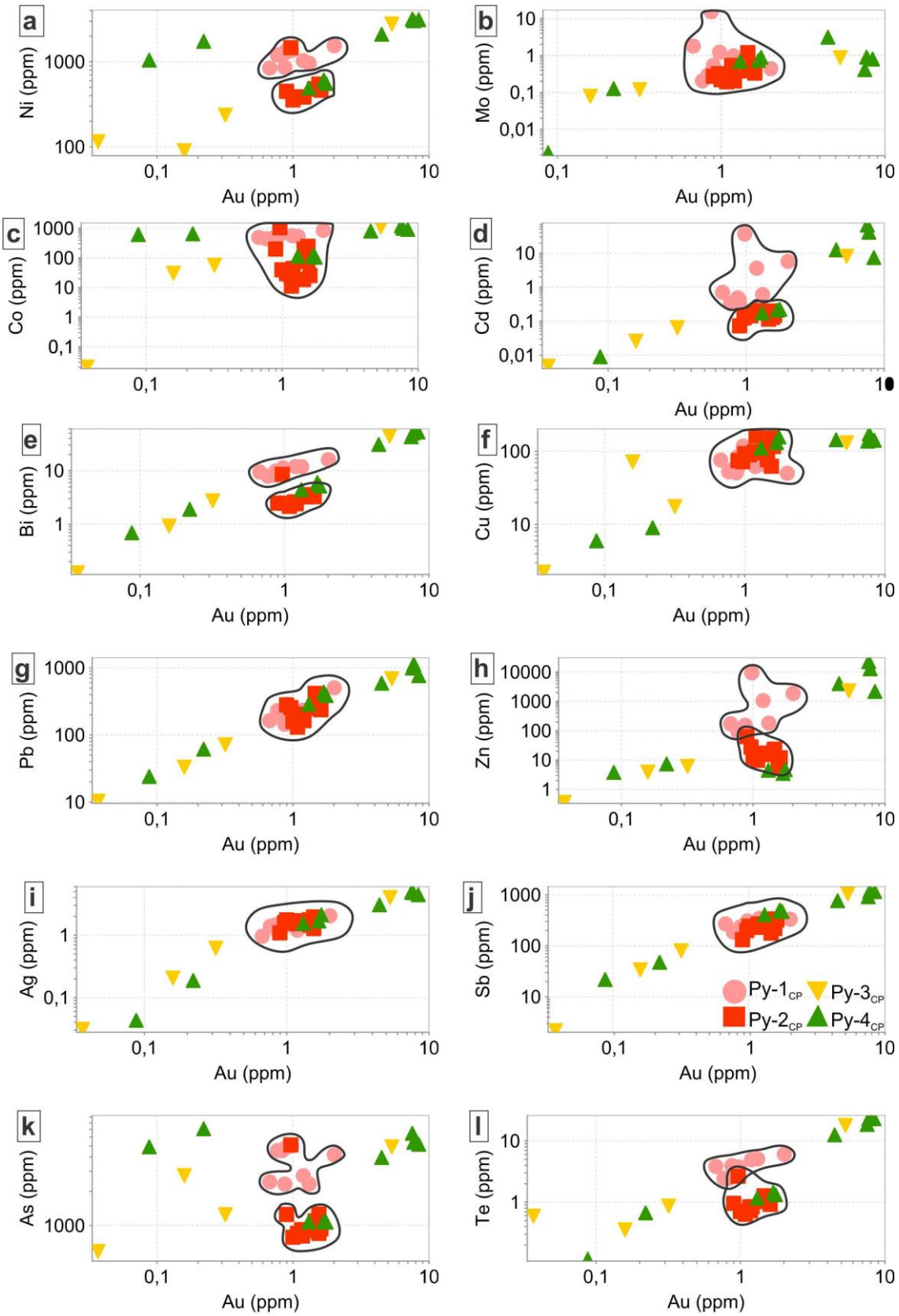

Figura 41: Binary plots of gold versus selected trace elements (Ni, Mo, Co, Cd, Bi, Cu, Pb, Zn, Ag, Sb, As, Te) corresponding to (a) to (l), analyzed on Py-1_{CP}, Py-2_{CP}, Py-3_{CP}, and Py-4_{CP} in carbonaceous pelite, Lamego gold deposit.

4.10.2 Pyrites and arsenopyrite from BIF

The most common lattice-bound elements in BIF pyrites are Mn, Ni, Cr, Mo, W, V, Co, Cd, Ti, Bi, Sn, Au, Ag, Sb, As, Te, and Se. On the other hand, Zr, Cu, Pb, Zn, Th and U display spikes, suggesting the presence of zircon, chalcopyrite, galena, sphalerite, and Th-rich and U-rich inclusions. For the specific case of Apy-1_{BIF}, Se, Bi, Te and Au are spikes, explained by nano-inclusions of tellurides (Figura 39).

Bearing in mind the average values (Tabela 10, Figura 39b) of LA-ICP-MS data of pyrites in BIF, eight configurations may be summarized: (1) vanadium Cd, Bi, Pb, Zn, Sn, Au, Ag and U decrease from Py-1_{BIF} to Py-3_{BIF}, and increase to Apy-1_{BIF}, (2) manganese, Mo and Zr decrease from Py-1_{BIF} to Apy-1_{BIF}, (3) tungsten, Ti and As increase from Py-1_{BIF} to Py-2_{BIF}, decrease to Py-3_{BIF}, and increase again in Apy-1_{BIF}, (4) copper, Se and Th increase from Py-1_{BIF} to Py-2_{BIF}, decrease to Py-3_{BIF} and Apy-1_{BIF}, (5) chromium and Sb decrease from Py-1_{BIF} to Py-2_{BIF}, and increase in Py-3_{BIF} and Apy-1_{BIF}, (6) Tellurium increases from Py-1_{BIF} to Apy-1_{BIF}, (7) nickel increases from Py-1_{BIF} to Py-3_{BIF}, and decreases to Apy-1_{BIF}, and (8) cobalt decreases from Py-1_{BIF} to Py-2_{BIF}, increases to Py-3_{BIF}, and decreases to Apy-1_{BIF}.

The compositional ranges (Tabela 9, Figura 40b) suggest the following: (1) cobalt, Zr, Bi, Cu, Pb, Au, and Ag display the same range for Py-1_{BIF} and Py-2_{BIF}, and also Py-3_{BIF} with Apy-1_{BIF}, these latter ones showing the highest range of Co, Bi, Cu, Pb, Au and Ag, while Py-1_{BIF} and Py-2_{BIF} display the highest range of Zr, (2) chromium, V, Sb, As and Te for Py-1_{BIF}, Py-2_{BIF}, Py-3_{BIF} statically are the same group with the lowest range, while Apy-1_{BIF} is different since it shows the highest values of these elements, (3) uranium and Th for Py-1_{BIF} and Py-3_{BIF} have the same range with lowest range, while Py-2_{BIF} together with Apy-1_{BIF} show the highest values, (4) tin in Py-1_{BIF} forms a distinctive group with the highest range, while Py-2_{BIF}, Py-3_{BIF} and Apy-1_{BIF} are statistically similar with the lowest values, (5) tungsten and Cd in Py-1_{BIF}, Py-2_{BIF} and Py-3_{BIF} display statistically the same range with high values; and Apy-1_{BIF} exhibits the lowest values, (6) nickel for Py-1_{BIF} and Py-2_{BIF} establishes a similar compositional range with the lowest values, while Py-3_{BIF} and Apy-1_{BIF} also have a similar compositional range with the highest values, (7) titanium and Zn display Py-1_{BIF}, Py-2_{BIF} and Py-3_{BIF} statistically similar results with the lowest range, while Apy-1_{BIF} has the highest values, (8) manganese for Py-1_{BIF} has the highest range values, whereas Py-2_{BIF} and Py-3_{BIF}, and Apy-1_{BIF} show the lowest range values, and (9) molybdenum has a similar range for Py-1_{BIF} and Py-2_{BIF}, Py-3_{BIF} has the lowest values, and Apy-1_{BIF} the highest values.

A binary plot between Au and Ag, Cu and Pb is displayed in Figura 42a-d. The gold values in ppm for pyrites are: Py-1_{BIF} 3.74 to 21.09 (average 9.65); Py-2_{BIF} 0.69 to 361.55 (average 3.56); Py-3_{BIF} 0.003 to 4.47 (average 0.08); and Apy-1_{BIF} 0.16 to 0.77 (average 0.37). Gold binary plots reveals, a discrete correlation only with Pb, Cu, As and Ag (Figura 42a-d).

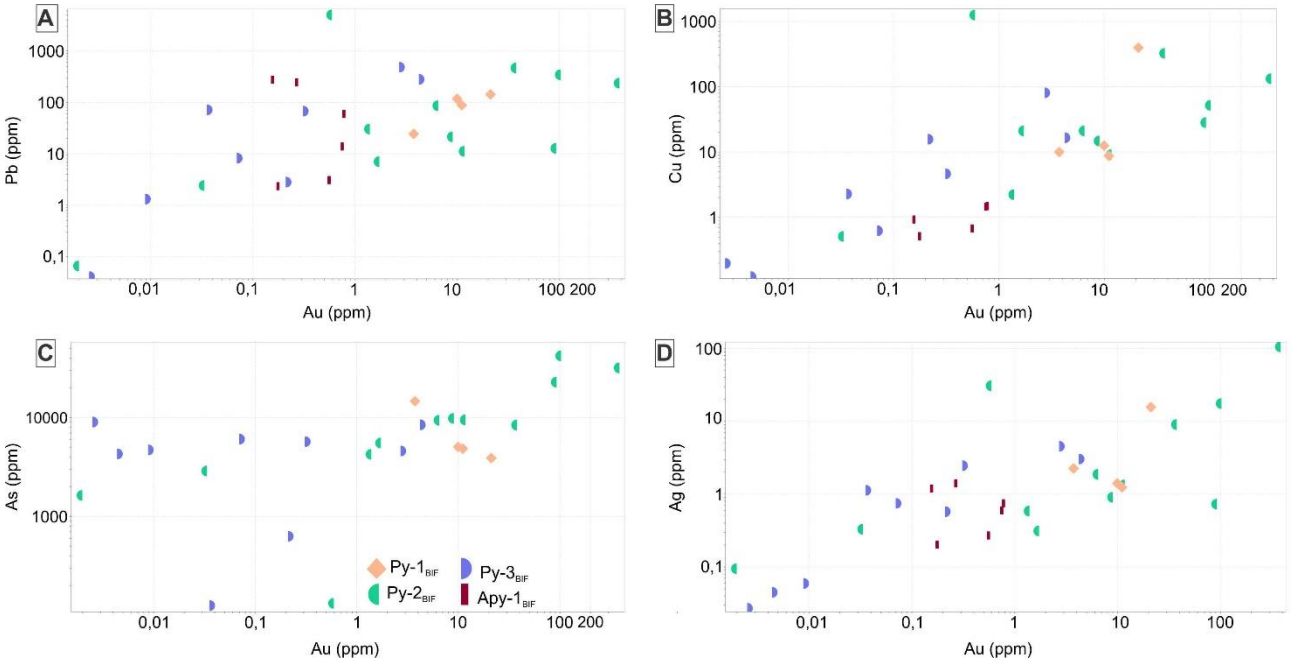

Figura 42: Binary plots of gold versus selected trace elements (Pb, Cu, As, Ag) corresponding to (a) to (d), analyzed on Py-1_{BIF}, Py-2_{BIF}, Py-3_{BIF}, and Apy-1_{BIF} in BIF, Lamego gold deposit. In all cases, Au is somewhat positively correlated to these elements.

4.11 Discussion

Textural features determined the classification of the four, Py-1_{CP}, Py-2_{CP}, Py-3_{CP} and Py-4_{CP}, and three Py-1_{BIF}, Py-2_{BIF} and Py-3_{BIF}, pyrite types in carbonaceous pelite (Figura 31a-m) and BIF (Figura 32a-k), respectively, as well as Apy-1_{BIF}. The carbonaceous pelite has a framboidal, microcrystalline, subhedral and euhedral Py-1_{CP}; Py-2_{CP} is nodular, subhedral; Py-3_{CP} is fine grained, clear, euhedral and recrystallized; and Py-4_{CP} is porous to clear, fine to coarse grained, euhedral and recrystallized. In the BIF, Py-1_{BIF} is porous and fine grained; Py-2_{BIF}, porous, subhedral and medium to coarse grained; and Py-3_{BIF}, clear, fine to medium grained

The earliest pyrites of the carbonaceous pelite, Py-1_{CP} and Py-2_{CP}, are interpreted as recrystallized, sedimentary-diagenetic, similar to those studied by Large et al. (2007), followed by the development of the hydrothermal Py-3_{CP} and Py-4_{CP}, discussed in more detail below. All three pyrites of BIF are epigenetic. The development of Py-3_{CP}, Py-4_{CP}, Py-1_{BIF} Py-2_{BIF}, and Py-3_{BIF} is closed related to the formation of the G_1structural generation, mainly controlled by the S_{1-2} foliation, whereas Py-1_{CP} and Py-2_{CP} are modified by them (Figura 42a-i).

A number of features based on the elemental mapping with EPMA and the in situ LA-ICP-MS data are used to compare pyrite types of carbonaceous pelite and BIF. The laser data have been described using both the compositional average and the statistical range, which lead to rather different configurations (Fig. 20). However, despite all the statistical similarities among these pyrite data, the statistical range comparison is notably hampered because the timing of development of Py-1_{CP} and Py-2_{CP}, Py-3_{CP} and Py-4_{CP}; Py-1_{BIF}, Py-2_{BIF}, Py-3_{BIF} and Apy-1_{BIF} is dissimilar (Figura 33).

4.11.1 Py-1_{CP}, Py-2_{CP}, Py-3_{CP} and Py-4_{CP} in carbonaceous pelite and their chemical patterns

The elemental mapping with EPMA shows that there is a unique distribution of As-Ni-Co whose concentration drops from Py-1_{CP} to Py-3_{CP}, and augments to Py-4_{CP} (Figuras 34, 35, 36 and 40), resulting in As-Ni-rich Py-3_{CP} and Co-rich Py-4_{CP} (Figura 42d, e). This clear metal zoning is marked by films of metallic concentration around the edges of pyrite crystals (As-Ni in Py-3_{CP} Figura 35c, j; As-Ni-Co in Py-4_{CP}; Figura 36c, j, k). This is likely to have resulted from metal diffusion due to fluid interaction flow during recrystallization, dissimilar to what is observed for elements such as gold.

The LA-ICP-MS average values of trace elements compare as following (Figura 40a): (1) Py-1_{CP} is rich in Mn, Cr, W, V, Ti, Zr, Bi, Zn, Sn, Te, Th and U, (2) Py-3_{CP} is rich in Se, (3) Py-4_{CP} is rich in Au, Ni, Mo, Co, Cu, Pb, Ag, Sb and As, (4) Py-1_{CP} has high trace element values when compared to Py2 $_{CP}$, except for Cu, (5) Py-3_{CP} has consistent range values, and in many cases a lower average except for Cr, Zr, Se and U, (6) Py-4_{CP} shows a large variation that is less expressive than that of Py-3_{CP}, but more than that of Py-1_{CP} and Py-2_{CP}, (7) Py-2 $_{CP}$ has more Au than Py-3_{CP}, the inverse being true for As, and (8) gold is best correlated with elements of crustal affinity, such as Bi, Pb, Sb, Te.

The three richest elements in Py-1_{CP} are As (2317.35 – 5035.65 ppm), Ti (95.26 – 3224.24 ppm) and Ni (844.32 – 1543.92ppm), whereas As, Ni and Co are the richest in Py-2_{CP}, Py-3_{CP} and Py-4_{CP}. Elements such as Ni, Co, Bi, Cu, Pb, Ag and Sb (Figura 40a) are best concentrated in Py-1_{CP} and Py-2_{CP}. In Py-3_{CP} and Py-4_{CP}, these elements show a positive correlation increasing with gold, that suggesting that gold was hydrothermally introduced in both these pyrites (Figuras 39a and 40a-l).

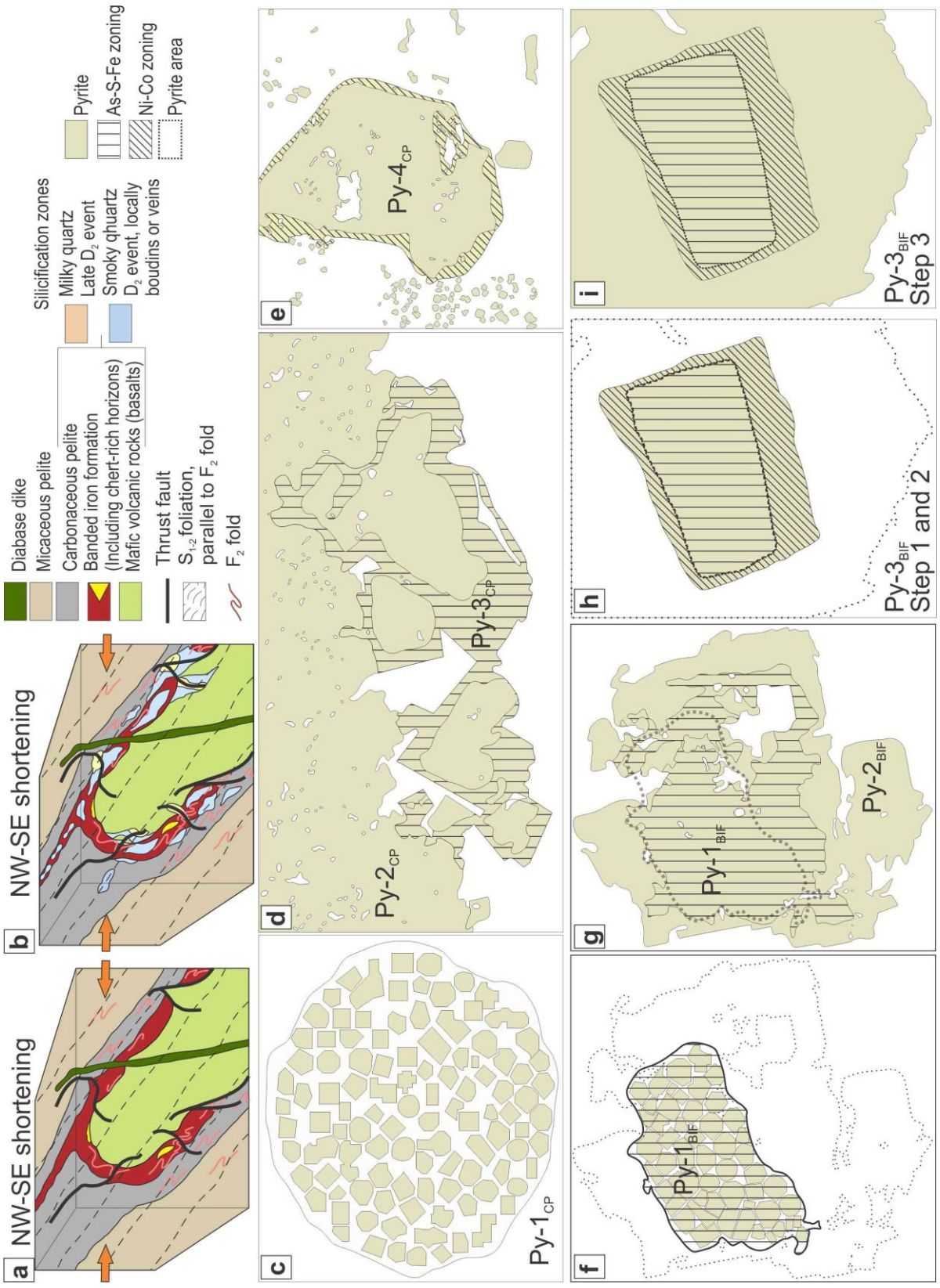

Figura 43: Diagrammatic model for the evolution of gold mineralization and pyrite development in carbonaceous pelite and BIF at the Lamego deposit. (a) and (b) Schematic cartoon structural model for the formation of the Lamego gold deposit (not to scale; modified after Martins et al. 2016). (a) Folded and sheared lithologies start to develop; (b) Veins evolve as shear zones progress and both function as pathways for hydrothermal fluids, which precipitated coarse-grained, irregular zones of

smoky quartz in massive veins and sufide minerals in host rocks. (c) to (e) Pyrite types in carbonaceous pelite. (c) Framboidal Py-1_{CP}; (d) Massive aggregation of Py-$1_{CP,}$ which is recrystallized to form Py-2_{CP}, which gives place to euhedral Py-3_{CP} developed along the edges of Py-2_{CP}, displaying As-S-Fe zoning surrounding Py-3_{CP}; (e) Coarse-grained, subhedral to euhedral Py-4_{CP} formed during deformation and recrystallization of Py-3_{CP}, showing Ni-Co zoning. (f) to (i) Pyrite types in BIF. (f) Fine-grained pyrites constituting an aggregate of porous of Py-1_{BIF} that exhibit As-Fe-S zoning; (g) Py-2_{BIF} that forms after Py-1_{BIF} exhibiting the same As-Fe-S zoning. (h) and (i) Development of coarse-grained Py-3_{BIF}. (h) As-Fe-S (step 1) and Co-Ni (step 2) euhedral zonings are highlighted; (i) Co-Ni zoning (step 3).

The relative enrichment of Ni, V, Zn, Pb, Ag (Figura 40a) in diagenetic pyrite, such as Py-1_{CP} and Py-2_{CP} (Figura 43c, d), has been discussed by various authors (e.g., Algeo and Barry, 2004; Coveney, 2000; Large et al. 2007, 2009, 2011; Ohfuji et al. 2005). They indicate that such elements were probably concentrated by organic processes during sedimentation and diagenesis of organic-rich sediments in euxinic environment.

The recrystallization of Py-1_{CP} and Py-2_{CP} to form euhedral Py-3_{CP} (Figura 42d) is marked by depletion of the average values of Mn, Ni, Cr, W, V, Co, Ti, Zr, Bi, Zn, Sn, Te, Th, U, as well as Au and As (Figura 40a), and these are all incremented in Py-4_{CP} (Figuras 39a and 42e). Notwithstanding this increment, the compositional range of Py-4_{CP} falls within the ranges of one or more of the other three pyrite types, denoting that certain trace elements from the pyrite structure were leached in an early-stage, and probably introduced in the evolving hydrothermal fluid to form in Py-4_{CP} (Figura 42c, d, e).

The narrow compositional range of the majority of trace elements in Py-1_{CP} and Py-2_{CP} (Figura 40a) may reflect the inherited sedimentary signature, and is syn-metamorphic (syn-genetic – before the onset of metamorphism I thought I read earlier) and therefore pre-hydrothermal, (must be diagenetic then) since both pyrites are recrystallized (Figura 42c, d) you can have hydrothermal pyrites that subsequently were recrystallized. A much wider range of values for most metals in Py-3_{CP} (Figura 42d), followed by a tighter spectrum in Py-4_{CP} (Figura 40a), reveals different buffering conditions, with a higher fluid-to-rock, buffered dominant stage during the formation of Py-4 (Figura 42e).

Due to the spike aspect in the La-ICP-MS results of trace elements such as Zn, Cd, Cu, Zr, Pb, Bi, Th, U and Ti (Figura 39), which have large ion size and/or different charge, it is possible that these elements form discrete mineral inclusions like sphalerite, chalcopyrite, zircon, galena, rutile and Th- and U-rich mineral phase in the metamorphic and/or hydrothermal pyrite. The same behavior of such elements is described by Cook et al. (2009, 2013), Deol et al. (2012), Large et al. (2009), and Oliver et al. (2015).

Gold plots have more restricted range values for Py-1_{CP} and Py-2_{CP} when compared to Py-3_{CP} and Py-4_{CP} (Figura 40a-l). For Py-1_{CP} and Py-2_{CP}, Mn, Mo, Cr, Cu, Pb, Ag, Sb, Se, Th and U are in the same group (Figura 40b, c, f, g, i, j) and elements Ni, Cr, W, Cd, Ti, Zr, Zn, Sn, As, and Te form a distinct group (Figura 40a, d, e, h, k, l) with both showing the same variation of gold content (Figura 40a-l). For Py-3_{CP} and Py-4_{CP} they show a wide distribution (Figuras 39a and 40a-l).

The weak correlation between Ni vs Au and V vs Au (Figuras 40a and 39a) in Py-1_{CP} and Py-2_{CP} (Figura 42c, d), implies the possibility that gold was also concentrated by a similar organic process, probably involving extraction from seawater onto sedimentary organic matter (Large et al. 2009, 2011). As for Py-3_{CP} and Py-4_{CP}, Au and As are clearly correlated (Figuras 39a and 40k), suggesting hydrothermal introduction of gold (Figura 42a, b, e). All pyrites from carbonaceous pelite are plotted above the gold solubility line (Figura 44 after Reich et al. 2005), indicating that gold is in the mineral structure as a lattice-bound element (Figura 44).

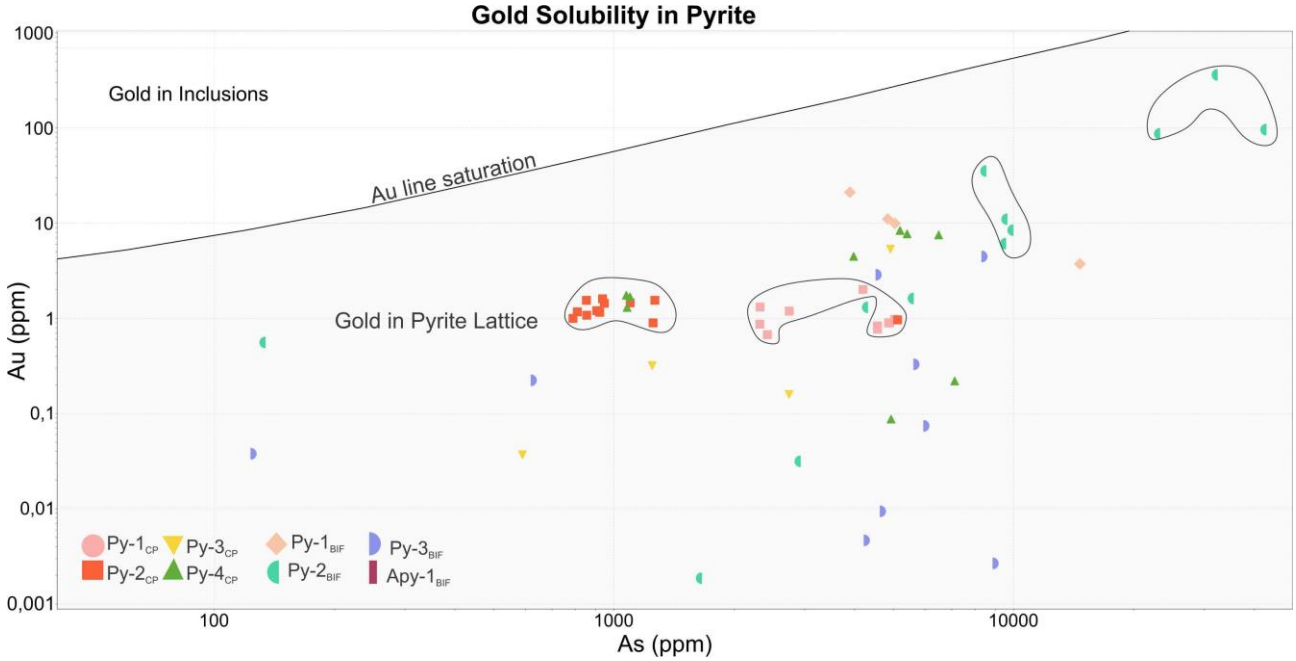

Figura 44: Gold saturation line (after Reich et al. 2005) marking the limit of gold dissolved in As-pyrite, showing the correlation between Au and As for the seven main pyrite types (Py-1_{CP}, Py-2_{CP}, Py-3_{CP}, Py-4_{CP}, Py-1_{BIF}, Py-2_{BIF} and Py-3_{BIF}) at the Lamego deposit. The As:Au ratio is below the gold saturation line indicating that gold is present in the structure of pyrite.

4.11.2 Pyrite trace element evolution in carbonaceous pelite

The origin and time of formation of pyrites are interpreted based on textural aspect, elemental mapping with EPMA (Figuras 34, 35 and 36) and LA-ICP-MS results (Tabelas 9 and 10). These data show a systematic trace element evolution in the formation of the four pyrite types in carbonaceous pelite (Figura 42e), three main stages can be recognized.

1 – Pre-hydrothermal (diagenetic) stage (Figura 33). The Py-1_{CP} marks the stage of diagenetic pyrite development and the beginning of formation of Py-2_{CP} (Figura 31b, e, f, g, Figura 42c, d). Most trace elements, such as Cu, Pb, Zn, Co, Ni, Mn, V, Mo, As, Bi, Au, Ag, Se, and Te, are invisible and locked into the pyrite structure (Figura 39).

As designated in Figura 14i, Au values raise from the center towards the more recrystallized border of the Py-1_{CP} grain, implying that this metal was furnished by the fluid during the early phases of hydrothermalism. In fact, during the analytical work, it became clear that there is a tendency towards a slight increase in gold from the nuclei to the limits of all four types of analyzed grains in carbonaceous pelite.

2 – Early hydrothermal stage (Figura 33). This corresponds to the massive aggregation of Py-$1_{CP,}$ which is recrystallized to form Py-2_{CP} (Figuras 31d, h, i and 43d), and to chemical changes comparatively to Py-1_{CP}. These encompass loss of Mn, Ni, Cr, Mo, W, V, Co, Cd, Ti, Zr, Bi, Zn, Sn, Sb, As, Te, Se, Th and U (Figura 40a), and gains of Cu, Pb, Au and Ag, here interpreted to reflect the early hydrothermal fluid-rock interaction (Figura 42a, b, d). Since this stage is dominated by recrystallization as well as development of a new pyrite type, it is interpreted to represent a metamorphic/hydrothermal stage.

3 – Early to main hydrothermal stage (Figura 33). Typified by the euhedral Py-3_{CP} developed along the edges of Py-2_{CP} (Figuras 31d, j, k and 43d). As it has an average larger grain size than the main metamorphic Py-2_{CP} and a large range of trace element values (Figura 40a), it is interpreted as resulting from the advance of recrystallization and attendant fluid interaction (Figura 43a, d). Apparently the release of some Ni, As, Co, Bi, Pb, Cu, Zn, Au, Ag, Te, Th and U (Figura 40a) into the fluid, from stages 1 to 2, allowed the development of the As-Ni zoning (Figuras 35c, j and 43d), and minute phases such as galena (Pb-Bi), chalcopyrite (Cu), sphalerite (Zn), electrum (Au-Ag), tellurides (Au, Ag, Te) and thorite (Th, U), which form inclusions mainly in Py-3_{CP}.

4 – Main to late hydrothermal stage (Figura 33). Recognized as the main hydrothermal stage for carbonaceous pelite, because Au content is the highest (up to 8.40 ppm; Figura 40a). The Py-4_{CP} (Figura 31d, l, m) is a subhedral to euhedral, smooth pyrite, formed during deformation and recrystallization of Py-3_{CP} (Figuras 31l, m and 43e). Comparing with Py-1_{CP}, Py-4_{CP} is relatively poor in some trace elements, and only exhibits enrichment in Au, Ni, Mo, Co, Cu, Pb, Ag, Sb and As (Figura 40a). Due to the Co-Ni-As zoning (Figura 36k, j, c) and the higher Au content (Figuras 40a and 41a-j; Tabelas 9 and 10), we suggest that the hydrothermal fluid at this stage was Au-As rich (Figura 43e). Large et al. (2011) describe late hydrothermal Au-As-free overgrowths on diagenetic, Au-As-bearing pyrite, and consider the latter as the most important gold-bearing stage. This is not

the case at the Lamego deposit, where Py-4_{CP} is the richest in Au and As (Figura 41a-l), reinforcing stage 4 as the most important for gold precipitation at Lamego (Figura 43a, b, e). The Py-4_{CP} can be correlated to the overgrowth crystals described by Large et al. (2011).

4.11.3 Py-1_{BIF}, Py-2_{BIF}, Py-3_{BIF} and Apy-1_{BIF} in BIF and their chemical patterns

Elemental mapping with EPMA of Py-1_{BIF} and Py-2_{BIF} (Figura 37) shows that these display outstanding As-S zonation (Figura 37c, b, e). The richest As-S zone is in the center of the image, where pyrite is dominantly porous (Py-1_{BIF}), while As-S is lower in the smooth edge corresponding to Py-2_{BIF} (Figura 43f, g).

Textural features indicate that Py-1_{BIF} forms at the expense of both fine-grained, metamorphic iron carbonate (dominantly siderite) bands, as well as medium- to coarse-grained hydrothermal carbonate (dominantly ankerite) of BIF (Figura 32a, b, c, d). The characteristic porous aspect of this pyrite suggests incomplete sulfidation reactions. The variation in the relative As-S content from Py-1_{BIF} to Py-2_{BIF} (Figura 40b) reveals different buffering stages of these two elements. Other elements such as Ni and Co show a homogenous distribution (Co>Ni; Figura 37i, j), similar to what is observed in pyrites of carbonaceous pelite.

The Py-3_{BIF} elemental mapping with EPMA (Figura 38) shows a less pronounced S-Fe-As zoning (Figura 38b, e, c) when compared with the Ni-Co zoning (Figura 38i, j) which is similar to the zonation observed in the Py-4_{CP} (Figura 36j, k). This Ni-Co zonation (Figura 38i, j) suggests that the growth of Py-3_{BIF} took place in three steps (Figura 43h, i) with the first (Figura 43h) being marked by a S-Fe-As zonation (Figura 38b, c, e); a homogenous distribution mainly of Sb and Co (Figura 38f, j); a corrosion-like textural aspect of Ni (Figura 38i); and minute silver nuggets (Figura 38g). The second step (Figura 43h) is recognized by a Ni-Co zonation (Figura 38i, j); As and Mg depletion (Figura 38c, d); and homogeneous distributions of S, Fe and Sb (Figura 38b, e, f). The third step (Figura 43i) shows As and Mn depletion; and homogeneous distributions of S, Fe, Sb, Co and Ni. Silver nuggets are seen between the first and second growth steps and towards the end of the third step (Figura 38g).

With regards to the LA-ICP-MS average values of trace elements (Figura 40b) in Py-1_{BIF}, Py-2_{BIF} and Py-3_{BIF}, the average Au pattern decreases from Py-1_{BIF} to Py-3_{BIF} and is mimicked by Mn, V, Cd, Zr, Bi, Pb, Zn, Sn, Ag and U. On the other hand, Mo, W, Ti, Cu, As, Se and Th increase from Py-1_{BIF} to Py-2_{BIF} and decrease from Py-2_{BIF} for Py-3_{BIF} (Figura 40b). Finally, Cr, Co and Sb decrease from Py-1_{BIF} to Py-2_{BIF} and increase further to Py-3_{BIF}. The only exception is Ni, that increases from Py-1_{BIF} to Py-3_{BIF} (Figura 40b).

Since Apy-1_{BIF} formed from Py-3_{BIF} (Figura 32h, j) it is important to address their chemical variation. Manganese, Ni, Co, Zr and Cu decrease in average values, while Cr, Mo, W, V, Ti, Bi, Pb, Zn, Sn, Au, Sb, As, Te, Se, Th and U increase. The exception is Ag that maintains the same value (Figura 40b).

4.11.4 Pyrite trace element evolution in BIF

The richest average LA-ICP-MS trace element values of the three BIF pyrites are highlighted, and they help establish the hydrothermal stages of pyrite formation in BIF, one of the main host to gold at Lamego deposit:

1 – Early hydrothermal (early-ore) stage (Figura 33). It is marked by the development of the porous Py-1_{BIF} (Figura 32a, d, e). Manganese, Cr, V, Cd, Zr, Bi, Pb, Zn, Sn, Au, Ag and Sb correspond to the highest trace elements in the early-ore hydrothermal stage (Figura 33) locked in the fine-grained pyrite structures (Figuras 41b and 43f, g).

2 – Main hydrothermal (syn-ore) stage (Figura 33). Recognized for the development of the subhedral Py-2_{BIF} (Figura 43g), which is commonly associated with Py-1_{BIF} (Figura 32d, h, i), and as the main syn-ore stage (Figura 33). The Py-2_{BIF} displays Mo, W, Ti, Cu, As, Se and Th as the highest trace elements. The more significant spread of Au, As, and the majority of other elements shown in Figura 40b is coherent with the transition from Py-1_{BIF} to Py-2_{BIF} as being the peak of gold precipitation. This stage is equivalent to the 3 – Main to late-hydrothermal stage described for carbonaceous pelite characteristic of the Py-4_{CP}.

3 – Late hydrothermal stage (Figura 33). It is characterized by the formation of Py-3_{BIF} and Apy-1_{BIF} (Figura 32j, k). Both exhibit Ni, Co and Te as the highest trace elements, with Apy-1_{BIF} also displaying Mo and Se (Figura 40b). These phases also define the late-ore stage (Figuras 33 and 43h, i), which is typified by depletion of most of all elements. The Apy-1_{BIF} develops after Py-3_{BIF} (Figura 32h, i) in the late-ore stage, and is marked by Mo, Ti, Zn, Sb, As, Te, Se, Th and U as the highest trace elements.

Gold shows a particular pattern, decreasing from Py-1_{BIF} to Py-3_{BIF} (Figura 40b), and is relatively mimetic by Ag, Pb, Sb and Cu; these elements also display a relatively, though not very clear, correlation with gold (Figura 42a-d). On the other hand, As increases from Py-1_{BIF} to Py-2_{BIF} and decreases to Py-3_{BIF} (Figura 40b). In light of these variations, the strong Au-As correlation (Figura 22a-d), and the fact that gold decreases from the early to the late hydrothermal stage (Figura 43a, b, h, i), it is possible that nuggets such as that mapped in (Figura 38h) precipitated upon gold

removal from the Py-1_{BIF} and Py-2_{BIF} structures (Cook et al. 2009). Alternatively, it may represent gold directly precipitated from the fluid.

4.11.5 The Lamego gold deposit ore-forming process

Integration of data present in this paper, by Martins et al. (2016) among other have established that sulfidation and silicification are some of the most important factors in the formation of the structurally controlled Lamego gold deposit (Martins et al. 2016). This provides useful insights into the precipitation process of gold and associated elements at the Lamego deposit.

Diagenetic pyrite is recognized in many orogenic gold deposits around the world always in association with black shales. This is the case of Sukhoi Log (Russia), Golden Mile and Bendigo deposits (Australia), Chang'an (China) and Morro do Ouro (Brazil), to cite a few (Gregory et al. 2015; Large et al. 2007, 2009; Oliver et al. 2015; Steadman et al. 2015; Zhang et al. 2014). At the Lamego deposit, the diagenetic pyrite Py-1_{CP} of the carbonaceous pelite (black shale; Figura 43a, b, c) has an average Au and As of 0.895 ppm and 4375.586 ppm, respectively, obtained by in situ LA-ICP-MS analyses (Tabela 10).

These contents indicate a pre-hydrothermal enrichment of both metals in pyrite of carbonaceous pelite as invisible Au and As in the pyrite structure (Figura 43a, b, c). In the 2 – Metamorphic/early hydrothermal stage, both Au and As must have been removed from gold-bearing Py-1_{CP} and incorporated into the metamorphic fluid during conversion of Py-1_{CP} to Py-2_{CP} and Py-3_{CP} (Figura 43a, b, c, d) with gold precipitation having its peak in Py-4_{CP} (3 – Main hydrothermal stage; Figura 43e).

In a recent contribution by Morales et al. (2016), the authors concluded that the ore-forming hydrothermal fluid at the orogenic Lamego gold deposit was metamorphic (Na>K>Ca>Mg), with a H_2O-CO_2 ± CH_4-NaCl dominant composition, 300 to 375ºC temperature range and pressure at 2.6 kbar. Fluid evolved as: (1) aqueous-carbonic trapped in Qtz (1), of low salinity (~ 2% equiv. wt.% NaCl), and (2) carbonic-aqueous fluid, of moderate salinity (average 9 eq. wt.% NaCl) hosted in Qtz (2) (Figura 25b, d).

In the Lamego BIF, there is no diagenetic pyrite, and the evidence shows that sulfide minerals grow from siderite and ankerite (Figura 25b, e, g, h). They replace mainly carbonate bands, forming pyrites and arsenopyrite (Figura 32f, h, i), corroborating their hydrothermal origin, probably related to the same metamorphic hydrothermal fluid that formed the pyrites of carbonaceous pelite (Figura 43a, b, f, g, h, i). The similarity between the chemical zonation of pyrites (As-S-Fe and Co-Ni-As) in both lithologies, as observed in elemental mapping with EPMA of Figuras 15 to 18, also stresses the

compatibility between fluids that affected both carbonaceous pelite and BIF. The Co-Ni-As zonation of BIF pyrites, mainly Py-3_{BIF} (Figura 43h, i), may have been influenced by the presence of centimeter-thick films of carbonaceous pelite interlayered in BIF.

Gold decreases from Py-1_{BIF} to Py-3_{BIF} (10.485 to 0.074 ppm), and increases again to Apy-1_{BIF} (0.385 ppm), but Apy-1_{BIF} shows less Au than Py-1_{BIF} and Py-2_{BIF}, suggesting that gold precipitation dominated in BIF during the early to main hydrothermal stages (Figura 43f, g). This pattern for gold in BIF is accompanied by Cr, V, Cd, Bi, Pb, Zn, Sn, Ag, Sb, and U (Figura 40b). This may be a potential mechanism for the migration of gold from wall rocks into the upward metamorphic fluids in the Rio das Velhas greenstone belt sequence, involving newly formed pyrite types in greenschist facies conditions, with Au transported mainly as Au(HS) complexes and precipitated together with arsenic.

Three vein systems are classified in silicification zones by Morales et al. (2016) with abundant smoky and milky (recrystallization product of smoky crystals) quartz veins. The authors reinforce that the S_{1-2} foliation-parallel V_2 veins are the main host to gold (Martins et al. 2016), in association with pyrite and arsenopyrite. In light of the common presence of free gold in the zones, Morales et al. (2016) suggested that the hydrothermal fluid was subjected to continuous pressure changes (Sibson et al. 1988) that must have favored silica and gold precipitation. Gold precipitation via pressure release may also be interpreted due to the presence of gold nuggets (Figura 38h) that coincide with pores of pyrite grains during sulphidation.

4.11.6 Significance for exploration

This study provides the first discussion regarding the geological characteristics and ore-forming process of BIF-hosted gold deposits of the Rio das Velhas greenstone belt sequence, based on in situ LA-ICP-MS analyses of sulfide minerals, and suggests a possible genetic model for their formation. Three features summarized below can be used as gold exploration tools in this region:

1) Gold shows a positive correlation with As, Sb, Ag, Pb and Bi (Figura 40a). Anomaly of these elements in soil or stream sediments may be used as an important indicator for exploration of new BIF-hosted gold orebodies in Rio das Velhas greenstone belt sequence.

2) Carbonaceous pelite has pyrite that is devoid of economic gold (Figura 40a), and increases with the intensity of hydrothermal alteration, where this metal is best concentrated in $Py4_{CP}$ (Figura 40b). The recognition of areas where sulfide-rich, carbonaceus pelite displays coarse-grained, subhedral to euhedral pyrite in the proximity of BIF and-or silicification zones can help identify economic blind orebodies.

3) The best gold values measured in pyrites from BIF are within Py-1_{BIF} (porous and fine grained) and Py-2_{BIF} (porous, subhedral and medium to coarse grained), while Py-3_{CP} (clear, fine to medium grained) exhibits the lowest values (Figura 40b). Since the distinction among these three pyrite types is macroscopically viable at non-weathered outcrops, the identification of areas that are richest in Py-1_{BIF} and Py-2_{BIF} may indicate drill sites.

4.12 Conclusions

Studies of the paragenetic sequence (Fig. 13) using textural observations, elemental mapping with EPMA and quantitative in situ LA-ICP-MS analyses on diagenetic and hydrothermal pyrites from carbonaceous pelite, as well as hydrothermal pyrites and arsenopyrite in BIF from the Lamego gold deposit (Figura 22), provide new information about ore genesis in the Rio das Velhas greenstone belt sequence (Figura 21), with the following conclusions summarized below:

- The paragenetic sequence pointed in Figura 33 for the Lamego deposit is mainly represented by sulfides, magnetites, sulfosalts, phosphates, and gold. Pyrite (FeS_2), arsenopyrite (FeAsS), sphalerite (ZnS), chalcopyrite ($CuFeS_2$), galena (PbS) and pyrrhotite (Fe(1-X)S) are the main sulfide phases. Magnetite (Fe_3O_4) is the only oxide; nikeline (NiAs) and tennantite-tetrahedrite ($Cu_9Fe_3Sb_4S_{13}$) represent the minerals of the sulfosalts group, while monazite is the identified phosphate.
- Seven types of pyrites are present, four in carbonaceous pelite (Figura 31a-m) and three in BIF (Figura 32a-k). The former has a framboidal, microcrystalline, subhedral and euhedral Py-1_{CP} (Figura 31b, e, f, g); Py-2_{CP} is nodular, subhedral (Figura 31d, h, I, j, k); Py-3_{CP} is fine grained, clear, euhedral and recrystallized (Figura 31d j, k); and Py-4_{CP} is porous to clear, fine to coarse grained, euhedral and recrystallized (Figura 31d, l, m). The BIF pyrites are Py-1_{BIF}, porous and fine grained (Figura 32b, e, f); Py-2_{BIF} that is porous, subhedral and medium- to coarse- grained (Figura 32b, d, h, i); and Py-3_{BIF} clear, fine- to medium-grained (Figura 32b, j, k).
- Four stages of evolution are recognized: (1) pre-hydrothermal (diagenetic), marked by the development of Py-1_{CP} and its initial recrystallization to form Py-2_{CP}; since Au values increase from the center towards the more recrystallized borders of Py-1_{CP} grains, gold precipitation must have started in the early phases of hydrothermalism, (2) early hydrothermal stage, where Py-2_{CP} continued to develop, Py-3_{CP} formed in carbonaceous pelite, and Py-1_{BIF} formed in the BIF, (3) main hydrothermal stage, recognized by the development of Py-4_{CP} and Py-$2_{BIF,}$ respectively in carbonaceous pelite and BIF, and where gold shows the best values, and (4)

late hydrothermal stage, marked by the final development of Py-4_{CP} in carbonaceous pelite and Py-3_{BIF} in BIF. The early hydrothermal stage is dominated by recrystallization as well as development of a new pyrite type (Py-2_{CP}), and it is thus interpreted to represent a metamorphic/hydrothermal stage.

- Interpretation of elemental mapping with EPMA shows that: (1) Py-1_{CP} and Py2_{CP} have a homogenous distribution of elements, such as Fe, S, As, Ni, Co and Sb (Figuras 34 and 35), (2) Py-3_{CP}, Py-1_{BIF} and Py-2_{BIF} exhibit As-S-Fe zonation (Figuras 35 and 37), and (3) Py-4_{CP} and Py-3_{BIF} display Ni-Co zonation (Figuras 36 and 38).
- LA-ICP-MS analyses of pyrites from carbonaceous pelite reveal (Fig. 20a): (1) Py-1_{CP} is rich in Mn, Cr, W, V, Ti, Zr, Bi, Zn, Sn, Te, Th and U, and has high trace element values when compared to Py2 $_{CP}$, except for Cu, (2) Py-2_{CP} has more gold than Py-3_{CP} and is is depleted in all elements, (3) Py3-$_{CP}$ is rich in Se, has more arsenic than Py-2_{CP}, has a consistent range of values, and in many cases a lower average except for Cr, Zr, Se and U, and (4) Py4-$_{CP}$ is rich in Au, Ni, Mo, Co, Cu, Pb, Ag, Sb and As, and shows a large variation that is less expressive than that of Py-3_{CP}, but more than that of Py-1_{CP} and Py-2_{CP}.
- The three richest elements in Py-1_{CP} are As (2317,347 - 5035,646), Ti (95,263 - 3224,243) and Ni (844,323 - 1543,923), whereas As, Ni and Co are the richest in Py-2_{CP}, Py-3_{CP} and Py-4_{CP} (Figura 40a).
- Gold in carbonaceous pelite pyrite display excellent affinity with crustal elements such as Bi, Pb and Sb, but good correlation is also observed with Ni, Co, Cu, Ag and Te (Figura 40a). Gold in carbonaceous pelite can be related with sedimentation and hydrothermal activity (Figura 43a-e). From Py-1_{CP} to Py-2_{CP} Au is constant while As decreases; from Py-2_{CP} to Py-3_{CP} Au and As decrease, but from Py-3_{CP} to Py-4_{CP} there is a notable Au and Au increase (Figura 40a), indicating an intense gold climax probably close to the final stage of deformation and related hydrothermal fluid flow (Figura 43a, b).
- The relative Ni, V, Zn, Pb, Ag (Figura 40a) enrichment in diagenetic pyrite, such as Py-1_{CP} and Py-2_{CP} (Figura 43c, d) may indicate that such elements were probably concentrated by organic processes during sedimentation and diagenesis of organic-rich sediments in euxinic environment (Algeo and Barry, 2004; Coveney, 2000; Large et al. 2007, 2009, 2011; Ohfuji et al. 2005;).
- The increment of Mn, Cr, W, V, Ti, Zr, Bi, Zn, Sn, Te, Th, U, as well as Au and As (Figura 40a) denotes that certain trace elements from the pyrite structure were leached in an early-stage and probably introduced in to the evolving hydrothermal fluid (Figura 43c, d,e).

- There is a unique metal distribution with As-Ni-rich Py-3_{CP} and Co-rich Py-4_{CP} (Figuras 34, 35, 36 and 43d, e). These are likely to have resulted from metal diffusion due to fluid interaction flow during recrystallization, dissimilar to what is observed for elements such as gold.
- A weak correlation between Ni vs Au and V vs Au (Figura 40a) in the syngenetic Py-1_{CP} and Py-2_{CP} (Figura 43c, d) d) implies the possibility that some gold was indigenous to the carbonaceous pelite and originally concentrated by an organic process similar to that proposed to Large et al. (2009, 2011). As for Py-3_{CP} and Py-4_{CP}, gold and arsenic are clearly correlated (Figuras 40a and 41k), suggesting hydrothermal metal introduction (Figura 43a, b, e).
- The Ni-Co zonation depicted by the elemental mapping with EPMA (Figura 38i, j) suggests that the growth of Py-3_{BIF} took place in three steps (Figura 43h, i) with the first (Figura 43h) being marked by a S-Fe-As zonation (Figura 38b, c, e); the second step (Figura 43h) recognized by a Ni-Co zonation (Figura 38i, j). An the third (Figura 43i) showing the As and Mn depletion with a homogeneous distributions of S, Fe, Sb, Co and Ni.
- LA-ICP-MS analyses for pyrites from BIF show (Figura 40b): (1) gold, followed by Mn, V, Cd, Zr, Bi, Pb, Zn, Sn, Ag and U decrease in average values from Py-1_{BIF} to Py-3_{BIF}, (2) molybdenum, W, Ti, Cu, As, Se and Th increase from Py-1_{BIF} to Py-2_{BIF}, and decrease from Py-2_{BIF} for Py-3_{BIF}, (3) chromium, Co and Sb decrease from Py-1_{BIF} to Py-2_{BIF}, and increase again to Py-3_{BIF}, and (4) nickel, that increase from Py-1_{BIF} to Py-3_{BIF}.
- The LA-ICP-MS Apy-1_{BIF} pattern from BIF (Figura 40b), considering that it formed after Py-3_{BIF} (Figura 32h, i; Figura 33),denotes: (1) manganese, Ni, Co, Zr and Cu decreasing in average values, (2) gold, followed by Cr, Mo, W, V, Ti, Bi, Pb, Zn, Sn, Sb, As, Te, Se, Th and U, increases, and (3) silver maintaining the same value.

4.13 Acknowledgments

This research is the result of the on-going Ph. D. thesis by the first author at the Federal University of Minas Gerais-UFMG, which is fully financed by Brazil's National Council of Technological and Scientific Development-CNPq, Vale and AngloGold Ashanti Córrego do Sítio Mineração S/A-AGA. The student's scholarship is granted by CNPq.

The authors thank AGA for their logistic and technical support, and for allowing the publication of this manuscript. Special thanks are due to Rodrigo Martins who has maintained his

commitment to our research group throughout. We also acknowledge the support of UFMG, UWA, CAPES, FAPEMIG and FUNDEP.

Special thanks to the Centre for Microscopy, Characterization and Analysis-CMCA at UWA, Perth, where back-scattered images and elemental mapping with EPMA on the sulfide minerals were produced, and to Sarah Gilbert from the Centre of Excellence in Ore Deposits-CODES, Hobart, who helped us with the LA-ICP-MS analyses and final quantification of the chemical elements. Bruna S. Cota assisted in the preparation of the figures.

PARTE 4 – Considerações Finais.

Capítulo 5: Implicações para exploração de ouro no QF

A combinação de diversas técnicas, mapeamento geológico (Figura 11), análise estrutural (Figuras 14 e 15), modelamento 3D de corpo de minério (Figura 18) e geocronologia (Figura 19), combinadas com estudos detalhados de sequência paragenética (Figura 33), usando observação textural (Figuras 31 e 32), mapeamento de elementos químicos por EPMA (Figuras 34, 35, 37 e 38) e análises quantitativas *in situ* LA-ICP-MS em piritas diagenética e hidrotermais de pelitos carbonosos (Figuras 40a e 41), bem como piritas e arsenopirita hidrotermais de FFB (Figura 40b e42) do depósito de ouro Lamego, fornecem informações significantes para a exploração de novas jazidas de ouro nos terrenos arqueanos do QF. Seis características principais podem ser sumarizadas:

1) Alvos de exploração litológica: No pacote de rochas vulcanossedimentares que hospeda o depósito Lamego (Figura 6), os pelitos carbonosos são um dos principais alvos litológicos, uma vez que formam envelopes em torno da zona de interesse econômico. Os mesmos (1) limitam e-ou contêm as zonas de silicificação de alto teor, e (2) formam o contato de capa da FFFB. Os pelitos carbonosos agiram como uma barreira impermeável dificultando a migração dos fluidos hidrotermais auríferos que, assim, ficaram contidos abaixo dessa litologia (Figura 11). Métodos de investigação indireta, como por exemplo geofísica, podem ser direcionados para delimitar as regiões de contato dos pelitos carbonosos com FFB e as zonas de silicificação associadas.
2) Alvos da exploração estrutural (i): Na porção NW da QF, próximo à área de Lamego, são as estruturas orientadas NE-SW, com mergulho para SE, que definem a foliação S_{1-2}, além das dobras reclinadas F_2 (Figura 14 e 15). Isto se faz verdade considerando que a foliação S_{1-2} controla as zonas de silicificação; e que zonas de charneiras de dobras na FFB representam os mais altos teores de ouro (Figura 18).
3) Alvos da exploração estrutural (ii): Falhas normais e clivagem de crenulação afetaram a área em torno do depósito Lamego, gerando estruturas orientadas NS, com mergulho para W, sendo relacionado ao evento regional Brasiliano-D_4. Essas estruturas causaram modificação espacial nos corpos de minério, incluindo seu deslocamento lateral e basculamento das zonas de minério. É possível que corpos interrompidos por essas estruturas mais jovens de fato tenham continuidade em profundidade, representando atualmente corpos cegos. É assim fundamental que a segmentação e possível extensão de corpos de minério abaixo dessas estruturas sejam consideradas durante as campanhas exploratórias.
4) Farejadores geoquímicos: Ouro nos sulfetos do pelito carbonoso mostram uma correlação

positiva com Ag e elementos crustais como Bi, Pb e Sb (Figura 40a), enquanto que na FFB está correlacionado com Ag, As, Pb e Cu (Figura 40b). Anomalias significativas desses elementos em campanhas de sedimentos de corrente e solo podem ser usados como indicadores para a exploração de novas ocorrências de ouro hospedados em FFB.

5) Paragênese mineral (i): Pelitos carbonosos possuem piritas que são desprovidas de ouro econômico (Figura 40a), sendo que o teor de ouro aumenta com a intensidade da alteração hidrotermal, onde este metal é mais concentrado na Py-4_{CP} (Figura 40a). O reconhecimento de áreas ricas em sulfetos, onde os pelitos carbonosos exibem pirita grossa, subédrica a euédrica (Py-4_{CP}), em proximidade com FFB e/ou zonas de silicificação, pode ajudar a identificar corpos cegos.
6) Paragênese mineral (ii): Os melhores valores de ouro medidos em piritas da FFB estão dentro da Py-1_{BIF} (porosa e fina) e Py-2_{BIF} (porosa, subédrica, granulação média a grossa), enquanto Py-3_{BIF} (clara, fina a média de granulação) exibe os valores mais baixos. Considerando que as diferenças entre esses três tipos de pirita são macroscopicamente viáveis em afloramentos não intemperizados, a identificação de áreas que são mais ricas em Py-1_{BIF} e Py-2_{BIF} podem ajudar a identificar locais de sondagem.

Capítulo 6: Conclusões

Com base nos dados de campo, petrográficos, geocronológicos, modelamento de corpo de minério, paragênese mineral, mapeamento de elementos químicos com EPMA e análises quantitativas *in situ* LA-ICP-MS, as principais conclusões práticas deste trabalho são listadas a seguir.

6.1 Estratigrafia (Capítulos 3 e 4)

1) Da base para o topo, a litoestratigrafia no depósito de Lamego é definida por rocha vulcânica máfica representado por metabasalto (xisto a clorita, carbonato, sericita, quartzo); *chert* bandado com FFB sendo ambos carbonosos e/ou ferruginosos; e pelitos carbonosos e micáceos (Figura 6). Contêm minerais metamórficos indicativos da fácies xisto verde.
2) Tanto *chert* quanto FFB são referidos como FFB Lamego. A FFB Lamego é caracterizada pela alternância de bandas escuras compostas por carbonato-quartzo (± magnetita) e bandas claras de quartzo-carbonato (Figura 10c, d).
3) Rochas peliticas são representadas por pelitos carbonosos e micáceos (Figura 10g, h), que envolvem todo o depósito Lamego.

6.2 Estruturas (Capítulo 3)

4) A macroestrutura em Lamego é representada pela dobra Lamego. Esta é uma dobra sem raiz, reclinada, isoclinal, cilíndrica com plano axial de direção NE-SW, mergulhando 30º para SE (Figura 7a). A zona de charneira no quadrante SW é representada pelo corpo de minério Cabeça de Pedra (Figura 7b); o flanco normal, no quadrante SE, compreende o corpo Arco da Velha (Figura 7c); o flanco invertido, no quadrante NW, envolve o corpo Queimada (Figura 7c); e a interseção dos flancos, quadrante NE, é o Corpo Carruagem.
5) Duas gerações de estruturas, G_1 e G_2, são reconhecidas no depósito Lamego (Tabela 8), sendo G_1 representada por: (i) estruturas planares como foliação S_{1-2}, veios V_1 e V_2, zonas de cisalhamento; estes são geralmente orientadas NE-SW, mergulho para a SE, com a exceção dos veios V_1 que mergulham para NE e provavelmente representam as estruturas mais antigas no depósito Lamego; e (ii) estruturas lineares como lineação L_{1-2} e eixos de dobras F_2 que mergulham para SE. Por outro lado, G_2 é representada: (i) pela clivagem de crenulação S_3 orientada N-S, mergulhando a E; e (ii) pelo eixo de dobras F_3 e lineação de crenulação L_3 que são orientados N-S e mergulham para S.
6) Como a foliação Paleoproterozóica relativa ao evento D_3 não é claramente reconhecida no depósito Lamego, e seu *trend* regional na área do depósito é similar ao acamamento

tectonizado S_0 e à foliação original S_{1-2}, é provável que a foliação regional se sobreponha à foliação S_{1-2}, e, portanto, ambos são indistinguíveis.

7) A clivagem espaçada/crenulação S_3 está relacionada com o evento regional Brasiliano-D_4 que resulta em dobras e empurrões orientados N-S com vergência para E. Estas dobras regionais D_4 movem as estruturas G_1 para a posição atual. As estruturas G_1 tinham uma posição original NW-SE, que provavelmente representava o *trend* do cinturão Rio das Velhas.

6.1 Estilos de mineralização e alteração hidrotermal (Capítulos 4 e 3)

8) Quatro estilos de mineralização de ouro são identificados, nomeadamente veios, substituição, disseminação e vênulas de pirita-quartzo. A mineralização em Lamego é principalmente hospedada pelo estilo de substituição, associada com sulfetos.
9) Nas zonas mineralizadas, quartzo, pirita, arsenopirita e pirrotita são os principais minerais hidrotermais. Eles desenvolvem-se em todas as rochas paralelamente a foliação S_{1-2}.
10) Quartzo ocorre em três tipos: (i) quartzo fumê, deformado, grosso em massas irregulares que podem ser concordantes ou discordantes com a zona mineralizada; (i) fino, granoblástico, branco e leitoso formado a da recristalização do quartzo fumê; (iii) quartzo leitoso, encontrado principalmente em zonas de falha cortando quartzo do tipo 1 e 2. Estes mesmos tipos de quartzo correspondem, respectivamente, aos quartzos (1), (2) e (3) da paragênese mineral (Figura 33).

6.3 Geometria de corpo de minério (Capítulo 3)

11) Lentes de alto de teor de ouro (Figuras 17a, d e 18a) mostram padrão esferoidal e estão distribuídas ao longo da foliação S_{1-2}. Estas lentes representam zonas de charneira de dobras reclinadas F_2 com o *plunge* de corpos de minério controlado pelos eixos de dobras.
12) Lentes de baixo teor de ouro são controladas por estruturas do tipo *pinch-and-swell*, localmente *boudins* de quartzo. Os *boudins* possuem duas direções ortogonais, uma para NW-SE e outra para NE-SW, exibindo um estilo de boudinagem do tipo tablete de chocolate.

6.2 Geocronologia U-Pb (SHRIMP; Capítulo 3)

13) A idade de 2730 ± 42 Ma obtida em monazita hidrotermal (Figura 19b) é interpretada como sendo a idade da mineralização de ouro, sincrônico com as estruturas G_1.
14) Entretanto, a idade discordante 2387 ± 46 Ma, também obtida em monazita hidrotermal (Figura 19b), pode ser interpretada como relativa aos estágios iniciais da orogenia

acrescionária Minas, e representa o registro no *greenstone belt* Rio das Velhas, que afetou a área do depósito Lamego. Esse registro é bem conhecido no cinturão Mineiro.

15) A idade de 518.5 ± 9 Ma obtida em xenotima hidrotermal é interpreta como um forte registro da Orogenia Brasiliana na região do QF. O mesmo é reconhecido: (i) pela formação de estruturas G_2, pós-mineralização, e que têm orientação N-S; relacionam-se às estruturas regionais D_4, correlatas com encurtamento regional E-W, e (ii) por importante evento magmático termal Brasiliano descrito no Orógeno Araçuaí, expresso localmente pela presença de pegmatitos que intrudem o Supergrupo Minas, e que se sobrepõem ao Supergrupo Rio das Velhas.
16) Apesar destas idades sideriana e cambriana, não consideramos ter havido remobilização da mineralização de ouro de idade arqueana nestes períodos, uma vez que a mobilização de depósitos de ouro exigiria grandes volumes de fluidos, o que não pode ser claramente estabelecido para o depósito Lamego.
17) Embora a deformação Brasiliana seja responsável pelo desenvolvimento das estruturas G_2 e pelo deslocamento dos corpos de minério no depósito Lamego, não há evidência para a formação de novos minerais hidrotermais, sulfetos e ouro.

6.3 Paragênese Mineral (Capítulo 4)

18) A sequência paragenética mostrada na Figura 33 é principalmente representada por sulfetos, magnetitas, sulfossais, fosfatos e ouro. Pirita (FeS_2), arsenopirita (FeAsS), esfalerita (ZnS), calcopirita ($CuFeS_2$), galena (PbS) e pirrotita ($Fe_{(1-X)}S$) são os principais sulfetos. Magnetita (Fe_3O_4) é o único oxido; nikelina (NiAs) e tenantita-tetraedrita ($Cu_9Fe_3Sb_4S_{13}$) os minerais do grupo dos sulfossais, enquanto monazita é o fosfato identificado.
19) Sete tipos de pirita estão presentes, quatro no pelito carbonoso (Figura 31a-m) e três na FFB (Figura 32a-k). A primeira é framboidal, microcristalina, subédrica a euédrica, e constitui a Py-1_{CP} (Figura 31b, e, f, g); a Py-2_{CP} é nodular, subédrica (Figura 31d, h, I, j, k); Py-3_{CP} é de granulação fina, límpida, euédrica e recristalizada (Figura 31d j, k); e Py-4_{CP} é porosa a límpida, fina a grossa, euédrica e recristalizada (Figura 31d, l, m). As piritas da FFB são Py-1_{BIF}, porosas e de granulação fina (Figura 32b, e, f); Py-2_{BIF} é porosa, subédrica, média a grossa (Figura 32 b, d, h, i); e a Py-3_{BIF} é límpida, fina a média (Figura 32b, j, k).
20) Quatro estágios de evolução são reconhecidos: (1) pré-hidrotermal (diagenético), marcado pelo desenvolvimento da Py-1_{CP} e sua recristalização inicial para formar Py-2_{CP}; considerando que os valores de Au aumentam do centro para as bordas mais recristalizadas dos grãos de

Py-1_{CP}, a precipitação de ouro deve ter iniciado nas fases iniciais de hidrotermalismo, (2) estágio cedo hidrotermal, onde Py-2_{CP} continuou a se desenvolver; Py-3_{CP} formou nos pelitos carbonosos, e Py-1_{BIF} formou na FFB, (3) estágio principal hidrotermal, reconhecido pelo desenvolvimento de Py-4_{CP} e Py-2_{BIF}, respectivamente nos pelitos carbonosos e na FFB, e onde o ouro mostra os melhores valores, e (4) estágio tarde hidrotermal, marcado pelo desenvolvimento final de Py-4_{CP} nos pelitos carbonosos e Py-3_{BIF} na FFB. O estágio cedo hidrotermal é dominado pela recristalização bem como desenvolvimento do novo tipo de pirita (Py-2_{CP}), e é assim interpretado como um estágio metamórfico/hidrotermal.

6.4 EPMA (Capítulo 4)

21) Interpretação de mapeamento de elemento químico com EPMA demonstra que: (1) Py-1_{CP} e Py2_{CP} possuem uma distribuição homogênea de elementos, como Fe, S, As, Ni, Co e Sb (Figuras 34 e 35), (2) Py-3_{CP}, Py-1_{BIF} ePy-2_{BIF} exibem zonamento de As-S-Fe (Figuras 35 e 37), e (3) Py-4_{CP} e Py-3_{BIF} exibem zonamento de Ni-Co (Figuras 36 e 38).
22) Há uma distribuição de metal única rica em As-Ni na Py-3_{CP} e rica em Co na Py-4_{CP} (Figuras 34, 35, 36 e 43d, e). Estes são provavelmente o resultado da difusão de metal, devido a interação de fluxo de fluido durante a recristalização, diferente do que se observa para os elementos tais como o ouro.
23) O zonamento de Ni-Co na Py-3_{BIF} (Figura 38i, j) sugere que o crescimento da Py-3_{BIF} aconteceu em três passos (Figura 43h, i) com o primeiro passo (Figura 43h) sendo marcado pelo zonamento de S-Fe-As (Figura 38b, c, e); o segundo passo (Figura 43h) reconhecido pelo zonamento de Ni-Co (Figura 38i, j); e o terceiro passo (Figura 43i) mostrando depleção em As e Mn com distribuição homogênea de S, Fe, Sb, Co e Ni.

6.5 LA-ICP-MS (Capítulo 4)

24) Análises de LA-ICP-MS em piritas do pelito carbonoso revelam (Fig. 20a): (1) Py-1_{CP} é rica em Mn, Cr, W, V, Ti, Zr, Bi, Zn, Sn, Te, Th e U, e possuem altos valores de elementos traço quando comparados com Py-2_{CP}, exceto para Cu, (2) Py-2_{CP} possui mais ouro do que Py-3_{CP} e é depletada em todos os outros elementos; (3) Py-3_{CP} é rica em Se, possui mais As do que Py-2_{CP}, possui uma variação consistente de valores, e em muitos casos uma menor média de valores exceto para Cr, Zr, Se e U, e (4) Py-4_{CP} é rica em Au, Ni, Mo, Co, Cu, Pb, Ag, Sb e As, e mostra uma grande variação destes elementos mas que são menos expressivas do que a variação observada para a Py-3_{CP}, mas mais do que as variações da Py-1_{CP} e Py-2_{CP}.

25) Os três elementos mais ricos na Py-1_{CP} são As (2317,347 - 5035,646), Ti (95,263 - 3224,243) e Ni (844,323 - 1543,923), enquanto As, Ni e Co são os três elementos mais ricos na Py-2_{CP}, Py-3_{CP} e Py-4_{CP} (Figura 40a).
26) Ouro no pelito carbonoso exibe excelente afinidade com elementos crustais, como por exemplo Bi, Pb e Sb, e boa correlação com Ni, Co, Cu, Ag e Te (Figura 40a).
27) Ouro no pelito carbonoso está relacionado com sua sedimentação, mas também com aatividade hidrotermal (Figura 43a-e). Da Py-1_{CP} para Py-2_{CP}, Au é constante, enquanto que As decresce; da Py-2_{CP} para Py-3_{CP} Au e As decrescem, mas da Py-3_{CP} para Py-4_{CP} há um notável incremento/aumento de Au e As (Figura 40a), indicando um intenso clímax do ouro provavelmente perto do estágio final de deformação e relacionado com fluxo de fluido hidrotermal (Figura 43a,b).
28) O relativo enriquecimento em Ni, V, Zn, Pb, Ag (Figura 40a) nas piritas Py-1_{CP} e Py-2_{CP} (Figura 43c, d) pode indicar que estes elementos foram provavelmente concentrados por processos orgânicos, durante a sedimentação e diagênese de sedimentos ricos em matéria orgânica, em ambiente euxínico.
29) O incremento em Mn, Cr, W, V, Ti, Zr, Bi, Zn, Sn, Te, Th, U, bem como Au e As (Figura 40a), denota que certos elementos traço na estrutura da pirita foram lixiviados no estágio cedo hidrotermal e provavelmente introduzidos no fluido hidrotermal (Figura 43c, d, e).
30) A fraca correlação entre Ni versus Au e V versus Au (Figura 40a), nas piritas singenéticas Py-1_{CP} e Py-2_{CP} (Figura 43c, d), implica na possibilidade de que algum ouro era nativo do pelito carbonoso e originalmente foi concentrado por processos orgânicos similar ao que foi proposto por Large et al. (2009, 2011). Como para Py-3_{CP} e Py-4_{CP}, ouro e arsênio estão claramente correlacionados (Figuras 40a e 41k), isso sugere introdução de metal por fonte hidrotermal (Figura 43a, b, e).
31) As análises por LA-ICP-MS de piritas da FFB evidenciam (Figura 40b): (1) ouro, seguido por Mn, V, Cd, Zr, Bi, Pb, Zn, Sn, Ag e U, decrescem em valores médios da Py-1_{BIF} para Py-2_{BIF}, (2) Molibdênio, W, Ti, Cu, As, Se e Th aumentam da Py-1_{BIF} para Py-2_{BIF}, e decrescem da Py-2_{BIF} para Py-3_{BIF}, (3) cromo, Co e Sb decrescem da Py-1_{BIF} para Py-2_{BIF}, e aumentam novamente para Py-3_{BIF}, e (4) níquel aumenta da Py-1_{BIF} para Py-3_{BIF}.
32) Por outro lado, os padrões observados na Apy-1_{BIF} (Figura 40b), considerando que ela se forma depois da Py-3_{BIF} (Figuras 32h, i e 33) denota: (1) manganês, Ni, Co, Zr e Cu decrescem em valores médios, (2) ouro, seguido por Cr, Mo, W, V, Ti, Bi, Pb, Zn, Sn, Sb, As, Te, Se, Th e U, aumentam, e (3) prata não apresenta variação.

33) Ouro na FFB exibe boa afinidade com Pb, Cu, As e Ag, (Figura 40a), o que combinado com o zonamento de As-Fe-S e Co-Ni, evidencia uma origem hidrotermal para os sulfetos.

Capítulo 7: Referências Bibliográficas

Algeo TJ, Maynard JB (2004) Trace-element behavior and redox facies in core shales of Upper Pennsylvanian Kansas-type cyclothems. Chemical geology 206:289-318.

Alkmim FF, Marshak S (1998) Transamazonian orogeny in the Southern São Francisco craton region, Minas Gerais, Brazil: evidence for Paleoproterozoic collision and collapse in the Quadrilátero Ferrífero. Precambrian Research 90:29-58.

Alkmim FF, Noce C (2006) The Paleoproterozoic record of the São Franscisco Craton.

IGCP 509 Field workshop, Bahia and Minas Gerais, Brazil. Field Guide & Abstracts. Brazil, pp 114.

Almeida FFMd (1967) Origem e evolução da plataforma brasileira. Deparamento Nacional da Produção Mineral - Divisão de Geologia e Mineralogia 241:36.

Almeida FFMd (1977) O Cráton do São Francisco. Revista Brasileira de Geociências 7:349-364.

Almeida FFMd, Hasui Y (1984).O pré-cambriano do Brasil. Edgar Blücher Ltda, São Paulo.

Almeida FFMd, Brito Neves BBd, Dal Ré Carneiro C (2000) The origin and evolution of the South American Platform. Earth-Science Reviews 50:77-111.

Armstrong J (1988) Quantitative analysis of silicate and oxide minerals: comparison of Monte Carlo, ZAF and phi-rho-z procedures. Microbeam analysis 23:239-246.

Ashanti A (2013) Annual Integrated Reported 2013 Annual Integrated Reported. http: //www.anglogoldashanti.com/en/Media/Reports/Integrated%20Reports/AGAannualintegratedreport2013.pdf.

Ashanti A (2014) AngloGold Ashanti 2013 Integrated Financial Report. http://www.aga-reports.com/13/ir/review/regional-reviews/americas.

Baltazar OF, Silva SL (1996) Relatório Mapa Geológico Integrado do Supergrupo Rio das Velhas, escala 1:100.000. In: Mineral DNdP (ed). Departamento Nacional de Produção Mienral, Belo Horizonte, pp 136.

Baltazar OF, Pedreira AJ (1998) Associações litofaciológicas. In: Mineral DNdP, Minerais CdPeR (eds). Belo Horizonte.

Baltazar O, Zucchetti M (2007) Lithofacies associations and structural evolution of the Archean Rio das Velhas greenstone belt, Quadrilátero Ferrífero, Brazil: A review of the setting of gold deposits. Ore Geology Reviews 32:471-499.

Bierlein FP, Groves DI, Goldfarb RJ, Dubé B (2006) Lithospheric controls on the formation of provinces hosting giant orogenic gold deposits. Mineralium Deposita 40:874-886.

Brandt RT, Gross GA (1972) Problems of nomenclature for banded ferroginous–cherty sedimentary rocks and their metamorphic equivalents. Economic Geology 67:682-684.

Brito Neves BB (2011) The Paleoproterozoic in the South-American continent: Diversity in the geologic time. Journal of South American Earth Sciences 32:270-286.

Carneiro MA, Teixeira W, Machado N (1994) Geological evolution of a sialic Archaean crustal fragment from the Quadrilátero Ferrífero in eastern-central Brazil, based on U-Pb, Sm-Nd, Rb-Sr, and K-Ar isotopic constraints. Terra Noxtra 2:12-13.

Chemale Jr F, Rosière CA, Endo I (1994) The tectonic evolution of the Quadrilátero Ferrífero, Minas Gerais, Brazil. Precambrian Research 65:25-54.

Cook NJ, Ciobanu CL, Mao J (2009) Textural control on gold distribution in As-free pyrite from the Dongping, Huangtuliang and Hougou gold deposits, North China Craton (Hebei Province, China). Chemical Geology 264:101-121.

Cook NJ, Ciobanu CL, Meria D, Silcock D, Wade B (2013) Arsenopyrite-pyrite association in an orogenic gold ore: tracing mineralization history from textures and trace elements. Economic Geology 108:1273-1283.

Coveney Jr R (2000) Metalliferous shales and the role of organic matter with examples from China, Poland, and the United States. Ore genesis and exploration: the roles of organic matter Rev Econ Geol 9:251-280.

Danyushevsky L, Robinson P, Gilbert S, Norman M, Large R, McGoldrick P, Shelley M (2011) Routine quantitative multi-element analysis of sulphide minerals by laser ablation ICP-MS: Standard development and consideration of matrix effects. Geochemistry: Exploration, Environment, Analysis 11:51-60.

Davis GH, Reynolds SJ (1996) Structural geology of rocks and regions. John Wiley (New York).

Deol S, Deb M, Large RR, Gilbert S (2012) LA-ICPMS and EPMA studies of pyrite, arsenopyrite and loellingite from the Bhukia-Jagpura gold prospect, southern Rajasthan, India: Implications for ore genesis and gold remobilization. Chemical Geology 326:72-87.

DeWitt E, Thorman C, Landis G, Zartman R (1996) A progress report on the age and origin of gold deposits hosted by iron-formation in the Belo Horizonte area. Minas Gerais, Brazil 7.

DeWitt E, Thorman C, Ladeira E, Zartman R, Landis G, Wooden J (2000) Origin and age of gold deposits at São Bento and Morro Velho, Brazil 31th International Geological Congress, Rio de Janeiro, Brazil, CD-ROM.

Donovan JJ, Snyder DA, Rivers ML (1993) An improved interference correction for trace element analysis Proceedings of the Annual Meeting-Electron Microscopy Society of America. San Francisco Press, pp 1646-1646.

Donovan JJ, Tingle TN (1996) An improved mean atomic number background correction for quantitative microanalysis. Microscopy and Microanalysis 2:1-7.

Dorr JVN (1957) Revisão da Estratigráfia Pré-cambriana do Quadrilátero Ferrífero: Brasil. In: Mineral DNPM (ed). Departamento Nacional de Produção Mineral, Minas Gerais, pp 81.

Dorr JVN (1969) Physiographic, Stratigraphic and Structural Development of the Quadrilátero Ferrífero, Minas Gerais, Brazil: Regional Geology of the Quadrilátero Ferrífero, Minas Gerais, Brazil.

Fletcher IR, McNaughton NJ, Aleinikoff JA, Rasmussen B, Kamo SL (2004) Improved calibration procedures and new standards for U–Pb and Th–Pb dating of Phanerozoic xenotime by ion microprobe. Chemical Geology 209:295-314.

Fletcher IR, McNaughton NJ, Davis WJ, Rasmussen B (2010) Matrix effects and calibration limitations in ion probe U–Pb and Th–Pb dating of monazite. Chemical Geology 270:31-44.

Foster G, Kinny P, Vance D, Prince C, Harris N (2000) The significance of monazite U–Th–Pb age data in metamorphic assemblages; a combined study of monazite and garnet chronometry. Earth and Planetary Science Letters 181:327-340.

Fyfe W (1987) Tectonics, fluids and ore deposits: mobilization and remobilization. Ore Geology Reviews 2:21-36.

Gair JE (1962) Geology and ore deposits of the Nova Lima and Rio Acima quadrangles, Minas Gerais, Brazil. US Government Printing Office.

Goldfarb R, Groves D (2001) Orogenic gold and geologic time: a global synthesis. Ore Geology Reviews 18:1-75.

Goldfarb RJ, Baker T, Dubé B, Groves DI, Hart CJ, Gosselin P (2005) Distribution, character, and genesis of gold deposits in metamorphic terranes. Economic Geology 100th Anniversary Volume:407-450.

Gregory DD, Large RR, Halpin JA, Baturina EL, Lyons TW, Wu S, Danyushevsky L, Sack PJ, Chappaz A, Maslennikov VV (2015) Trace element content of sedimentary pyrite in black shales. Economic Geology 110:1389-1410.

Gross GA (1965) Geology of iron deposits in Canada. Department of Mines and Technical Surveys, Canada.

Gross GA (1980) A classification of iron formations based on depositional environments. The Canadian Mineralogist 18:215-222.

Groves DI, Goldfarb RJ, Gebre-Mariam M, Hagemann S, Robert F (1998) Orogenic gold deposits: a proposed classification in the context of their crustal distribution and relationship to other gold deposit types. Ore Geology Reviews 13:7-27.

Groves DI, Goldfarb RJ, Robert F, Hart CJ (2003) Gold deposits in metamorphic belts: overview of current understanding, outstanding problems, future research, and exploration significance. Economic Geology 98:1-29.

Hagemann S, Cassidy KF (2000) Archean orogenic lode gold deposits. Gold in. pp 9-68.

Hagemann S, Gill HA (2011) Oxygen and hydrogen isotope study of the Archean granulite-hosted Griffin's Find gold deposit, Western Australia In: Reich M, Barra F, Tornos F (eds) Let's Talk Ore Deposits Proceedings of 11th Biennial SGA Meeting. Antofagasta, Chile.

Hartmann LA, Endo I, Suita MTF, Santos JOS, Frantz JC, Carneiro MA, McNaughton NJ, Barley ME (2006) Provenance and age delimitation of Quadrilátero Ferrífero sandstones based on zircon U–Pb isotopes. Journal of South American Earth Sciences 20:273-285.

Herz N (1970) Gneissic and igneous rocks of the Quadrilátero Ferrífero, Minas Gerais, Brazil. US Government Printing Office.

Hill EJ, Oliver NH, Cleverley JS, Nugus MJ, Carswell J, Clark F (2013) Characterisation and 3D modeling of a nuggety, vein-hosted gold ore body, Sunrise Dam, Western Australia. Journal of Structural Geology.

Hill E, Oliver NH, Fisher L, Cleverley JS, Nugus MJ (2014) Using Geochemical Proxies to Model Nuggety Gold Deposits: An example from Sunrise Dam, Western Australia. Journal of Geochemical Exploration.

Hobbs BE (1987) Principles involved in mobilization and remobilization. Ore Geology Reviews 2:37-45.

James HL (1954) Sedimentary facies of iron-formation. Economic Geology 49:235-293.

Junqueira P, Lobato L, Ladeira E, Simões E (2007) Structural control and hydrothermal alteration at the BIF-hosted Raposos lode-gold deposit, Quadrilátero Ferrífero, Brazil. Ore Geology Reviews 32:629-650.

Kerrich R, Goldfarb RJ, Groves DI, Garwin S (2000) The geodynamics of world-class gold deposits: characteristics, space-time distribution, and origins Reviews in Economic Geology. Society of Economic Geologist, Boulder, Colorado, pp 501-551.

Kerrich R, Goldfarb RJ, Richards JP (2005) Metallogenic provinces in an evolving geodynamic framework. Economic geology 100:1097-1136.

Ladeira EA (1980a) Metallogenesis of gold at the Morro Velho Mina and in the Nova lima District, Quadrilátero Ferrífero , Minas Gerais , Brazil. Geology. University of Western Ontario, Canada, pp 272.

Ladeira E (1980ab) Geology, Petrography and Geochemistry of Nova Lima Group, Quadrilátero Ferrífero, Minas Gerais, Brasil. XVII Geowiss Lateinamer. Heidelberg, pp 47-48.

Ladeira E (1980c) Gênese do Ouro na Mina de Morro Velho e no Distrito de Nova Lima, Minas Gerais, Brasil. In: Geologia SBd (ed) 31º Congresso Brasileiro de Geologia. Sociedade Brasileira de Geologia, Camboriu, pp 371.

Ladeira E, Geologia SBd (1985) Metalogênese do ouro na Mina de Morro Velho e no distrito de Nova Lima, quadrilátero ferrífero, Minas Gerais, Brasil. Contribuição à Geologia e à Petrologia: Dedicado à Memória de Djalma Guimarães.

Ladeira EA (1991) Genesis of gold in Quadrilátero Ferrífero: a remarkable case of permanency, recycling and inheritance-a tribute to Djalma Guimarães, Pierre Routhier and Hans Ramberg Brazil Gold. pp 11-30.

Lana C, Alkmim FF, Armstrong R, Scholz R, Romano R, Nalini Jr HA (2013) The ancestry and magmatic evolution of Archaean TTG rocks of the Quadrilátero Ferrífero province, southeast Brazil. Precambrian Research 231:157-173.

Large RR, Maslennikov VV, Robert F, Danyushevsky LV, Chang Z (2007) Multistage sedimentary and metamorphic origin of pyrite and gold in the giant Sukhoi Log deposit, Lena gold province, Russia. Economic Geology 102:1233-1267.

Large RR, Danyushevsky L, Hollit C, Maslennikov V, Meffre S, Gilbert S, Bull S, Scott R, Emsbo P, Thomas H (2009) Gold and trace element zonation in pyrite using a laser imaging technique: implications for the timing of gold in orogenic and Carlin-style sediment-hosted deposits. Economic Geology 104:635-668.

Large RR, Bull SW, Maslennikov VV (2011) A carbonaceous sedimentary source-rock model for Carlin-type and orogenic gold deposits. Economic Geology 106:331-358.

Lima TM, Neves CAR (2014) Sumário Mineral 2014 In: Mineral DNPM (ed). Ministério de Minas e Energia, Brasília, Distrito Federal, pp 148.

Lobato LM, Vieira FWR (1998a) Styles of hydrothermal alteration and gold mineralization associated with the Nova Lima Supergroup of the Quadrilátero Ferrífero: Parte I, Description of Selected Gold Deposit. Revista Brasileira de Geociências 28:339-354.

Lobato LM, Vieira FWR (1998b) Styles of hydrothermal alteration and gold mineralization associated with the Nova Lima Supergroup of the Quadrilátero Ferrífero: Parte II, The Archean mesothermal gold-bearing hydrothermal system. Revista Brasileira de Geociências 28:355-366.

Lobato LM, Ribeiro-Rodrigues LC, Zucchetti M, Noce CM, Baltazar OF, da Silva LC, Piva Pinto C (2001a) Brazil's premier gold province. Part I: The tectonic, magmatic and structural setting

of the Archean Rio das Velhas greenstone belt, Quadrilátero Ferrífero. Mineralium Deposita 36:228-248.

Lobato LM, Ribeiro-Rodrigues LC, Vieira FWR (2001b) Brazil's premier gold province. Part II: geology and genesis of gold deposits in the Archean Rio das Velhas greenstone belt, Quadrilátero Ferrífero. Mineralium Deposita 36:249-277.

Lobato L, Santos J, McNaughton N, Fletcher I, Noce C (2007) U–Pb SHRIMP monazite ages of the giant Morro Velho and Cuiabá gold deposits, Rio das Velhas greenstone belt, Quadrilátero Ferrífero, Minas Gerais, Brazil. Ore Geology Reviews 32:674-680.

Lobato LM, Martins BdS, Rosière CA, Figueiredo e Silva RC, Lemos LHA, Villanova FLSP, Amaral LFS (2013) Depth variation characteristics at the Carruagem orebody, Archean BIF-hosted Lamego gold deposit, Quadrilátero Ferrífero, Brazil In: Applied SG (ed) 12th SGA Biennial Meeting - Mineral Deposit Research for a High-Tech World. SGA, Uppsala, Sweden, pp 1144-1147.

Longerich H, Jackson S, Gunther D (1997) Laser ablation inductively coupled plasma mass spectrometric transient signal data acquisition and analyte concentration calculation (vol 11, pg 899, 1996). Royal Societ of Chemistry, Thomas Graham House, Science Park, Milton Road, Cambridge, England CB4 4WF, pp 391-391.

Ludwig KR (2003) User's manual for Isoplot 3.00: a geochronological toolkit for Microsoft Excel. Kenneth R. Ludwig.

Ludwig K (2009) SQUID 2: a user's manual. Berkeley Geochronology Center 100.

Machado N, Noce CM, Oliveira OAB, Ladeira EA (1989) Evolução geológica do Quadrilátero Ferrífero no Arqueano e Proterozóico Inferior com base em Geogronologia U-Pb. In: Geologia SBd (ed) Anais do V Simpósio de Geologia de Minas Gerais. Núcleo Minas Gerais, Belo Horizonte, pp 1-4.

Machado N, Carneiro MA (1992) U-Pb evidence of Late Archean tectonothermal activity in the southern São Francisco shield, Brazil. Canadian Journal Earth Science 29:2341-2346.

Marshak S, Alkmim FF (1989) Proterozoic contraction/extension tectonics of the southern São Francisco region, Minas Gerais, Brazil. Tectonics 8:555-571.

Martins BdS (2011) Controle da Mineralização Aurífera de Lamego, Sabará, Quadrilátero Ferrífero, MG. Geologia. Universidade de Minas Gerais, Belo Horizonte, pp 250.

Martins BdS, Rosière CA, Lobato LM, Figueiredo e Silva RC, Baars FJ, Tschiedel MW, Oliveira H, Penha UC (2011) Mineralization control of the Lamego gold deposit, Sabará, Quadrilátero Ferrífero, Minas Gerais, Brazil In: Applied SG (ed) 11th SGA Biennial Meeting "Let´s Talk Ore Deposits". Society Geology Applied, Antofagasta, Chile, pp 583-585.

Martins BdS, Lobato LM, Rosière CA, Hagemann SG, Santos JOS, Villanova FLdSP, e Silva RCF, de Ávila Lemos LH (2016) The Archean BIF-hosted Lamego gold deposit, Rio das Velhas greenstone belt, Quadrilátero Ferrífero: Evidence for Cambrian structural modification of an Archean orogenic gold deposit. Ore Geology Reviews 72:963-988.

Martins Pereira SL, Lobato LM, Ferreira JE, Jardim EC (2007) Nature and origin of the BIF-hosted São Bento gold deposit, Quadrilátero Ferrífero, Brazil, with special emphasis on structural controls. Ore Geology Reviews 32:571-595.

Morales MJ, e Silva RCF, Lobato LM, Gomes SD, Gomes CC, Banks DA (2016) Metal source and fluid–rock interaction in the Archean BIF-hosted Lamego gold mineralization: Microthermometric and LA-ICP-MS analyses of fluid inclusions in quartz veins, Rio das Velhas greenstone belt, Brazil. Ore Geology Reviews 72:510-531.

Noce CM (1995) Geocronologia dos eventos magmáticos, sedimentares e metamórficos na região do Quadrilátero Ferrífero, Minas Gerais. Intituto de Geociências - Departamento de Geologia. Universidade de São Paulo, São Paulo, pp 128.

Noce CM, Zuccheti M, Baltazar OF, Armstrong R, Dantas E, Renger F, Lobato LM (2005) Age of felsic volcanism and the role of ancient continental crust in the evolution of the Neoarchean Rio das Velhas Greenstone belt (Quadrilátero Ferrífero, Brazil): U–Pb zircon dating of volcaniclastic graywackes. Precambrian Research 141:67-82.

Noce CM, Tassinari C, Lobato LM (2007) Geochronological framework of the Quadrilátero Ferrífero, with emphasis on the age of gold mineralization hosted in Archean greenstone belts. Ore Geology Reviews 32:500-510.

Ohfuji H, Rickard D (2005) Experimental syntheses of framboids—a review. Earth-Science Reviews 71:147-170.

Oliveira OAB (1984) As falhas de empurrão e suas implicações na estratigrafia e metalogênese do Quadrilátero Ferrífero-MG. 34º Congresso Brasileiro de Geologia. Minas Gerais, pp 1074-1087.

Oliver NH, Thomson B, Freitas-Silva FH, Holcombe RJ, Rusk B, Almeida BS, Faure K, Davidson GR, Esper EL, Guimarães PJ (2015) Local and Regional Mass Transfer During Thrusting, Veining, and Boudinage in the Genesis of the Giant Shale-Hosted Paracatu Gold Deposit, Minas Gerais, Brazil. Economic Geology 110:1803-1834.

O'Rourke JE (1957) The stratigraphy of the metamorphic rocks of the Rio de Pedras and Gandarela quadrangles, Minas Gerais, Brazil Geology Department. University of Winscosin, Winscosin, pp 106.

Paquette J-L, Nédélec A, Moine B, Rakotondrazafy M (1994) U-Pb, single zircon Pb-evaporation, and Sm-Nd isotopic study of a granulite domain in SE Madagascar. The Journal of Geology:523-538.

Pedreira AJ, Silva SL (1996) Sistemas deposicionais do greenstone belt Rio das Velhas, Quadrilátero Ferrífero, Minas Gerais. 39º Congresso Brasileiro de Geologia. Salvador, pp 138-140.

Pedrosa-Soares A, De Campos CP, Noce C, Silva LC, Novo T, Roncato J, Medeiros S, Castañeda C, Queiroga G, Dantas E (2011) Late Neoproterozoic-Cambrian granitic magmatism in the Araçuaí orogen (Brazil), the Eastern Brazilian Pegmatite Province and related mineral resources. Geological Society, London, Special Publications 350:25-51.

Percival F (1954) Sedimentary facies of iron formation. Economic Geology 49:905.

Ramsay J (1968) Folding and fracturing of rock. New York, pp 568.

Ramsay JYH (1987) The techniques of modern structural geology, volume 2: Folds and fractures. Academic Press, London.

Reich M, Kesler SE, Utsunomiya S, Palenik CS, Chryssoulis SL, Ewing RC (2005) Solubility of gold in arsenian pyrite. Geochimica et Cosmochimica Acta 69:2781-2796.

Ribeiro-Rodrigues LC (1998) Gold in Archaen banded ironformation of the Quadrilátero Ferrífero, Minas Gerais, Brazil - The Cuiabá Mine. Aachen University of Technology, Augustinus Verlag, Aachener Geowissenschaftliche Beiträge, pp 264.

Ribeiro-Rodrigues LC, de Oliveira CG, Friedrich G (2007) The Archean BIF-hosted Cuiabá Gold deposit, Quadrilátero Ferrífero, Minas Gerais, Brazil. Ore Geology Reviews 32:543-570.

Robert F, Poulsen KH, Cassidy KF, Hodgson CJ (2005) Gold Metallogeny of the Superior and Yilgarn Cratons. Economic Geology 100th Anniversary Volume:1001-1034.

Sales M (1998) The Geological Setting of the Lamego Banded Iron-Formation-Hosted Gold Deposit, Quadrilátero Ferrífero District, Minas Gerais-Brazil. Geology Department. Queen's University, Ontario pp 182.

Schorscher HD (1988) NE Quadrilátero Ferrífero and adjacent areas. International Conference Geochemical Evolution of the Crust. Poços de Caldas, pp 1.

Seixas LAR, David J, Stevenson R (2012) Geochemistry, Nd isotopes and U–Pb geochronology of a 2350 Ma TTG suite, Minas Gerais, Brazil: Implications for the crustal evolution of the southern São Francisco craton. Precambrian Research 196:61-80.

Sibson RH, Robert F, Poulsen KH (1988) High-angle reverse faults, fluid-pressure cycling, and mesothermal gold-quartz deposits. Geology 16:551-555.

Steadman JA, Large RR, Meffre S, Olin PH, Danyushevsky LV, Gregory DD, Belousov I, Lounejeva E, Ireland TR, Holden P (2015) Synsedimentary to early diagenetic gold in black shale-hosted pyrite nodules at the Golden Mile Deposit, Kalgoorlie, Western Australia. Economic Geology 110:1157-1191.

Stern R, Sanborn N (1998) Monazite U–Pb and Th–Pb geochronology by high-resolution secondary ion mass spectrometry. Radiogenic age and isotopic studies: Report 11:1-18.

Stern RA, Rainbird RH (2001) Advancements in xenotime U-Pb geochronology by ion microprobe Eleventh Annual VM Goldschmidt Conference. pp 3872.

Taylor RG, Pollard PJ (1993) Mineralized breccia systems: Methods of recognition and interpretation. Economic Geology Research Unit.

Teixeira W, Ávila C, Dussin I, Neto AC, Bongiolo E, Santos J, Barbosa N (2015) A juvenile accretion episode (2.35–2.32 Ga) in the Mineiro belt and its role to the Minas accretionary orogeny: Zircon U–Pb–Hf and geochemical evidences. Precambrian Research 256:148-169.

Thorper RI, Cumming Gl, Kristic D (1984) Lead isotope evidence regarding age of gold deposits in the Nova Lima district, Minas Gerais, Brazil. Revista Brasileira de Geociências 14:147-152.

Tomkins AG, Mavrogenes JA (2002) Mobilization of gold as a polymetallic melt during pelite anatexis at the Challenger deposit, South Australia: a metamorphosed Archean gold deposit. Economic Geology 97:1249-1271.

Tomkins AG, Pattison DRM, Zaleski E (2004) The Hemlo Gold Deposit, Ontario: An example of melting and mobilization of a precious metal-sulfosalt assemblage during amphibolite facies metamorphism and deformation. Economic Geology 99:1063-1084.

Tomkins AG, Grundy C (2009) Upper temperature limits of orogenic gold deposit formation: constraints from the granulite-hosted Griffin's Find deposit, Yilgarn Craton. Economic Geology 104:669-685.

Vial D, Abreu G, Schubert G, Ribeiro-Rodrigues L (2007a) Smaller gold deposits in the Archean Rio das Velhas greenstone belt, Quadrilátero Ferrífero, Brazil. Ore Geology Reviews 32:651-673.

Vial DS, DeWitt E, Lobato LM, Thorman CH (2007b) The geology of the Morro Velho gold deposit in the Archean Rio das Velhas greenstone belt, Quadrilátero Ferrífero, Brazil. Ore Geology Reviews 32:511-542.

Vial D, Duarte B, Fuzikawa K, Vieira M (2007c) An epigenetic origin for the Passagem de Mariana gold deposit, Quadrilátero Ferrífero, Minas Gerais, Brazil. Ore Geology Reviews 32:596-613.

Vieira FWR (1991) Textures and processes of hydrothermal alteration and mineralization in the Nova Lima Group, Minas Gerais, Brazil. In: Ladeira EA (ed) Proceedings of Brazil GOLD '91, Belo Horizonte/MG. AA Balkema/Rotterdam/ Brookfield, pp 319-327.

Villanova FLSP (2011) Mapeamento Geológico em escala 1:5.000 da superfície e região circunvizinha da Mina Lamego, Sabará, Minas Gerais. Universidade Federal de Minas Gerais, pp 80.

Vollgger SA, Cruden AR, Cowan JE (2013) 3D implicit geological modelling of a gold deposit from a structural geologist's point of view In: Applied SG (ed) 12th SGA Biennial Meeting - Mineral Deposit Research for a High-Tech World. SGA, Uppsala, Sweden.

Wilkinson JJ, Boyce AJ, Earls G, Fallick AE (1999) Gold remobilization by low-temperature brines: Evidence from the Curraghinalt gold deposit, Northern Ireland. Economic Geology and The Bulletin of the Society of Economic Geologists 94:289-296.

Zhang J, Deng J, Chen H-y, Yang L-q, Cooke D, Danyushevsky L, Gong Q-j (2014) LA-ICP-MS trace element analysis of pyrite from the Chang'an gold deposit, Sanjiang region, China: Implication for ore-forming process. Gondwana Research 26:557-575.